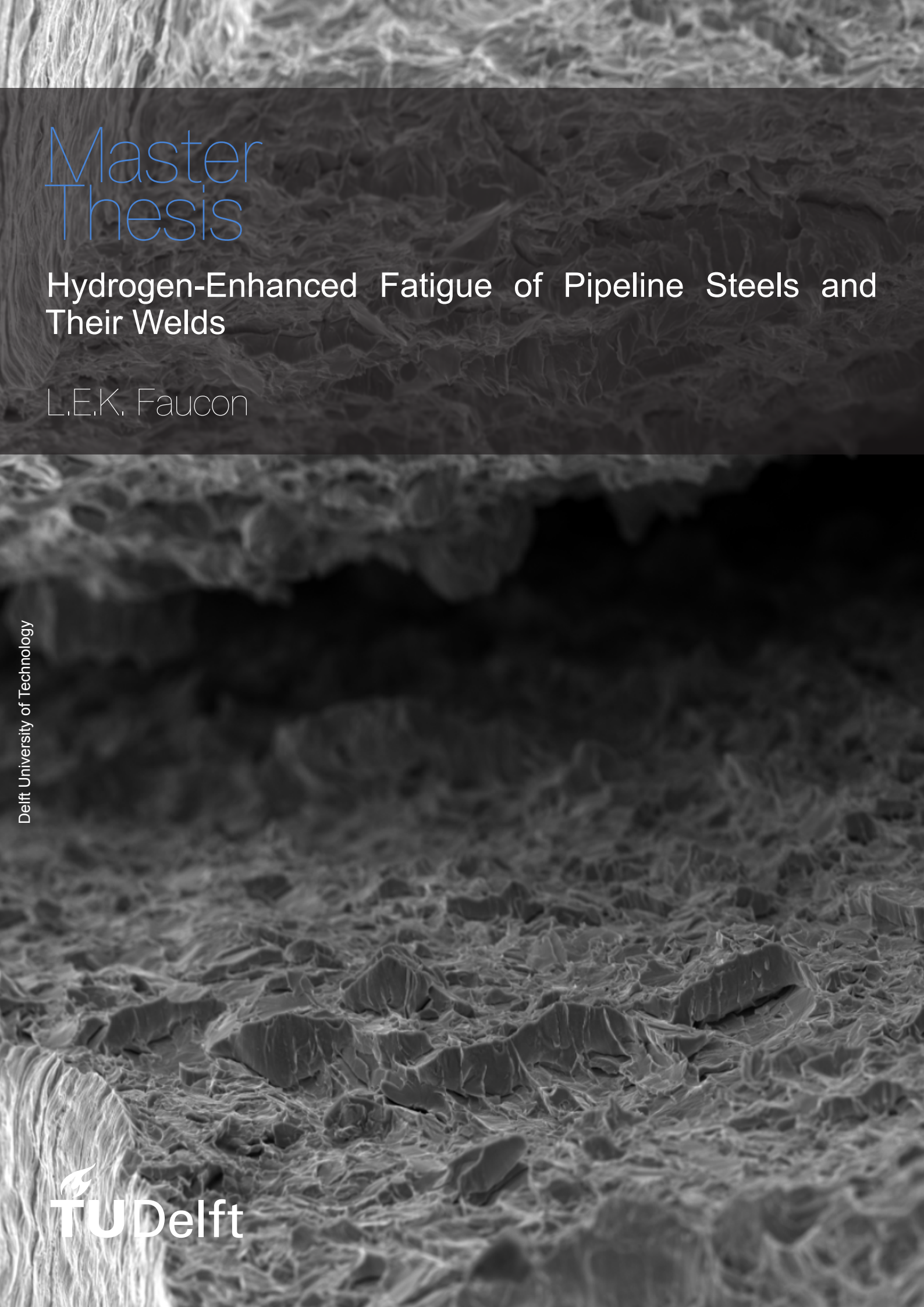
Master
Thesis
Hydrogen-Enhanced Fatigue of Pipeline Steels and Their Welds
L.E.K. Faucon
Delft University of Technology
TU Delft

Hydrogen-Enhanced Fatigue of Pipeline Steels and Their Welds

by

L.E.K. Faucon

A master's dissertation submitted in partial fulfillment of the requirement
for the award of Master of Science (MSc) degree in Materials Science and Engineering,
at the Delft University of Technology,
to be defended publicly on Tuesday September 13, 2022 at 9:30 AM

Student Number: 4632966
Project Duration: February 1, 2021 - September, 2022
Thesis Committee:

Dr. Vera Popovich	TU Delft Department of MSE, supervisor
Ir. Tim Boot	TU Delft Department of MSE. supervisor
Dr. Marcel Hermans	TU Delft Department of MSE
Dr. Poulumi Dey	TU Delft Department of MSE
Dr. Ping Liu	Intecsea

Cover Image: Liquid nitrogen induced brittle fracture of X60 steel.

TU Delft

Acknowledgements

A special gratitude I give to Dr. Vera Popovich, for her stimulating suggestions, daily supervision and most importantly for offering me the chance to work on a fascinating project in the field of materials engineering. Furthermore, I would like to express my appreciation to Tim Boot and Dr. Ton Riemslag who invested their effort in guiding my experiments. In addition, thanks to Sean Scott for providing support in the lab and creative solutions. I am grateful to Dr. Ping Liu and Intecsea for the collaboration. My special thanks are extended to Dr. Niels Kerstens and Ruud Selker, from whom I learned a lot about the offshore industry. Furthermore, a special thank you to Dr. Poulumi Dey and Dr. Marcel Hermans for their participation in my assessment committee. A final thank you to my family, friends and partner who have encouraged me through this challenging MSc project. They taught me to overcome and handle non-successful situations, listened to my challenges I have faced during this project and ultimately, reminded me of the amazing work I contribute to.

L.E.K. Faucon
Delft, September 2022

Abstract

Hydrogen as an alternative energy source has risen in popularity due to increased environmental awareness. Existing natural gas infrastructure is considered as a means to transport hydrogen, due to practicality and financial aspects. However, hydrogen can deteriorate the fatigue behaviour and thus induce premature failure. Since fatigue is a common failure mode in pipelines, a more thorough understanding of the effects of hydrogen on fatigue behaviour is required.

In this work, the hydrogen fatigue of X60 pipeline steel and its girth welds was investigated through a combined approach of modelling and in-situ fatigue testing. A novel in-situ gaseous hydrogen charging fatigue set-up was developed, which involves a sample geometry that mimics a small-scale pipeline with high internal hydrogen gas pressure. The specimen geometry involved an internal circumferential notch that induces a stress concentration factor (K_t = 3.0) related to the worst case scenario for pipelines. The effect of hydrogen was investigated by measuring the onset of crack initiation and growth using a newly designed direct current potential drop setup which probes the outer surface of the specimen. A FEA modelling approach was used to estimate the hydrogen equilibrium concentration in the specimens, as well as to determine the stress states in the material.

Results showed that both materials experienced a reduction in fatigue life in the presence of hydrogen. For the base metal, the reduction in fatigue life (37%) manifested solely in the crack growth phase; hydrogen accelerated the crack growth (factor 4). In contrast, the reduction in fatigue life (68%) of the weld metal was due to accelerated crack growth (factor 8) and a decrease in resistance to crack initiation (57%). Varying the hydrogen gas pressure from 70 barg to 150 barg did not cause any differences in the fatigue behaviour.

The presence of hydrogen influenced the fracture mechanisms of both materials. The fracture path of the base metal transitioned from transgranular and ductile in nature, to a mixed-mode transgranular and intergranular quasi-cleavage fracture. The weld metal exhibited a similar transition, however in the inert environment some intergranular features were observed at the prior austenite grain boundaries. The presence of hydrogen reduced the crack tortuosity. This is associated with a decrease in roughness- and plasticity-induced crack closure, thereby accelerating the crack growth. It is inferred that hydrogen-enhanced localised plasticity (HELP) and hydrogen-enhanced decohesion (HEDE) were the dominant types of hydrogen embrittlement mechanisms during fatigue of this pipeline material.

It was concluded that the weld metal is more susceptible to hydrogen fatigue than the base metal in a gaseous hydrogen environment. The worst-case scenario for pipelines is in the case of weld defects. The weld defects involved in this work were macropores (0.5-1.0 mm) with a spheroid morphology. When these defects were located at the notch surface, the resistance to crack initiation decreased by 92% compared to non-porous specimens in nitrogen. The existing natural gas infrastructure could have accumulated similar flaws during service life, which would make them unreliable for safe hydrogen transport. The costs associated with the repurposing of these pipe segments could raise unexpected economic hurdles, hindering the transition to a hydrogen economy.

Contents

Acknowledgements i

Abstract ii

Nomenclature v

List of Figures vi

List of Tables ix

1 Introduction 1
- 1.1 Hydrogen Projects . . . 1
- 1.2 Hydrogen Embrittlement . . . 2
- 1.3 Problem Statement . . . 3
- 1.4 Thesis Structure . . . 3

2 State of the art 4
- 2.1 Pipeline Steels . . . 4
  - 2.1.1 Pipeline Steel Grades . . . 4
  - 2.1.2 Alloy Composition and Processing Treatments . . . 4
- 2.2 Hydrogen and its Interaction with Steel . . . 5
  - 2.2.1 Entry of Hydrogen . . . 5
  - 2.2.2 Hydrogen Trapping . . . 7
  - 2.2.3 Hydrogen Embrittlement Mechanisms . . . 8
- 2.3 Fatigue in Inert Environments . . . 10
- 2.4 Fatigue in Hydrogen Environments . . . 12
  - 2.4.1 Effect of Gas Pressure . . . 13
  - 2.4.2 Effect of Stress Ratio . . . 14
  - 2.4.3 Effect of loading frequency . . . 15
  - 2.4.4 Effect of microstructure . . . 16
- 2.5 Characteristic Hydrogen Fatigue Fracture Surfaces . . . 17
- 2.6 Hydrogen Fatigue Testing . . . 21
  - 2.6.1 Hydrogen Charging Methods . . . 21
  - 2.6.2 Techniques to monitor crack initiation and growth . . . 22
- 2.7 Conclusions and Research Objectives . . . 25
  - 2.7.1 Conclusions . . . 25
  - 2.7.2 Research Objectives . . . 26
  - 2.7.3 Approach . . . 26

3 Materials and Methods 27
- 3.1 Material Characterisation . . . 27
  - 3.1.1 Pipe Type . . . 27
  - 3.1.2 Specimen Design . . . 27
  - 3.1.3 Microstructure Preparation . . . 29
  - 3.1.4 Characterisation Methods . . . 29
- 3.2 In-situ Gaseous Fatigue Set-up . . . 31
  - 3.2.1 In-situ Gaseous Charging Design . . . 31
  - 3.2.2 Direct Current Potential Drop . . . 32
  - 3.2.3 Test Matrix and Procedure . . . 36
- 3.3 Computational Methods . . . 38
  - 3.3.1 Hydrogen Diffusion Model . . . 39
  - 3.3.2 Fatigue Model . . . 42

4 Results and Discussion **44**
4.1 Material Characterisation . . . 44
4.1.1 Base Material . . . 44
4.1.2 Weld Metal and HAZ . . . 45
4.1.3 Mechanical Properties . . . 49
4.2 Hydrogen-Enhanced Fatigue of Base Metal . . . 51
4.2.1 BM Fatigue Model . . . 51
4.2.2 The Effect of Environment . . . 54
4.3 Hydrogen-Enhanced Fatigue of Weld Metal . . . 59
4.3.1 WM Fatigue Model . . . 59
4.3.2 The Effect of Environment and Hydrogen Gas Pressure . . . 61
4.4 Fracture Surface Analysis . . . 66
4.4.1 Fatigue Fracture Surface Overview . . . 66
4.4.2 Weld Defects . . . 68
4.4.3 Base Metal . . . 71
4.4.4 Weld Metal . . . 75
4.4.5 Crack Path Analysis . . . 79
4.4.6 Base Metal versus Non-Defected Weld Metal . . . 86

5 Conclusions and Recommendations **87**
5.1 Conclusions . . . 87
5.2 Recommendations . . . 89

References **100**

Appendices **101**
A Test Details . . . 101
A.1 Engineering Drawing of Specimen with Full Specifications . . . 101
A.2 Test Procedure DCPD . . . 101
B Insulation . . . 103
B.1 Electrical Insulation for Electromechanical Testing Machine . . . 103
C Additional information for design and computational models . . . 104
C.1 Specimen Design . . . 104
C.2 Effect of Stress Concentration Factors on HE and HA-FCG . . . 104
C.3 Stress Concentration Factor of Designed Notch . . . 104
C.4 Calculation Sievert's Law . . . 105
D Direct Current Potential Drop Calibration Results . . . 106
E Additional Information For Fatigue Model . . . 107
E.1 Plastic strain in air specimen . . . 107
E.2 End-cap Effect . . . 107
E.3 Stress Triaxiality . . . 107
F Supplementary Figures Weld Metal Outgassing Effect . . . 109
G Supplementary Figures Fracture Surface Analysis . . . 111
G.1 SEM Fractography Area III BM . . . 111
G.2 SEM Fractography BM Air . . . 113
G.3 SEM Fractography 70 barg Hydrogen WM . . . 114
G.4 SEM Fractography Area III WM . . . 115
H Electrical Discharge Machined Surface . . . 116

Nomenclature

Abbreviations

Abbreviation	Definition
AIDE	Adsorption Induced Dislocation Emission
BM	Base Metal
DCPD	Direct Current Potential Drop
FCG	Fatigue Crack Growth
FCGR	Fatigue Crack Growth Rate
HA-FCGR	Hydrogen-Assisted Fatigue Crack Growth Rate
HE	Hydrogen Embrittlement
HEDE	Hydrogen Enhanced Decohesion
HELP	Hydrogen Enhanced Localized Plasticity
HESIV	Hydrogen Enhanced Strain Induced Vacancy Formation
IG	Intergranular
LT_{CI}	Percentage of lifetime spent in the crack initiation phase
LT_G	Percentage of lifetime spent in the crack growth phase
N_{CI}	Number of cycles spent in the crack initiation phase
N_G	Number of cycles spent in the crack growth phase
N_F	Number of cycles till failure
TG	Transgranular
SCF	Stress Concentration Factor
WM	Weld Metal

Symbols

Symbol	Definition	Unit
ΔK	Nominal stress intensity range	[MPa$\sqrt{\text{m}}$]
a	Crack length	[mm]
F	Force	[N]
f	Loading frequency	[1/s]
N	Number of cycles	
R	Stress ratio	
σ	Stress	[MPa]

List of Figures

1.1 Expected mature hydrogen pipeline infrastructure in Europe by 2040. 2

2.1 Evolution of pipeline steel grades. 5
2.2 The hydrogen uptake process of metals. 6
2.3 Schematic illustrations of possible hydrogen trapping sites in metals. 9
2.4 Characteristics of the fatigue crack growth rate curve, d*a*/d*N* versus ΔK. Adapted from [154]. 11
2.5 The types of fatigue crack growth behaviour observed in hydrogen environments [194]. 12
2.6 d*a*/d*N* versus ΔK plot of low carbon steel JIS-SM490B [197]. 14
2.7 d*a*/d*N* versus ΔK curves of X52 pipeline steel[176]. The data of X42 in nitrogen environment was taken from the work of Cialone et al. [42]. 14
2.8 Relative d*a*/d*N* versus cyclic loading frequency for low-carbon steel JIS-SM490B [197]. 15
2.9 Comparison between SEM fractographs of samples tested for fatigue in different environments [135]. (a) low ΔK in ambient air, (b) at high ΔK in ambient air, (c) CH_4/H_2 gas mixture pressurised to 10 MPa containing 1% H_2 and (d) 100 % H_2 gas pressurised to 10 MPa. (e) And (f) serve as schematic representations of the fatigue fracture morphologies under ambient air and a hydrogen-containing environment, respectively. 18
2.10 Figure including illustrations of fracture mechanisms in metals [170] and an example of a dimpled fracture surface of 316L stainless steel [105] 19
2.11 The model of hydrogen-induced intergranular fracture proposed by Shinko et al. Adapted from [169]. 20
2.12 SEM fractographs of hydrogen-fatigued X70 pipeline steel [53]. The specimen were tested at a H_2 gas pressure of 5.5 MPa, a *R* of 0.5 and a *f* of 1 Hz. 21
2.13 HA-FCG results of X100 pipeline steel divided into three regions: A, B, and C [6]. The fatigue tests conducted in the hydrogen environments and air environment were both tested at a *R* of 0.5 and a *f* of 1 Hz. 21
2.14 Principles of the direct current potential drop technique. 23
2.15 Arrangement of the notched rod for multiple potential drop measurements (PD). 24
2.16 Experimental results of a crack initiation in the position in close proximity to potential probe 1. 24

3.1 Engineering drawing illustrating the geometry of the specimen and its notch. 28
3.2 Orientation of the prepared specimens of the pipeline material. 28
3.3 Illustration of sample preparation for crack path analysis. 30
3.4 General overview of the test setup, displaying a specimen enclosed by DCPD parts, the adapters used, and the gas supply system. 31
3.5 Illustration of the modified adapters made compatible with DCPD measurements. The (modified) parts are indicated by annotations. 33
3.6 Illustration of the positions of the DCPD probes. 34
3.7 Insulation of the MTS hydraulic testing machine. 34
3.8 DCPD results and analysis of air specimen A1.1. 35
3.9 Illustration of the fatigue test conditions. 38
3.10 Boundary conditions of the diffusion models. 40
3.11 a) Diffusion model of a 6 hour 150 barg H_2 gas pre-charged weld specimen. Units are mol/mm^3. b) Close-up of the notched weld region of a). In both a) and b) it is assumed that a hydrogen equilibrium state was reached. The purple line indicates the separation between the base and weld metal regions. 41
3.12 The evolution of the hydrogen concentration profile, at different pre-charging durations, at the notch surface of a 150 barg internally pressurised weld specimen. 41

3.13 Boundary conditions and loads of the fatigue model. 43

4.1 Keyence image of the banded microstructure in X60 pipeline steel base material consisting of ferrite (white) and pearlite (black). 44
4.2 Microstructure at the outer surface of the pipe wall a) and microstructure at the middle section of the pipe wall b). Differences in grain sizes can be observed and the elongated appearance of the grains can be seen. Both images were taken at 50 times magnification. 45
4.3 SEM close-up image of the centerline segregation band in the X60 pipeline steel base material. The segregation band was identified to consist of the microstructures degenerated pearlite and bainite. 46
4.4 Macro. 46
4.5 The microstructure of the weld metal revealing a) columnar prior austenite grains and b) Widmanstätten ferrite structures from the prior austenite grain boundaries. 47
4.6 X100 magnification of the acicular ferrite microstructural phase in the weld metal exposing their short needle-like basket weave appearance. 48
4.7 Overview of microstructures present. 49
4.8 Vickers Hardness (HV1) measurement indentation locations. 50
4.9 Local and global longitudinal stress plotted over time for air and 150 barg pressurised BM specimens. 52
4.10 Display of the longitudinal stress in the internally pressurised (150 barg) specimen at F_{max} (a) and F_{min} (b). 53
4.11 Display of (a) the maximum principal plastic strain in the internally pressurised (150 barg) specimen after loading to F_{max}, and (b) the Von Mesis equivalent stress at F_{max}. 53
4.12 Representative normalised potential drop curves for BM specimens. 54
4.13 Bar graph of the number of cycles spent in the crack initiation phase (N_{CI}) and the growth phase (N_G), and the total number of cycles till failure (N_F) of BM. 56
4.14 Bar graph of the fraction (%) of lifetime spent in the crack initiation phase and growth phase of BM. 57
4.15 Bar graph of the normalised results of the number of cycles spent in the crack initiation phase (N_{CI}) and growth phase (N_G), and the number of cycles till failure (N_F) of BM. . 58
4.16 Comparison of the 150 barg N_2 and 150 barg H_2 normalised potential drop data during gas leak. 59
4.17 Local and global longitudinal stress plotted over time for 150 barg pressurised WM specimen. 60
4.18 Display of the maximum principal plastic strain present, after loading to F_{max}, in the internally pressurised (150 barg) a) BM and b) WM specimen. 60
4.19 Representative normalised potential drop curves for WM specimens. 61
4.20 Bar graph of the number of cycles spent in the crack initiation phase (N_{CI}) and the growth phase (N_G), and the total number of cycles till failure (N_F) of WM. 62
4.21 Bar graph of the fraction (%) of lifetime spent in the crack initiation phase and growth phase of WM. 63
4.22 Bar graph of the normalised average results of the cycles till crack initiation (N_{CI}) and cycles to failure (N_F) of set B. 65
4.23 Normalised potential drop data of a 150 barg H_2 WM specimen with annotations indicating the areas spent in the characteristic fracture area. 67
4.24 Normalised potential drop data of a 150 barg N_2 WM specimen with annotations indicating the areas spent in the characteristic fracture area. 67
4.25 Macropore identification of 150 barg H_2 defected WM specimens. 68
4.26 Micropore identification in 'non-defected' WM specimens. 70
4.30 Magnification of region I (see Fig. 4.29a) for a 150 barg H_2 a) and 150 barg N_2 b) BM tested specimen. The blue arrows indicate secondary cracking. The red arrows mark triple points. 73
4.31 Magnification of region II (see Fig. 4.29a) for a 150 barg H_2 a) and 150 barg N_2 b) BM tested specimen. The blue arrows indicate secondary cracking. The yellow arrows mark ductile striation formation. 73
4.32 Striations in Area II in air a), 150 barg H_2 a) and 150 barg N_2 b) BM tested specimen. . 74

4.33 Transition from Area II to Area III in 150 barg N_2 BM tested specimen. a) Indicates an overview of the transition and b) a close-up view where the increase in spacing of striations can be seen. The crack growth direction is perpendicular to striation formation and is indicated with an arrow. 74
4.34 Overview of Area I in a) 150 barg H_2 and 150 barg N_2 b) WM tested specimen. In a) yellow arrows indicate brittle transgranular cleavage facets, which are postulated to manifest in prior austenite grain boundaries. In b) river patterns are depicted with red arrows. The white arrows in both subfigures indicate ratchet marks. Regions I and II annotated in red, are further magnified in Fig. 4.36 and 4.37, respectively. 75
4.35 Magnification of the fracture surface close to the notch of 150 barg H_2 a) and 150 barg N_2 b) WM tested specimens. 76
4.36 Magnification of region I from 150 barg H_2 a) and 150 barg N_2 b) WM tested specimens. 77
4.37 Magnification of region II from 150 barg H_2 a) and 150 barg N_2 b) WM tested specimens. 77
4.38 Striations in Area II in 150 barg H_2 WM tested specimen. 78
4.39 Transition from Area II to Area III in 150 barg N_2 WM tested specimen. 78
4.40 Crack path analysis on 150 barg N_2 BM specimen. 80
4.41 Crack path analysis on 150 barg H_2 BM specimen. 81
4.42 Crack path analysis on 150 barg N_2 WM specimen. 83
4.43 Crack path analysis on 150 barg H_2 WM specimen. 85

C.1 Display of the longitudinal stress in the specimen when subjected to a nominal stress of 100 MPa. 105
D.1 Identification of the crack surface area a) that corresponds to the potential drop data b). 106
D.2 Relation of potential drop signal to crack surface area (mm^2) 106
E.1 Display of the maximum principal plastic strain present in the internally pressurised (150 barg) specimen after loading to F_{max}. 107
E.2 Display of the triaxial stress-state at F_{max} in a 150 barg pressurised BM specimen. . . . 108
F.1 Zoomed-in projection on the potential drop curves visualising the effect of outgassing on fatigue behaviour. 110
G.1 SEM Analysis of Area III for 150 barg N_2 and 150 barg H_2 BM tested specimens. 111
G.2 SEM fracture surface images of BM air specimen (A1.2). 113
G.3 SEM fracture surface images of 70 barg H_2 WM specimen. 114
G.4 Transition from Area II to Area III in 150 barg N_2 WM tested specimen. 115
G.5 Magnification of the fine-dimple void region from 150 barg H_2 a) and 150 barg N_2 b) WM tested specimens. 115
H.1 The recast layer on the surface of the specimen, resulting from the electrical discharge machining to produce the notch. 116

List of Tables

3.1 X60 commercial pipeline dimensions. 27
3.2 X60 base metal and (girth) weld metal chemical composition (%wt) from the work of Boot et al. [30]. Included are limits on chemical composition as specified in standard API 5L (PSL 2). 29
3.3 Test Matrix including experimental goals. 36
3.4 Base material input data for the Abaqus fatigue model. Values were taken from [30]. . . 42

4.1 Vickers Hardness (HV1) results of the X60 base and weld metal. 49
4.2 Number of cycles spent in the crack initiation phase (N_{CI}) and the crack growth phase (N_G), and the total cycles till failure (N_F) of BM. The data is reported as an average of the subset and also includes the standard deviation. 56
4.3 Fraction of lifetime spent in the crack initiation phase (LT_{CI}) and the growth phase (LT_G) of BM. LT_{CI} and LT_G are calculated with Eq. 4.3 and Eq. 4.4, respectively. The data is reported as an average of the subset and includes the standard deviation. 57
4.4 Normalised values of the average number of cycles spent in the crack initiation phase (N_{CI}) and growth phase (N_G), and the normalised average number of cycles till failure (N_F) of BM. The data of each environment is normalised with respect to the 150 barg N_2 environment. 58
4.5 Number of cycles spent in the crack initiation phase (N_{CI}) and the crack growth phase (N_G), and the total cycles till failure (N_F) of WM and BM specimens. 62
4.6 Fraction of lifetime spent in the crack initiation phase (LT_{CI}) and the growth phase (LT_G) of WM and BM. LT_{CI} and LT_G are calculated with Eq. 4.3 and Eq. 4.4, respectively. The data is reported as an average of the subset and includes the standard deviation. BM data of pressurised environments is included 63
4.7 Normalised values of the average number of cycles spent in the crack initiation phase (N_{CI}) and growth phase (N_G), and the normalised average number of cycles till failure (N_F) of WM and BM. The data of each environment is normalised with respect to their corresponding 150 barg N_2 environment. Data of the pressurised hydrogen environment of the BM is included. 65
4.8 Relation between weld defects and hydrogen fatigue. 69

1 Introduction

The ever-increasing concern about the impact of climate change on sectors important to society, such as human health and ecosystems, has prompted the necessity for a vast transition towards a sustainable society. Forced to adapt the method of sourcing and utilization of energy, hydrogen has surged as a promising alternative energy source indispensable for climate neutrality [19]. The intermittency of other renewable energy sources (RE), such as wind and solar power, forms stability issues for electricity distribution networks. Hydrogen has the potential to form the essential component for RE; namely, the excess energy produced during on-peak hours can be converted into hydrogen through water electrolysis. In this way, energy is stored as hydrogen gas, and the hydrogen gas can be reformed into water to release electricity when demand for energy is high. Ultimately, the (green) hydrogen produced from RE advances the decarbonisation of economic and human activities that rely on fossil fuels [3].

1.1. Hydrogen Projects

Although the potential of hydrogen is renowned, its distribution forms the main hurdle for realization of its development as an alternative energy source [7]. Large-scale implementation of hydrogen necessitates major changes to our existing energy infrastructure, involving huge capital investments. To move forward with national hydrogen strategies, a decision must be made whether to directly re-purpose the existing natural gas (NG) infrastructure, whether the existing NG grid should be partially refurbished or completely replaced by the construction of a new pipeline network with more suitable materials [56]. The impediment to the hydrogen economy is therefore essentially a dilemma between cost-efficiency and reliability.

In July 2022, the Netherlands decided on its next steps forward regarding their hydrogen transport infrastructure. Its latest national hydrogen strategy, '*Hydrogen Infrastructure* (*Gasunie*)', includes ambitious (sub-)projects that should ultimately lead to a 40-50% reduction of CO_2 emissions in the Netherlands by 2030 and a carbon-neutral country by 2050 [66]. The sub-projects are outlined as follows: the expansion of wind farms in the North Sea for sustainable hydrogen production (*NortH2*), the implementation of underground salt caverns for storage (*HyStock hydrogen storage*) and the re-purpose of 85-90% of existing natural gas pipelines for hydrogen transport (*Hydrogen network Netherlands*). The kick-start of the hydrogen market further extends to Europe with a parallel hydrogen project, *European Hydrogen Backbone* (*Guidehouse*) [72]. This project aims to deliver a mature hydrogen (pipeline) infrastructure of 53,000 kilometers in length, connecting 28 European countries by 2040. The total expected capital expenditure for this project concludes €27-64 billion. This estimate assumes that the infrastructure is constructed of approximately 60% re-purposed NG pipelines and of 40% new hydrogen pipeline segments. A graphical representation of the expected hydrogen backbone of Europe in 2040 is shown in Figure 1.1.

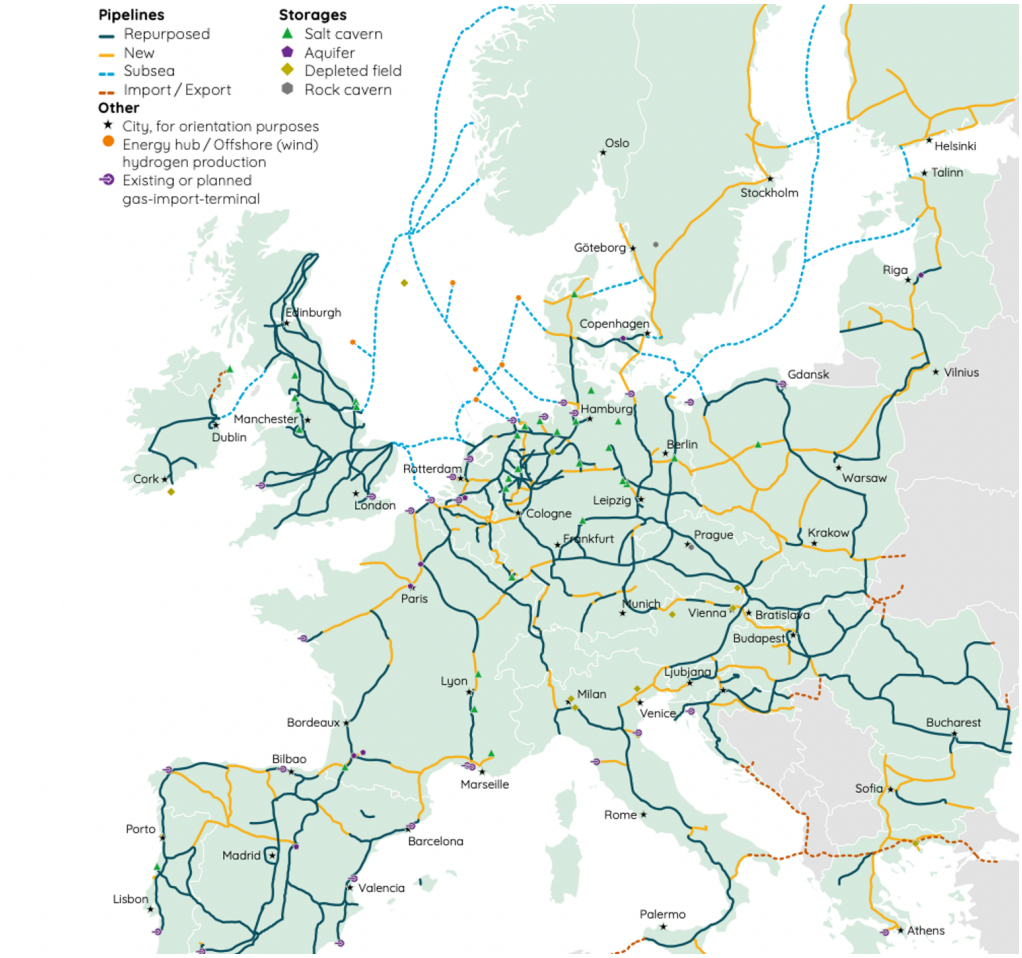

Figure 1.1: Expected mature hydrogen pipeline infrastructure in Europe by 2040. Adapted from [72].

1.2. Hydrogen Embrittlement

The re-purpose of the existing NG infrastructure can be considered questionable in terms of reliability [56]. In particular, the possible introduction and diffusion of hydrogen into pipeline steel has garnered attention regarding safety, as it can cause metal embrittlement, a phenomenon referred to in the literature as *hydrogen embrittlement* (HE). Typical features of HE are reduced ductility and fracture strength, thus the risk of pipeline rupture increases drastically. The interplay between the amounts of (pressurised) hydrogen, the material's microstructure and the mechanical stresses govern the degree of HE [133].

The current network of pipelines consists mainly of ferrous materials, which are known to be susceptible to HE. The effect of HE has already proved catastrophic, as it is a frequent cause of failure in the pipeline industry. While cathodic protection is applied with the aim of protecting offshore structures from corrosion, the negative potential that inhibits corrosion reactions acts as a driving force for the dissociation of hydrogen atoms from seawater and its entry into steel [138]. To prevent hydrogen from entering the steel, coatings are applied to the surface of the pipeline that isolate the structure from the seawater. Once the coating cracks, hydrogen ingress is promoted and a vulnerable area for hydrogen entry, and thus for HE failure, is created [141].

Pipeline hydrogen transport involves constant exposure of the pipe's inside surface to hydrogen, thereby allowing hydrogen to diffuse into the steel. This hydrogen exposure combined with mechanical stresses experienced during field use can adversely affect the lifetime of the structure. Pipeline welds, in particular, are considered to be at high risk of HE failure due to: the combination of localised stress concentrations in weld misalignment, weld porosity and the susceptible microstructure itself [161, 10, 160].

Therefore, the use of the existing NG infrastructure for the transport of hydrogen cannot be undertaken completely without concerns.

1.3. Problem Statement

Fatigue cracking and fractures arising from stress concentrators are at the origin of more than 90% of failures during operation [35]. While experimental evidence supports that hydrogen affects the mechanical properties of steels, fundamental understanding of the effects that hydrogen has on the initiation and propagation of fatigue cracks has not yet been achieved [74, 203, 59]. Since fatigue is a common failure mode in pipelines, the effect of hydrogen on fatigue behaviour necessitates a more thorough understanding. This master's thesis project is a collaboration between TU Delft and Intecsea, and has as its main focus the evaluation of the safety of re-purposed offshore NG pipelines. This thesis aims to approach this objective by gaining new insights in, and reflecting on, the effects of hydrogen gas on the fatigue of X60 pipeline steels and their girth welds.

1.4. Thesis Structure

This thesis presents new knowledge on the influence of hydrogen gas on the fatigue behaviour of X60 pipeline steel and its girth weld. Results have been obtained with the realisation and use of a novel *in-situ* gaseous hydrogen fatigue test set-up, which can monitor the initiation of fatigue cracks. In this thesis, several topics are addressed, each in a separate chapter. **Chapter 2** is a comprehensive literature review on the interaction of hydrogen with steel, the resultant embrittlement effects it has on the fatigue behaviour and how this embrittlement is characterised. **Chapter 3** focuses on the characterisation of the X60 pipeline material, the experimental procedures conducted and the computational models used in this thesis. **Chapter 4** presents and discusses the results of the (fatigue) tests. This thesis concludes with **Chapter 5**, which draws firm conclusions based on the comparison of various results and formulates recommendations for future research in the similar metallurgical field.

2

State of the art

This Chapter serves to outline relevant findings from academic sources and is conducted in preparation for the experimental research in this thesis. First, background information on pipeline steels is provided. Secondly, the interaction of hydrogen with steel is outlined, focusing on the ingress of hydrogen and its distribution in steel. Then, the resulting effect of hydrogen is addressed by describing various embrittlement mechanisms. Following this, the general concepts related to fatigue are recalled and a comparison with the hydrogen environment is made by elaborating on the effect of internal and external parameters, and the characterisation of the hydrogen effects. Lastly, an overview is given of various hydrogen fatigue test methods, including hydrogen charging methods and crack growth measurement techniques.

2.1. Pipeline Steels

2.1.1. Pipeline Steel Grades

Various types of pipeline steels with different properties exist, which have been characterised in the API (American Petroleum Institute) Specification 5L; a standard covering specifications for seamless and welded steel pipes purposed for transportation of petroleum and NG [12]. This standard covers distinct steel grades: A, B and X42-120. Each grade can be distinguished by delivery conditions, chemical composition and limits of mechanical properties (i.e. yield strength, tensile strength and elongation). Regarding the X42-120 grades, the numbers refer to the minimum yield strength in *ksi*, where one *ksi* is equivalent to 6.9 MPa. In general, pipelines are designed to be tough and ductile rather than strong. For their application, high strain capacity is needed to distribute deformation more uniformly, thus reducing the onset of localised deformation. In this way, pipeline steels are able to sustain plastic deformation in hostile environments [162].

Since the 1970's, the dominant types of NG offshore pipeline steel are grades X52, X60 and X70 [57]. The main reason behind this is that a cost-effective and relative ductile structure can be achieved, which simultaneously takes into consideration the need for negative buoyancy and protection against plastic collapse or buckling [71, 62]. Pipelines constructed of the above-mentioned grades typically operate at pressures between 3.5-10 MPa. These steel grades would be compatible for hydrogen gas transportation, since 1-5.0 MPa is the expected pressure range at which hydrogen pipelines will operate. [53].

2.1.2. Alloy Composition and Processing Treatments

As early as the 1940's, it became evident that by controlling the alloy composition an increase in strength could be achieved. This result can nowadays be attributed to the principles of solid-solution hardening, precipitation hardening and microstructure refinement [189, 184]. While the effect of solid solution hardening is intricately linked to the type of alloying element, precipitation hardening and grain refinement effects highly depend on the interaction between the chemical compositions and processing conditions.

The introduction of thermomechanically controlled processes (TMCP), which is in principal a combination of deformation operations and heat treatments, has lead to simplification of chemical compositions [86]. In the initial stages of pipeline manufacturing, steels were hot rolled or normalised after hot rolling, and had a characteristic ferrite-pearlite microstructure [192]. The invention of accelerated cooling (AcC) resulted in acicular ferrite, pearlite, and bainite with overall grain size refinement [69]. The quenching and tempering of pipeline steels resulted in microstructures containing tempered martensite, bainite and ferrite. Overall, this heat treatment achieves smallest grain sizes. In addition, due to the hardening constituents in its microstructure, yield stress and ultimate tensile strength of these steels are higher than steels with ferrite-pearlite rich microstructures [68]. Also, excess hardness and residual stresses are significantly reduced due to the tempering process. Further controlling the cooling rates promotes bainite in the microstructure, thereby strengthening the material. For the reason that grain refinement results in enhanced strength and toughness, higher graded pipeline steels conventionally have smaller average grain sizes compared to the lower grades. Fig. 2.1 summarises the changes in processing conditions and (main) alloying elements that have resulted in different steel grades throughout the years. It is evident that grain refinement and yield strength have increased over the years, leading to modern steels of high grades.

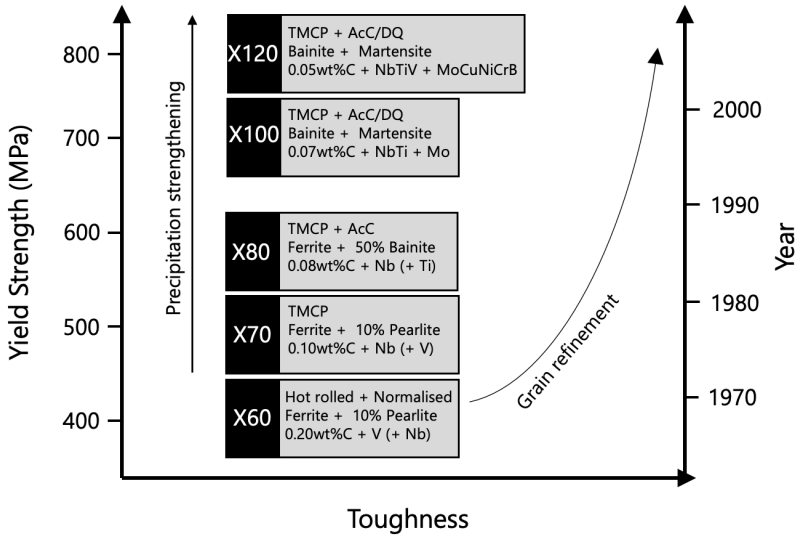

Figure 2.1: Evolution of pipeline steel grades [162]. AcC refers to accelerated cooling, DQ stands for direct quenching, and TMCP is short for thermomechanical controlled processing. Based on the work of [162].

2.2. Hydrogen and its Interaction with Steel

The detrimental effects of hydrogen on the mechanical behavior of metallic materials is a series of multiple time-dependent physical processes. Hydrogen-induced degradation invariably initiates with the supply of molecular or atomic hydrogen to the structure and its subsequent introduction therein. In terms of supply, a distinction is made between the introduction of hydrogen during the manufacturing chain and during the operational conditions of structures involving environmental exposure of hydrogen. This section deals exclusively with the latter case, focusing specifically on gaseous and ionic hydrogen.

2.2.1. Entry of Hydrogen

Gaseous Hydrogen

The transition of hydrogen in its gas phase to it diffusing within the bulk metal can be described by the successive occurrence of three different steps: *physisorption*, *chemisorption* and *absorption* [108]. As can be seen in Fig. 2.2, gaseous H_2 in the vicinity of the metal is first adsorbed to the metal surface. The initial step of adsorption is physisorption. H_2 gas comes into contact with the metal surface and Van der Waals forces 'bind' the H_2 molecules to the solid metal surface. This is a reversible process and the energy for physisorption is relatively low (< 20 kJ mol^{-1}) as it does not involve sharing or trans-

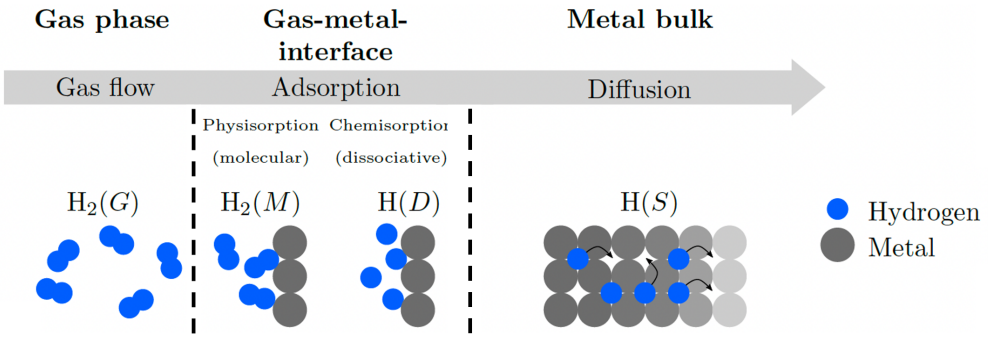

Figure 2.2: The hydrogen uptake process of metals. Illustrated are the sequential steps of the initial gas phase, the ad- and absorption process, and the bulk diffusion. Adapted from[13].

fer of electrons [146]. The second step is chemisorption, where diatomic hydrogen disassociates to two H atoms that subsequently adsorb on the surface and in sub-surface layers (H_{ads}) of the steel due to short-range chemical interactions (Eq. 2.1). Similarly to physisorption, chemisorption is also a reversible process. However, chemisorption is relatively slow due to the high dissociation energy (4.47 eV) of hydrogen gas molecules and high adsorption energy ($\sim$ 200 kJ mol^{-1}) [151].

An adsorbed H atom can be absorbed (Eq. 2.2), which signifies a state where a H atom resides in the crystal surface layer as an interstitial solute (H(*S*) in Fig. 2.2). Instead of being absorbed by the metal, the adsorbed hydrogen can also recombine into hydrogen gas (reverse reaction of Eq. 2.1). For absorbed hydrogen atoms, the hydrogen concentration gradient promotes diffusion into the metal bulk as the system pursues chemical equilibrium.

$$H_2(g) \rightleftharpoons 2H_{ads} \tag{2.1}$$

$$H_{ads} \rightleftharpoons H_{abs} \tag{2.2}$$

Both of the above-mentioned equations represent reversible reactions, hence equilibrium will be reached eventually between the concentration of hydrogen in the steel and the hydrogen gas in the environment. Sieverts was the first to describe this equilibrium for diatomic gases in 1929 [172]. The "Sieverts' law" he formulated is more commonly known in the form described by Hirth [78]:

$$c_0 = 0.00185\sqrt{P_{H_2}}\exp^{\frac{-3440}{T}} \tag{2.3}$$

This equation is used to predict the concentration of dissolved hydrogen in a metal under thermodynamic equilibrium. c_0 denotes the atom fraction of atomic hydrogen at the surface and sub-surface layers, in equilibrium with the partial pressure of the H_2 gas, P_{H_2} (in bar). The term 0.00185 was empirically obtained for diatomic gases. T refers to the absolute temperature (in K).

Ionic Hydrogen

This form of hydrogen typically originates from corrosion processes, and therefore is predominant in pipelines operating in acidic soil conditions and ones that transport sour gas or liquid containing H_2S [204]. Ionic hydrogen can migrate from the corrosive environment to the pipeline steel through its electrophoretic mobility, which is induced by cathodic protection. Saturation of the pipeline steel with hydrogen is then possible due to the cathodic current or potential created in the metal [185]. For *in-situ* HE studies, the simulation of this form of hydrogen (entry) is generally favoured over gaseous hydrogen. This is attributed to the relatively simpler testing requirements for electrochemical (hydrogen) charging systems compared to high-pressure hydrogen gas set-ups [196, 202, 51].

For corrosion processes and electrochemical charging, hydrogen entry into steel occurs through different reactions. Hydrogen atoms adsorb on the metal surface and in sub-surface layers either through hydrogen ion reduction (Eq. 2.4) or water reduction (Eq. 2.5), which are the predominant reactions in acidic and alkaline solutions, respectively [187].

$$H^+ + e^- \rightleftharpoons H_{ads} \tag{2.4}$$

$$H_2O + e^- \rightleftharpoons H_{ads} + OH^- \tag{2.5}$$

The adsorbed hydrogen can then absorb into the pipeline material, or recombine into molecular hydrogen. In the latter case, the hydrogen dissolves in the environment until its solubility limit has been reached, thereafter it forms gas bubbles on the metal surface.

As the effect of gaseous hydrogen on fatigue is the main focus of this thesis, further concepts related to ionic hydrogen are not included. This introductory information on ionic hydrogen is provided to the reader to understand and relate the hydrogen entry into steel during electrochemical studies to gaseous hydrogen studies.

Impeding Hydrogen Entry (I): the role of an oxide layer
Hydrogen adsorption can be strongly influenced by the surface conditions of the metal. For instance, an oxide layer residing on the metal surface can drastically impede H_2 adsorption and H absorption reactions [114]. As a result, the hydrogen flux and hydrogen diffusion efficiency into the metal reduce significantly, thereby ultimately delaying or even preventing HE [27].

Oxide layers may be produced on the surface of the pipeline steel prior to their operation, but may also be formed, to some extent, passively by corrosion in the presence of oxygen. However, this heavily depends on the chemical composition of the steel and electrochemical conditions. Li et al. studied the effect of a Fe_2O_3 structured oxide layer (thickness of 1.61 μm) on X80 pipeline steel [106] and reported that the slow diffusion rate of hydrogen in the oxide film, which was 31-fold lower than the rate of hydrogen diffusion in the base metal, limited the ability of hydrogen to reach the base metal surface. In their study, slow strain rate tensile (SSRT) tests were performed in a 10 MPa high-pressure hydrogen atmosphere and it was showed that the decreased plasticity due to the hydrogen environment (HE index) lowered from 40.96% to 11.61%. These findings appear to be consistent in literature [200].

Impeding Hydrogen Entry (II): the role of gas impurities
The presence of large defects in the oxide layer that expose the pipeline steel to the hydrogen environment does not necessarily imply that HE will be induced. In fact, this also depends on the gas purity to which the (pipeline) steel is exposed [134, 176, 160]. There exists conclusive evidence that gas impurities, with the most important one being oxygen, can inhibit embrittlement processes. These impurity gas molecules can adsorb on the steel surface through chemisorption, thereby blocking the adsorption of hydrogen on the surface. There is however a concern with the addition of oxygen to hydrogen gas, as it might impose flammability issues when the two gases are mixed [63].

The extent to which oxygen impurities can prevent hydrogen penetration during fatigue depends on the oxygen concentration ($\geq$ 100 vppm for an inhibiting effect) and the crack size, which must be sufficiently small. Staykov et al. proposed that inhibition by oxygen impurities is attributed to the competitive interaction of hydrogen and oxygen on the steel surface [178]. Based on density functional theory calculations, it was stated that the reaction rate constant for hydrogen dissociation on an iron surface is significantly lower in the presence of oxygen. In particular, the reaction rate in a pure hydrogen environment can be up to nine orders of magnitude higher. In contrast to hydrogen, oxygen can dissociate at the metal surface without an activation barrier. Therefore, oxygen adsorbs to the metal surface more readily than hydrogen. Somerday et al. similarly suggested that oxygen impedes hydrogen adsorption; it forms a layer that passivates the crack tip [176]. However, when a crack reaches a critical crack length, the rate of new surface creation out-competes the repassivation rate of oxygen, thereby exposing the iron surface to atomic hydrogen and allowing embrittlement [93].

2.2.2. Hydrogen Trapping

Absorbed hydrogen can move within the metal by jumping from one interstitial site to another, which is a mechanism called interstitial diffusion. The theoretical and computational models describing hydrogen diffusion are often based on perfect lattices, thus not accurately reflecting reality [75, 89, 166].

Localised hydrostatic stress regions, such as the near-tip region of cracks act as accumulation zones for diffusible hydrogen [104]. In a similar manner, lattice imperfections and microstructural features can act as *trapping sites* that hinder hydrogen diffusion [140, 186].

The different types of trapping sites that can be present in a metal are illustrated in Fig. 2.3. Hydrogen atoms tend to occupy these trapping sites, rather than interstitial sites, as it reduces the free energy of the hydrogen-steel system. The release of hydrogen from a trapping site requires an energy value greater than the sum of the trapping site's binding energy and the saddle energy [115].The saddle energy is often set to the activation energy for hydrogen diffusion in interstitial lattice sites ($\approx$ 4-10 kJ mol^{-1} H) [92]. As the saddle energy is constant for all types of trapping sites, the binding energies are used for determining (relative) trapping strengths [26]. Lynch investigated the strength of distinct trapping sites, and arranged them accordingly [113]:

Voids and internal cracks
Inclusion/matrix interfaces
Precipitate/matrix interfaces and strain fields around precipitates
Grain boundaries
Dislocation cores and strain fields
Mono-vacancies and vacancy clusters
Free surfaces and the sites between the first few atomic layers below a surface.
Solute atoms

↑ Trap strength

Trapping sites can be categorised, based on their binding energy, into reversible and irreversible traps. Sites with a low binding energy are called reversible traps, because they allow hydrogen to escape at ambient thermal conditions. Irreversible traps, on the other hand, have a characteristic high(er) binding energy that allows hydrogen to escape only at elevated temperatures. In general, 50 kJ mol^{-1} is considered to be the critical binding energy that separates the reversible traps from the irreversible ones [103, 60, 107]. Care must be taken with the presence of large voids in steel, as this trap is sufficiently large to allow locally accumulated H atoms to recombine into H_2 gas molecules [198]. H atoms in the vicinity of these defects continuously diffuse towards them, intensifying the local pressure build-up of hydrogen gas, with the eventual risk of local cracking of the material.

Several studies have highlighted that high prevalence of irreversible traps increases the amount of hydrogen in steel, but decreases the degree of diffusible hydrogen within the lattice [152, 73, 22]. According to these studies, irreversible traps causes the steel to be less susceptibility to HE, because potential crack initiation sites in the steel lattice are deprived of hydrogen. On the other hand, due to their low binding energy, reversible traps facilitate hydrogen diffusion. Reversible traps can thus act as crack growth enhancers due to their continuous supply of hydrogen to the crack, thereby increasing the HE susceptibility. [70, 122]. The behavior of deep irreversible traps (i.e. defects and large voids), however, deviates from these assertions, as they can themselves act as crack initiation points.

2.2.3. Hydrogen Embrittlement Mechanisms

Throughout the years, several mechanisms have been proposed to explain the phenomena of HE. This section elaborates on the following HE mechanisms: *hydrogen enhanced decohesion* (HEDE), *hydrogen enhanced localised plasticity* (HELP), *adsorption induced dislocation emission* (AIDE) and *hydrogen enhanced strain induced vacancy formation* (HESIV). There exists, however, consensus that HE cannot be explained by a single embrittlement mechanism on its own. Current advances in fractographic analysis and computational approaches have led to the conclusion that different HE mechanisms can coexist and co-operate synergistically to induce HE in a complex manner [48, 49, 45]. For a detailed review including the most recent experimental evidence and computational approaches for describing the interplay of HE mechanisms in steels and iron see [50].

Hydrogen Enhanced Decohesion

The foundation of HEDE dates back to 1960, where it was first observed that inter-atomic bonds at the crack tip are weakened by the presence of locally accumulated hydrogen [179]. The accumulated hydrogen decreases the cohesive energy of the metal matrix, resulting in decohesion of the atomic

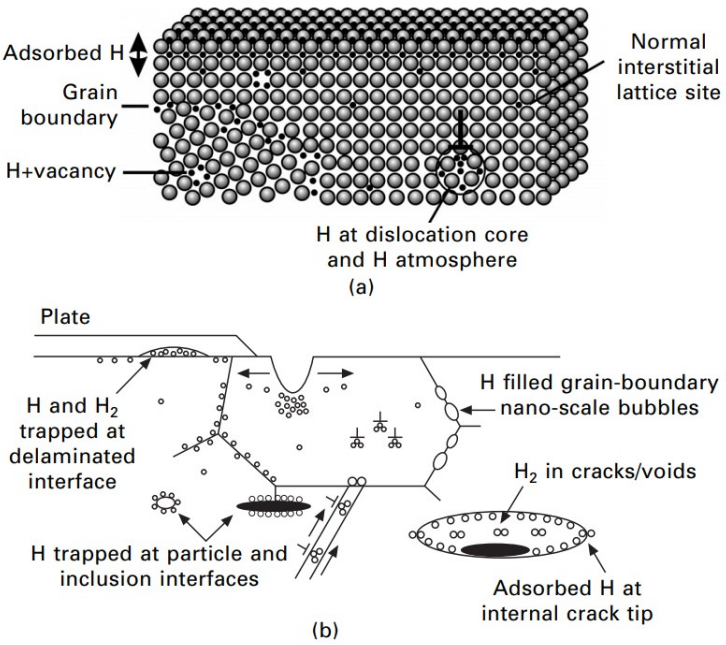

Figure 2.3: Schematic illustrations of possible hydrogen trapping sites in metals [113]. (a) And (b) depict the hydrogen trapping sites on atomic scale and microscopic scale, respectively.

lattice rather than slip [139, 91, 138]. Lynch reported that hydrogen-enrichment can manifest and cause atomic hydrogen decohesion at several locations: (i) sharp crack tips, (ii) regions ahead of crack tips, such as particle-matrix interfaces, certain crystallographic planes or where dislocation shielding effects lead to the utmost tensile stress, and (iii) at locations where maximum hydrostatic stress exists [113]. Lynch also stated, based on observations in high-strength steels, that both brittle transgranular fracture and brittle intergranular fracture are often associated with HEDE. The existence of the mechanism of HEDE is however debatable as there is no experimental demonstration of atomic hydrogen decreasing the interatomic force-displacement relationship. This lack in experimental support is attributed to the difficulty of observing crack growth at the atomic scale. Du et al., however, with an atomistic simulation model, supports the existence of the HEDE mechanism. By increasing the hydrogen concentration a lower tensile strength of the grain boundary was observed [54].

Hydrogen Enhanced Localised Plasticity

In 1972, based on the observation of tear ridges on brittle fracture surfaces, Beachem proposed the HELP mechanism [24]. The HELP model suggests that atomic hydrogen increases the propagation rate of dislocation networks under reduced stresses, thereby promoting deformation at localised regions. This plastic instability manifests as subcritical crack propagation by microvoid coalescence [156, 163]. As its name suggests, HELP exhibits localised plastic-type fracture rather than embrittlement. This theory could therefore be considered as hydrogen induced degradation of a (relatively) plastically deformed material. According to the HELP mechanism, hydrogen not only increases dislocation mobility, but also decreases dislocation-dislocation interactions, which in turn promotes planar slip and increases dislocation pile-up stacking phenomena that lead to damage initiation [39]. In contrast to HEDE, there is direct experimental evidence that supports the existence of HELP. Robertson used *in-situ* transmission electron microscopy (TEM) to investigate the effect of hydrogen on dislocation dynamics [155]. The presence of hydrogen increased the number of dislocations in a pile up, propagated stationary dislocations and accelerated (by 10-100 fold) the movement of mobile dislocations. Additional experimental evidence of HELP includes: the observation of localised slip bands near crack tips in hydrogen-charged metal samples [2, 126], and facilitated dislocation nucleation observed during (nano-)indentation experiments on in situ hydrogen-charged nickel [21]. Depending on the microstructure of the metal and the location of the hydrogen accumulation, the related fracture mechanism is either intergranular or transgranular.

Adsorption Induced Dislocation Emission
Introduced by Lynch in 1977, the AIDE mechanism is another mechanism of HE that comprises dislocation nucleation and emission, causing increased plastic deformation of steel [110]. This model is based on the work of Clum in 1975, which suggested that adsorbed hydrogen facilitates dislocation nucleation at surfaces [44]. This mechanism elucidates the phenomenon that metal brittleness occurs when the crack growth rate is virtually too high to allow hydrogen to diffuse ahead of the crack tip. AIDE proposes that the crack tip is supplied with hydrogen through adsorption. This enables hydrogen-induced weakening of atomic bonds and increases the dislocation emission of the crack tip surfaces where hydrogen is adsorbed. This dislocation emission involves both dislocation nucleation and its subsequent movement away from the crack front along intersecting surfaces that geometrically promote the opening of sharp cracks. The stresses required for dislocation emission are sufficiently high to induce the nucleation and growth of microvoids in front of crack tips. These microvoids can coalesce and tend to (re-)sharpen crack tips, thereby accelerating crack growth. Observations of high concentrations of adsorbed hydrogen on metal surfaces (and within few atomic distances of surfaces), combined with embrittlement at crack growth rates that are too high for hydrogen to diffuse towards the crack tip, form indirect proof of AIDE [41, 111]. In general, the main evidence for AIDE is fractographic [24, 110]. Cleavage-like and/or intergranular facets with high density of (very) small dimples are characteristic of AIDE [112].

Hydrogen Enhanced Strain Induced Vacancy Formation
In 2004, Nagumo et al. observed that hydrogen–vacancy complexes contribute to hydrogen related failure of steels, and proposed the most recent model that describes HE, the HESIV mechanism [131]. This mechanism suggests that hydrogen accelerates the formation of strain-induced vacancies and that hydrogen concomitantly stabilises the created vacancy clusters [164]. Agglomeration of vacancies promotes void initiation and subsequent growth. This process reduces resistance to ductile crack growth and in turn causes premature failure. Experimentally this mechanism has been evidenced by tensile tests on hydrogen-charged specimens; during straining in a hydrogen environment the hydrogen absorption capacity prominently increases by strain-induced defects [182]. As a result, the fracture surfaces for hydrogen-charged specimen undergoing HESIV exhibit a higher microvoid density compared to non-charged specimen. Rather than serving as a theory describing embrittlement, the HESIV model explains the increased presence of voids in hydrogen-charged metals. The HESIV model is therefore often combined with other HE mechanisms to explain observations of fracture paths in hydrogen-charged steels.

2.3. Fatigue in Inert Environments

In the previous section, the fundamental mechanisms behind hydrogen embrittlement were discussed. Before one can understand hydrogen-assisted fatigue behaviour, the general mechanism of fatigue in an inert environment must be understood. This section therefore introduces the general concepts of fatigue in inert environments.

Metal fatigue is a phenomenon in which the material gradually deteriorates until it fails, when subjected to cyclic loading with stress levels well below the static yield strength (and ultimate tensile strength) of the material [23]. Fatigue can be divided into high-cycle fatigue (HCF) and low-cycle fatigue (LCF), based on the amount of cycles required for failure and the dominant type of strain present. HCF requires the material to undergo more than 10^3 cycles before failure and is characterised by elastic strain, whereas LCF requires fewer cycles ($< 10^3$) and is dominated by plastic strain. The generic nature of fatigue crack growth in metals and its description by fracture mechanics are summarised in Fig. 2.4, which illustrates the variation in crack growth per cycle (da/dN) with the nominal stress intensity range ($\Delta K = K_{max} - K_{min}$). It is important to realise that not all cracks are destined to propagate. This depends largely on the fatigue process zone (FPZ), which is the the area ahead of the crack tip. This region may deform plastically for relatively ductile materials due to local stress concentrations exceeding the yield strength. This plastic zone can impede crack growth and therefore can contain cracks without causing immediate failure, in contrast to brittle materials.

The crack growth curve in Fig. 2.4 exhibits three different regions, which are characteristic to fatigue in all metallic materials:

Region I: Fatigue crack initiation and threshold region
Region II: Stable crack propagation
Region III: Unstable crack propagation

Region I: Fatigue crack initiation and threshold region
This region represents the early development of a fatigue crack at low values of ΔK and d*a*/d*N*. Initiation of microcracks occurs near locations with high stress concentrations, such as defects or particles. For stress intensity values lower than the fatigue threshold (ΔK_{th}), fatigue cracks are considered dormant (d*a*/d*N* $< 10^{-6}$ mm/cycle) [33]. Above this threshold, however, multiple (micro)cracks begin to propagate along high shear stress planes orientated at 45° with respect to the applied load [61]. Crack growth in Region I is rather slow due to microstructural features (i.e. grain boundaries or inclusions) that act as barriers and that cannot accommodate the initial crack growth direction. According to Morris, for short cracks, grain boundaries reduce the effective stress intensity of the crack tip, resulting in the characteristic retardation of crack growth in Region I [124]. The short-crack arrest at a grain boundary is governed by the grain boundary's resistance against slip transfer, or in other words the transfer of dislocation motion from the plastic zone ahead of a crack tip to an adjacent grain.

Region II: Stable crack propagation
Region II is the intermediate region where crack growth exhibits power-law behaviour described by the Paris equation [143]:

$$\mathrm{d}a/\mathrm{d}N = C(\Delta K)^m \tag{2.6}$$

Where *C* and *m* represent material scaling constants that are determined experimentally. Despite the fact that ΔK is considered as the primary variable in metal fatigue, in actuality fatigue crack growth is far more complex and depends on a multitude of factors other than ΔK:

$$\mathrm{d}a/\mathrm{d}N = \mathrm{function}[\Delta K, R, f, \mathrm{environment}, ...]$$

In which *R* and *f* represent the stress ratio and cyclic loading frequency, respectively. The rate of crack growth can be correlated with the size of plastic zone. Generally, the larger the plastic zone size, the higher the fatigue crack growth rate. For steels, the extended size of the plastic zone in Region II can encompass several grains, thereby exhibiting a lower microstructure-dependency [94]. Therefore, continuum approaches can be applied to describe crack growth behaviour. Note, however, that this statement regarding the size of the plastic zone in Region II may not hold for dissimilar materials, such as titanium alloys [67]. The macroscopic cracks in Region II tends to grow transgranular and propagates perpendicular to the load direction. The underlying principle of this shift in the crack growth

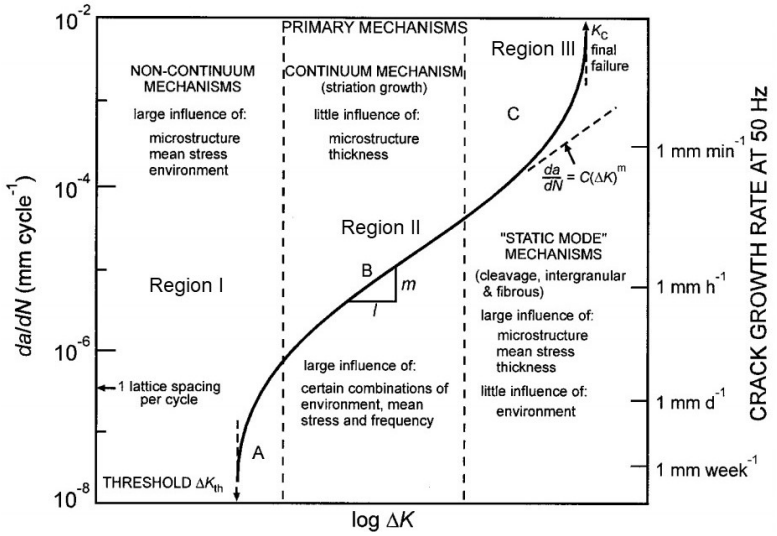

Figure 2.4: Characteristics of the fatigue crack growth rate curve, d*a*/d*N* versus ΔK. Adapted from [154].

direction is the increasing stress concentration at the crack tip, which activates secondary slip systems. Another characteristic feature of Region II, especially for ductile materials, is striation formation [98].

Region III: Unstable crack propagation
Region III, also known as the static fracture mode region, is characterised by significant increases in (unstable) crack growth as K_{max} approaches the critical stress intensity factor (K_C), or K_{IC} in the case of plane strain conditions. The accelerated crack growth behaviour cannot be described by the Paris equation (Eq. 2.6); it underestimates the crack growth as it does not take into account the effect of monotonic fracture mechanisms contributing to additional striation growth. Examples of such mechanisms are: cleavage, intergranular cracking and microvoid coalescence. Due to the occurrence of these mechanisms, it is believed that the crack growth rate in this region is markedly sensitive to the microstructure and K_{max} [153]. In Region III, macro-cracks propagate further, eventually leading to fatigue failure due to the continuous reduction of the load-bearing cross-section of the specimen. At a certain stage, the plastic flow is no longer limited to the crack tip, but extends to the remaining cross-section. In other words, general yielding takes place that ultimately leads to complete failure of the structure.

2.4. Fatigue in Hydrogen Environments

Hydrogen Fatigue Crack Initiation
Several studies highlight that crack initiation, rather than the crack growth phase, governs the fatigue failure in hydrogen environments [80, 8, 31, 5]. This implies that, in order to prevent HE fracture in hydrogen transport pipelines, utmost precaution should be taken to prevent crack initiation rather than to retard crack growth. The relative importance of fatigue crack initiation has been particularly emphasised in a study by Capelle et al. on X52 steels [35]. The fatigue test conditions included a load ratio (*R*) of 0.5, a frequency (*f*) of 0.05 Hz and a hydrogen electrolytic charging test set-up. It was found that the number of cycles till crack initiation in air was approximately 60% of the total fatigue life, whereas it was 80% under hydrogen influence. In addition, the overall number of cycles till failure decreased significantly in the hydrogen environment. Thus, apart from hydrogen inducing premature failure, the impact of crack initiation dominates hydrogen-assisted fatigue failure. Bellahcene et al. followed up on this finding in close cooperation with Capelle, and confirmed that under identical test conditions, crack initiation similarly governs the hydrogen fatigue life of X70 steel [25].

Hydrogen Fatigue Crack Growth Behaviour
Crack growth behaviour of materials in hydrogen environments deviate significantly from inert environments. Wie and Simmons studied the effect of hydrogen on the fatigue behaviour of high strength steels in 1973, and proposed that fatigue behaviour in hydrogen environments can be categorised in three different types (Fig. 2.5). The fatigue behaviour of each type is explained with the distinguished contribution of HE and hydrogen-assisted fatigue crack growth (HA-FCG). Although HE and HA-FCG

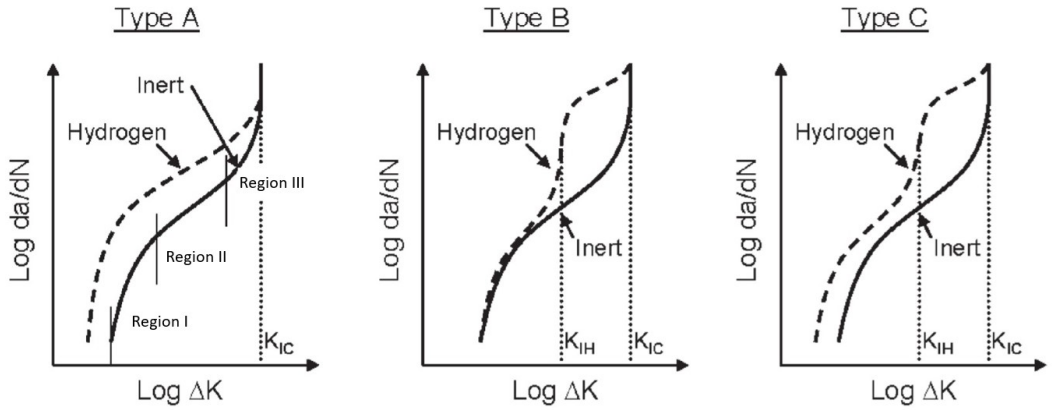

Figure 2.5: The types of fatigue crack growth behaviour observed in hydrogen environments [194].

both refer to increased crack growth behaviour due to atomic hydrogen, it is important to realise that in this concept HE regards the increased monotonic crack growth, while HA-FCG addresses the increased cyclic crack growth. The following paragraphs describe the three (A, B and C) types of fatigue behaviour of hydrogen-exposed materials.

Characteristic for Type A is that hydrogen decreases the stress intensity required to activate substantial crack growth (ΔK_{TH}), thereby prematurely initiating Region I. An other important feature is that the material exhibits HA-FCG in Region II, however the static fracture modes in Region III seem rather unaffected by hydrogen. In particular, the monotonic crack growth threshold in hydrogen (K_{IH}) does not differ from that of inert environments, which implies that K_{IH} is equal to K_{IC} and that the material is not susceptible to static HE. In contrast to Type A, materials behaving according to Type B are susceptible to static HE ($K_{\mathrm{IH}} < K_{\mathrm{max}} < K_{\mathrm{IC}}$). However, HA-FCG during cyclic loading at $K_{\mathrm{max}} < K_{\mathrm{IH}}$ is not observed. In practice, many materials behave according to Type C. This Type states that fatigue behaviour in a hydrogen environment involves combined effects of HE and HA-FCG for cyclic stress intensities below K_{IC} [133].

Fatigue behaviour in hydrogen environments remains a subject of extensive research, with the aim of clarifying the mechanisms that are involved and optimizing pipeline design standards. A general consensus has emerged that the (type of) hydrogen-assisted behaviour depends on various external and internal test variables. This will be further detailed in the following sections.

2.4.1. Effect of Gas Pressure

As introduced in section 2.2.1 (Eq. 2.3), the hydrogen partial pressure influences the hydrogen concentration in steel, which consequently influences the magnitude of HA-FCG. According to Holbrook et al., the dependency of FCGR on the hydrogen pressure is of the power 0.36. It can be noted that this value deviates significantly from the square root relation described by Sievert's law [80]. It was postulated that two main factors influenced the deviation in hydrogen pressure dependency: (i) the reduced amount of hydrogen at the fatigue crack damage zone due to irreversible trapping of atomic hydrogen, and (ii) the impeded ability for dissolved hydrogen to reach equilibrium due to the dynamic loading that cyclically deforms the crack tip. Although this study suggests that the theorised hydrogen concentration actively involved in embrittlement differs from practice, it also documents that there is a tendency for the crack growth rate to increase at higher hydrogen pressures thereby inducing premature failure. A reduced fatigue lifetime due to the effect of increasing the (partial) pressure of hydrogen is a consistent finding in academic literature [31, 8]. Important to note is that crack initiation governs the reduction of fatigue life at higher hydrogen partial pressures. When the partial pressure of hydrogen increases, the number of cycles required for crack initiation decreases.

Recent studies elucidated that the effect of hydrogen pressure on fatigue heavily depends on ΔK. Yamabe et al. studied the FCGR of low-carbon steel (JIS-SM490B, σ_y = 360 MPa) in gaseous hydrogen at a *R* of 0.1 and a *f* of 1 Hz [197]. The pressure of the pure hydrogen environments ranged from 0.1-90 MPa. Their d*a*/d*N* versus ΔK results (Fig. 2.6) indicate that in the low ΔK regime (ΔK < 20 MPa$\sqrt{\mathrm{m}}$) HA-FCG significantly accelerated with an increase in ΔK. In addition, the extent of HA-FCG increased with higher hydrogen pressures, which is a consistent finding [176]. Although the hydrogen environment, compared to air, clearly shows a higher crack growth rate in the higher regime ($\Delta K > 20$ MPa$\sqrt{\mathrm{m}}$), no additional accelerating HA-FCG has been observed with an increase of ΔK. In fact, in this regime equal slopes of the FCGR curves can be noted. Important to realise is that in the work of Yamabe et al., the studied ΔK range commenced with $\approx$ 12 MPa$\sqrt{\mathrm{m}}$. This directly served as the threshold of ΔK, which Suresh and Ritchie defined as K_{max} [180], at which deviation between the FCGR curves in hydrogen and inert environment exists and crack growth accelerates abruptly (K_{IH} in Fig. 2.5). Note that in the following passages of this thesis, the term K_{IH} is used to describe this phenomenon. The work of Amaro et al. on HA-FCG in X52 and X100 pipeline steel (*R* of 0.5 and *f* of 1 Hz), however, included a lower ΔK range. It was observed that the FCGR remained unaffected at low hydrogen pressures and sufficiently low ΔK [5]. In this particular study the HA-FCG behaviour could therefore be described as *Type B* behaviour.

Slifka et al. studied X100 steel fatigue behaviour (*R* of 0.5 and a *f* of 1 Hz), and observed an identical

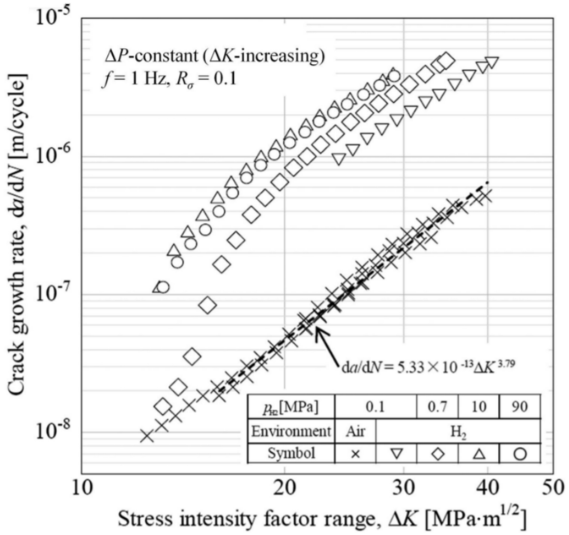

Figure 2.6: d*a*/d*N* versus ΔK plot of low carbon steel JIS-SM490B [197].

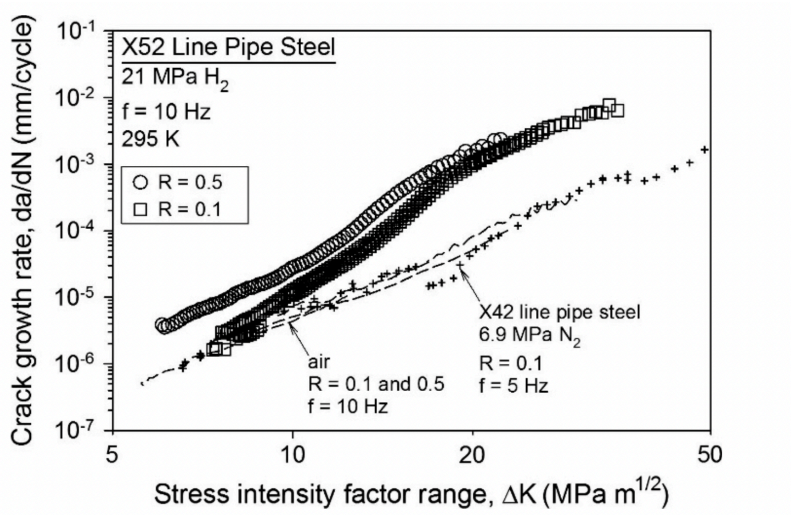

Figure 2.7: d*a*/d*N* versus ΔK curves of X52 pipeline steel[176]. The data of X42 in nitrogen environment was taken from the work of Cialone et al. [42].

abrupt transition in hydrogen-assisted fatigue crack growth rate (HA-FCGR) behaviour at a threshold of ΔK = 15 MPa$\sqrt{\text{m}}$ [173]. Yamabe et al. and Slifka et al. attributed the increase in HA-FCG at the lower ΔK regime to a steep hydrogen concentration at the crack tip region. This steep gradient caused localised plasticity, which prevented crack tip blunting and promoted crack tip sharpening. Ultimately, this increased the crack growth per cycle. For the phenomenon that crack growth behaviour was independent of hydrogen gas pressure at higher ΔK values, it was proposed that the hydrogen concentration reached maximum saturation in the crack process zone, or that a critical hydrogen concentrations was reached. It is believed that the non-existent effect of hydrogen at $\Delta K < K_{\text{IH}}$, is also dependent on the test frequency.

2.4.2. Effect of Stress Ratio

Hydrogen gas transporting pipelines can be subjected to *R* values greater than 0.5 during pressure fluctuations from compression stations or (large) variable wind patterns [101]. However, the hydrogen generation from wind and solar farms, and its usage during peak demand are associated with smaller values of *R* ($\sim$0.25). It is therefore of high importance to understand the effect of different *R* values on

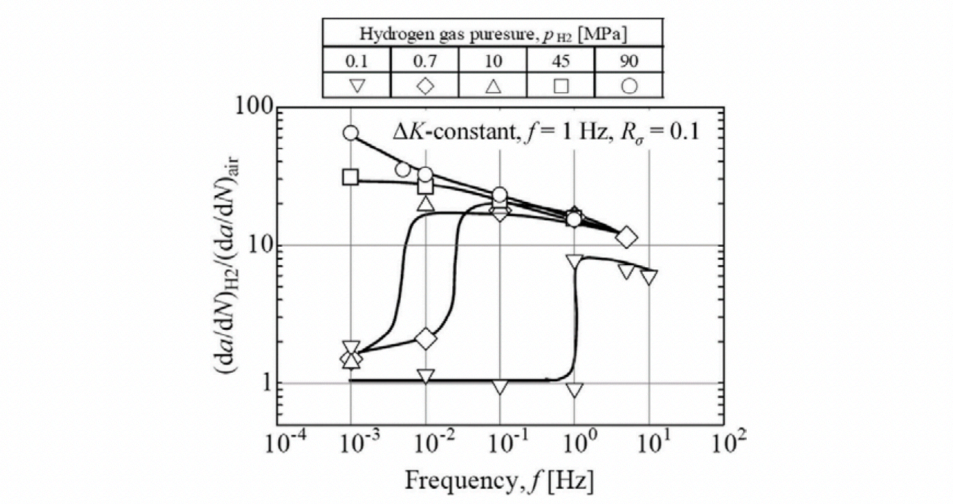

Figure 2.8: Relative d*a*/d*N* versus cyclic loading frequency for low-carbon steel JIS-SM490B [197].

pipeline steels. The relation between ΔK, *R* and K_{max} can be described as follows [173]:

$$\Delta K = (1 - R)K_{max} \tag{2.7}$$

From this equation it can be deduced that for higher values of *R*, K_{max} increases for a given ΔK.

Somerday et al. studied the fatigue behaviour of X52 pipeline steel in a 21 MPa pressurised hydrogen environment at a *R* of 0.1 and 0.5 [176]. Fatigue crack growth behaviour exhibited similar characteristics at both values for *R*, as can be seen in Fig. 2.7. From the figure, it can be deduced that the fatigue crack growth in air did not depend on *R*. Compared to *R* = 0.1, *R* = 0.5 shifted the onset of K_{IH} to lower ΔK. In addition, the FCGRs in the hydrogen environment were higher for all values of ΔK when tested at the higher *R* value (*R* of 0.5). Roy et al. studied HA-FCG behaviour in a high strength low alloyed steel (σ_{ys} = 650 MPa) at load ratios in the range of 0.1-0.5. Higher *R* values increased the FCGR for both the hydrogen and air environments, with the increase in FCGR being much greater ($\approx$7-fold) in the hydrogen environment. The observation that FCGR increased with *R* for the inert environment, contradicts the finding of Somerday et al. [176]. Nevertheless, Roy et al. proposed that higher *R* resulted in accelerated HA-FCG behaviour due to the high mean stresses which promote the stress-driven hydrogen diffusion towards the crack tip. In addition, it was suggested that the high mean stresses enhance plastic damage and therefore facilitate mechanical fatigue effects.

Ho and Yu proposed that high *R* values can show contradictory effects on the HA-FCGR [79]. At high *R* values, the high mean stresses could promote the generation of vacancies at the near crack tip region, which enhances the hydrogen transport. However the effect of hydrogen at certain *R* values depends on the compressive stress gradient, which is a function of $\Delta\sigma$ (= σ_{max} - σ_{min}), experienced by the hydrogen during unloading. At high $\Delta\sigma$, Ho and Yu suggested that more hydrogen should leave the near crack tip region (i.e. through crack faces), this depletion of hydrogen at the crack tip region therefore impedes HA-FCG. This 'pumping out of hydrogen' from the (near) crack tip region becomes less effective with increasing *R* values, because $\Delta\sigma$ is not sufficiently high. It is important to realise that the effect of pumping out of hydrogen can be neglected in the study performed by Roy et al., because their fatigue tests were conducted at constant values of $\Delta\sigma$.

2.4.3. Effect of loading frequency

There is unanimity that HA-FCG depends on the ability of hydrogen to adsorb and diffuse to high stress areas. It is therefore generally believed that sufficiently low cyclic loading frequencies provide hydrogen ample time to diffuse to the crack tip per cycle, thereby increasing the HA-FCGR. Holbrook et al. performed fatigue tests on X42 pipeline steel, while varying the frequency from 0.1-10 Hz, and concluded that loading frequencies within this range did not influence the HA-FCGR [80]. Other studies similarly reported the lack of frequency dependency within this range [191, 190]. However, more recent studies

elucidated that frequency dependency exists at lower frequencies ($\leq$ 0.1 Hz) [197, 176, 4]. Yamabe et al. studied low-carbon steel (JIS-SM490B, σ_{ys} = 360 MPa) at a constant ΔK of 30 MPa$\sqrt{\text{m}}$, at hydrogen pressures ranging from 0.1-90 MPa and test frequencies from 0.001-10 Hz (Fig. 2.8) [197]. For hydrogen pressures $\leq$ 10 MPa the FCGR gradually increased with a decrease in *f*, but peaked out at a certain threshold *f* after which the FCGR dropped to the FCGR in inert environment. Increasing the pressure up to 10 MPa shifted the onset of the FCGR drop towards lower frequencies. At a hydrogen pressure of 45 MPa, the FCGR peaked out at 0.01 Hz, but no abrupt decrease was observed. This sudden drop was absent at a hydrogen pressure of 90 MPa.

Matsuoka et al. hypothesise that the onset of HA-FCG, at a low frequency and sufficiently low hydrogen pressure, occurs once a steep hydrogen gradient at the crack tip is reached [119]. Based on the general consensus that an increased hydrogen concentration near a crack tip can be achieved at lower frequencies and at higher (partial) pressures of hydrogen, Yamabe et al. introduced a novel parameter $(P_{H2} \times f)^{1/2}$. Yamabe et al. state that this parameter could be interpreted as a rough quantification of the hydrogen concentration gradient near a crack tip. Upon the introduction of this criterion, Yamabe et al. reassessed the results presented in Fig. 2.8 and reported a more understandable view of their results. Namely, that the onset of FCG acceleration occurs at a $(P_{H2} \times f)^{1/2} \geq 0.1$, which is the threshold value describing a sufficiently steep hydrogen concentration gradient at the crack tip to induce HA-FCG.

2.4.4. Effect of microstructure

Grain boundaries

A study by Cialone and Holbrook in the 1980s reported that the deleterious effect of gaseous hydrogen on fatigue (*R* of 0.1, *f* of 1 Hz and gas pressure of 6.9 MPa) of a fully ferritic steel manifests in the grain boundaries [43, 80, 81]. Fractographic analysis evidenced that the fully ferritic alloy changed from 100% transgranular in the inert environment, to almost entirely through the grain boundaries in the hydrogen environment. This early study strongly implied that grain boundaries play a profound role in the phenomenon of HE. In a more recent study of Slifka et al., it was postulated that higher volume of grain boundaries in steels enhances the diffusivity for hydrogen-induced damage [174]. Therefore, materials with larger grain sizes, and therefore lower volume of grain boundaries, should exhibit greater resistance to hydrogen-induced damage as the transport of hydrogen to the crack tip is limited. These findings are in line with the statement of Jack et al., who proposed that grain boundaries act as the primary diffusion pathway for hydrogen [87]. However, according to Jack et al., steel with finer grains, hence higher number of boundaries, has lower effective diffusion due to the increased ratio of hydrogen traps per surface area. On the contrary, larger grains will have a higher hydrogen diffusion rate due to the decrease in trapping sites per surface area. Masoumi et al. concluded that finer grains with higher grain boundary densities are relatively more susceptible to HE due to the high trapping efficiency [118].

It is interesting to note that fine grains may be advantageous in inert environments and disadvantageous in hydrogen environments. Fine grains may inhibit crack growth in inert environments due to the large number of grain boundaries present. However, in hydrogen environments, the fine grains with high density of grain boundaries may be able to trap a high volume fraction of hydrogen, thereby promoting crack growth.

Microstructural phases

Research shows that the accumulation of hydrogen atoms and HE are occurring more frequently in welded joints, owing to in-homogeneous hydrogen diffusion and resulting hydrogen localisation [201]. The specific microstructural phases at which localisation of hydrogen manifests, is dependent on their hydrogen trapping efficiency. An example of some phases arranged according to increasing trapping efficiency: small second phase particles, coarse pearlite, fine pearlite, bainite, ferrite, and martensite [109, 144]. Note that trapping efficiency is virtually an opposing term for the 'effective diffusivity' of hydrogen within those phases. However, the extent of hydrogen trapping is not directly linked to accelerated crack propagation as this also depends on the toughness of the phase. For instance, acicular ferrite has higher toughness than bainitic ferrite due to the high density of high angle grain boundaries and dislocations. Despite the high trapping efficiency of the phase, the greater toughness of acicular ferrite arrests crack propagation more extensively than bainitic ferrite [40, 144].

Microstructural banding
A banded microstructure with alternating layers (of ferrite and pearlite) elongated in the rolling direction is characteristic for thicker walled-pipeline steels [97]. Ronevich et al. studied X65 pipeline steel (R of 0.5 and f of 1 Hz) and observed that cracks oriented perpendicular to the banded pearlite exhibited slower FCGRs in hydrogen gas than cracks oriented parallel [158]. Generally, the boundaries of alternating layers are known to act as barriers for crack propagation. This is usually evidenced by optical micrographs showing that primary crack growth perpendicular to the band structure is accompanied by secondary microcracks branching off from the primary crack plane [95, 129]. Crack branching (and subsequent arrest) typically occurs when the crack-tip encounters hard phases such as pearlite or cementite. These phenomena shield the crack tip(s) from the applied stress, thereby ultimately reducing the fatigue crack growth rate. In a hydrogen environment, the perpendicular orientation of the crack deprives the crack tip of hydrogen due to the limited hydrogen supply through the alternating layers. The orientation and subsequent propagation of a crack may therefore play an important role in the severity of HE for pipeline steels.

2.5. Characteristic Hydrogen Fatigue Fracture Surfaces

It was mentioned in section 2.3 that striation formation is a characteristic feature of Region II fatigue (stable crack propagation phase). However, striation formation is less pronounced in a hydrogen environment and, if present, the striations appear irregular in shape [128]. Fatigue in an inert environment typically exhibits striations triangular in shape, consistent in height and spacing. On the contrary, striations in hydrogen-charged samples are inconsistent both in spacing and height, and all striations appear lower in height compared to the inert environment. It is generally believed that the reduction in striation height is owing to the increased localised plastic deformation at the crack tip due to hydrogen (HELP). As a result, the plasticity-induced crack closure reduces, since the plastic zone wake decreased significantly. According to Nguyen et al., the additional contribution of the HEDE mechanism further sharpens the crack, thereby accelerating fatigue crack growth due to enhanced brittle behaviour [135]. Schematic representations of mechanisms inducing the differences in fatigue fracture morphologies under ambient air and a hydrogen environment are illustrated in Figures 2.9.e-f. This figure is taken from the study of Nguyen et al. on hydrogen fatigue behaviour of X70 pipeline steel [135]. Under ambient air conditions (Figures 2.9a-b), the striations (spacings) became more pronounced at higher ΔK, although the exact values for ΔK were not mentioned. Two hydrogen environments were tested: a CH_4/H_2 gas mixture containing 1% H_2 (Fig. 2.9c) and a 100% H_2 gas environment (Fig. 2.9d), both pressurised at 10 MPa. Hydrogen significantly affected the fracture behaviour of the specimens; it was virtually impossible to identify fatigue striations on the fracture surfaces of hydrogen-exposed specimens. Instead of showing apparent fatigue striations, the fracture surfaces of both hydrogen environments exhibited quasi-cleavage. Other studies on API 5L pipeline steel grades [53, 6] similarly reported that the fracture surfaces of hydrogen-charged specimen are dominated by cleavage-like facets. The next subsections elaborate on the characteristics of brittle (quasi-)cleavage fracture in hydrogen fatigue.

Characteristic Fracture Types of Hydrogen Fatigue
Cleavage and Quasi-Cleavage
Cleavage can be defined as rapid crack growth along specific crystallographic planes and occurs when plastic flow is restricted. Brittle materials therefore often fail by cleavage. The preferred planes for cleavage are those with the lowest packing density, since fewer bonds are required to be broken [11]. Oftentimes, in the case of a hydrogen environment, one speaks of quasi-cleavage rather than cleavage. While the facets of quasi-cleavage look identical to cleavage fracture, there exists a difference between the two fracture types. Quasi-cleavage fracture surfaces are characterised by a smaller average misorientation angle between facets and therefore do not cohere to the well defined cleavage planes of 'true' cleavage fracture [121].

Transgranular Cleavage Fracture
Fracture modes may differ markedly in their fracture mechanism, but they may share characteristics in terms of their fracture path, and thus can be categorised accordingly. Fracture is either transgranular or intergranular. This subsection first elucidates on transgranular fracture. Information regarding intergranular fracture can be read in the subsequent section.

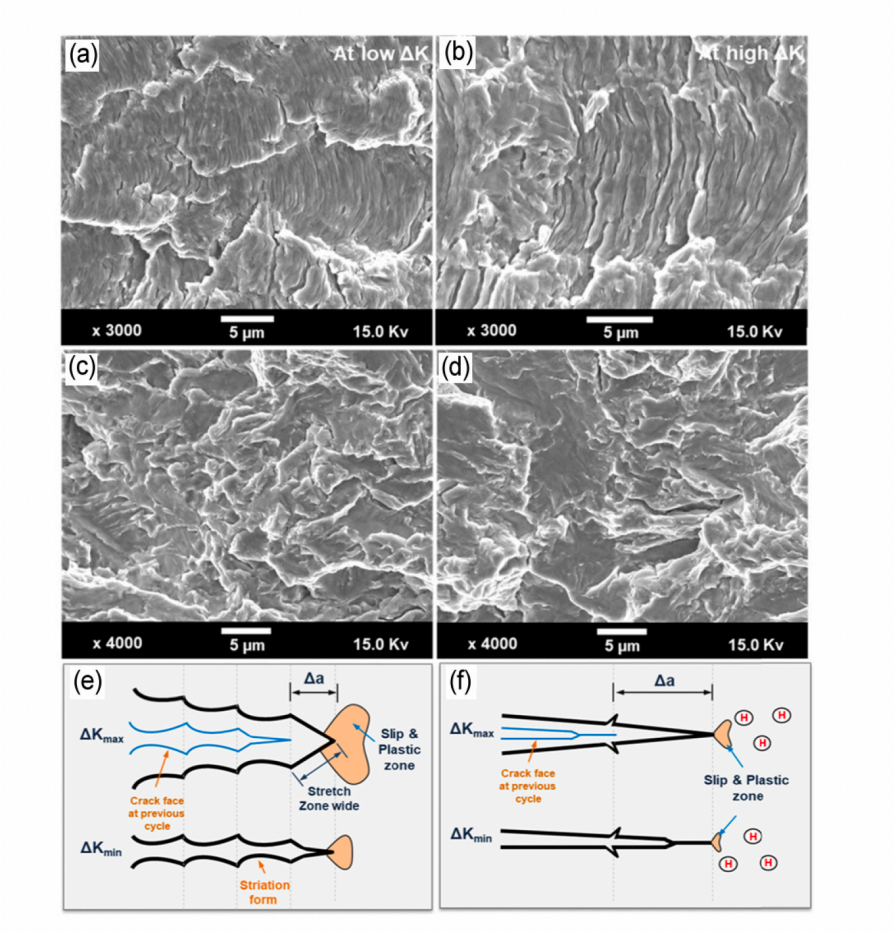

Figure 2.9: Comparison between SEM fractographs of samples tested for fatigue in different environments [135]. (a) low ΔK in ambient air, (b) at high ΔK in ambient air, (c) CH_4/H_2 gas mixture pressurised to 10 MPa containing 1% H_2 and (d) 100 % H_2 gas pressurised to 10 MPa. (e) And (f) serve as schematic representations of the fatigue fracture morphologies under ambient air and a hydrogen-containing environment, respectively.

As its name implies, transgranular fracture travels through the grains of the material (see Fig. 2.10a). Each time the propagating crack crosses a grain boundary, it seeks the most favorably oriented cleavage plane in the adjoining grain and changes its propagation direction accordingly. As a result, the associated fracture surface displays an overall (smooth) faceted texture. Characteristic of transgranular cleavage fracture is that the fracture surfaces exhibit so-called river patterns, recognizable as multiple lines merging into one, similar to tributaries of a river. When the nearest cleavage plane of the adjacent grain is oriented with a (finite) twist angle relative to the current cleavage plane, multiple cracks form on several parallel planes to accommodate for the twist mismatch. These cracks can converge into a single crack due to tearing between planes, creating the characteristic river patterns. The direction of crack propagation can therefore be inferred from river patterns. [46]. Shinko et al. suggested that cleavage fracture occurs through either the HEDE or AIDE mechanism [169]. However, it has also been evidenced that HEDE mechanism can be accompanied by the HELP mechanism, which links voids and microcracks with the crack tip thus accelerating transgranular decohesion [175].

The above-mentioned description of transgranular fracture generally holds for fatigue Region I and II. Although transgranular cleavage is conventionally classified as brittle in nature, the occurrence of tearing indicates that some plasticity may be involved. Ductile characteristics of transgranular failure further manifests in Region III fatigue, where slip rather than cleavage prevails. Note that in this Region, similarities are shared with uni-axial tests. A common mechanism associated with slip is the material separating internally by the initiation of voids (see Fig. 2.10b). The fracture surface progresses through void coalescence which gives rise to a characteristic dimpled appearance. In engineering alloys, voids

tend to initiate by decohesion of the particle-interface matrix or by fracture of the particles. In the former case, the fracture surface can exhibit particles residing in the valley of the dimples (see Fig. 2.10d). The loading conditions affect the shape of the dimples; equiaxed and elongated dimples, are created under stresses normal to the plane and under shear or tear, respectively [76]. In a hydrogen environment, the dimples are smaller in size due to the enhanced formation of voids that allow coalescence under less growth [117]).

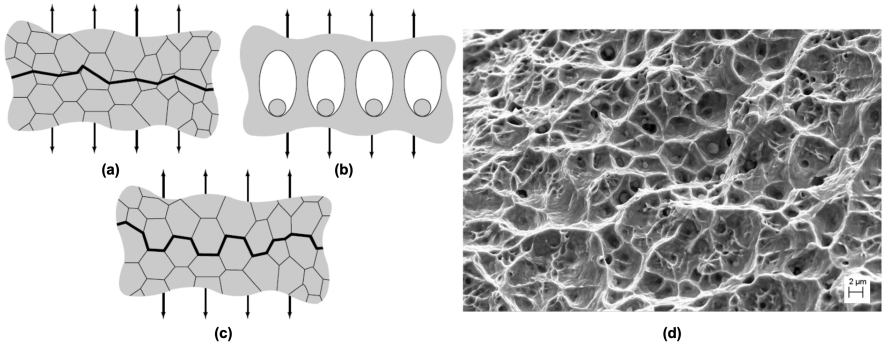

Figure 2.10: Figure including illustrations of fracture mechanisms in metals [170] and an example of a dimpled fracture surface of 316L stainless steel [105]. The following fracture mechanisms are illustrated: a) transgranular fracture, b) void coalescence and c) intergranular fracture [170]. In d) a SEM image a dimpled fracture surface, resulting from void coalescence, of 316L stainless steel can be seen. Visible are the second-phase particles in the valleys [105].

Intergranular Cleavage Fracture

Cracks can also initiate and propagate along the grain boundaries through a fracture mechanism known as intergranular fracture (see Fig. 2.10c). Although it is evident that hydrogen can reduce the cohesive strength of grain boundaries, and thus facilitate intergranular fracture, the underlying mechanisms are not well understood. Recently however, a more profound explanation of the mechanisms of hydrogen-induced intergranular fracture has been proposed by Shinko et al [169]. Since the proposed model is rather complex, Fig. 2.11 is provided to visualise the concepts that will be discussed. Hydrogen atoms diffuse towards the highly stressed region near the crack tip and are subsequently swept-in by the dislocations in front of the crack tip (Fig. 2.11a) The plastic strain ahead of the crack tip causes the hydrogen-carrying dislocations to pile-up and organise into a cellular structure (Fig. 2.11b) [183]. The accumulation of dislocations and hydrogen atoms reduces the cohesion energy of the grain boundary and initiate nucleation of microvoids (HESIV) at the grain boundary (Fig. 2.11c). Intergranular decohesion is then accelerated through microvoid coalescence (Fig. 2.11d). This model considers HEDE as the dominant hydrogen-damaging mechanism with a synergistic contribution of intergranular plasticity (HELP).

Mixed-modes and Transitions of Fracture Mechanisms

Instead of a single fracture mechanism, (hydrogen-assisted) fatigue fracture surfaces often exhibit mixed intergranular-transgranular fracture. The more pronounced mechanism depends on the fatigue regime. For instance, in a study of Drexler et al. on X70 pipeline steel, in the region where an abrupt change in fatigue is observed (transient regime, $\Delta K > K_{IH}$) the fracture surface was dominant in intergranular fracture (Fig. 2.12a) [53]. At higher ΔK, where in general the FCG curves of air and hydrogen are parallel (steady state regime), the crack path transitioned to a transgranular nature with characteristic river patterns (Fig. 2.12b). The transition from intergranular fracture to transgranular fracture has been evidenced by other studies as well; the ones of Slifka et al. on X70 pipeline steel (transition at ΔK of 12 MPa$\sqrt{\text{m}}$) [174], and on X52 and X100 pipeline (transition between ΔK 12-15 MPa$\sqrt{\text{m}}$) [173]. Slifka et al. did not mention the underlying fracture mechanisms that lead to an intergranular fracture path. However in the work of Ogawa et al. it emphasised that the phenomenon of intergranular fracture occurs due to formation of microvoids (HESIV) and their subsequent coalescence, and grain boundary decohesion (HEDE) [137].

A more recent study of Amaro et al. more specifically examined and discussed the HA-FCG related fracture surfaces of X100 pipeline steel by dividing the HA-FCG response into three regions (Fig. 2.13)

[6]:

- Region A ($\Delta K < 8$ MPa$\sqrt{\text{m}}$): the fracture surface closely resembled the one tested in air.
- Region B (8 MPa$\sqrt{\text{m}} < \Delta K < 15$ MPa$\sqrt{\text{m}}$): the fracture surface appeared more brittle, it was dominated by crystallographic faceting (intergranular fracture).
- Region C ($\Delta K > 15$ MPa$\sqrt{\text{m}}$): significantly reduced amount of crystallographic faceting and shared similarities with the fracture surface of the specimen tested in air. The fracture surface primarily exhibited quasi-cleavage with some river patterns. Similar to the study of Drexler et al. [53] the crack morphology in this region was dominant in transgranular crack growth.

Relating the approach of Amaro et al. to the study of Drexler et al., the discussion of SEM fractographs (Fig. 2.12) of the low ΔK and high ΔK regions translate to Region B and Region C, respectively. Amaro et al. postulated that the fracture mechanism in Region A should not be affected by hydrogen, since the range of ΔK did not reach the critical K-value (K_{IH}). Their claim was confirmed by the observation that the fracture surfaces of the hydrogen and air tested samples closely resembled each other. On the other hand, Region B and Region C both experienced HA-FCG behaviour, and the transition from Region B to Region C was governed by the fatigue plastic zone (FPZ). For Region B, the crack extension per cycle fell within the FPZ and fatigue damage was dominated and accelerated by the hydrogen accumulation at the crack tip. The fracture surface exhibited crystallographic facets, hence evidencing brittle behaviour. On the contrary, the hydrogen effect became saturated in Region C, resulting in a fracture surface exhibiting components of utmost hydrogen-induced damage (Region B) combined with ductile characteristics similarly found in Region A. In Region C, the crack extension fell outside the FPZ, resulting in HA-FCG behaviour that depended on the far-field hydrogen accumulation inside the material. Consequently, the HA-FCG response partly conformed to the FCG behaviour of traditional fatigue mechanisms, and the fracture surface thus shared some characteristic ductile appearances.

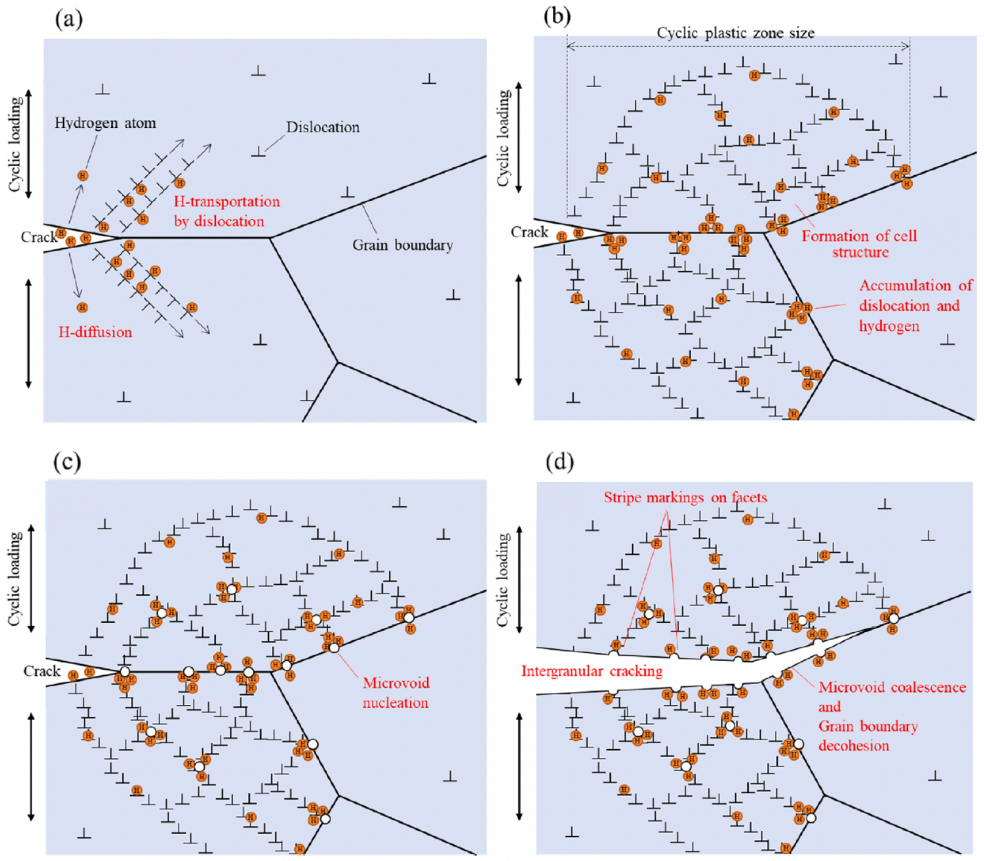

Figure 2.11: The model of hydrogen-induced intergranular fracture proposed by Shinko et al. Adapted from [169].

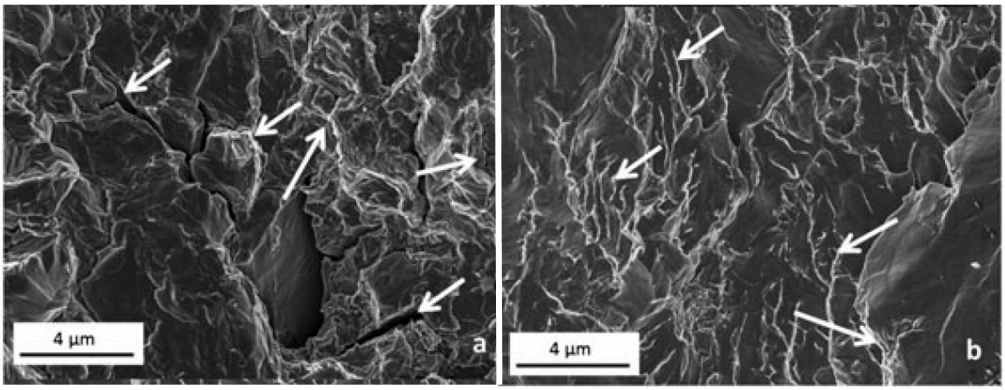

Figure 2.12: SEM fractographs of hydrogen-fatigued X70 pipeline steel [53]. The specimens were tested at a H_2 gas pressure of 5.5 MPa, a *R* of 0.5 and a *f* of 1 Hz. The white arrows in the transient regime (a) and steady state regime (b), indicate the individual grains characteristic of intergranular fracture and river marks from transgranular fracture, respectively.

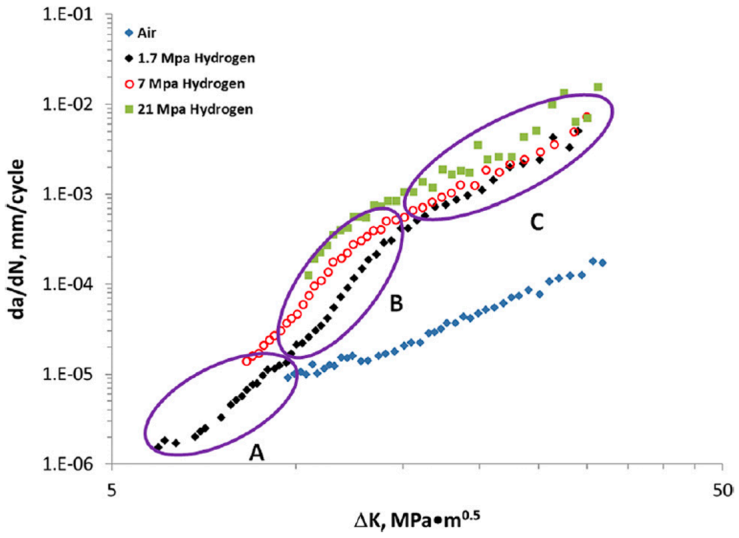

Figure 2.13: HA-FCG results of X100 pipeline steel divided into three regions: A, B, and C [6]. The fatigue tests conducted in the hydrogen environments and air environment were both tested at a *R* of 0.5 and a *f* of 1 Hz.

2.6. Hydrogen Fatigue Testing

Accurate test methods that simulate the operating environmental conditions to which pipelines are exposed, are paramount for quantifying the effect of hydrogen on fatigue behaviour. This section deals with different types of test methods used to assess the susceptibility of a material to hydrogen-assisted fatigue. First, it is elaborated on the different hydrogen charging methods. Thereafter, the concepts of a powerful method (i.e. the Direct Current Potential Drop) to study the fatigue crack growth is discussed. The relevant findings presented serve as the key insights and framework for the realisation of the designed test set-up in this thesis.

2.6.1. Hydrogen Charging Methods

Conventionally, hydrogen fatigue studies simulate the hydrogen environment through hydrogen electrochemical charging the steel or exposing it to hydrogen gas. Electrochemical charging can produce high concentrations of hydrogen in a relatively short time because the forced movement of protons (due to the electric potential) in the aqueous electrolyte is faster than the random movement of the hydrogen molecules in hydrogen gas. Thus, electrochemical charging is often preferred when time plays a considerate role [17]. In addition, research facilities that cannot justify being explosion proof, or which are constrained by the high costs associated with special high-pressure equipment, often choose

electrochemical charging instead.

This section exclusively deals with the discussion of gaseous charging setups, as this thesis is focused on the design of an *in-situ* gaseous hydrogen fatigue test setup.

Gaseous Hydrogen Charging
Gaseous hydrogen charging is conducted by exposing the specimen to high pressure hydrogen gas. The most conventional method is to pressurise the specimen externally in a pressure vessel [173, 132]. Prior to pressurising the hydrogen up to test pressure, the system is purged with an inert gas to ensure that the system is free of any residual gas(es) that could potentially inhibit HE. A critical necessity is to minimise the risk of any explosion. The precautions taken often include minimizing the size of the pressure vessel and, if the setup allows, exposing the surface of the pressure vessel to an inert gas (e.g. argon) to reduce the risk of combustion [36]. In a recently published study by Boot et al., the HE of X60 steel was researched with hollow cylindrical tensile specimens mimicking pipelines on a small and testable scale [30]. The innovatory feature was that the test specimen was pressurised internally. In addition to accurately representing the internal gas exposure of hydrogen transporting pipelines, the safety of the test environment was markedly improved by the limited hydrogen gas volume.

Besides the charging gas pressure, the key parameters influencing the resulting hydrogen concentration profile are the surface conditions of the steel (i.e. the role of an oxide layer, section 2.2.1), the charging time and temperature. For instance, charging at an elevated temperature can significantly increase the diffusion rate of hydrogen in the steel [5, 202].

Relevance of *in-situ* charging
In situ charging set-ups most accurately represent in-service conditions because the pipeline steel specimens are constantly exposed to hydrogen during testing. While pre-charging and *ex-situ* charging already simulate the environment less accurately, they have an additional drawback. When the specimens are taken out of the charging environment, hydrogen out-gassing occurs, which reduces the hydrogen concentration in the specimen. A common approach to minimise the extent of out-gassing before testing, is to store the charged specimen in liquid nitrogen. However, diffusion is a thermally activated process thus during warming to the test temperature hydrogen diffuses out of the specimen. Electroplating the specimen with, for example, zinc is a slightly superior method as it also partially limits the out-gassing during testing [45]. 'Partially' is an opted-for term because out-gassing is limited to the point at which the coating cracks, after which hydrogen diffuses out of the specimen.

2.6.2. Techniques to monitor crack initiation and growth
Several techniques exist that can be used to investigate fatigue crack initiation and its growth. In literature it is suggested to perform a combination of multiple methods in order to validate the results of one another, thereby achieving more reliable results. In this section, solely the methods of *Optical observation* and *Direct current potential drop* (DCPD) are discussed. The discussion of other powerful methods, such as acoustic emission, has been omitted because they are not part of the experimental work in the thesis.

Optical observation
The most straightforward method for studying crack lengths is by optical observation. Due to recent technological advances in the resolution of cameras and microscopes, and because of its simplicity, it is considered a reliable and widely used technique for crack growth studies. However, the main disadvantage of using cameras to record the onset of cracking is the observable field; the area in focus is considerably small. It can be troublesome to focus the camera on the area of interest and successfully capture the onset of crack initiation. Another limitation of this technique is that optical access to the region of interest is required, thereby not allowing the study of internal cracks. (Optical) microscopy, however, in addition to quantitatively measuring the crack size, is a powerful tool for observing the crack path it follows in relation to the microstructure.

Direct Current Potential Drop

The DCPD technique is based on running a constant current through the specimen while simultaneously probing the electrical potential across the crack plane. As the crack increases in size, the uncracked sectional area of the specimen decreases, which is correlated with an increase in electrical resistance along this plane. For the fact that a change in voltage is directly related to a change in electrical resistance, one can measure the change in potential between points on a sample and ultimately relate it to crack growth. This technique allows for crack (size) identification independent of the orientation and position of the crack in the material. Therefore, this measuring technique is particularly valuable when the test conditions do not allow optical access to the crack [38]. As it is an indirect method, it requires a calibration to relate the change in electrical potential to the crack size. Optical inspection, overload surface marking and (liquid N_2) forced brittle fracture are some examples of calibration methods.
Fig. 2.14 illustrates the principles of the DCPD method. Apart from the crack size itself, the measured potential (ΔV) depends on the specimen geometry, the distance of the potential probes (blue) from the crack and the current leads locations (red). Higher sensitivity of changes in crack dimensions are achieved when the distance of the probes to the crack decreases. This results from the ability to capture steeper changes on the equipotential field lines (blue dotted lines) localised in vicinity of the crack. Generally, the measurable crack length increment of the DCPD method is close to 50 μm. Due to the high sensitivity of measuring the crack size, it is a measurement technique suitable for the study of capturing the onset of crack initiation. The number of cycles to crack initiation in literature studies is selected as the inflection point at which the DCPD baseline voltage signal begins to continuously increase [102, 147, 90, 34]. The physical crack size associated with the definition of a (measurable) crack initiation with DCPD is approximately between 0.15-0.30 mm [136]. Another definition of crack initiation by Meneghetti et al., specifically defined for pure bending and axial loading, is the number of cycles where the voltage has increased 0.5% from the baseline. This definition was initially set at 0.05% based on FEA calculations, however this is not within the accuracy range of DCPD systems [120].

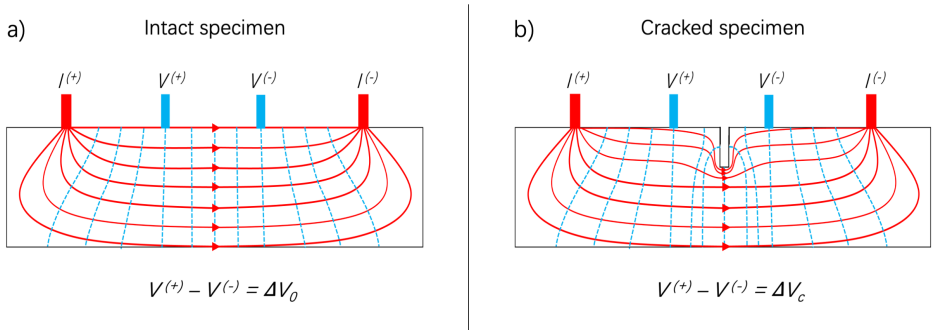

Figure 2.14: Principles of the direct current potential drop technique. The current leads (red) run a constant current (red lines) through the specimen. The voltage probes (blue) measure the changes in electrical potential. In a) an intact specimen is shown where the equipotential field lines (blue dotted lines) are parallel to each other in the area of interest. Once a crack initiates b), the trajectory of the current deviates thereby affecting the measured potential (ΔV).

Through the years, innovative DCPD designs have been engineered. In the work of Bär [20], a method to detect and localise cracks was presented for circumferentially notched cylindrical specimen (X8CrNi18-9 steel with diameter of 19.8 mm, Fig. 2.15a). The potential change over the notch was captured with spot-welded wires at a distance of 0.5 mm from the upper and lower edge of the notch (Fig. 2.15b). Above and below the notch, three measuring points were equidistantly arranged along the circumference of the sample with an angle of 120° in between two points (Fig. 2.15c). The measured potential of each probe (U_i) was normalised by the baseline value $U_{i,0}$ (average of first 10 cycles). Thus, $P_i = \frac{U_\mathrm{i}}{U_\mathrm{i,0}}$. From the results in Fig. 2.16, it can be deduced that the relative potential of probe 1 shows a steeper increase compared to the other two probes that output nearly identical signals. This is indicative of crack initiation near probe 1. The relation between potential and fractured area was estimated by marking the crack front with applying overloads within the regular fatigue cycles (see top

left corner of Fig. 2.16).

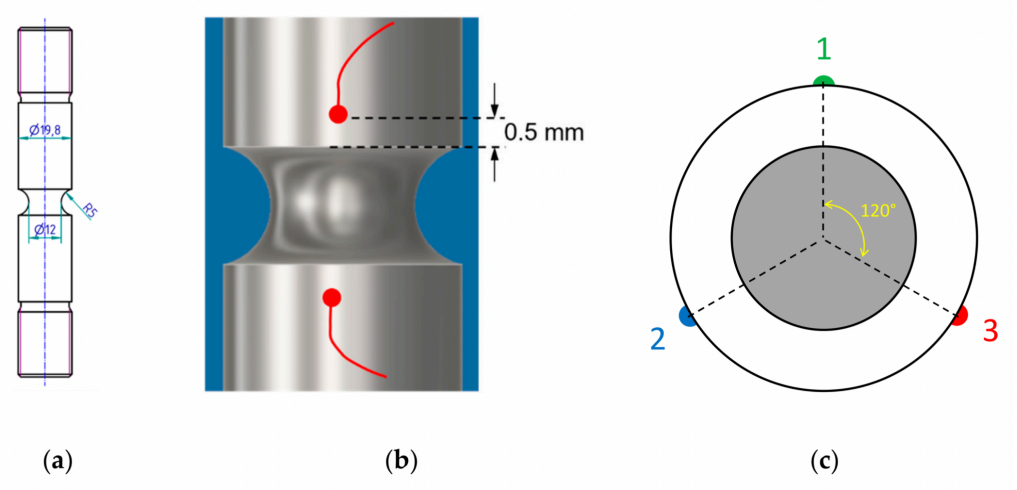

Figure 2.15: Arrangement of the notched rod for multiple potential drop measurements (PD): (a) an engineering drawing of the specimen including relevant dimensions, (b) position of the potential probes with respect to the notch; (c) position of the potential probes on the circumference [20].

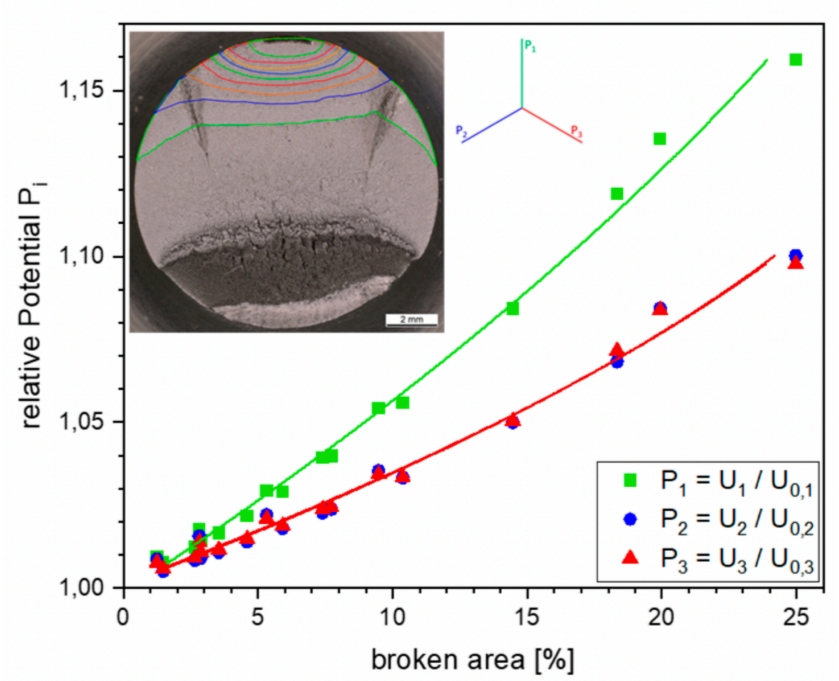

Figure 2.16: Experimental results of a crack initiation in the position in close proximity to potential probe 1. The crack front was marked by the application of overloads (coloured lines); (a) the relative potential P_1 displays a steeper increase in comparison to the values of P_2 and P_3 [20].

2.7. Conclusions and Research Objectives

The written literature review focused on presenting relevant and state-of-the-art findings on the hydrogen fatigue behaviour of API 5L pipeline steels. This research serves as the main framework for the experimental work in thesis project, as it enables the design choices of the engineered test setup to be followed (Chapter 3), and the results to be related to academic sources (Chapter 4). This section outlines the conclusions that can be drawn from the literature review and provides an overview of the research objectives set for this thesis.

2.7.1. Conclusions

- Increased environmental awareness has led to the development of hydrogen as an alternative energy source and the use of the existing natural gas infrastructure as a means of transporting it.
- Continuous exposure of pipeline steel to gaseous hydrogen ultimately drives the system to reach an equilibrium concentration of dissolved hydrogen.
- Trapping sites can hinder hydrogen diffusion and consequently alter the mechanical response of pipeline steels. Irreversible traps have the potential to function as crack initiation sites, while reversible trapping sites can act as crack propagation enhancers due to their continuous hydrogen supply. There is no consensus on whether irreversible or reversible traps govern accelerated hydrogen-induced failure.
- Hydrogen occupying trapping sites embrittles the material by several HE mechanisms: HEDE, HELP, AIDE, and HESIV. Oxygen impurities and an oxide layer can play a profound role in inhibiting HE; they restrict the adsorption of hydrogen on the steel surface.
- Certain regions of the pipeline, such as the welds, are more susceptible to HE due to heterogeneous hydrogen diffusion and hydrogen localisation. This results from (local) differences in microstructural phases and alloy compositions. Currently there is no consensus on the susceptibility of phases to HE. This depends on the interplay of other characteristic internal parameters: the trapping efficiency of the phases and its toughness, and the grain boundary area per unit volume that either efficiently traps hydrogen or promotes diffusion.
- Fatigue crack initiation governs hydrogen-assisted fatigue failure. Higher hydrogen (partial) pressures increase the HA-FCGR, which accelerates failure. However, the effect of hydrogen on the FCGR diminishes when the hydrogen concentration reaches maximum saturation, this effect occurs in the higher regime of ΔK ($\geq$ 15-20 MPa$\sqrt{\text{m}}$).
- Higher load ratios result in accelerated HA-FCG behaviour due to increased stress-driven hydrogen diffusion to the crack tip, facilitated plastic damage and the reduced the degree of effective hydrogen pumping out of the crack tip.
- Only at $f \leq 0.1$ Hz the HA-FCG behaviour experiences a frequency dependency. In this frequency range, HA-FCG tends to increase with a decrease in f. However, for low hydrogen pressures ($\leq$ 10 MPa), the HA-FCGR peaks out and drops to the FGCR of air. It is postulated that the onset of HA-FCG acceleration occurs at a sufficiently steep hydrogen concentration gradient at the crack tip. This threshold is described as $(P_{H2} \times f)^{1/2} \geq 0.1$.
- In general, fatigue striations are absent in hydrogen-charged specimens, and the fracture surfaces tend to transition from intergranular fracture to transgranular fracture in the higher regime of ΔK ($\geq$ 12-15 MPa$\sqrt{\text{m}}$). An exact understanding of how the interplay between HE mechanisms affects fracture has not yet been achieved.
- *In situ* charging set-ups most accurately represent in-service conditions since the pipeline steel specimens are constantly exposed to hydrogen during testing. The choice to perform E-charging or G-charging depends on the research facilities and intended hydrogen profile with respect to the actual application. E-charging is faster and is capable of producing a higher hydrogen content in the sample. G-charging more closely resembles operating conditions, but has increased safety risks and higher test equipment costs.
- A combination of optical observation and direct current potential drop could serve as a powerful tool to measure crack initiation and growth. The sensitivity of the measured crack size (and crack

initiation) is dependent on the distance of the probes from the notch (or crack location). The highest degree of sensitivity can be achieved by minimising this spacing.

2.7.2. Research Objectives

From the current literature it became evident that there exists a research gap in hydrogen-assisted fatigue crack growth behaviour. Some of these unresolved concepts are set as research objectives that are aimed to be resolved in this thesis. In particular, the behaviour of X60 pipeline steels in a high-pressure gaseous environment is of major interest to Intecsea, and has not been adequately discussed in the literature. For the reason that welds form primarily a risk of rupture, both for NG and the situation of hydrogen transport, the fatigue behaviour of the weld metal is of prime importance.

A main research objective has been formulated based on the research gaps and Intecsea's interest: *"Assessing the hydrogen-assisted fatigue crack growth behaviour of X60 pipeline steel and its girth welds in a novel high pressure gaseous test set-up."* To approach this main research objective, several sub-objectives are defined:

1. To develop an *in-situ* gaseous hydrogen charging fatigue set-up, suitable for internally pressurised specimens with an internal circumferential notch (in the weld) and capable to monitor fatigue crack initiation and growth.
2. To quantify the effect of high-pressure hydrogen gas on the crack initiation in, and total fatigue lifetime of, X60 pipeline steel and its girth weld.
3. To identify how the hydrogen gas (pressure) affects the fracture behaviour of the X60 base and weld metal, and what embrittlement mechanisms induced fatigue failure.
4. To evaluate the safety of hydrogen transport in X60 (welded) pipes, by assessing their resistance against HA-FCG.

2.7.3. Approach

The approach to answer the research objectives in this thesis is a combination of experimental and computational work. The *in-situ* hydrogen gas charging setup for tensile specimens from Boot et al. is adapted for compatibility with fatigue experiments and the DCPD method [30]. Similar to the study by Boot et al, the geometry of the specimen mimics a small-scale pipeline. However, the specimen introduced in this work is notched internally instead of externally. Finite element analysis (FEA) models are constructed to estimate the pre-charging time required for the specimen to reach hydrogen equilibrium, and to model the stress states experienced by the specimen under the fatigue test conditions. The results of the fatigue tests are combined with optical and scanning electron microscopy to characterise the embrittlement mechanisms and study the crack path in the material.

3

Materials and Methods

This chapter is devoted to the preliminary work of the performed experiments. First, **section 3.1** focuses on the methods used to characterise the API 5L X60 pipeline steel. This is followed by **section 3.2**, which highlights the design choices related to the technical test set-up, specimen, and test procedures. This chapter closes with **section 3.3**, which details two finite element models; the hydrogen equilibrium state in the specimen prior to the being tested and the existing stress states in the specimen during the experiments.

3.1. Material Characterisation

3.1.1. Pipe Type

The material examined in this thesis is API 5L X60 pipeline steel, which was supplied as axial segments of a circumferential piece of pipe containing a girth weld (see Fig.3.2.a). This figure will be discussed in further detail later. The pipe sections were manufactured by UOE (U-ing and O-ing) forming. This is a process in which the steel sheet is first bent into a U-shape using a U-press and then formed into an O-shape using an O-press. The (beveled) edges of the sheets are then seam-welded to form a pipe. In the Expansion process, which is the final step of the UOE forming process, a mechanical expander expands the pipes by plastic deformation to closely meet the tolerances defined in the pipe specification. In addition, the expansion homogenises the residual stresses resulting from the bending and seam welding [77]. Table 3.1 shows the dimensions of the original commercial X60 pipeline.

3.1.2. Specimen Design

Test pieces were extracted from the piece of pipe discussed in the previous section. This section deals with the design and machining methods for the test specimens. First, the general design concepts and manufacturing methods of the specimen geometry are discussed. The same concepts, but with respect to the notch, are then described.

Specimen Geometry

A schematic drawing of the geometry of the specimen is provided in Fig. 3.1. The engineering drawing with full specifications, including a detailed explanation of the design choices, can be found in Appendix A.1. It was aimed to adhere to ASTM G142 ("*Standard Test Method for Determining the Susceptibility of Metals to Embrittlement in a Hydrogen-Containing Environment at High Pressure, High Temperature, or Both*"), however since this thesis involves a fatigue setup with a novel specimen design, some dimensions are bound to deviate.

Table 3.1 X60 commercial pipeline dimensions.

Outside diameter	Internal diameter	Wall thickness
609.6 mm (24 inches)	577.8 mm	15.9 mm

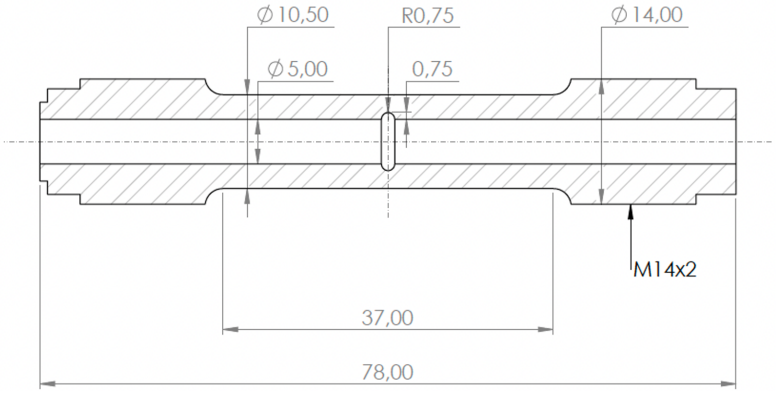

Figure 3.1: Engineering drawing showing the geometry of the specimen and notch. The dotted lines indicate the center of the specimen, and the hatched area represents the cross-sectional area. Dimensions are in mm. The engineering drawing with complete specifications is included in Appendix A.1.

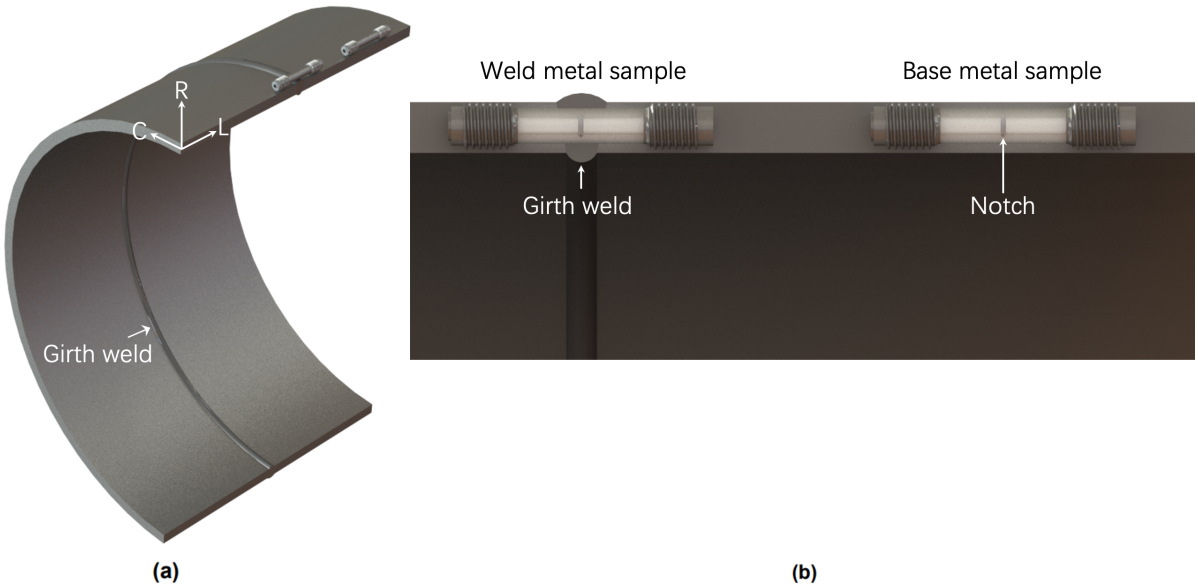

Figure 3.2: Orientation of the prepared specimens of the pipeline material. a) Cross section of the pipe where the girth weld and two samples are shown. The zoomed-in normal projection of the pipe wall (b), identifies the two samples as a weld metal and base metal sample. This subfigure shows the relative size of the samples to the thickness of the pipe wall. The transparent view of the gauge allows the orientation of the notch in the material to be seen. The orientations in a) are indicated relative to the original X60 welded pipe: L-Longitudinal, C-Circumferential, R-Radial.

The hollow cylindrical specimens were machined from an X60 pipe in the orientation illustrated in Fig. 3.2a. This subfigure includes the girth weld of the pipe and two samples to indicate their respective size to the pipe. Fig. 3.2b represents a zoomed-in normal projection of the pipe wall where the two samples are identified as a weld and base metal sample. This figure is supplemented to emphasise that for all weld specimens the notch was machined to be located in the center of the girth weld. Thus, the weld metal sample can be considered as a small scale pipe that includes a matching girth weld. From this figure it can also be seen that all base metal and weld metal samples originated from the longitudinal direction of the pipe.

The specimens are made entirely hollow, as this allows for an accurate evaluation of their eccentricity. By sealing the end of the specimen, a closed space volume is created from the gas supply source to the end of the specimen. This is the volume that pressurises the specimen internally with gas during the tests.

Notch Design
The notch allows the location of the failure to be controlled in the tests performed. The notch has a semi-circular shape with a radius of 0.75 mm, which results in a stress concentration factor (SCF) of 3.0. An increase of the SCF raises the local stresses in the notch, which can accelerate the time to failure. It can be noted that the SCF value is higher than the SCF ($\approx$ 2.20) defined in the standard assessment for welds during pipelaying operation and service life [52]. This thesis aimed for a notch that induces a SCF simulating the worst case scenario for a weld during hydrogen fatigue; hence the value of 3.0. Examples of worse scenarios would be local stresses arising from misalignment or weld defects such as porosity. Several concepts were involved in the design of a suitable SCF; a separate brief literature study was carried out for this process which is supplied in Appendix C.1. This literature study emphasises on hydrogen fatigue standards (Appendix C.1) and the effects of stress concentrations on HE (Appendix C.2). The FEA used to determine the SCF can be found in Appendix C.3. The internal notch was machined through EDM with a tolerance of +/- 0.05 mm (measured on the diameter). As the EDM process was carried out by an external party, the process parameters are unknown.

3.1.3. Microstructure Preparation
The preparation of the microstructure characterisation involved a series of steps: cutting, embedding, sanding, polishing and etching. Smaller pieces of the original pipe were cut in sizes compatible with hot-mounting (Struers CitoPress). The embedded piece was then sanded (from P80 up to P4000 EU SiC grit) and polished up to 1 µm (Struers MD/DP-Nap Diamond 1µm abrasive cloth) by using a Struers LaboPol-25. A 5% nital solution was then used for etching, enabling the microstructures to be made visible and studied with microscopy. All microstructural studies in this work were conducted on the radial-longitudinal plane of the pipe.

3.1.4. Characterisation Methods
Since the primary focus of this work is elucidating the effect of hydrogen on the crack initiation and growth in fatigue of X60 pipeline steel and its girth weld, both materials must be characterised. Proper characterisation forms the fundamental basis for relating the individual material response to microstructural features. This section discusses the different characterisation methods used in this thesis.

Compositional Analysis
Data regarding the compositional identification and combustion analysis is extracted from the work on the same pipeline (material) by Boot et al. [30]. In that particular study, XRF scanning was performed to analyse the different elements in the metal, additionally a LECO composition analyser was used to support the XRF data (cross-verification of Si content) and to measure the carbon content. The compositions of the base metal and weld metal are presented in Table 3.2 below. This Table also contains the mass fraction (%) limits of the chemical composition mentioned in the API 5L (PSL 2) standard for steel grade X60. As can be deduced from the data, all elements of the base metal and weld metal are present in acceptable quantities; they are within the range of the maximum allowable limit of the API 5L standard. At first glance one might conclude that the mass fraction content of Mn in base metal exceeds the API 5L limit. However, for each decrease of 0.01% below the specified maximum for C, an increase of 0.05% above the specified maximum for Mn is allowed (up to a maximum of 1.75% for X60). Mn is therefore also present in an acceptable quantity. Although the Si in weld metal exceeds the specified limit, a deviation may be agreed upon depending on the particular manufacturing demands.

Table 3.2 X60 base metal and (girth) weld metal chemical composition (%wt) from the work of Boot et al. [30]. Included are limits on chemical composition as specified in standard API 5L (PSL 2).

Specification	C	Mn	Si	Cr	Nb	Al	P	S	Rest
Base metal	0.06	1.66	0.26	0.06	0.04	0.04	< 0.01	< 0.01	97.88
Weld metal	0.07	1.45	0.58	0.05	0.01	0.01	0.01	0.01	97.81
API 5L limit (%wt) [12]	0.12	1.60	0.45	0.50	Nb + V + Ti $\leq$ 0.15	- *	0.025	0.015	-

* = limit value not documented in the API 5L specification sheet.

Microstructure and Crack Path Analysis
The microstructural characterisation involved optical microscopy, using a Leica Microsystems Wetzlar GmbH light microscope (type 020-520.007 DM/LP) and VHX-5000 Keyence digital microscope, and scanning electron microscopy with a Jeol JSM IT-100. In the subsequent sections those microscopes are referred to as 'Leica', 'Keyence' and 'scanning electron microscope', respectively. Prior to microscopical observation, the prepared pieces (see section 3.1.3) were placed in an ultrasonic bath (Branson 5510) with 2-isopropanol for 5 min. For the samples investigated by SEM, the samples were first degassed up to $\leq$ 1.0 x 10^{-1} mbar for 15 minutes prior to analysis. In addition, a voltage of 20.0 kV was used to obtain images at low vacuum mode. This degassing procedure and imaging settings were used for all SEM operations.

In order to analyse the crack path and its relation to the microstructure, fatigue tests were stopped at a 3.0-4.0% increase from the normalised baseline voltage. This range was chosen because, as was confirmed from the DCPD calibration (see Appendix D), crack initiation occurred and the growth was substantial. Four samples were embedded in resin and thinned using a lathe to visualise the internal crack, until the observed crack was sufficiently large to determine whether the crack trajectory was dependent on the microstructure. Details of this process, including the orientation of the embedded specimen, are illustrated in Fig. 3.3. The four samples for crack path analysis included the base metal and the weld metal, each examined for the 150 barg tested N_2 and H_2 environment.

Hardness Measurements
The hardness of the base and weld metal were measured on a piece prepared according to section 3.1.3 and by placing it under an automatic Vickers micro-hardness testing machine (ZwickRoell DuraScan 70). Seven rows of hardness measurements were taken on the polished surface. These rows extended from the base metal through the weld section. After the hardness measurements, surface etching distinguished the base metal, HAZ and weld, and allowed each hardness measurement to be evaluated individually for identification with respect to the material. Several optical images, not included in this thesis, were taken to accurately distinguish between measurements inside or close to the HAZ. The applied force was 1 N, and thus the Vickers hardness values are measured and reported of the type HV1. Measurements were made in accordance with ASTM E92-17 (*Standard Test Methods for Vickers Hardness and Knoop Hardness of Metallic Material*) [85].

Fracture Surface Analysis
The analysis of the fracture surface after complete failure included imaging with the Keyence and scanning electron microscope. The two fractured halves of each sample were removed from the set-up and ultrasonically cleaned for 5 minutes with 2-isopropanol. A (low magnification) overview picture was made with the Keyence. The overview images fulfill two main purposes: correlating the fracture surfaces with their respective fatigue areas (I, II and III, see section 4.4.1) and detecting weld defects or other anomalies. The surface of the fatigue fracture was then analysed using the SEM. At least one half of each specimen fatigue tested in this thesis was analysed by following this procedure.

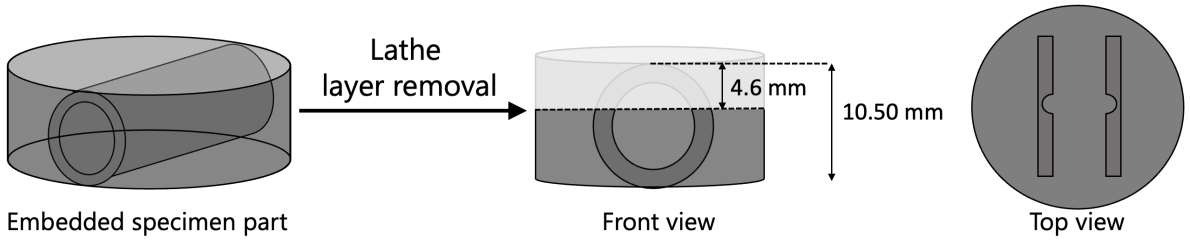

Figure 3.3: Illustration of the preparation of a sample for crack analysis. The left side of the arrow shows an embedded (cut) piece of the specimen containing the notch region. The right side of the arrow shows the removed layer (4.6 mm, transparent appearance) of the total diameter (10.50 mm) from a front view perspective and the notch region that was studied with microscopy from a top view perspective. The sketch is not to scale.

3.2. In-situ Gaseous Fatigue Set-up

This section is devoted to enlightening the designed components that construct a novel hydrogen fatigue test set-up. First, the fatigue set-up itself is discussed. Thereafter, the direct current potential drop method is explained in detail. The emphasis is on expounding design choices and their implementation.

3.2.1. In-situ Gaseous Charging Design

It is desired to design a test setup in which the hydrogen charging accurately simulates the environmental conditions of hydrogen pipelines. In this thesis, the design of an *in-situ* gaseous charging setup was chosen because this method is more representative of the operational conditions of hydrogen pipelines.

The construction of the setup is based on placing a hollow specimen under internal pressure with hydrogen gas, thereby mimicking a pipeline on a small scale. In order to convert the standard hydraulic 4-column load frame (MTS 311.21 ServoHydraulic Load Frame) into a machine compatible with *in-situ* gaseous hydrogen fatigue testing, two hollow aluminium 7075-T6 adapters were adapted from Boot et al. [30]. A cross-sectional view of the top and bottom adapter are illustrated in Fig. 3.4b, and Fig. 3.4c, respectively. Note that these adapters were further modified to allow DCPD measurements to be performed. This is a subject addressed separately in section 3.2.2. The specimen connects to the adapters through threaded (M14x2) holes. As can be seen from Fig. 3.4a, the top adapter further connects to a tubing system enabling gas transport. The left side of the top adapter is connected to N_2 and H_2 gas cylinders, as well as to a pressure gauge. This design allows gas supply to the specimen and simultaneous real-time monitoring of the gas pressure (in bar) to which the specimen is exposed. The piping system on the right side of the top adapter is connected to i) a relief valve that allows for the removal of the gas during any requisite occasion, and ii) a vacuum pump that can be used to evacuate the system of any gas. A nitrile O-ring is placed in the designed chamfer at the top end of the specimen, which seals the connection between the specimen and the top adapter (see Fig. 3.4b). The bottom end of the specimen is made airtight by placing an annealed copper washer (6 x 10 x 1 mm) under a bolt head (M6x1, DIN933-8.8) which, by tightening the bolt, seals the hole (see Fig. 3.4c).

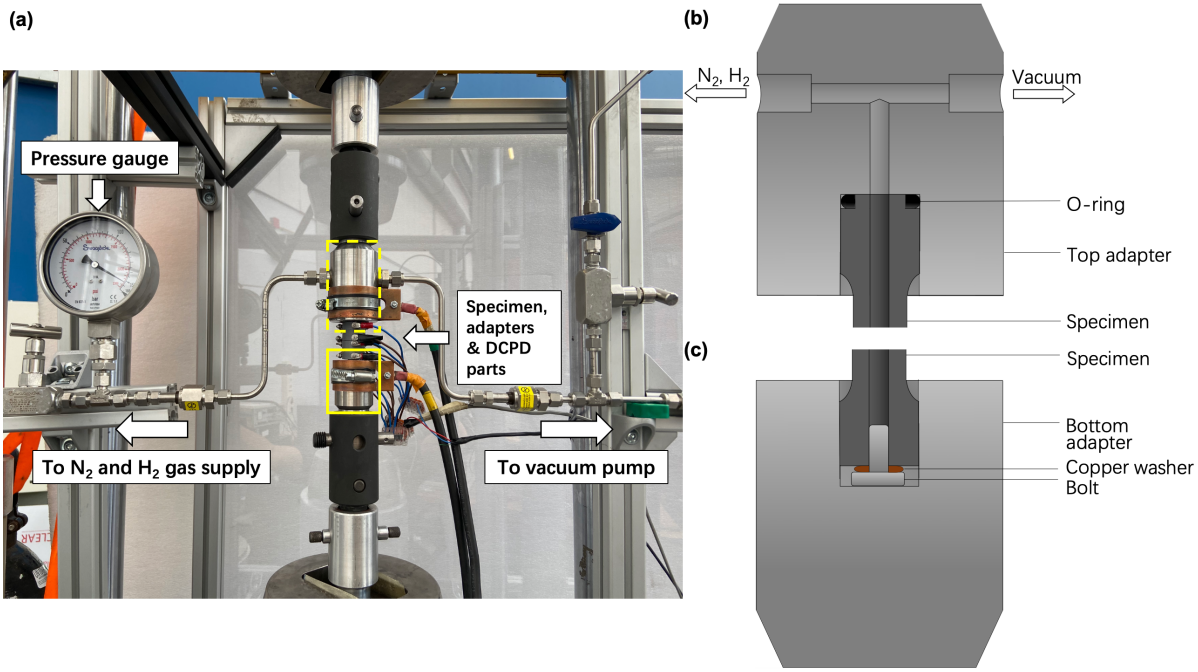

Figure 3.4: a) General overview of the test setup, displaying a specimen enclosed by DCPD parts, the adapters used, and the gas supply system. b) Cross section of the yellow dashed region in a) showing the connection between the specimen and the top adapter, and the airtight sealing of the top of the specimen. c) Cross section of the yellow solid region in a) showing the connection between the specimen and the bottom adapter, and the airtight sealing of the bottom of the specimen.

The integration of multiple valves throughout the piping system allows a segment containing the specimen to be sealed to a volume of approximately $\approx$ 10 mL. This confined volume is created for safety reasons, as it serves to minimize the amount of hydrogen gas released when the specimen fractures.

By pressurising the sample internally, rather than creating a containment volume that pressurizes the outside of the sample, complications related to crosshead movement and associated leakage problems are minimized. At least two advantages are now achieved with the current design, the containment volume itself expands during testing and the volume of hydrogen gas is significantly lower compared to an external gas chamber. The volume of hydrogen that may be present in combustible amounts is between 0.5 and 2.5 L only. Without ignition sources in this zone, no combustion is expected to occur. However, since the DCPD is used and thus there is a risk of spark emission from the electricity, the utmost attention and precautions are taken to arrest the DCPD measurement prior to the rupture of the specimen. Thus, for hydrogen gas measurements, the DCPD measurements only comprise data for crack initiation and subsequent short growth. On the other hand, for N_2 gas experiments, data are collected up to the time of fracture, as N_2 is inert and non-flammable.

Released hydrogen is assumed to diffuse rapidly into the air, diluting to non-flammable concentrations. Therefore, removing the DCPD current flow would be a sufficient precaution to safely conduct hydrogen fatigue tests *in-situ*. In addition, as an extra precaution, the setup is surrounded by a polycarbonate box (plates' thickness of 8 mm) that is structurally supported with aluminium profiles to protect the operator and the environment from particles that could be ejected from the setup by the high test pressure.

3.2.2. Direct Current Potential Drop

Set-up

For the specimen design proposed in this thesis, the crack initiation is expected at the internal surface. Optical access to the crack is thus limited. The combination of effectiveness, reliability, and independence from optical access led to the application of the DCPD technique to monitor the initiation and growth of fatigue cracks.

As became evident from the literature review, the DCPD technique relies on the flow of a current through the specimen. A current connection system was engineered and attached on the adapter(s) as shown in Fig. 3.5. A copper strip surrounds the adapter and is tightened by an aluminium hose clamp. Underneath the surface of the aluminium clamp, a rubber strip is placed to allow a method of uniform tightening. The current cable of the DCPD is attached to this copper strip by a bolted connection.

M2 bolts were utilised as DCPD voltage measurement probes. The probes are held in place by a 3D printed thermoplastic structure, referred to as the 'probe holder' in this thesis. It is a 100% infill PLA tubular structure that surrounds the gauge of the specimen. Heat inserts (Ruthex, RX-M2x4 Brass Threaded Bushings) were inserted into the probe holder by heating them and forcing them in holes, having a smaller diameter than the inserts, of the probe holder. The PLA deforms locally and surrounds the inserts. Cooling compresses the plastic against the inserts thereby fixating them in place. The firmly anchored inserts are threaded internally, allowing the DCPD bolts to be tightened to (or loosened from) the specimen gauge. Each bolt end was sharpened to enhance the accuracy of the contact area to the gauge. The other end of the bolts have an (M2) eye clamp compressed against the bolt head. The DCPD measuring wires that transmit the voltage signal to the measuring device are connected to these eye clamps.

Two probe holders surround the specimen. One probe holder measures voltages at positions below the notch and the other measures above the notch. The underlying thought for this decision is that precautions were taken for ductile failure of specimens tested in inert environments. To prevent the bolts from shifting while the specimen stretches, or to avoid plastic collapse of the probe holder, it was decided to use two probe holders instead of one.

Flexibility is the key advantage this system offers over conventional systems where the probes are connected by spot-welding. The probes in this thesis can be easily attached and removed. In addition,

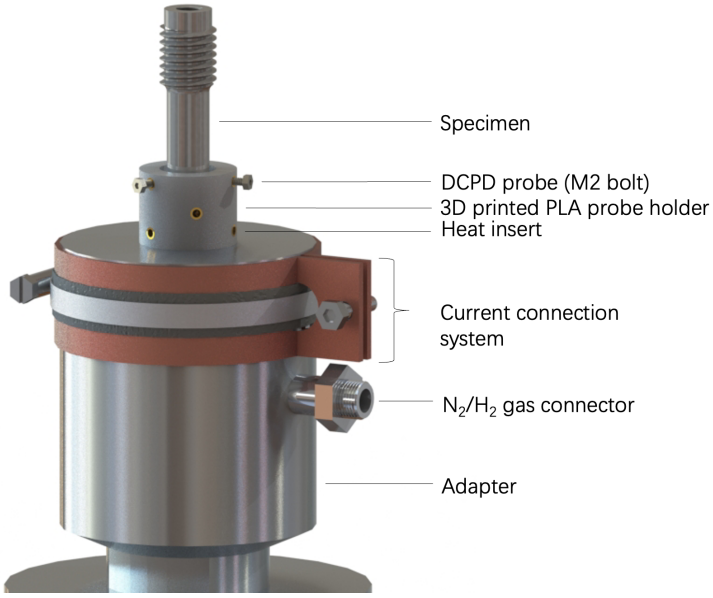

Figure 3.5: Illustration of the modified adapters made compatible with DCPD measurements. Note that two adapters are required during testing and thus each component, with the exception of the H_2 gas connector, is mirrored vertically across the center of the specimen.

misalignment of the probes can be corrected by moving the probe holder or even by reheating the inserts, if desired.

Probe positioning

The probes cannot be placed on the internal surface since the specimens are not accessible from the inside. However, this does not restrict this study because the phenomenon of equipotential surfaces applies. In its most fundamental form, this theory implies that a voltage at the internal surface can be sensed at a location at the external surface if measured at the same equipotential surface. This theorem justifies the decision to perform the voltage measurements by mounting the probes on the external surface of the specimen gauge.

The positions of the probes on the specimen during testing are illustrated in Fig. 3.6. Subfigure 3.6a shows a cross-sectional view of the specimen and two stacked probe holders. From this figure, the distances of the probes relative to the notch can be derived. The probes measuring across the semi-circular notch are denoted 'X', and are located 1.75 mm from the side of the notch. This was the shortest distance that could be achieved while maintaining high structural integrity of the edges of the probe holder. Any lesser distance would result in excessive plastic deformation at the edge, as the remaining area is unable to accommodate the heat experienced during the placement of the inserts. The other bolts, annotated with 'Y', are the reference probes and spaced 14.0 mm from the edge of the notch. Subfigure 3.6b illustrates a top view of the cross section of the specimen and probe holder. At each of the bolts' heights shown in subfigure 3.6a., three bolts are placed equidistantly along the circumference of the gauge. These three bolts, spaced 120° apart, are installed into a parallel circuit connection by a terminal connection clamp. As became evident from section 2.6.2, multiple connections significantly enhance the accuracy of measurements regarding the capture of the onset of cracking.

Insulation

To limit the current to the specimen under investigation, the components of the setup were electrically insulated. Proper electrical insulation between specimen and testing machine avoids effects of the machine on the measured potential, and vice versa. Another relevant practical problem avoided by insulation is the possibility of an alternative current path through the set-up, which short-circuits the specimen.

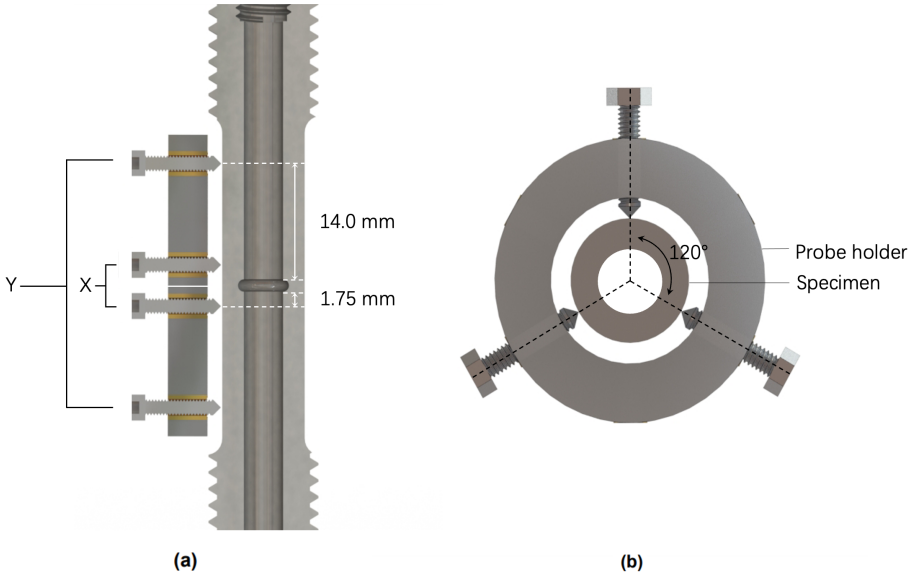

Figure 3.6: Illustration of the positions of the DCPD probes. a) Cross-sectional view of the specimen and two stacked probe holders. X and Y indicate the probes over the notch and the reference probes over the gauge, respectively. The distance between the measurement location of these probes and the side of the notch are annotated. b) Top cross-sectional view of the specimen and the probe holder. Each measurement height of the 4 bolts shown in a) is provided as an output averaged over the voltages measured by three probes equidistantly arranged along the circumference.

To increase the stability and sensitivity of the measurements, the following measures were taken regarding the insulation:

1. The gas connectors, one of which is visible in Fig. 3.5, are insulated from the rest of the gas transportation system by the insertion of a dielectric fitting (SS-4-DE-6 Swagelok). This fitting interrupts the current, but allows full fluid flow. This precaution was taken to restrict current flow to the N_2 and H_2 tanks.
2. The wedge grips were insulated from the hydraulic grips of the MTS machine (see Fig. 3.7) by applying fibreglass plates between them. This precaution was taken to avoid current flow to the load cell (cables).

In this project, preparatory work was carried out using an electromechanical testing machine (Zwick, *Z100*). The engineered insulation of that machine has proved to be working and is provided in Appendix B.

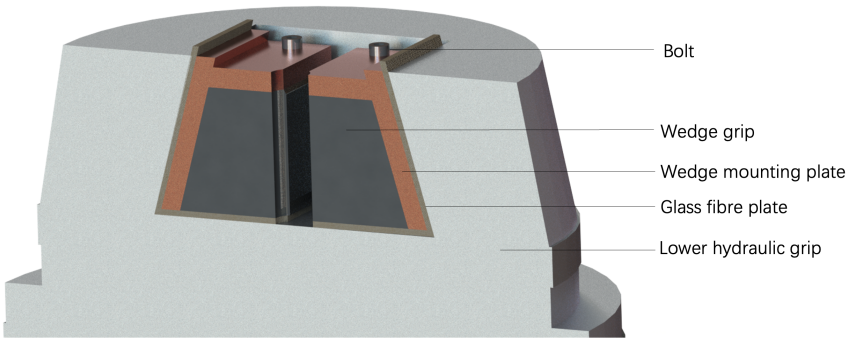

Figure 3.7: Electrical insulation of the MTS hydraulic test machine. Shown is the lower hydraulic grip of the MTS machine and annotations indicate the parts used. The wedge mounting plates were bolted to the wedges. Insulation is achieved by installing fiberglass plates that separate the wedge mounting plates from the hydraulic grip. The same modifications were performed on the upper hydraulic grip. Note that the wedge mounting plate is an optional component and can be removed if desired.

DCPD Test Settings

The output later introduced in the results sections is reported as a normalized value, namely $\frac{V_x}{V_y}$, to 'normalize' any variations such as thermoelectric effects. The self heating effect by the applied current was further reduced by pulsing the direct current. The pulse divider was set to '4', which ensues the current being pulsed four times within one loading cycle of the MTS testing machine. Each experiment was conducted with a current of 20 A. Peak-valley data acquisition was applied, with a sensitivity of 1000 N, to minimize the effect of crack closure on the voltage output (i.e. extracting voltages at the maximum load peaks where the crack fronts experience greatest separation).

DCPD Calibration Method

The DCPD output signal was correlated with the crack size by terminating the fatigue test before complete failure. It was aimed to stop the fatigue test at the onset of crack initiation, at an 4% increase of the normalised baseline voltage and at a voltage increase between those points. This process was performed for the base and weld metal, both for the N_2 and H_2 environment. The sample was fractured by means of liquid N_2 induced brittle fracture in an electromechanical tensile tester (ZwickRoell Z100). After ultrasonically cleaning the sample, it was placed under the Keyence such that the fatigue surface area could be distinguished from the tensile brittle region. In addition, the software options in the Keyence allowed for fatigue surface area determination for each sample. The specimens stopped at crack initiation additionally underwent SEM analysis in order to more accurately distinguish the fatigue fracture surface form the liquid N_2 induced brittle fracture surface. The results of the DCPD calibration are provided in Appendix D.

DCPD Data Filtering and Interpretation

The output of the DCPD device is the potential drop, $\frac{V_x}{V_y}$, as a function of time (s). It was decided to present the data as a function of the number of cycles instead, such that the results are more generic for fatigue data. An example of a representative (post-processed) output curve from the potential drop measurement, taken from specimen A1.1 (air environment), is presented in Fig. 3.8. This figure is

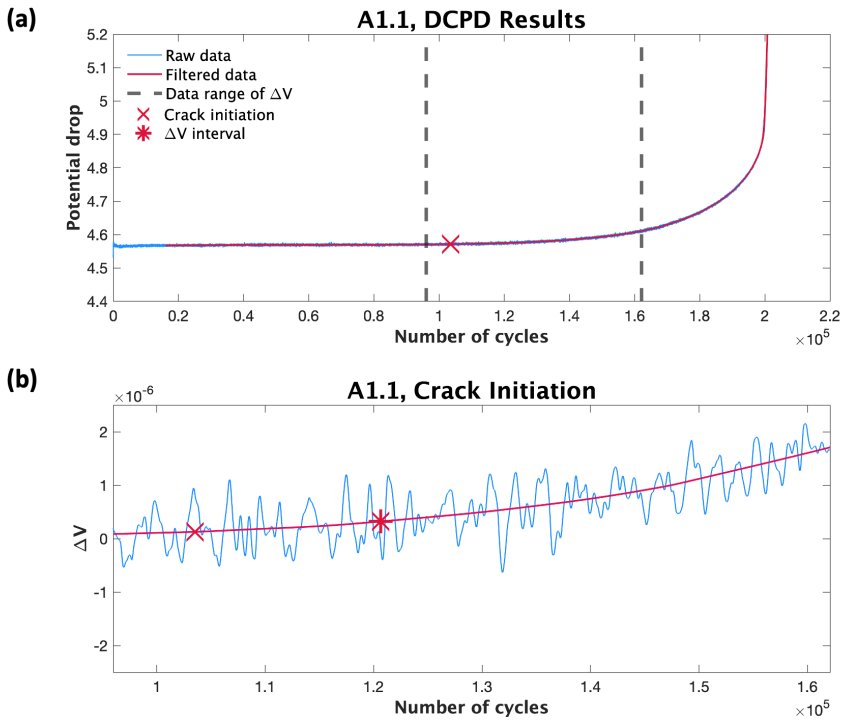

Figure 3.8: DCPD results and analysis of air specimen A1.1. Fig. 3.8a presents the raw and filtered potential drop results, where the crack initiation is marked (red cross). The dotted black lines indicate the region studied for crack initiation. This region is further plotted in Fig. 3.8b, where the changes in slope (ΔV) are presented. The region spanned by the red cross and red asterisk, represents the interval at which the threshold value (150%) for crack initiation was observed. The legend presented in the top corner of Fig. 3.8a applies for both subfigures.

divided into two sub-figures. Fig. 3.8a presents the raw data (blue) and filtered data (red) as a function of the number of cycles. Firstly, filtering in Fig. 3.8 was performed by the method of local regression using weighted linear least squares with a linear polynomial model (lowess filtering). It was decided to model the entire set of DCPD output data with a linear polynomial model, as this allows for a more accurate determination of the onset of cracking, via slope calculations, as the noise in the data is reduced. Second, a smoothing span of 1% was used. This value defines the width of the sliding window when smoothing the data, and thus determines the proportion of observations used in each local regression. A range of 1% signifies that each of the local regressions used to produce points on the curve, comprises 1% of the total number of data points.

As can be seen from Fig. 3.8a, the DCPD curve exhibits first a stable signal, referred to as the baseline voltage. After the crack has initiated (red cross), the voltage starts to increase which is an indication of crack growth. Thereafter, the crack growth rate increases substantially (observed with a steeper increase in voltage), until the specimen ultimately fails. The data up to and including the time of failure are recorded; failure occurs at a DCPD voltage output of 10 V. However, most of the figures that will be presented will cover a lower voltage limit, because due to the steep increase the plotted limit is sufficient to represent the moment of failure. Moreover, the voltage limit in the figure allows a well-founded investigation of the most important aspects; the moment of crack initiation and its (early stage of) growth.

Fig. 3.8b presents the method for determining the onset of crack initiation. It zooms in on the region between the dashed lines in Fig.3.8a. In Fig. 3.8b, the change in voltage slope is plotted against the number of cycles. The crack initiation point is marked with a red cross, and the offset was determined by identifying a threshold of 150% increase in the change of slope. The smallest range where this 150% increase change was found within the studied range is marked with a red asterisk. In reference to the state-of-the art (section 2.6.2), this thesis uses the point of deflection relative to the baseline voltage as the definition of crack initiation. The data were filtered using lowess filtering with a span of 20%, this value was chosen to obtain a more general tendency of the moving average with a greater reduction of noise.

The principles and methods discussed in Fig. 3.8 were computed for each individual specimen tested in this thesis. Therefore, in the subsequent sections, when there is spoken of 'onset of crack initiation' it refers to the result (red cross) in Fig. 3.8b.

3.2.3. Test Matrix and Procedure

The effects of various aspects of the fatigue test specimens, such as the influence of the weld metal, its expected divergent behaviour in a hydrogen environment compared to the base metal, and the presence of an internal notch, have yet to be resolved. Each of those aspects must be examined separately to be able to draw a well-founded conclusion based on the data gleaned from the experiments carried out. A comprehensive visualised overview of the tests, the so-called 'Test Matrix', is constructed to pursue a structural approach to testing. This section will cover the format of the Test Matrix by discussing the characteristics of each test along with the intended goal to be achieved. Furthermore, the test procedure developed for the setup will be discussed briefly.

Test Matrix

The Test Matrix for the fatigue tests is outlined in Table 3.3. This table is structured to present different subsets, each specified by sample type, test environment conditions and test objectives. The nonlinear stress states in the notch, the hydrogen evolution and the effect of internal gas pressure on the stress

Table 3.3 Test Matrix including experimental goals.

Sample	Subset	Sample amount	Environment	Objective
Base metal (BM) notched	A1	2	Ambient conditions	Fatigue life time determination
	A2	4	150 barg N_2	Effect of nitrogen gas pressure
	A3	4	150 barg H_2	Effect of hydrogen
Weld metal (WM) notched	B1	4	150 barg N_2	Weld metal properties
	B2	5	150 barg H_2	Effect of hydrogen
	B3	2	70 barg H_2	Effect of hydrogen gas pressure

state are treated separately for both materials. As shown in Table 3.3, two subsets are created; A and B, representing the notched base metal and notched weld metal sample, respectively. Set A and B both have multiple subsets characterised by a different (environmental) testing condition in order to study distinct objectives. Note that each subset is tested atleast in triplo for repeatability.

Set A is divided into three subsets. Subset A1 is performed on notched base metal samples in ambient conditions; the environmental conditions of the lab. The main objective of this subset is to obtain information on the basic fatigue performance of the X60 steel. Subset A2 is focused on studying the effect of applying an internal gas pressure of 150 barg N_2 on the specimen. Subset A3 substitutes the N_2 gas with H_2 gas. The pressure remains unchanged when moving from subset A2 to A3. Being identical in pressure, the sole parameter of change is the gas composition to which the sample is exposed. Subset A3 is performed to reveal the effect of H_2 on the initiation and growth of fatigue cracks and is compared to A2 that serves as a reference.

Similar to Set A, Set B is divided into three subsets. Subset B1 tests the weld material under identical conditions and sample geometry to Subset A2. Thus, B1 highlights the differences in fatigue behaviour of the two materials in a 150 barg inert N_2 gas environment. In Subset B2 the N_2 gas is substituted by H_2 gas. This gas substitution allows to identify the effect of H_2 on the weld metal. In Set B, subset B1 serves as a reference for B2 since the only parameter of change is the gas itself.

The remaining subset B3 consists of weld metal H_2 tests conducted at a H_2 pressure of 70 barg. This H_2 pressure is chosen because it is currently the pressure used in H_2 transport in onshore pipelines.

DCPD data will be collected and compared for each sample and forms the main piece of information on which conclusions on the performance of the samples are drawn. Combining the DCPD data with fracture surface analysis allows for a more profound understanding of the fatigue behaviour, i.e. the dominating fracture mechanisms in the different subsets.

Test Procedure

The fatigue tests included two parts that were performed: i) a pre-charging period and ii) the fatigue test phase itself. This section provides a concise description of the procedures followed in these parts. For an overview of the charging procedure, it is referred to the preliminary work of Boot et al. [29]. A detailed step-by-step of the fatigue procedure can be found in Appendix A.2.

The specimens tested in a H_2 environment were pre-charged to allow H_2 to diffuse into the specimen and to reach an (H_2) equilibrium diffusion state within the steel. As became evident from the literature review, small amounts of oxygen can significantly inhibit H_2 absorption. It was therefore aimed to exclude any oxygen contamination in the pressurised gas to which the specimen is subjected. This was achieved by flushing the system thrice with N_2 first. Note that the N_2 gas was evacuated within each flushing sequence. After N_2 flushing, the system (with specimen) was filled with H_2 gas and pressurised to the test pressure. This precharging period was initiated the day prior to the testing phase and marked a duration of 17 hours, which is the approximate time after which the fatigue test started under this held pressure.

The specimens were cleaned prior to their installation in the set-up. The cleaning process aimed to remove any residual grease and solidified particles from electrical discharge machining of the notch. The following cleaning procedure was performed:

1. Internally cleaning the specimen with a cotton swab
2. Placing the specimen in an ultrasonic bath in isopropanol for at least 5 minutes
3. Drying the sample and once again removing residual contamination with a cotton swab.
4. Sanding the inside with a brush containing 600 (EU) grit Al_2O_3
5. Sanding the inside with a brush containing 1000 (EU) grit SiC particles
6. Placing the specimen in an ultrasonic bath in isopropanol for at least 5 minutes.

After pre-charging, the DCPD components were set up and the connections to the measurement device were made. To ensure that the DCPD probes were properly connected to the specimen, a multimeter was used to check the conductivity of each probe. Thereafter, a pre-load of 5000 N was approached by the hydraulic machine to eliminate any play in the adapter connections. After the pre-load was reached, the fatigue procedure was started.

The DCPD voltage output, (applied) force values and displacement were recorded and stored at 8 Hz and 32 Hz. A minor phase-shift was applied to monitor different points in each cycle. In addition, these values were once more stored at the maximum and minimum applied force for each fatigue cycle (peak valley data acquisition).

The BM and WM fatigue tests were force controlled and performed with the following test conditions: f of 8 Hz, R of 0.1, F_{min} of 1.71 kN ($\sigma_{nom,min}$ = 25.60 MPa) and F_{max} of 17.1 kN ($\sigma_{nom,max}$ = 256.0 MPa). An overview of the fatigue test conditions is provided in Fig. 3.9. The end-of-test criterion was defined as fracture itself, indicated by the moment when the load drops 5% below the minimal force of the fatigue cycles. When the H_2 fatigue tests were finished, the system was flushed with N_2 in order to evacuate any residual H_2 gas in the set-up.

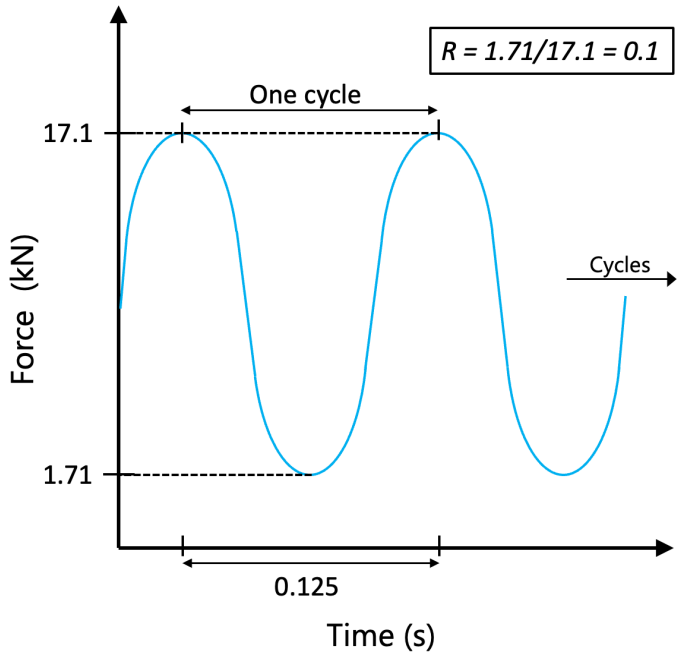

Figure 3.9: Illustration of the fatigue test conditions.

3.3. Computational Methods

This section discusses two finite element models that were used to i) comprehend and visualise the H_2 equilibrium state of the (pre-charged) specimen prior to fatigue experiments, and ii) to evaluate the stress states experienced in the notch during the fatigue cycles. Models i) and ii) are referred to as the hydrogen diffusion model and the fatigue model, respectively. Each model was created by defining the specimen gauge length with an axisymmetric mesh in SIMULIA Abaqus/CAE (2021). The models had an identical geometry, however the mesh sizes varied. The fatigue model had finer elements, as this was necessary to obtain mesh convergence during the calculation of the different stress states. The mesh sizes for the hydrogen diffusion model ranged from 10 µm to 70 µm and from 30 µm to 400 µm for the notch and gauge section, respectively. Regarding the fatigue model, the mesh sizes ranged from 0.3 µm to 3.0 µm and from 0.3 µm to 50 µm for the notch and gauge section, respectively.

3.3.1. Hydrogen Diffusion Model

The pre-charging time required to reach a H_2 equilibrium state in the specimen was calculated by developing a diffusion model with standard quadratic axisymmetric heat transfer nodes DCAX8. This model essentially represents the evolution of H_2 concentration from the interior of the specimen to its external surface. The mesh used in the model is of the type 'structural', to maintain consistency in the use of quadratic mesh elements. The structural mesh thus eliminates the use of other, or a combination of other, element types which the quadratic ones are incompatible with (i.e. triangular elements). Below, the material input data and boundary conditions of the diffusion model can be read in respective order.

Material Input Data

For the notched weld specimen, the structural mesh of the entire piece is partitioned into two sections: a base metal section and a weld metal section. Fig. 3.12a represents an overview of the H_2 concentration profile at equilibrium, where the transition from base metal to weld is illustrated with a purple line. The base metal and weld regions were assigned with their corresponding specific diffusivity from literature. Mohtadi-Bonab et al. reported a value of 0.81 mm^2h^{-1} for the effective diffusivity (D_{eff}) of X60 pipeline steel [123]. As for the weld metal, Panico et al. tested an ER70S-6 weld and determined a D_{eff} of 1.044 mm^2h^{-1} for the material [142]. The test method in these studies were both based on electrochemical permeation tests in a modified Devanathan-Stachursky setup. The article by Panico et al. did not disclose the welding parameters used, but since the same weld metal was used as in this study, it is assumed that the reported diffusivity is sufficiently representative of our material. It is notable that the specific diffusion of the weld material is higher than that of the base material. This is attributed to the higher density of grain boundaries in the weld, which serve as the main diffusion pathway for hydrogen.

Boundary Conditions

Two boundary conditions were set to model the hydrogen diffusion of the specimen. First, the equilibrium sub-surface concentration of hydrogen at ambient conditions of 293 K and 150 barg was calculated using Sieverts' Law [171]. The result from this calculation was a hydrogen concentration of 2.559×10^{-11} mol/mm^3. This condition was modelled by defining this hydrogen concentration value on the inside surface of the specimen. The involved calculations in the determination of this hydrogen concentration are provided in Appendix C. In order to accurately represent the initial conditions, i.e. the period before the H_2 gas valves were opened for specimen pre-charging, the bulk concentration was set to 0 mol/mm^3 in the initial step of the model. The evolution of the concentration gradient over time was then studied by performing an explicit dynamic analysis.

The outer surface does not experience a pressurised H_2 environment. Therefore, according to Sieverts' law an additional boundary condition has to be set. Namely, that the hydrogen concentration at the external surface must be 0 mol/mm^3. This implies that hydrogen desorps from the outer surface rather than allowing a fully saturated state to be reached. If we relate this to the work of Lynch et al, it is a coherent statement because a free surface (and the sites between the first few atomic layers below a surface) acts as a weak (reversible) site for containment compared to the main diffusion pathway (grain boundaries) [113]. An option for a boundary condition representing the process of desorption does not exist in Abaqus. Therefore, simply defining the boundary condition of 0 mol/mm^3 hydrogen at the outer surface neglects any interfacial reaction effects and is thus a simplification of the actual test conditions. Fig 3.10 below summarises the discussed boundary conditions of the diffusion model in an illustration.

Abaqus uses an extended form of Fick's equations for mass diffusion, and solves for ϕ as solution variable:

$$\phi = c/s \tag{3.1}$$

ϕ represents the normalised concentration, *c* the mass concentration of the diffusing material, and *s* is solubility within the base material. In principle, solving for ϕ can be thought of calculating the 'activity' of the diffusing material. This method ensures that the normalised concentration is continuous over mesh elements that share nodes. Implying that for this model, with significance at the boundary between the base metal and weld metal, the normalised concentration is continuous over this boundary where nodes are shared. In this study, the concentration is normalised with respect to the value of Sieverts' law on the inside surface. This implies that a solubility value is not necessarily needed and that it can be set to '1'. The outputted normalised concentrations can therefore be directly interpreted as the actual

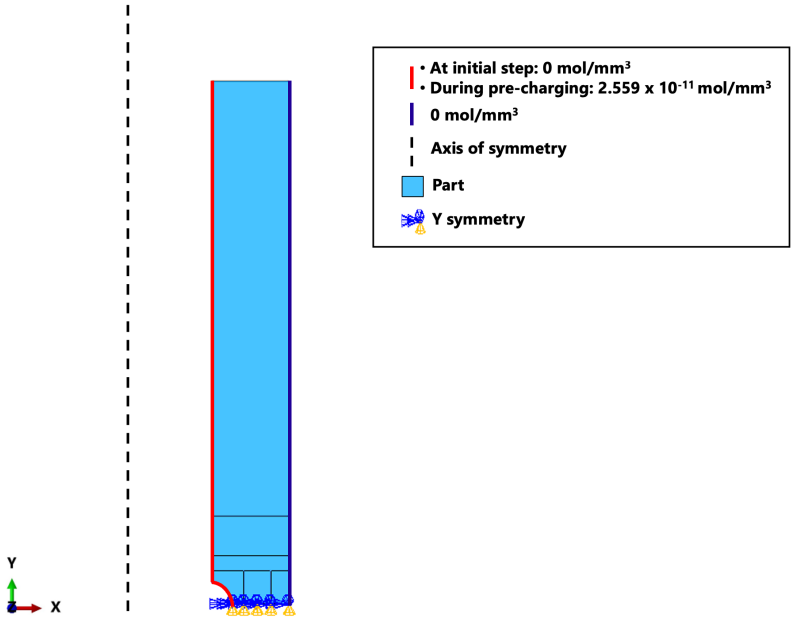

Figure 3.10: Boundary conditions of the diffusion model. The internal surface (red) was set to a concentration of 0 mol/mm^3 in the initial step. During pre-charging this value switched to the value equilibrium concentration value from Sieverts' law; 2.559 x 10^{-11} mol/mm^3. In addition, the outer surface (navy blue) was set to 0 mol/mm^3 which also results from Sieverts' law. The axis of symmetry and y-symmetry boundary conditions are depicted with dashed black lines and a combination of blue and orange arrows, respectively.

concentration. This approach can be considered to be valid since the solubility becomes of significant importance when the solubility limit of the material will be reached. Inspection of the solubilities of the materials resulted in the finding that the solubility limits are roughly a factor 100 higher than the concentrations reached in this model. In other words, diffusion is not limited by the solubility for both the base and weld metal.

The hydrogen equilibrium state of the pre-charged specimen is presented in Fig. 3.11. Subfigures 3.11a and 3.11b both show the hydrogen concentration. For visualisation and ease of interpretation of the diffusion model geometry, the mesh is hidden in Fig. 3.11a. A close-up of the notch area is shown in Fig. 3.11b. Values of hydrogen concentration along the notch root plane were extracted from the nodes at different charging durations and plotted in Fig. 3.12. Hydrogen gradually diffuses through the wall thickness and distributes itself within a relatively short period of time. It can be noted that a near equilibrium state is reached after 4 hours. Additional simulations were performed for time steps of 30 minutes for a total of 17 hours, corresponding to the duration of precharging overnight. After 6 hours of precharging, nodals' change in hydrogen concentration were found to be less than 0.03% for the 5.5-6 hour time step. This percentage change is considered to be sufficiently small to assume that after 6 hours, a steadily decreasing hydrogen concentration profile from 2.559×10^{-11} mol/mm^3 on the inner surface to 0 mol/mm^3 on the outer surface has been reached.

It is important to note that this model does not account for local equilibrium changes caused by variations in the (local) stress state present during cyclic loading. Since this model simulates an unloaded specimen, the hydrogen concentration is only representative of the equilibrium state prior to testing. Simulations were also performed for the base metal specimens. Similar results were found and thus overnight charging is adequate for both the weld and base metal to reach equilibrium in the notch region.

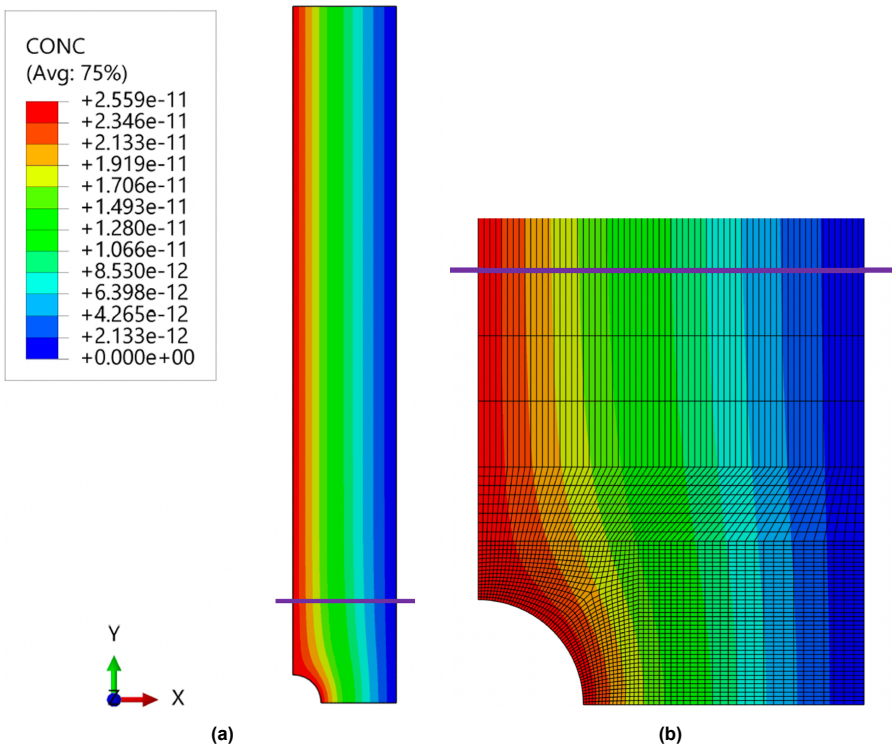

Figure 3.11: a) Diffusion model of a 6 hour 150 barg H_2 gas pre-charged weld specimen. Units are mol/mm^3. b) Close-up of the notched weld region of a). In both a) and b) it is assumed that a hydrogen equilibrium state was reached. The purple line indicates the separation between the base and weld metal regions.

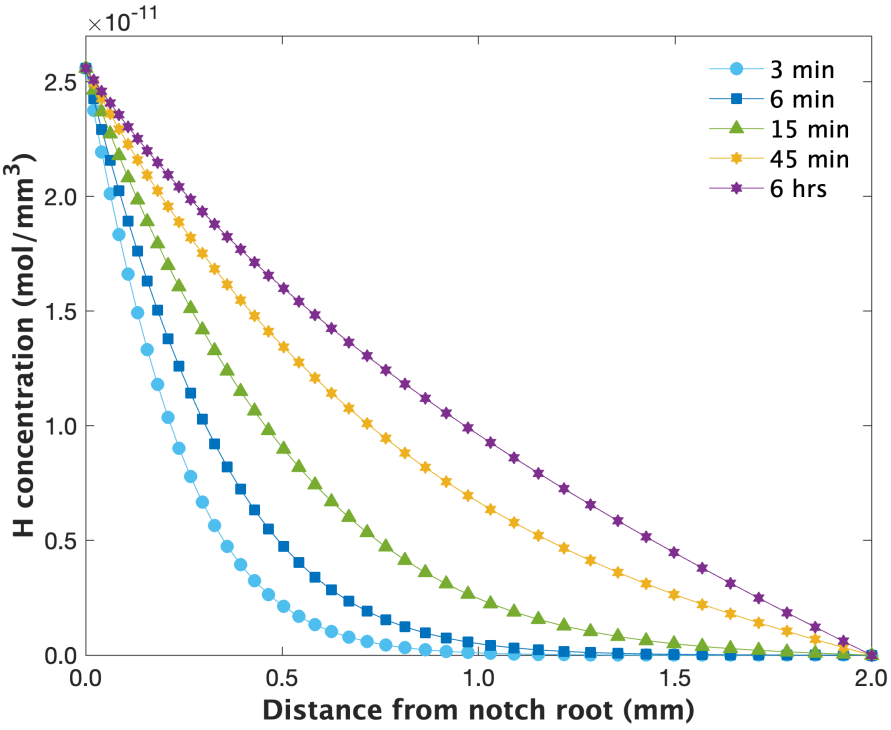

Figure 3.12: The evolution of the hydrogen concentration profile, at different pre-charging durations, at the notch surface of a 150 barg internally pressurised weld specimen. Equilibrium is reached after 6 hours.

3.3.2. Fatigue Model

This section deals with the FEA model that simulates the fatigue cycles of the base metal specimens. The internal notch in the specimen acts as a local stress raiser that ultimately affects the mechanical response of the material. To achieve a deeper understanding of the stress states in the notch at the point of loading and unloading, a fatigue model is established. The geometry and mesh used for the fatigue model are identical to those of the hydrogen diffusion model presented in section 3.3.1. However, while the diffusion model used quadratic heat elements DCAX8, the mesh elements for the fatigue model were changed to quadratic deformation elements CAX8.

Boundary Conditions and Loads

First, in order for the (axisymmetric) model to represent the entire gauge width of the specimen, a symmetric boundary condition was applied to the bottom plane. The symmetry was defined as y-symmetry. Note that in the global coordinate system used, the x, y and z axes represent the radial, longitudinal and circumferential directions of the specimen. Therefore, taking into account the y-symmetry, for visualisation of the behaviour of the entire specimen, the later introduced figures concerning the stress states can be interpreted as ”mirrored” over the notch-root plane.

Two loads were applied to the model, which were also activated at different time frames, or so-called ’steps’ in the Abaqus software. At the initial step of the model, the internal pressure of 150 barg (from either N_2 or H_2 gas) was defined by applying a pressure load of 15 MPa to the inner surface. The succeeding steps describe the fatigue phase. A series of 10 fatigue cycles were modeled to observe whether the fatigue behaviour was consistent and to reveal any anomalies that may have occurred, such as hardening behaviour. The maximum (17.14 kN) and minimum forces (1.714 kN) exerted by the MTS machine during the fatigue cycles were converted to the resulting nominal stresses on the gauge; these were 256.0 MPa and 25.6 MPa, respectively. These nominal stresses were modeled by defining them as a distributed load applied to the upper plane, also known by the term ’pressure load’ in the field of engineering. A pressure load can represent a tensile stress by taking its negative. Thus, at the peak load of the fatigue cycle, the upper plane of the gauge is subjected to a pressure of -256 MPa. The same principle applies to the minimum load of the fatigue cycle, however, with a pressure of -25.6 MPa. To study the mechanical behaviour during the loading and unloading cycles, the defined loads were applied in increments (10 per fatigue cycle/step). For each increment, the stresses and strains for all nodes were stored. Fig 3.13 below summarises the discussed boundary conditions and loads of the fatigue model in an illustration. Important to realise is that the internal pressure step of the model was not modelled in the study of the fatigue behaviour in the air environment.

The fatigue loading conditions in this thesis induce both linear elastic behaviour and plastic deformation in the test specimens. To study the stress conditions under plastic deformation in the Abaqus model, the option ’Nlgeom’ (non-linear geometry) was switched on and a (multilinear) kinematic hardening model was used. Kinematic hardening means that during deformation the yield surface moves as a rigid body without any rotation in stress space. Therefore, in the case of yielding in tension, the yield surface translates to that stress value, which consequently causes the compressive yield strength to be translated by the same vector.

Material Input Data

The fatigue model was developed only for the base metal, and is therefore representative only for test set A. The underlying reason is that the material data for the specific weld used in this thesis are not available. Extracting weld data is also not straightforward; according to the offshore standard DNV-OS-F101, the minimum strength of the weld material must (over-) match the maximum strength of the base metal [188]. Theoretically, weld data could be extracted from a tensile test on a smooth cylindrical specimen with a weld at the center of the gauge body. However, it could be understood that this would be a challenging process as the material is expected to deform first in the base metal as opposed to the weld metal. Apart from the related difficulties, the extraction of material data for the weld metal is

Table 3.4 Base material input data for the Abaqus fatigue model. Values were taken from [30].

True plastic strain e_p	0.00	0.01	0.03	0.05	0.075
True stress σ (MPa)	453	486	530	557	576

also beyond the scope of this thesis. Instead, the data points used as input for the base material model were taken from the research of Boot et al. and are presented in Table 3.4 [30]. The values resulted from a SSRT test in air performed on a smooth cylindrical base metal specimen and were taken up to the onset of necking. In order to still be able to estimate the stress states in the weld metal, the base material input data is multiplied by a factor of 1.3 to approximate the weld data. This estimation was made based on comparing the onset of yielding in the SSRT curves of the notched base and weld metal. The factor of 1.3 is a rough approximation. Consequently, the weld model fulfills the purpose of being indicative of stress states rather than being an in-depth simulation from which well-founded conclusions can be drawn.

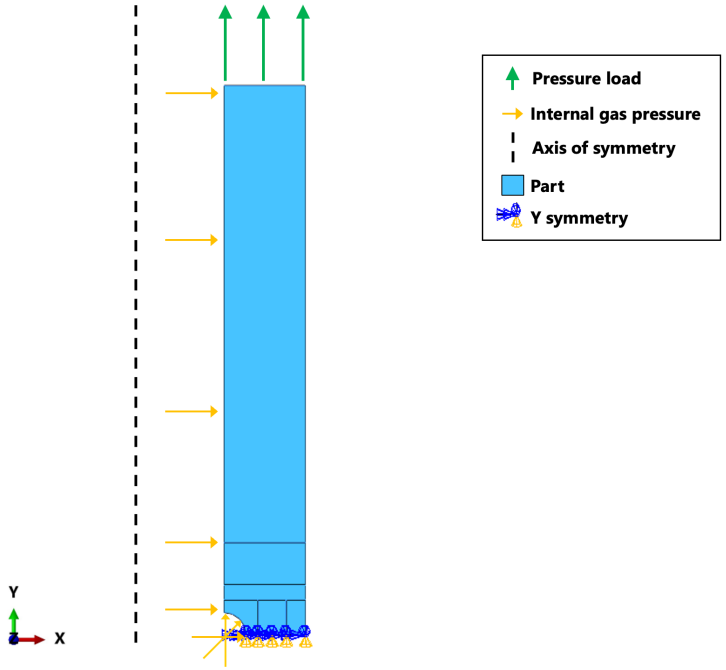

Figure 3.13: Boundary conditions and loads of the fatigue model. In the case of the N_2 and H_2 environments, applying the internal gas pressure was the initial step of the model (orange arrows). The tensile stress was modelled by a pressure load applied to the top surface (green arrows). This load varied from -256 MPa to -25.6 MPa at the loading and unloading steps, respectively. The axis of symmetry and y-symmetry boundary conditions are depicted with dashed black lines and a combination of blue and orange arrows, respectively.

4

Results and Discussion

This Chapter is devoted to present the results obtained from the experiments conducted. First, in **section 4.1**, the results from the material characterisation are discussed. Thereafter, in **section 4.2**, the obtained hydrogen enhanced fatigue results of the base metal are critically assessed. Next, in **section 4.3**, a similar discussion is performed on the hydrogen enhanced fatigue behaviour of the weld material. This Chapter closes with **section 4.4**, where the fatigue results are related to the fracture behaviour of the materials.

4.1. Material Characterisation

4.1.1. Base Material

Microstructure

Figure 4.1 below is a low magnification optical image of the microstructure at the centre of the pipe-wall. The material exhibits a banded microstructure of alternating layers of polygonal ferrite (white) and pearlite (black) elongated extending along the rolling direction, which is parallel to the longitudinal axis of the pipe. It is evident that the polygonal ferrite in the base metal exists in relatively larger proportion than the the colonies of pearlite. This is due to the the low carbon content in the structure; the amount

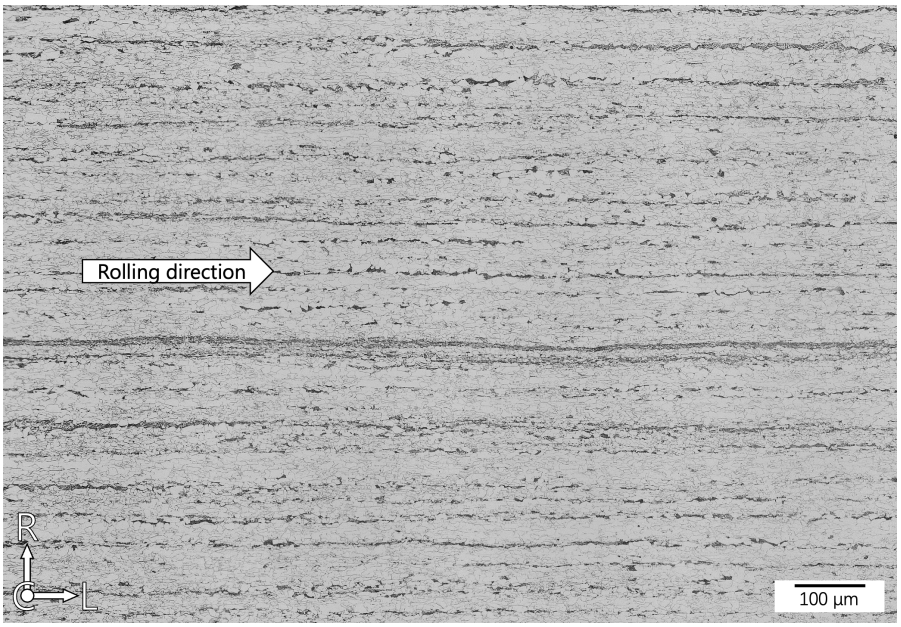

Figure 4.1: Optical image of the banded microstructure in X60 pipeline steel base material consisting of ferrite (white) and pearlite (black). The rolling direction is horizontal and the pipe-wall thickness is vertical in the image plane.

of pearlite in the structure increases with increasing carbon content [65]. Note that such a banded microstructure with ferrite and pearlite layers elongated in the rolling direction, is a typical feature of thick-walled ferrite-pearlite commercial pipeline steels [96].

Figure 4.2 shows two microstructure images of the base metal. This image shows two typical characteristics of rolled steel: i) elongated grains in the rolling direction and ii) grain refinement on the surfaces of the steel plate. The former feature is due to the shear forces exerted during the rolling process and the latter is a direct result of the shear forces being of highest magnitude at the surfaces. The grain refinement can be clearly observed in Figure 4.2a, which shows the outer surface of the steel plate, as the grains are smaller compared to those visible in Figure 4.2b, which shows the microstructure in the middle of the pipe wall thickness. The elongated appearance of the grains is evident in both subfigures.

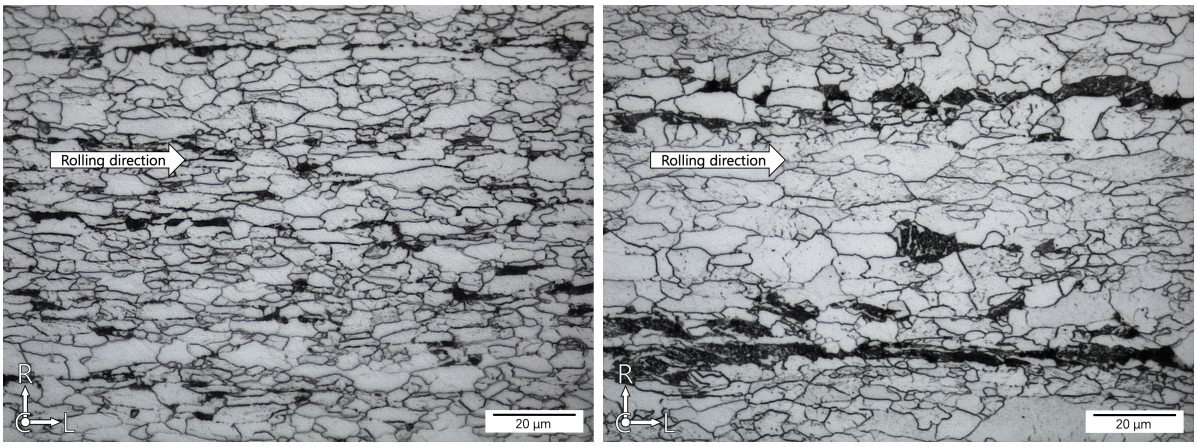

(a) (b)

Figure 4.2: Microstructure at the outer surface of the pipe wall a) and microstructure at the middle section of the pipe wall b). Differences in grain sizes can be observed and the elongated appearance of the grains can be seen. Both images were taken at 50 times magnification.

In the center of the pipe wall, visible in the center of the image plane of Figure 4.1, centerline segregation bands are present. These bands are also commonly referred to as abnormal segregation bands. Figure 4.3 is a SEM-image that provides a close-up of the segregation band in Figure 4.1. The segregation band comprises upper bainite and degenerated pearlite, and is surrounded by a matrix of ferrite. Essentially, enrichment in the centerline region with elements such as carbon, manganese, molybdenum, and/or chromium leads to the formation of harder microstructural features such as the upper bainite present in this steel. (Upper)bainite generally has a higher hardness than ferrite and is known to reduce ductility more severely in a hydrogen environment compared to complete ferrite-pearlite steels [58]. However, the volume fraction of upper bainite (and degenerated pearlite) is considered sufficiently low to assume that it has no significant influence on the overall fatigue behaviour of the specimens in this study. Therefore, further discussion of these microstructures is excluded.

4.1.2. Weld Metal and HAZ

Weld Metal Macrostructure

The macrostructure of the X60 girth weld is provided in Figure 4.4. In this cross sectional overview the geometry of the weld can be seen, and the heat affected zone (HAZ) and the BM can be distinguished from the weld by their appearance. The region around the weld metal is the HAZ (light gray faded appearance) and can be identified as the zone that separates, or acts as a transition between, the base metal (dark appearance) and the weld metal. Although the composition of the HAZ is similar to that of the base metal, the heating to which the HAZ was exposed during the welding passes ultimately affected the microstructure of this region. In view of this, the microstructure and hardness were characterised separately. The girth weld of the pipeline from which the specimens were extracted was made automatically and is therefore viewed as being consistent along the circumference of the pipe. The start-stop locations of the welding process were identified and excluded in this study.

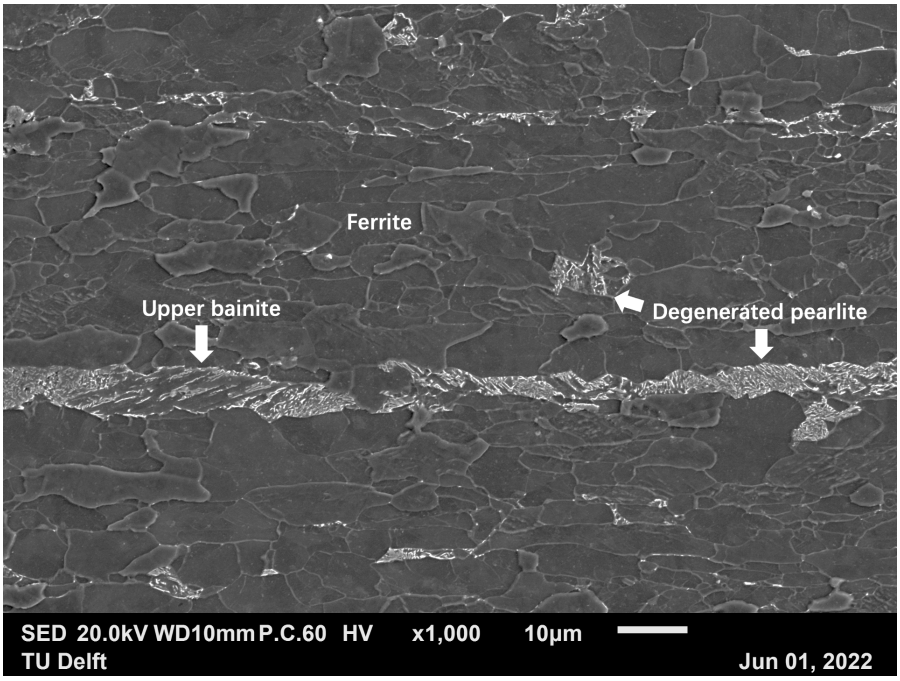

Figure 4.3: SEM close-up image of the centerline segregation band in the X60 pipeline steel base material. The segregation band was identified to consist of the microstructures degenerated pearlite and bainite.

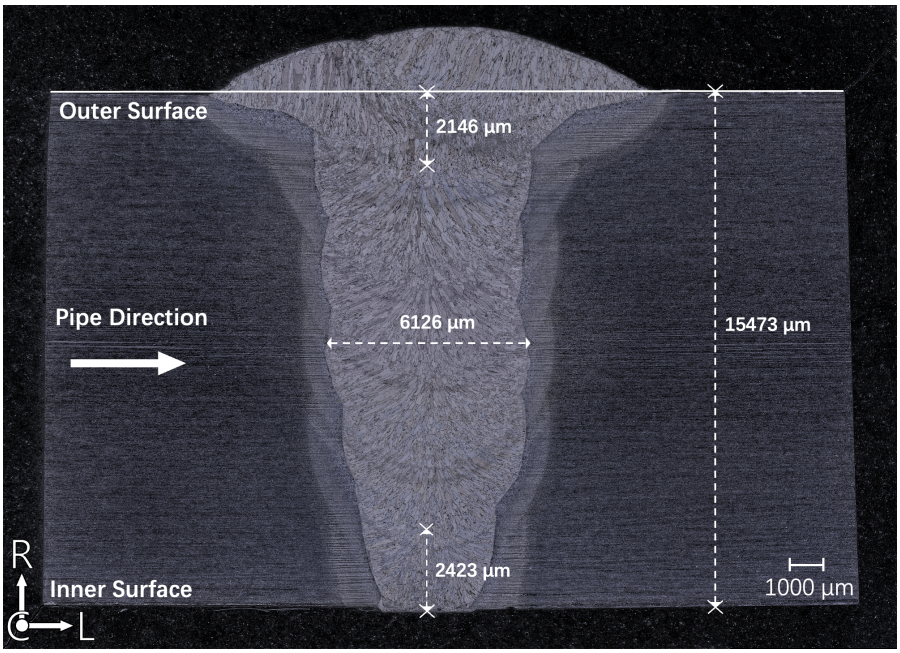

Figure 4.4: Macrostructure of the X60 girth weld. The longitudinal axis is annotated as 'pipe direction' and is horizontal in the image plane. Relevant dimensions are annotated in a white colour; the pipe-wall thickness is approximately 15.5 mm, the width of the weld is roughly 6.1 mm and the distances (measured from the surface) of the first and last weld passes are both less than 2.5 mm.

The weld in this thesis is classified as a butt weld that required multiple weld passes due to the thickness of the pipe. The individual weld passes can be directly observed in Figure 4.4. The thickness of the first (at inner surface) and last (at outer surface) weld passes were measured vertically in the image plane and their length are reported to be both under 2.5 mm. Investigating such features is an important action for the design of the fatigue test specimens; namely, the different residual stresses present in the test specimens could locally affect the hydrogen diffusion or their mechanical response.

For instance, conventionally, butt welded joints have residual compressive stresses at the center and tensile stresses at the faces [177, 37]. Tensile stressed regions are considered to be more susceptible to fatigue and fracture than compressively stressed regions [159, 157]. However, it is important to realize that residual stresses can relax when the specimens are machined from the pipe. Hence, the residual stress distribution in the samples differs from the one present in an intact welded pipe.

Weld Metal Microstructure

Even with the naked eye, when inspecting an etched weld, the differences in microstructure with respect to the base metal can be directly identified. The distinct appearance of the microstructures of the weld metal and base metal already became evident from Figure 4.4. This subsection focuses explicitly on the weld metal microstructure. As shown in Figure 4.4, the microstructure of the weld metal appears to exhibit columnar coarse grains. This columnar appearance is the result of austenitisation of the material during the welding process. During solidification after each weld pass, the grains preferentially orient themselves in the direction of the solidification gradient. The heat flux of this weld was unidirectional and hence the columnar appearance formed. After solidification has occurred and the metal cools further, austenite separates into ferrite and cementite phases. However, since the nucleation of these phases is initiated in the grain boundaries of the austenite grains and then progresses within the grains itself, the structure of the austenite grain is retained. For this reason, the columnar grains in Figure 4.4 are also called prior austenite grains. A higher magnification of the prior austenite grains is provided in Figure 4.5a.

The microstructural phases that have ultimately formed on cooling depend mainly on the cooling rate and the microalloying elements. The most important of these is carbon; the carbon content determines the balance between ferrite and carbide phases in the final microstructure of the metal. While cooling down, initially the rate of diffusion of atoms is relatively fast due to the kinetic energy from the high temperature. At this initial stage of cooling, ferrite starts to be created at the austenite grain boundaries. As the temperature further decreases, the diffusion rate of carbon out of the ferrite phase decreases. Carbon starts to diffuse non-homogeneously out of the grain boundary ferrite and laths of ferrite start to grow from protuberances on the grain boundary. Carbon diffuses parallel to the grain boundary ferrite, instead of perpendicularly, allowing the plate-tips to further advance in fresh austenite. Ultimately, columnar lath-like structures called Widmanstätten structures are formed, which are visible in Figure 4.5b.

As the cooling progresses, and thus lower temperatures are reached, nucleation of ferrite grains at inclusions occurs in preference to further growth of existing grain boundary ferrite. These newly nucleated ferrite grains grow in a similar manner to Widmanstätten structures, but radiate in three dimensions and are therefore rather chaotically ordered. When studying this formed microstructure with a two-dimensional view, the characteristic ”basket weave pattern” of short ferrite needles can be seen. It is a

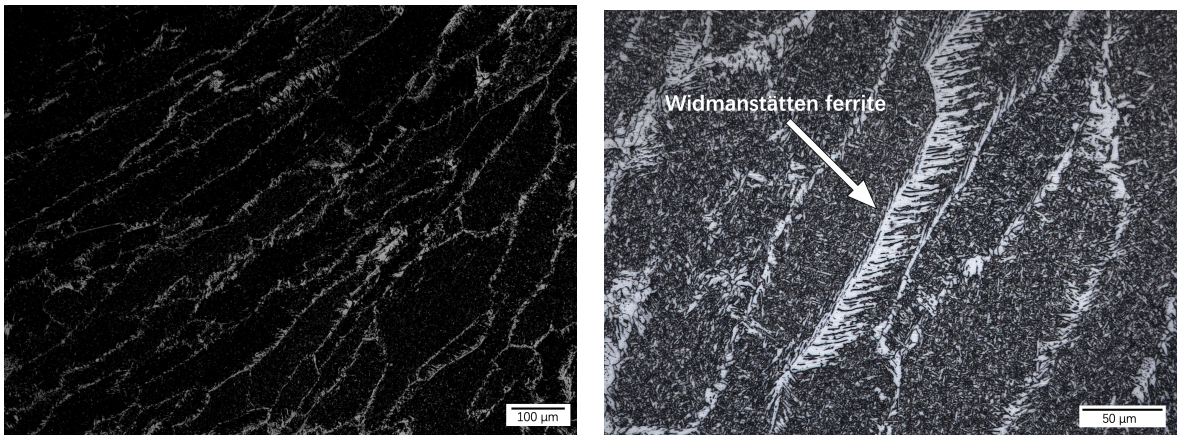

(a) (b)

Figure 4.5: The microstructure of the weld metal revealing a) columnar prior austenite grains and b) Widmanstätten ferrite structures from the prior austenite grain boundaries.

fine-grained interlocking microstructure called acicular ferrite. In the ongoing cooling process, usually at low to medium cooling rates, bainite forms. It is the cooling rate that controls the time period in which each phase is formed. However, the exact cooling rates of this commercial pipe are confidential and therefore not readily available. Nevertheless, in the girth welds studied in this thesis the following microstructural phases were identified: grain boundary ferrite, Widmanstätten ferrite and acicular ferrite.

Figure 4.6 is a high magnification image showing the basket weave pattern of the acicular ferrite in the weld metal. Highlighted (circular, yellow) are spots in the microstructure that can be identified as inclusions where nucleation of acicular ferrite grains has originated.

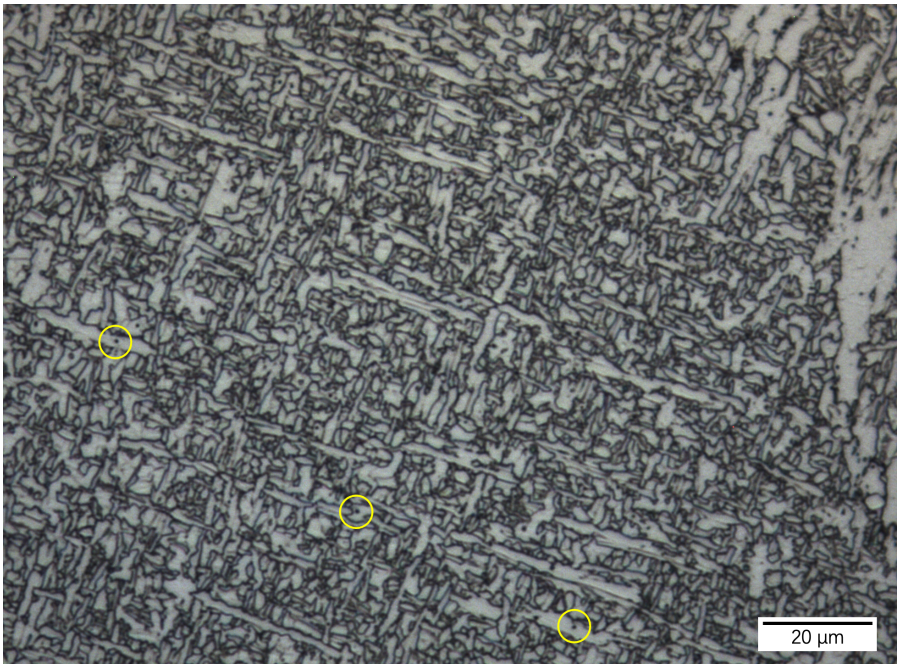

Figure 4.6: X100 magnification of the acicular ferrite microstructural phase in the weld metal exposing their short needle-like basket weave appearance. Marked (circular, yellow) are inclusions that might have served as nucleation sites for acicular ferrite grains.

HAZ Microstructure

Figure 4.7 is an overview of the microstructures present in the heat affected zone, and of the transition from the base and weld metal to the HAZ. It is evident that this small area of the pipe material contains many different microstructures. In the HAZ, near the side of the weld metal, the grains are coarser in appearance. Along the direction of the base metal, this coarse-grained zone transitions into a fine-grained region and eventually progresses to polygonal grains of the unaffected base metal. The existence of larger grains in the HAZ close to the weld metal is a direct result of the frequent weld passes the material underwent. This HAZ region is adjacent to the weld and consequently the peak temperature of the multiple heating cycles allowed for more recrystallization and grain growth. In view of the fact that the HAZ was originally base metal, the microstructure in the HAZ is expected to transition to that of the X60 base metal within their adjacent region.

The large variety of microstructures within this short area creates locally vast differences in the mechanical behaviour of the material. It is expected that this anomalous mechanical behaviour applies not only to an inert environment, but also to an environment containing hydrogen gas. The failure behaviour of the HAZ is therefore considered unpredictable and complex, since the behaviour can hardly be related to a single microstructural feature.

The (internal) circumferential notch of the specimens used in this thesis is localised at the center of the weld, and thus the failure zone is expected to be located within the weld region. Therefore, an in-depth

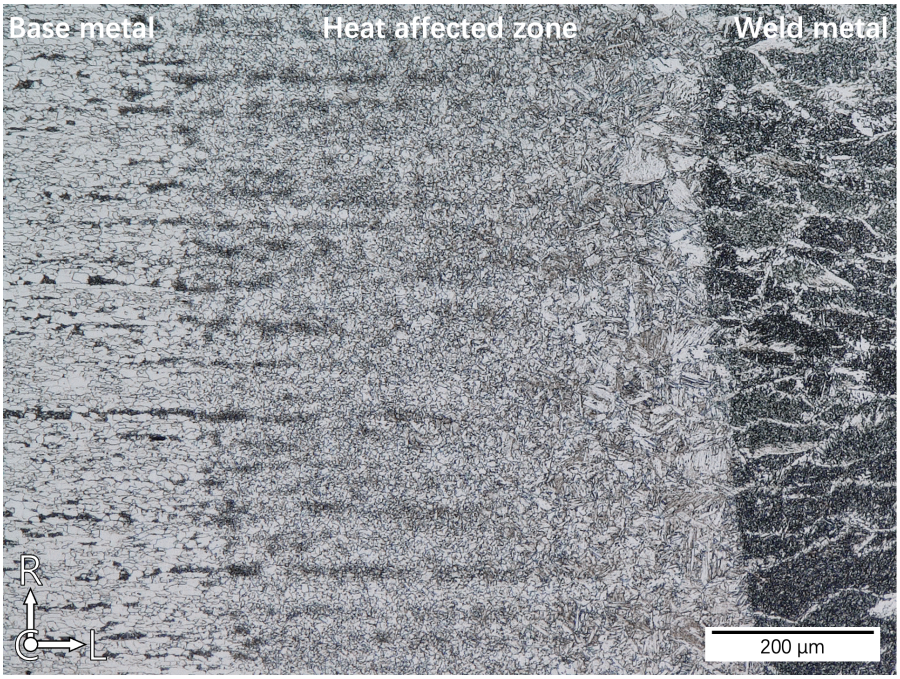

Figure 4.7: Overview of the different microstructures present in the heat affected zone. In this figure, the base metal and the weld metal are to the left and right side of the heat affected zone, respectively.

characterisation of the HAZ is not included in the thesis, nor are aspects concerning the behaviour of the HAZ discussed further.

4.1.3. Mechanical Properties

Hardness

Seven rows of hardness measurements were made on a polished surface. These rows extended from the base metal through the weld section. The locations of the hardness indentations are shown in Figure 4.8 and the results (type HV1) are presented in Table 4.1. Each indentation had a diagonal of more than 85 µm, which is significantly larger than the grain size in both the base metal and the weld metal. In light of this, the microhardness tests performed can practically be considered as macro measurements. This means that the possibility of attributing deviations in the measurements to a microstructural property, such as the assumption that an indentation was made at a (single) grain boundary, is eliminated. The large standard deviation for the hardness value of the HAZ results from the differences between the microstructures in this region. It is evident that the hardness gradually increases when the material transitions form the base metal, to the heat affected zone and ultimately the weld metal.

When transitioning from the weld metal through the HAZ to the base metal, it is clear that hardness gradually decreases. This is a direct result of the temperature gradient from the heat treatment (i.e. the multiple weld passes). The reason that the standard deviation of the weld metal is higher than that of the base metal, is owing to measurements being taken on different weld passes. It is a generally understood that the hardness can vary along the weld metal, from cap to root pass, due to the multiple weld passes [64]. Regarding the standard deviation of the base metal measurement; recalling the microstructural observation in Figure 4.2, the rolling process affected the grain sizes present in the material. The strain induced from the rolling process was experienced to a higher extent on the outer

Table 4.1 Base metal average and standard deviation were taken from 75 measurements. The data of the heat affected zone was calculated from 32 measurements. The weld metal comprised 43 indentations.

	Base metal	**Heat affected zone**	**Weld metal**
Hardness (HV1)	199 ± 5	219 ± 20	239 ± 9

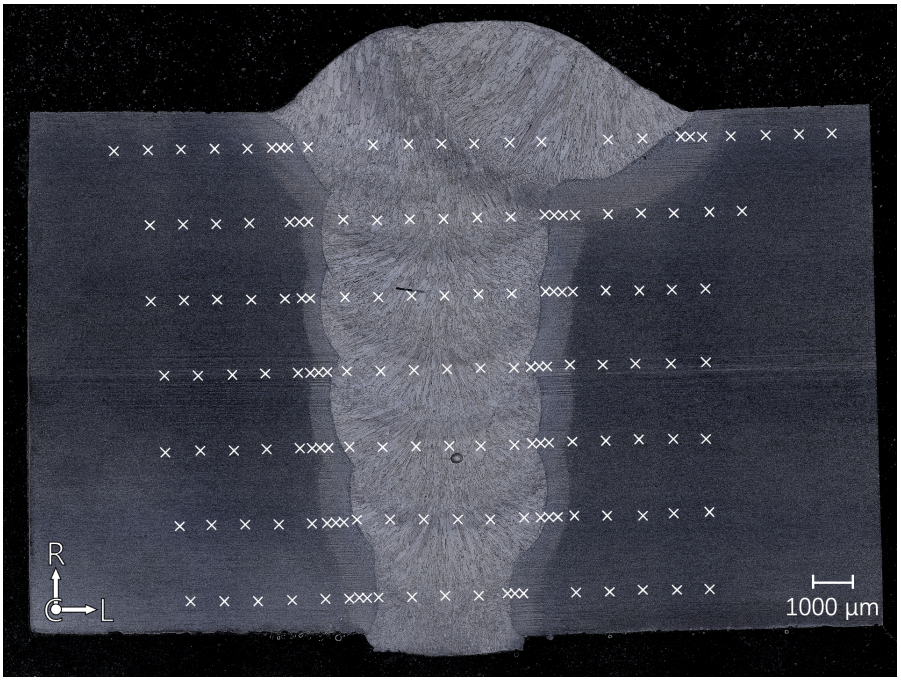

Figure 4.8: Vickers Hardness (HV1) measurement indentation locations. The indentations are depicted with white crosses.

surface compared to the middle part. This directly affected the hardness; the hardness of the base metal row closest to the outer surface is higher (HV1 of 204 $\pm$ 4) than the middle section (HV1 of 198 $\pm$ 5). For the reason that Table 4.1 reports the average of the hardness measurements across all rows, the standard deviation in the base metal could result from the hardness variations across the pipe thickness due to the rolling process.

Tensile Properties

According to the API 5L standard, X60 pipeline steel requires a minimum tensile strength of 490 MPa [12]. From the SSRT results of Boot et al. it can be confirmed that the weld metal is stronger than the base metal and that it meets this standard [30]. However, an exact value of the tensile strength of the weld metal is not available. As an approximation, it is expected that the weld in this thesis will have a similar tensile strength as reported (690 MPa) in the data sheet of an ESAB 70S-6 weld, since the same material was used to make the welds in this pipeline [1].

4.2. Hydrogen-Enhanced Fatigue of Base Metal

This section presents the results of the BM. Firstly, the results of the BM fatigue model are discussed in **section 4.2.1**. The fatigue model serves to clarify the stress conditions in the specimen during fatigue loading. The model served two purposes: i) to validate the fatigue test parameters, and ii) to determine the local stress concentrations and the types (and magnitudes) of strains present. The latter purpose is important because, as became clear from the literature review, the (local) stress conditions can influence the hydrogen fatigue response. Second, the fatigue results of the tests are presented in **section 4.2.2**. Although the tests in the test matrix were divided into series with different (sub)objectives: determination of the fatigue life (A1), effect of the nitrogen gas pressure (A2), and effect of the hydrogen gas (A3) (see section 3.2.3). In section 4.2.2, the sub-objectives are answered by combining the results and presenting them as a whole. This decision was made because it facilitates comparison between the environments and provides a concise overview. This section is therefore titled 'The Effect of Environment, since the effects of the environments are directly evident through this approach.

4.2.1. BM Fatigue Model

Global and Local Stress Range During Fatigue

First, the stress range in the gauge and the notch during fatigue were computed in the model. In this work, the stresses in the gauge and at the notch root-tip are henceforth referred to as the global stress and the local stress, respectively. The applied force during testing was uni-axial in the longitudinal direction. The determination of the global stress range was therefore calculated as the absolute difference between the maximum and minimum experienced longitudinal stress in the gauge:

$$\sigma_{22,max} - \sigma_{22,min} = |256 - 25.6| = 230.4 \text{ MPa} \tag{4.1}$$

By varying the stress amplitude, a relationship can be obtained between the stress range and the number of cycles to failure, which can then be expressed in the form of a SN curve. In general, the global stress range is used in this approach to quantify the fatigue life. For the test specimens in this thesis, however, the stress-raising effect of the notch translated the applied global stress into a higher local stress range. Since the notch is the location of failure, it is more accurate to formulate that the local stress range, rather than the global stress range, governed the fatigue life of the specimens. The global and local longitudinal stresses are calculated for the non-pressurised (air) environment and 150 barg pressurised (N_2) environment, and plotted over time in Fig. 4.9. Comparison of those stresses in the two environments allows an evaluation of the effect of the internal gas pressure on the local stress field in the notch.

Fig. 4.9 shows 10 fatigue cycles with their onset of application at 0.125 s. Prior to this time point, the specimen is subjected to the applied gas pressure or to no stress at all for the gaseous and air environment, respectively. Regarding the pressurised environment, the pressure linearly increases up to half-way of 0.125 s, the time at which 150 barg was reached. When viewing this time frame in Fig. 4.9, it can be noted that the gas pressure induced a longitudinal stress (20.6 MPa) in the notch (red line) but not at the inner surface of the gauge (blue line). This is attributed to the 'end-cap effect'. Every pressurised specimen, regardless of the type of gas to which it was exposed, experienced this effect. Consequently, its behaviour is not necessarily relevant for HA-FCG. Therefore, the explanation of the end-cap effect is given in Appendix E.2.

Strain Hardening and Fatigue Cycle Convergence

The local longitudinal stress in the first fatigue cycle deviates from the cycles that followed. The dissimilar behaviour can be observed in Fig. 4.9 near the maximum loading point (F_{max}) and its onset can be pin-pointed directly to the yield point. When the local stress exceeds the yield stress, the slope of the stress response decreases which signifies local strain hardening. As can be seen from the figure, strain hardening continues up to moment when the loading phase of the fatigue cycle is completed. From these observations, it can be inferred that the initial fatigue cycle can be considered as a plastic overload cycle. Plastic strain was involved to facilitate the hydrogen ingress; it was expected that the plastic strain would break the oxide (passivation) layer, if present, on the material's surface that can impede hydrogen entry (see section 2.2.1). The subsequent local fatigue cycles, however, show a constant

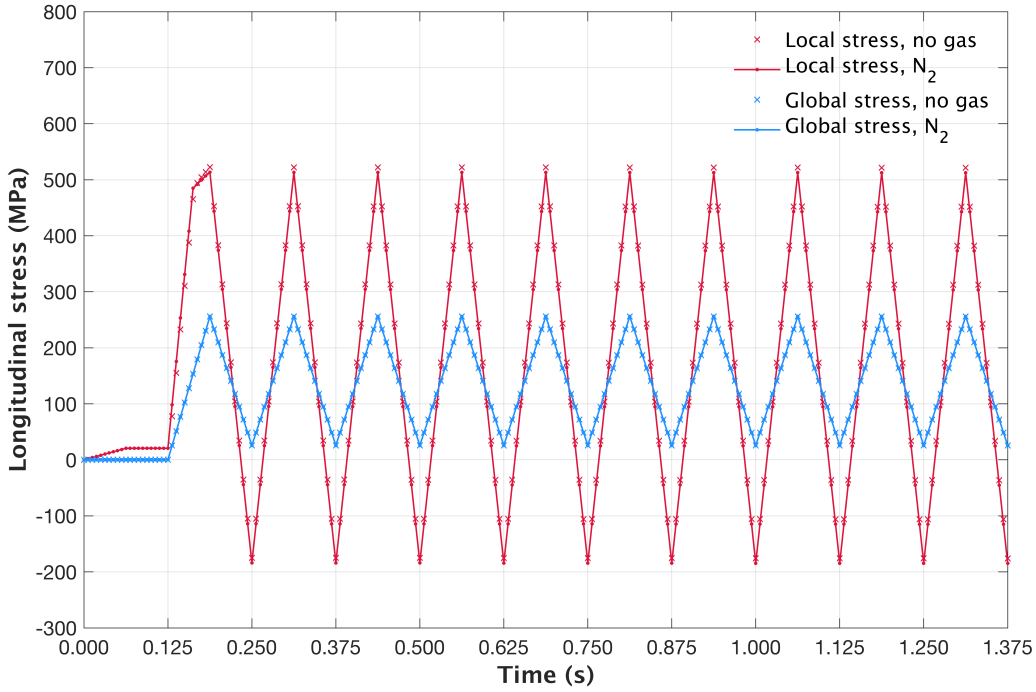

Figure 4.9: Local and global longitudinal stress plotted over time for air and 150 barg pressurised BM specimen. Plotted are 10 fatigue cycles that commence after 0.125 seconds. For the pressurised environment, the test pressure was reached after 0.0625 s.

absolute slope between loading and unloading, indicating linear elastic behaviour. Such consistent behaviour is observed for the entirety of the global longitudinal stress. Therefore, the global stress range is linear elastic throughout all fatigue cycles. The fact that the shapes of the global and local stresses in both environments are consistent after the first cycle, indicates that the fatigue response has converged.

Plastic Strain and Von Mesis Equivalent Stress

From Fig. 4.9 two additional features can be noted: i) the global stress range is entirely tensile in nature, whereas locally the material experiences tensile and compressive stresses, and ii) the entire local stress range is shifted slightly lower in the pressurised N_2 environment compared to the air environment. Regarding point i), the fact that the notch root experienced compressive stresses during tension can be explained by the residual-stress field. The integral of the combined vertical stresses on the cross-section of the test-piece shall be equal to the force acting on it. Since the material at the notch plastically 'elongated' at the first fatigue cycle, they should be loaded in compression at force removal. Other sections in the cross-section must then be loaded in tension to compensate for this stress. This stress compensation ensures that stress integral remains equal to the total force. This is visualised in Fig. 4.10, which displays the plot of the longitudinal stress (as σ_{22}) in the notch region at the maximum (Fig.4.10a) and minimum load (Fig. 4.10b) application of the 150 barg internally pressurised specimen. From this figure it is clear that during unloading the notch root experiences compression and that the maximum σ_{22} moves inwards the material in the radial direction (x-axis in the figure). Considering feature ii), the difference in local $\sigma_{22,max}$ for the two environments is approximately $\approx$ 9 MPa. However, the stress range remains unaffected. From an (offshore) engineering point of view, the magnitude of the offset is minor considering the entire stress range. Therefore, the offset is not further discussed.

As was concluded from Fig. 4.10b., $\sigma_{22,max}$ moves inward the material during unloading due to the compression of the notch-tip resulting from the residual-stress field. The compression was a result from the residual-stress field induced during plastic straining. The plastic strain at the notch-tip is 0.22% (see Fig.

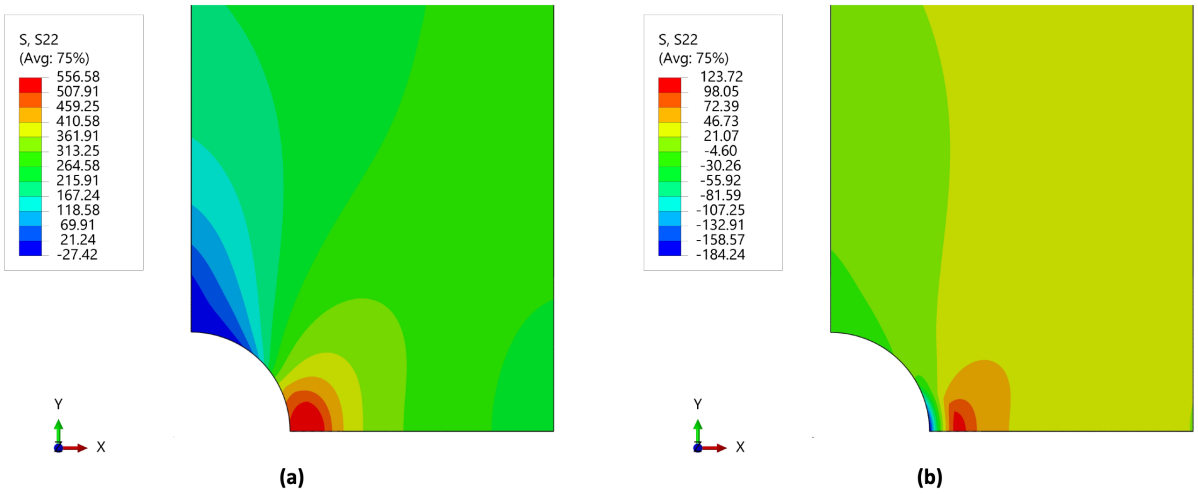

Figure 4.10: Display of the longitudinal stress in the internally pressurised (150 barg) specimen at F_{max} (a) and F_{min} (b). The x,y and z coordinate system in the figure translate to the radial, longitudinal and circumferential direction, respectively.

4.11a) for the pressurised environment and is higher than the one experienced in the air environment, which is 0.20%. The plastic strain distribution of the air specimen is given as a supplementary figure in Appendix E (Fig. E.1), since the distribution is relatively similar to the pressurised specimen. The higher plastic strain for the pressurised environment is associated with a higher residual stress-field. Therefore, the notch-tip experiences compression at higher absolute magnitude in the pressurised environment. As a result, the $\sigma_{22,max}$ during loading translates slightly further into the material compared to the air environment.

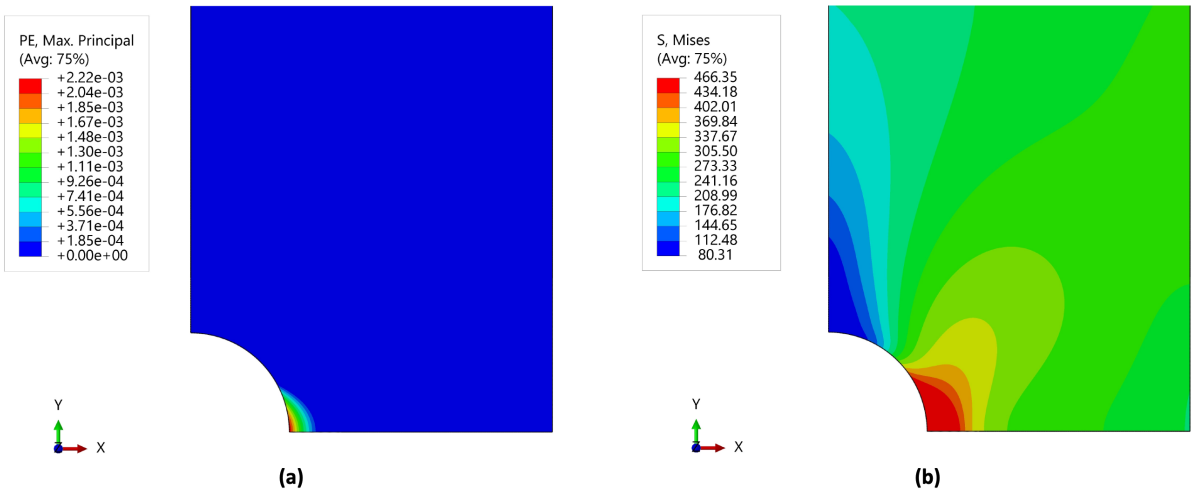

Figure 4.11: Display of (a) the maximum principal plastic strain in the internally pressurised (150 barg) specimen after loading to F_{max}, and (b) the Von Mesis equivalent stress at F_{max}. Values represented in the legend of (a) can be interpreted as % plastic strain when multiplied by a factor 100.

Von Mesis Equivalent Stress

For the study of the susceptibility to plastic deformation, the Von Mesis yield criterion was applied:

$$\sigma_v = \sqrt{\frac{(\sigma_1 - \sigma_2)^2 + (\sigma_2 - \sigma_3)^2 + (\sigma_3 - \sigma_1)^2}{2}} \tag{4.2}$$

In this equation, σ_1, σ_2 and σ_3 are the different principal stresses with each their magnitude being positive when acting in tension. σ_1 is the maximum tensile principal stress and thus refers to σ_{22} in the

studied fatigue model. Yielding occurs when the Von Mesis equivalent stress σ_v exceeds the yield strength of the material. In the simple case of an uni-axial longitudinal stress, $\sigma_1 \neq 0$, $\sigma_2 = \sigma_3 = 0$, the Von Mesis criterion reduces to $\sigma_1 = \sigma_v$. For this stress condition the material yields when the longitudinal stress exceeds the yield strength of the material. However, for the specimens tested, the internal gas pressure creates non-zero stresses in different directions. Introducing other stresses than σ_1 would affect the Von Mesis equivalent stress, and therefore the onset of plastic deformation. As was observed in Fig. 4.9, the notch in the pressurised environment yielded at a lower longitudinal stress. This indicates that the internal gas pressure facilitated plastic deformation. The region that underwent plastic deformation was validated by inspecting the Von Mesis equivalent stress at F_{max} (see Fig. 4.11b); the region where the Von Mesis equivalent stress exceeds the yield strength of the material ($\approx$ 453 MPa) is consistent with the region that underwent plastic strain (4.11a).

Note that this subsection excludes the visualisation of the stress states in the air tested specimen. This decision was made because the experienced stress states in air and 150 barg are closely analogous, however with a minor difference in magnitude (see Fig. 4.9). For the purpose of this thesis, the aforementioned stress state descriptions, with the sole inclusion of the 150 barg plots, fulfill the purpose of understanding the stress states in the specimens. For additional details of the stress state regarding the stress triaxiality, it is referred to Appendix E.3.

4.2.2. The Effect of Environment

Potential Drop Curves

In Fig. 4.12 below, representative normalised DCPD curves are shown for three environments: air (grey, circles), 150 barg N_2 (black, squares) and 150 barg H_2 (red, triangles). Note that the colour coding for the environments is maintained for all figures in this section. First, the total fatigue life can be assessed. It can be seen from Fig. 4.12 that each environment has a fatigue life in the order of 10^5 cycles. This indicates that the studied fatigue can be classified as HCF. This is in agreement with the finding of the fatigue model (section 4.2.1); that the test conditions induced stresses in the elastic range.

Two main features can be directly noted from Fig. 4.12: i) each curve starts with the normalised value

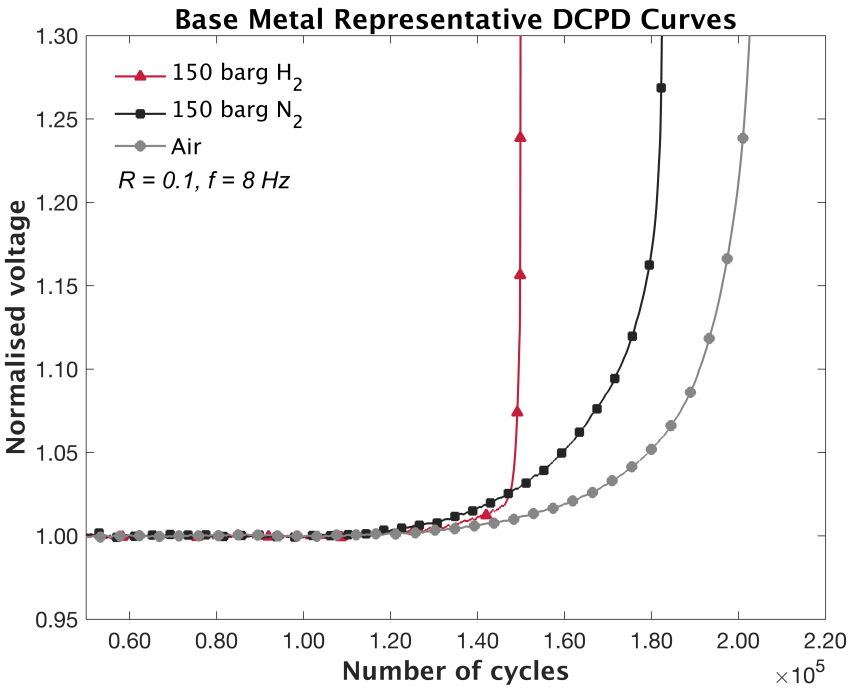

Figure 4.12: Representative normalised potential drop curves for BM specimens. Three environments are plotted: 150 barg H_2 (red, triangle), 150 barg N_2 (black, square) and air (grey, circle)

"1" and maintains a stable baseline until the moment of crack initiation, and ii) after crack initiation the curves diverge due to their different fatigue crack growth rate. Regarding the moment of crack initiation, which can be denoted from the point of deflection, its onset is virtually consistent for each environment. This indicates that there is no effect of 150 barg N_2 and 150 barg H_2 on the crack initiation phase.

From a comparison of the overall shape of the growth phase part, it can be derived that the H_2 environment exhibits deviating behaviour that commences at approximately 1.40-1.50 x 10^5 number of cycles. This change in behaviour exists as a steep increase in the voltage response. Since the potential voltage drop response is proportional to the growth rate of the fatigue crack, the transition can be identified as the onset of HA-FCG. Before this transition, however, the three environments show a fairly uniform voltage-slope response. This implies that a critical crack size has to be reached in order for H_2 to adversely affect fatigue. At the onset of HA-FCG, the fatigue crack growth rate per cycle increases to such an extent that complete failure of the specimen quickly follows. This can be seen in Fig. 4.12, where the potential drop response is nearly vertical. Considering its detrimental effect on the remaining lifetime, the onset of HA-FCG could essentially be regarded as the moment of failure itself. This is in contrast to the air and N_2 environment, as the potential drop curves (and thus the crack growth rates) steadily increase between crack initiation and failure. It can also can be noted that for air and 150 barg N_2, the voltage responses in their growth phase are relatively similar. Considering that also the moment of crack initiation was not influenced for these two environments, it can be stated that the fatigue behaviour is not noticeably affected by 150 barg N_2. This assertion will be further explored in the next section, where the crack initiation phase and the growth phase are precisely determined for all environments.

Number of Cycles till Crack Initiation and Failure
Analysis of the potential drop curves for all specimens in set A resulted in the determination of the number of cycles spent in the crack initiation phase and the crack growth phase. These results, along with the total fatigue life, are presented as a bar chart in Fig. 4.13. The representative data for each environment is reported in Table 4.2. In Fig. 4.13, the single hatched and double hatched areas represent the number of cycles spent in the crack initiation phase (N_{CI}) and the crack growth phase (N_G), respectively. The total number of cycles till failure (N_F) is depicted with a solid area. The main goal of this work is to clarify the effect of H_2 on crack initiation, therefore this discussion will primarily elaborate on N_{CI}. The N_G is included in the figures to relate changes in N_{CI} to the reduction in the growth phase of the total lifetime.

From 4.13, it can be inferred that the change in environmental conditions did not significantly affect N_{CI}. This is also evident from inspecting the values in Table 4.2; the averages and standard deviations of N_{CI} are effectively within the same range for the three environments. Thus, with respect to the air environment, 150 barg N_2 and 150 barg H_2 had relatively no influence on the susceptibility to crack initiation in the BM. The absence of the influence of H_2 on N_{CI} agrees with the work of Arnaudov [13]. According to Arnaudov, hydrogen has no influence on crack initiation (and fatigue life) when tested at a total strain amplitude of $\leq$ 0.20%. According to various researchers, a sufficiently high cyclic strain causes hydrogen-induced slip localisation, which in turn lowers N_{CI} [13, 125, 181]. The findings presented in this thesis are in line with this statement since fatigue was in the elastic range (i.e. varying strain amplitudes $<$ 0.20%).

The deleterious effect of 150 barg H_2 on fatigue is clearly visible in Fig. 4.13. The presence of H_2 reduced the total fatigue life by 37%, by affecting the growth phase (N_G). The reduction in N_G indicates that fewer cycles were required to reach failure. This emphasises that fatigue in the presence of H_2 is associated with a higher crack growth rate per cycle. The underlying mechanisms that are responsible for this could be traced back to dislocation movement, modified crack-closure behaviour or hydrogen-induced decohesion at grain boundaries. Results of fractographic analysis are needed in order to accurately relate the behaviour to those mechanisms. This discussion is provided in the corresponding section (section 4.4).

Crack Initiation and Growth Lifetime
The representation of N_{CI}, N_G and N_F by their average values and standard deviations may be considered misleading for the characterisation of the fatigue behaviour of each subset. For instance, due

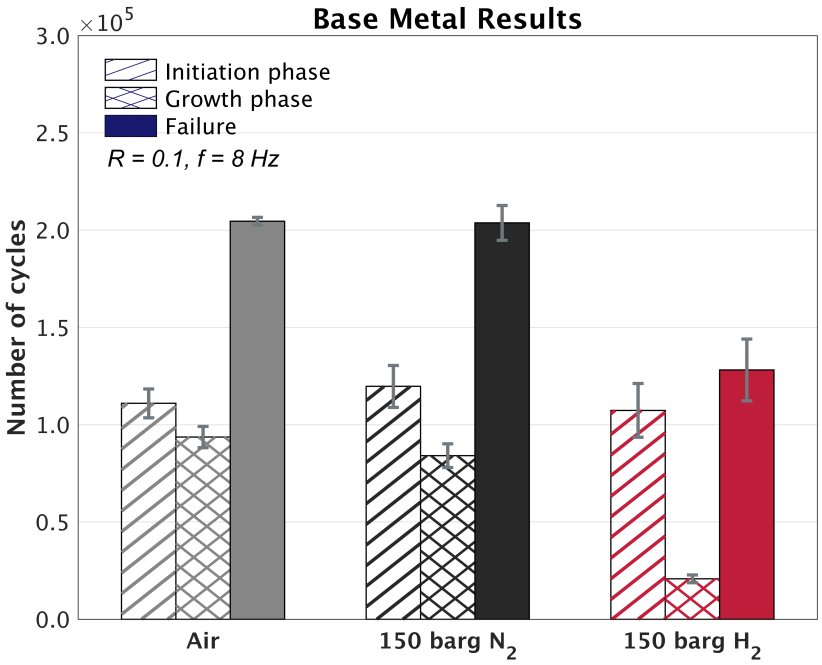

Figure 4.13: Bar graph of the number of cycles spent in the crack initiation phase (N_{CI}) and the growth phase (N_G), and the total number of cycles till failure (N_F) of BM.

Table 4.2 Number of cycles spent in the crack initiation phase (N_{CI}) and the crack growth phase (N_G), and the total cycles till failure (N_F) of BM. The data is reported as an average of the subset and also includes the standard deviation.

Environment	N_{CI}	N_G	N_F
Air	110,948 ± 7,412	93,628 ± 5,444	204,576 ± 1,968
150 barg N_2	119,678± 10,772	84,044 ± 6,118	203,722 ± 8,915
150 barg H_2	107,348 ± 13,865	20,803 ± 1,994	128,151 ± 15,853

to the standard deviation plotted on the average in Fig. 4.13, it is unclear whether the percentage of lifetime spent in the crack initiation phase (LT_{CI}) varies, or that it remains constant, for each specimen in the subset. In this context, LT_{CI} is expressed as follows:

$$LT_{CI} = 100 * \frac{N_{CI}}{N_F} \tag{4.3}$$

From this equation, it follows that the percentage of lifetime spent in the crack growth phase (LT_G) can be calculated as:

$$LT_G = 100 - LT_{CI} \tag{4.4}$$

Fig. 4.14 represents the N_{CI}, N_G and N_F data of Fig. 4.13 in the form of LT_{CI} and LT_G. The LT_{CI} of air, 150 barg N_2 and 150 barg H_2 are 54.2 ± 3.1%, 58.5 ± 3.4%, and 83.6 ± 0.5%, in respective order. Those values, along with the values of LT_G, are also provided in Table 4.3. The LT_{CI} results presented in this work are in line with the ones of Capelle et al., who reported a LT_{CI} of ≈ 60% and 80% for air and H_2, respectively [35]. The LT_{CI} and LT_G of air and 150 barg N_2 are within the same range when the mean results and standard deviations are examined. It can however be noted, that the average lifetime spent in the growth phase is higher in air (45.8%) when compared to 150 N_2 (41.5%). This indicates that for N_2 fewer number of cycles are needed for the crack to grow till failure. In other words, the fatigue crack growth rate is slightly higher. This could be attributed to the increased triaxial stress sate at the crack tip caused by the gas pressure.

The LT_{CI} of 150 barg H_2 is distinctly higher compared to the other environments. This signifies that most of the hydrogen fatigue life is spent in the crack initiation phase. A higher magnitude of LT_{CI} is

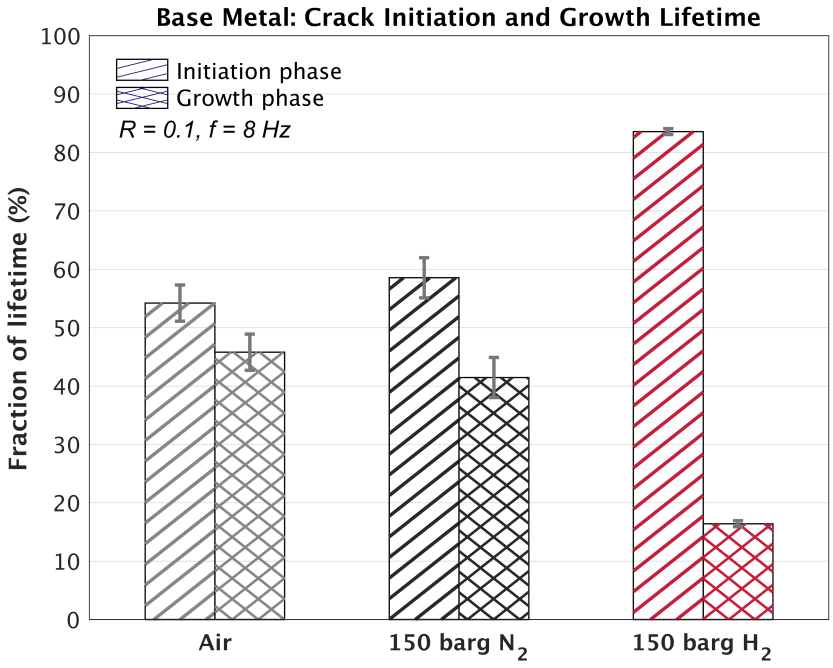

Figure 4.14: Bar graph of the fraction (%) of lifetime spent in the crack initiation phase and growth phase of BM. LT_{CI} and LT_G are calculated with Eq. 4.3 and Eq. 4.4, respectively.

Table 4.3 Fraction of lifetime spent in the crack initiation phase (LT_{CI}) and the growth phase (LT_G) of BM. LT_{CI} and LT_G are calculated with Eq. 4.3 and Eq. 4.4, respectively. The data is reported as an average of the subset and includes the standard deviation.

Environment	LT_{CI} (%)	LT_G (%)
Air	54.2 ± 3.1	45.8 ± 3.1
150 barg N_2	58.5 ± 3.4	41.5 ± 3.4
150 barg H_2	83.6 ± 0.5	16.4 ± 0.5

related to a reduction in the remaining proportion of fatigue life after crack initiation (LT_G). The result that H_2 has the highest LT_{CI} of all environments, highlights the accelerating effect of hydrogen on the crack growth rate. From those statements it is evident that crack initiation, rather than growth, governs the fatigue life of the 150 barg H_2 environment. This finding is agreement with the trend in literature on hydrogen fatigue [80, 8, 31, 5, 25].

The relative low standard deviations of LT_{CI}, compared to the ones of N_{CI}, indicates that the percentage of lifetime spent in the crack initiation phase is constant for each specimen in their respective subset. This is especially visible from the differences in standard deviations of the 150 barg H_2 environment in Fig. 4.13 and Fig. 4.14. This implies that an absolute change in N_F is accompanied with a proportional change in N_{CI}, thereby maintaining a 'constant' LT_{CI} (and thus 'LT_G'). The fatigue behaviour in each subset of A is therefore consistent.

Normalised Results with Respect to Nitrogen

Another method to present the results is to normalise the data of N_{CI}, N_G and N_F with respect to the 150 barg N_2 environment. The normalised results are shown in Fig. 4.15 and the values of the plotted data are given in Table 4.4. This method of data representation underlines the reduction in N_F in the H_2 environment. The decrease in fatigue lifetime due to H_2 is approximately 100.00%-62.9% $\approx$ 37%. The normalised N_G reduced to 24.8%, which indicates that H_2 reduced the lifetime by accelerating the overall crack growth by a factor 4 ($\approx$ 100/24.8). As can be noted, the crack initiation was affected relatively similar for air and 150 barg H_2. However, both values are below 100%, which indicates that N_2 has slightly better resistance to crack initiation. The fact that the normalised N_G of air is greater

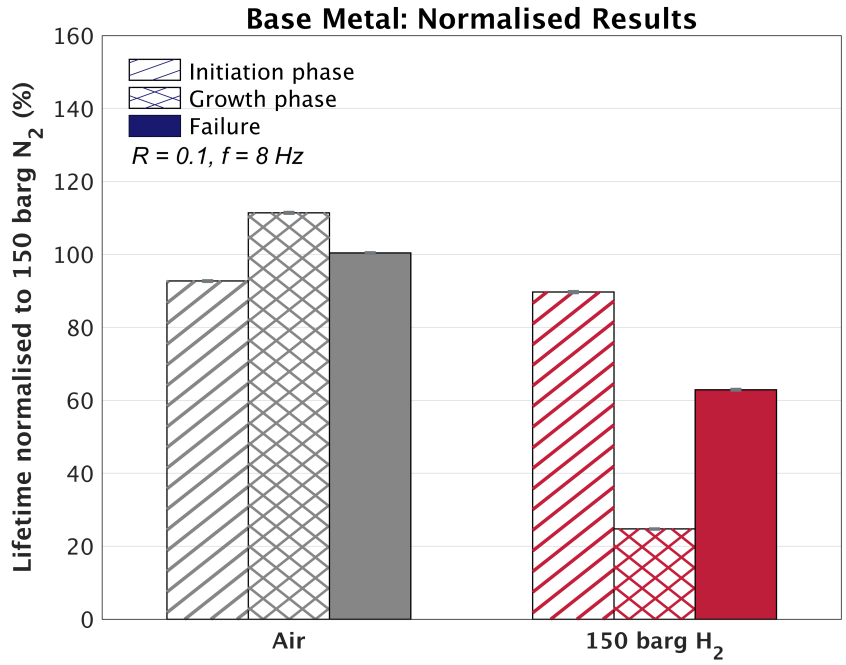

Figure 4.15: Bar graph of the normalised results of the number of cycles spent in the crack initiation phase (N_{CI}) and growth phase (N_G), and the number of cycles till failure (N_F) of BM. The data of each environment is normalised with respect to the 150 barg N_2 environment.

Table 4.4 Normalised values of the average number of cycles spent in the crack initiation phase (N_{CI}) and growth phase (N_G), and the normalised average number of cycles till failure (N_F) of BM. The data of each environment is normalised with respect to the 150 barg N_2 environment.

Environment	Normalised N_{CI} (%)	Normalised N_G (%)	Normalised N_F (%)
Air	92.7 $\pm$ 0.10	111.4 $\pm$ 0.10	100.4 $\pm$ 0.05
150 barg H_2	89.7 $\pm$ 0.14	24.8 $\pm$ 0.03	62.9 $\pm$ 0.08

than 100%, once more highlights the accelerating effect of the gas pressure on crack growth.

Hydrogen Supply for HA-FCG

The internal gas escaped the instant the area of the fatigue crack surface reached the outermost remaining material of the ligament. The crack initiation and growth of the specimens were asymmetric. Hence, the fatigue tests in the pressurised environments also included a 'gas-free' phase. The H_2 gas escape significantly influenced the crack growth rate. This can be seen in Fig. 4.16, where the normalised voltage responses of 150 barg N_2 and 150 barg H_2 specimens are superimposed. The main feature that can be derived from this figure is the inflection point in the 150 barg H_2 curve, which is non-existent in 150 barg N_2. The normalised voltage at which the gas leak initiated, is indicated in the figure by a dotted line and annotated as 'onset of pressure drop'. The HA-FCG effect started to diminish at this point in fatigue, as can be inferred from the decrease in slope. The moment at which the entire internal gas volume escaped is indicated in the figure as 'complete gas escape'. The reduction in HA-FCG in the cycles between the pressure drop and the complete gas escape can be attributed to: i) the reduction in gaseous hydrogen supply to the crack tip and ii) the loss of the contribution that the gas pressure had on the stress triaxiality at the crack tip. After complete gas escape and up to the moment of the inflection point, the sole supply of H_2 to the crack tip stems from the diffusion of residual H_2 in the material. Since the HA-FCG effect in this area declines rapidly, it is assumed that exposure to gaseous hydrogen drove the hydrogen supply required for HA-FCG.

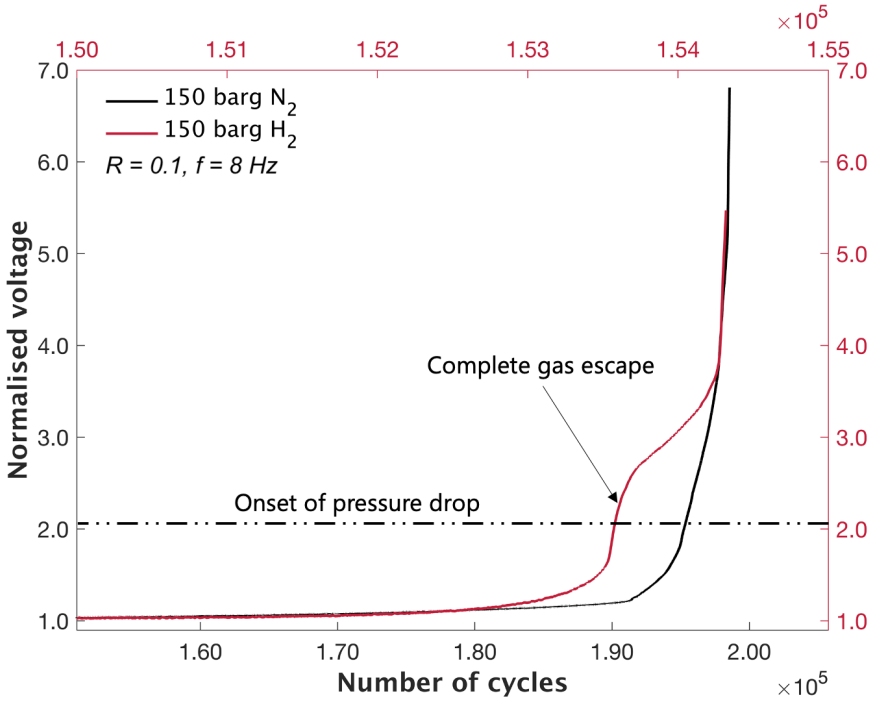

Figure 4.16: Comparison of the 150 barg N_2 and 150 barg H_2 normalised potential drop data during gas leak. Data was extracted from specimen A2.4 and A3.4, which are representative of 150 barg N_2 (black) and 150 barg H_2 (red), respectively. The data of the environments should be read with the corresponding color coded axes.

4.3. Hydrogen-Enhanced Fatigue of Weld Metal

This section presents the results of the WM. Firstly, the results of the fatigue model are discussed in **section 4.3.1**. The fatigue model serves to elaborate on the similarities and differences in stress and strain conditions of the BM and WM. Next, the fatigue results of the tests are presented. The different sub-objectives are addresses as a whole in **section 4.3.2**, which is titled 'The Effect of Environment and Gas Pressure'. The results are also directly compared with the ones of BM. The effects of weld defects are included in the presented data. This section concludes with a short discussion on the findings of the BM and WM.

4.3.1. WM Fatigue Model

For the calculation of the WM fatigue models, the same procedure was applied as for the BM fatigue models. The results of the WM fatigue model are presented as a longitudinal stress over time (t) plot, below in Figure 4.17. The two models have several features in common:

- The internal pressure induces a longitudinal stress of 20.6 MPa prior to load application
- The fatigue includes strain hardening; the first fatigue cycle induced a plastic overload.
- The fatigue behaviour converged
- The local stress range is markedly higher than the global stress range
- The global (230.4 MPa) and local (697.2 MPa) stress ranges are similarfor both materials

The main difference between the BM and WM model is that the local stress range for WM has a higher stress (amplitude) offset. The fatigue test conditions thus induce a higher mean longitudinal stress for the WM. Nevertheless, analogous to BM, the plastic deformation during the first load cycle causes compression to occur at the approach of F_{min}. The finding that plastic deformation occurs at a higher local stress than in the BM is due to the higher yield stress of the WM. A thorough analysis of the stress conditions in the WM is not presented due to the lack of data input. Also, in order to accurately model the entire area of the notch, the HAZ must be considered as well. The plastic deformation in the WM notch region is visualised in Fig 4.18b. This figure also includes the repetition of the BM plastic strain as Fig. 4.18a. As can be deduced from the displayed values, the maximum plastic strain ($\approx$ 0.10%)

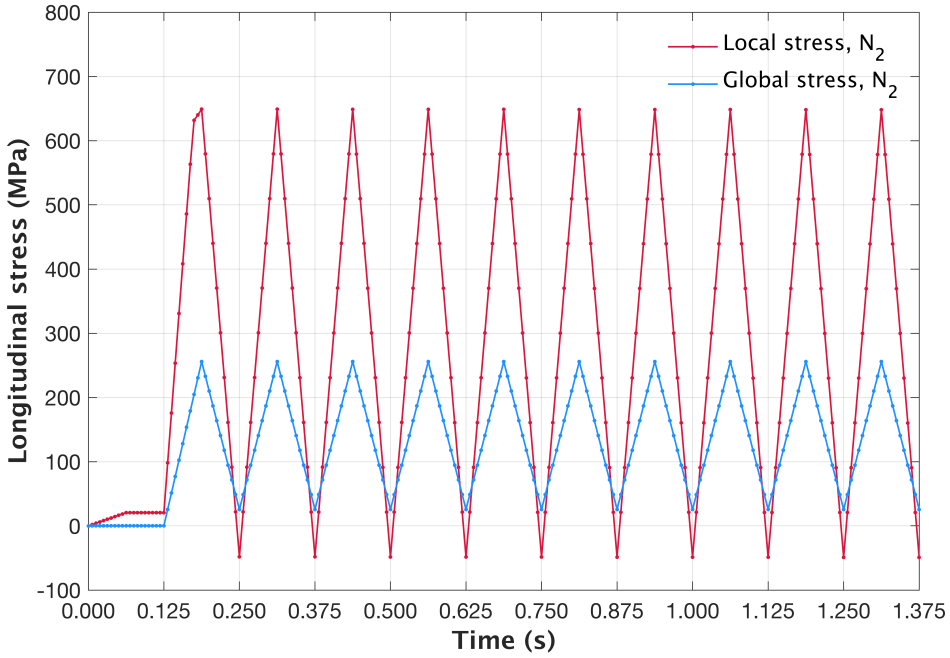

Figure 4.17: Local and global longitudinal stress plotted over time for 150 barg pressurised WM specimen. Plotted are 10 fatigue cycles that commence after 0.125 seconds. The 150 barg test pressure was reached after 0.0625 s.

is considerably lower than that in the BM (0.22%). Moreover, the BM plastic strain region appears to encompass a more extended area compared to the WM. This is to be expected, as it was a force-controlled test and thus depending on the yield properties of the material, the experienced strain may differ. The result of the WM plastic strain should be considered as a rough approximation, as the input data was approximated by multiplying the BM stress-strain data by a factor of 1.3.

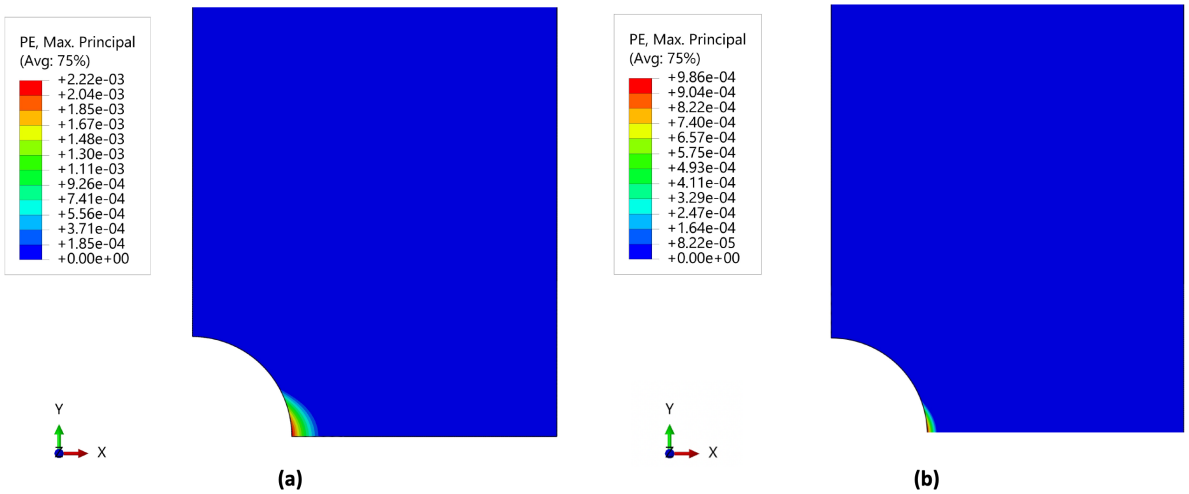

Figure 4.18: Display of the maximum principal plastic strain present, after loading to F_{max}, in the internally pressurised (150 barg) a) BM and b) WM specimen. Values represented in the legend can be interpreted as % plastic strain when multiplied by a factor 100.

4.3.2. The Effect of Environment and Hydrogen Gas Pressure

Potential Drop Curves

The representative normalised potential drop results of the WM are shown in Fig. 4.19. It is worth noting that the 150 barg H_2 data is taken from a non-porous sample, and is therefore not representative of the entire subset which also included macroporous specimens. This concept is further elaborated in the next section. Note that the somewhat fluctuating response of N_2 is due to filtering over a region with more noise.

Firstly, similar to BM, it can be concluded that the fatigue is classified as HCF. Second, a steep voltage response is observed after baseline deflection (crack initiation), which is associated with HA-FCG. The main difference with the BM series is that the effect of hydrogen is more pronounced for WM. This can be deduced from the larger differences in the number of cycles between the vertical response of the specimens in Fig.4.19. Another feature that distinguishes the WM response from the BM, is that the crack initiation moment in WM varies for N_2 and H_2. These aspects will be discussed in more detail in the following sections.

Number of Cycles till Crack Initiation and Failure

The results of N_{CI}, N_G and N_F for WM are shown in the form of a bar graph in Fig. 4.20. The data used to plot the figure is presented in Table 4.5. This table includes data from the BM for ease of comparison. Whilst set B (see section 3.2.3) was introduced as being divided into three characteristic subsets: 150 barg N_2, 150 barg and 70 barg H_2, the data in the figure is expressed as four separate representative sets. Post-mortem analysis of the fracture surface led to the finding that the WM specimens contained macropores. In this context, macropores are considered to have significantly influenced the hydrogen fatigue behaviour, and are therefore treated separately. The dimensions of the pores and details relating to the fracture surfaces will be discussed in section 4.4.2.

The first feature that can be noted from Fig. 4.20 is that the weld metal had a longer lifetime in the N_2 environment compared to BM. It can be stated that the number of cycles required for the WM to fail in 150 barg N_2 is a factor 2.1 (= $\frac{\text{Average } N_{F,WM}}{\text{Average } N_{F,BM}}$) larger than for 150 barg H_2 BM. Translating

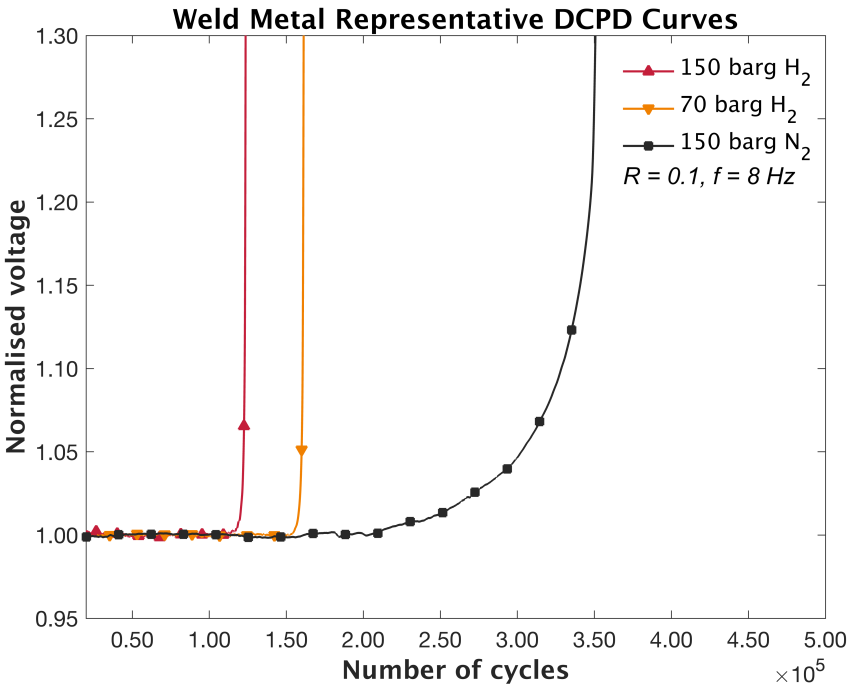

Figure 4.19: Representative normalised potential drop curves for WM specimens. Plotted are three environments: 150 barg H_2 (red, triangle), 70 barg H_2 (orange, inverted triangle) and 150 barg N_2 (black, square).

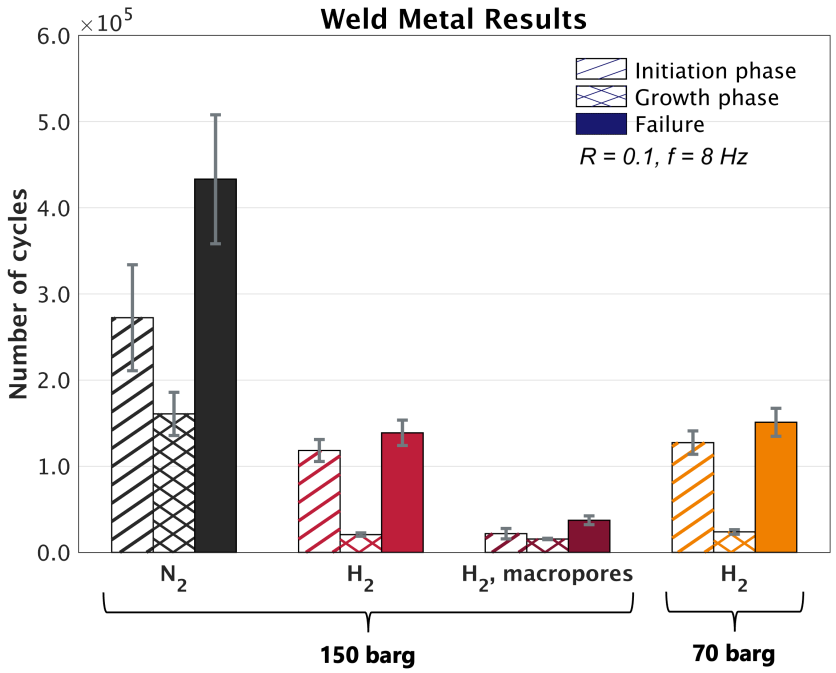

Figure 4.20: Bar graph of the number of cycles spent in the crack initiation phase (N_{CI}) and the growth phase (N_G), and the total number of cycles till failure (N_F) of WM.

Table 4.5 Number of cycles spent in the crack initiation phase (N_{CI}) and the crack growth phase (N_G), and the total cycles till failure (N_F) of WM and BM specimens. Regarding the BM, only the data in the pressurised environments are included. The data is reported as an average of the subset and also includes the standard deviation.

Material	Environment	N_{CI}	N_G	N_F
WM	150 barg N_2	272,294 ± 61,519	160,824 ± 25,094	433,118 ± 74,954
	150 barg H_2	118,154 ± 12,768	20,608 ± 1,959	138,762 ± 14,712
	150 barg H_2, macropores	21,692 ± 5,949	15,548 ± 0,756	37,240 ± 5,193
	70 barg H_2	127,372 ± 13,540	23,712 ± 2,720	151,084 ± 16,260
BM	150 barg N_2	119,678± 10,772	84,044 ± 6,118	203,722 ± 8,915
	150 barg H_2	107,348 ± 13,865	20,803 ± 1,994	128,151 ± 15,853

this into the concept of fatigue resistance, it can be calculated that the WM lifetime increased with: $\frac{\text{Average } N_{F,WM} - \text{Average } N_{F,BM}}{\text{Average } N_{F,BM}} * 100 \approx 113\%$. This can be interpreted as WM having a superior fatigue resistance under the concerned test conditions. This finding could be related to the result of the fatigue model; the fact that the area affected by the plastic deformation is smaller for WM. Moreover, this result is inherent to the microstructure. The finer grains in the WM give the material higher strength and toughness, thereby increasing its resistance to fatigue.

The relative difference of N_{CI}, with the exception of a direct comparison between 150 barg H_2 (non-porous) and 70 barg H_2, is the second salient feature of Fig. 4.20. To reiterate briefly, in the case of BM the N_{CI} remained relatively unaffected by H_2. On the contrary, Fig. 4.20 shows that hydrogen has a deleterious effect on the fatigue life by affecting both N_{CI} and N_G. Therefore, in the WM, H_2 reduces the resistance to crack initiation and accelerates the fatigue crack growth rate. The fatigue performance is even more severely affected when the weld metal contains macropores. This is visible form the decrease in N_F. Regarding the 150 barg H_2 environment, the average number of cycles till failure is a factor 3.1 smaller compared to the 150 barg N_2 environment. This factor becomes 11.6 when 150 barg H_2 macroporous samples are compared with 150 barg N_2. Hence, this highlights that the worst case scenario for hydrogen fatigue is for macro porosity in welds. A different H_2 gas pressure does not influence the fatigue; the results of 70 barg and 150 barg are in the same range.

The phenomenon that the hydrogen fatigue behaviour is independent of the gas pressure can be re-

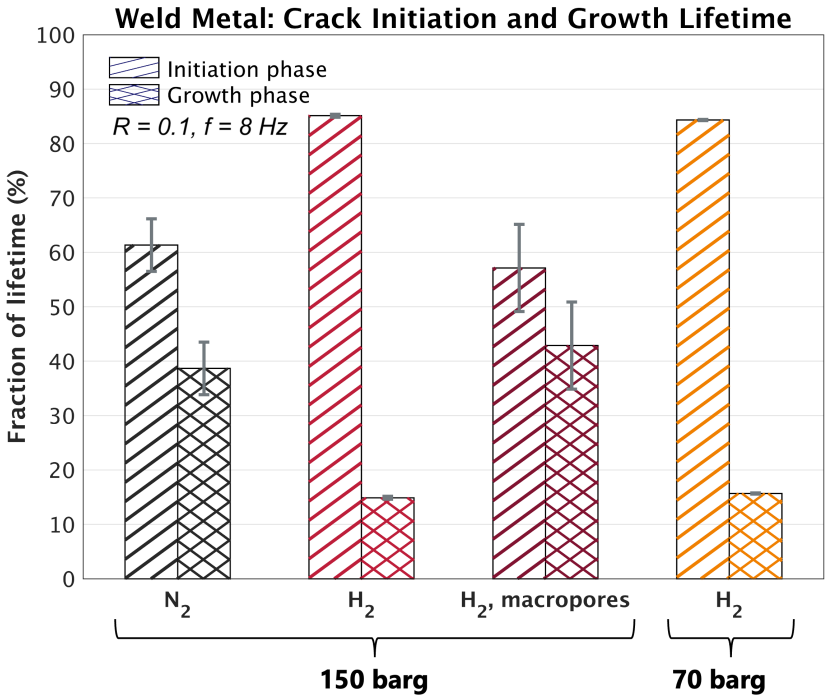

Figure 4.21: Bar graph of the fraction (%) of lifetime spent in the crack initiation phase and growth phase of WM. LT_{CI} and LT_G are calculated with Eq. 4.3 and Eq. 4.4, respectively.

Table 4.6 Fraction of lifetime spent in the crack initiation phase (LT_{CI}) and the growth phase (LT_G) of WM and BM. LT_{CI} and LT_G are calculated with Eq. 4.3 and Eq. 4.4, respectively. The data is reported as an average of the subset and includes the standard deviation. BM data of pressurised environments is included

Material	Environment	LT_{CI} (%)	LT_G (%)
WM	150 barg N_2	61.32 ± 4.83	37.68 ± 4.83
	150 barg H_2	85.11 ± 0.26	14.89 ± 0.26
	150 barg H_2, macropores	57.13 ± 8.01	42.87 ± 8.01
	70 barg H_2	84.32 ± 0.11	15.68 ± 0.11
BM	150 barg N_2	58.5 ± 3.4	41.5 ± 3.4
	150 barg H_2	83.6 ± 0.5	16.4 ± 0.5

lated to the principle proposed in more recent studies; a maximum hydrogen saturation in the cracking process zone is reached [173, 197]. These studies emphasised that a critical ΔK must be reached to neglect the gas pressure dependence of HA-FCGR. The data in this thesis covers a range of ΔK starting at zero and, if it were to exist, such an onset must therefore be observed. On the other hand, it could be that the HA-FCGR before the critical ΔK was so subtle that the effect on N_{CI} and N_F was within the standard deviation range of the 150 barg and 70 barg H_2 tests. In this case, the HA-FCGR difference before the pressure independence onset did not affect the total fatigue behaviour nor life. In order to further elaborate on this issue, the FCGR should be more critically assessed.

Crack Initiation and Growth Lifetime

The percentage of lifetime spent in the crack initiation phase and growth phase of the WM is presented in Fig. 4.21. The corresponding data is provided in Table 4.6. This table includes data from the BM for ease of comparison. It becomes clear that the results of WM and BM are relatively similar: BM 150 barg H_2 $LT_{CI} \approx 84\%$ versus WM 150 barg H_2 $LT_{CI} \approx 85\%$, and BM 150 barg N_2 $LT_{CI} \approx 59\%$ versus WM 150 barg N_2 $LT_{CI} \approx 61\%$. This indicates that the type of environment does not affect the material differently with regard to the fraction of the lifetime spent in the crack initiation and crack growth phases. Focusing on the non-porous samples, it can be stated that the crack initiation governs fatigue life, especially in H_2. This can be deduced from the higher values of LT_{CI}; it is evident that the LT_{CI}

increased for the H_2 environments. In Fig. 4.20 it was shown that for the non-porous 150 barg and 70 barg H_2, the data of N_{CI} and N_F fell within the same range. From the results of the LT_{CI} it can be deduced that the lifetime spent in crack initiation, and thus also in growth phase, are nearly identical. This highlights that both the crack initiation phase and growth phase are not affected by the difference in gas pressure. This contradicts the assertion of Holbrook et al. that the dependence of FCGR on hydrogen pressure is of the power 0.36 [80]. In such a case, almost a $(150/70)^{0.36}$ = 1.32 faster crack growth rate would have been present. A noticeably shorter LT_{CI} would then have to be accompanied by the 150 barg H_2 environment. Note that the study of Holbrook et al. dates from 1982. As a result, modern found phenomena such as the effect of hydrogen saturation were not taken into account.

The LT_{CI} of WM N_2 and H_2 with macro pores are within the same range. This does not entail that both subsets behave identically. A comparison of N_G for all hydrogen environments (including BM 150 barg H_2), leads to the conclusion that the number of cycles in the growth phase is relatively constant. To give an indication, N_G in the presence of hydrogen averages to 20200 cycles. Taking into account that the lifetime of the porous sample is considerably shorter and that N_G remains the same, one arrives at the result that the relative proportion of N_G increases. An increase in N_G is accompanied by a decrease in LT_{CI}. This explains the low average of LT_{CI} (57.1%) for the 150 barg H_2 macroporous, which is close to the average LT_{CI} of 150 barg N_2 WM (61.3%). Based on these interpretations, the fatigue behaviour of the porous specimens in hydrogen can be described in a concise form; the resistance to crack initiation decreases with macropores but does not additionally accelerate the effect of HA-FCG.

Normalised Results with Respect to Nitrogen

The normalised results with respect to 150 barg N_2 are shown in Fig 4.22. The data used to plot the graph is provided in Table 4.7. This table also repeats the normalised BM data of the pressurised environments. Note that the BM and WM results were normalised to their corresponding 150 barg N_2 data. The data can be interpreted mainly by subtracting the reported values from 100 (indicating the N_2 environment to which is normalised). The result of such an calculation results in the effect (%) of the environment on the fatigue behaviour. Fig. 4.22 highlights the similar fatigue behaviour of non-porous 150 barg H_2 and 70 barg H_2, confirming that pressure had no significant influence on the degree of HA-FCG. Regarding the normalised N_F of WM and by comparing it with BM, it can be inferred that WM is more prone to hydrogen fatigue behaviour. The presence of 150 barg H_2 reduced the resistance to crack initiation by 57% (10% for the BM). The fact that the normalised N_G for WM 150 barg H_2 is lower than the one of BM, indicates the shorter growth phase and hence the accelerated hydrogen-induced crack growth. Regarding the WM, the growth phase accelerated by a factor $100/12.81 \approx 8$, which was 4 for the BM. Ultimately, for the WM, the total reduction in fatigue life due to hydrogen is 68% (=100-32) for the WM, whereas this was 37% for the BM. Thus, the effect of hydrogen on the reduction in lifetime is a factor of 2 higher for the WM. Hence, the deleterious effect of H_2 on fatigue is more pronounced in the WM.

The deleterious effect of H_2 is more detrimental in the presence of weld defects; the lifetime reduced by $\approx$ 91% (=100-8.6) for the porous specimens. The adverse effect of hydrogen on the lifetime effect manifests in the reduced resistance to crack initiation of 92% (=100-8). This is as expected, as it has been documented that the presence of a defect may increase HE susceptibility, as a high stress/strain concentration at the defect may accelerate the rate of hydrogen diffusion [193, 47]. A defect therefore more readily reaches the critical hydrogen concentration required for hydrogen cracking. It is therefore recommended that a component should be critically assessed for defects if its intended purpose is related to the exposure of hydrogen environments.

Even though the detrimental effects of hydrogen on fatigue are known, it has been nevertheless decided that hydrogen can be transported in offshore pipelines. The research that led to this conclusion is mainly based on (pre-)cracked specimens, with sharp notches from which crack propagation occurs within the first few cycles [135]. The fatigue life is mainly determined by its portion spent in the initiation phase and small-crack stage. Hence, pre-cracking approaches are therefore a less accurate estimation of the overall fatigue life. The uniqueness of this study is that a blunt notch is used, without pre-cracking. Thereby capturing the behaviour in the initiation phase and small crack stage as well. This approach

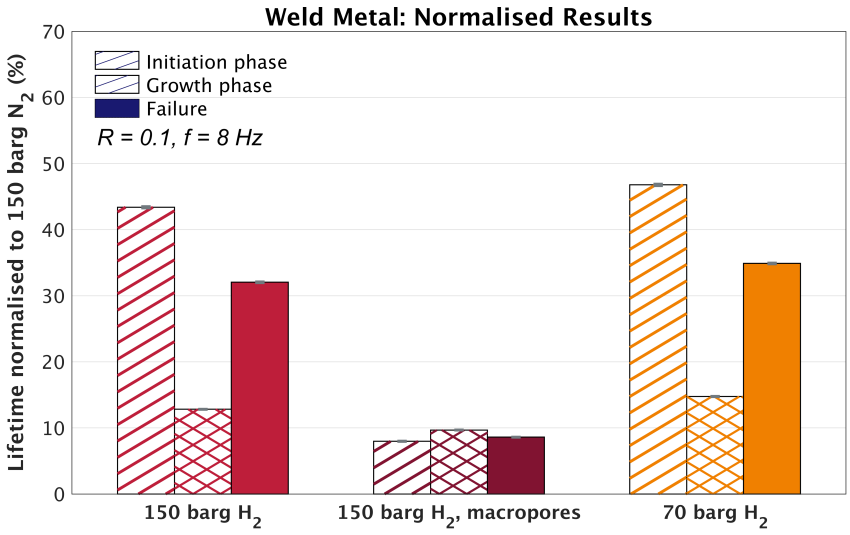

Figure 4.22: Bar graph of the normalised average results of the cycles till crack initiation (N_{CI}) and cycles to failure (N_F) of set A. The data of each environment is normalised with respect to 150 barg N_2.

Table 4.7 Normalised values of the average number of cycles spent in the crack initiation phase (N_{CI}) and growth phase (N_G), and the normalised average number of cycles till failure (N_F) of WM and BM. The data of each environment is normalised with respect to their corresponding 150 barg N_2 environment. Data of the pressurised hydrogen environment of the BM is included.

Material	Environment	Normalised N_{CI} (%)	Normalised N_G (%)	Normalised N_F (%)
WM	150 barg H_2	43.39 $\pm$ 0.11	12.81 $\pm$ 0.02	32.04 $\pm$ 0.07
	150 barg H_2, macropores	7.97 $\pm$ 0.03	9.67 $\pm$ 0.02	8.60 $\pm$ 0.02
	70 barg H_2	46.78 $\pm$ 0.12	14.74 $\pm$ 0.03	34.88 $\pm$ 0.07
BM	150 barg H_2	89.7 $\pm$ 0.14	24.8 $\pm$ 0.03	62.9 $\pm$ 0.08

led to a key point; namely, that H_2 significantly influences the initiation in WM. Studies that excluded the initiation phase are therefore too conservative regarding the estimation of the hydrogen fatigue life of welds.

Gas as Hydrogen Supply for HA-FCG

The WM samples show a uniform behaviour in terms of reduced HA-FCG when the internal gas escapes from the sample. In line with the case of BM, the retarding crack growth during outgassing is an exclusive feature of the H_2 environment. As this behaviour is consistent in BM and WM, this topic is not discussed further. Instead, it is covered in Appendix F. This Appendix also includes all WM H_2 normalised potential drop curves with zoomed in data on the outgassing phase.

4.4. Fracture Surface Analysis

Fractographic analysis was performed on the fractured specimens using optical microscopy and SEM with the aim of further clarifying the findings of the fatigue tests. The BM and WM will each be discussed in separate sections. This chapter opens with a brief overview of the characteristic fatigue fracture surface. This is followed by the identification of the pores. The chapter concludes with a section on the effect of hydrogen on fatigue by detailed examination using SEM. The main purpose of applying the SEM is to correlate the HE behaviour with the models presented in the literature.

4.4.1. Fatigue Fracture Surface Overview

An overview of a fracture surface in H_2 and N_2 can be seen in Fig. 4.23 and Fig. 4.24, respectively. These images are obtained with the Keyence Optical Microscope and showcase a 150 barg H_2 WM specimen (Fig. 4.23b) and a 150 barg N_2 WM specimen (Fig.4.24b). Note that the onset of outgassing for the 150 barg H_2 WM was accurately determined by measuring the pressure drop. However, this was not the case for N_2. Since the areas of the fractures are relatively equal, the value of the potential at the time of outgassing for the H_2 specimen was used and projected onto the N_2 specimen. These figures thus serve as a rough approximation and are mainly intended to indicate that the fracture surfaces passed through three zones. This information is vital to accurately assess the extent of the HE behaviour and to relate it to the source of the hydrogen present.

The fracture surfaces have three distinctive areas:

1. **Area I**: Area fatigued under pressure, with the sole exception of the test series of BM in air. The transition from Area I to Area II essentially marks the fatigue life, since the crack front has travelled through the entire ligament of the structure. In addition, the remaining life after area I is considerably short. Extracting the voltage value at which outgassing occurs from Fig 4.23, indicates that the most valuable data of the potential drop is measured up to a normalised voltage of approximately 1.5. A normalised voltage of 1.5 is a 50% increase from the baseline value. Note that this value is reasonable because, according to Meneghetti et al. a crack initiation occurs at a baseline increase of 0.50% [120]. If we relate this to the 50% increase in area (I to II) transition, it can be said that up to a 50% increase the crack has grown significantly, even to failure, depending on the specimen geometry.
2. **Area II**: Area that is fatigued without internal pressure. The stress response is relatively steep, indicating rapid crack growth. This can be attributed to the fact that the load-bearing area had decreased significantly. Since the stress response is inversely proportional to the area, further crack growth is accompanied by a more intense stress range. The interplay between these factors inevitably leads to faster crack growth.
3. **Area III**: Area that can be considered as the overload zone or fast fracture zone. In this stage of fatigue, the remaining material teared. The phenomenon of tearing can also be seen in the figures by the reduction of the cross-section in Area III. The relatively large size of the overload zone indicates that the part was heavily stressed at the time of final fracture. Relating this information to the (normalised) voltage response, it can be estimated that the Area III lies on the last data points of the signal.

From the overview of the fatigue fracture surface and by examining the distribution of the three areas discussed, it can be stated that asymmetry was involved. The fact that the position of each area relative to the MTS hydraulic machine was consistent for each specimen, indicates the existence of a systematic error in the set-up and rather than a specimen-related flaw. The effect of asymmetry on the fracture surface was not observed when performing a tensile test with this setup. The misalignment is therefore minor. The maximum inclination in the set-up was estimated to be 0.30°. This slight deviation has no consequence on the resultant F_{max} and F_{min}, and thus also not on σ_{max} and σ_{min}. It could however be postulated that an interplay between the misalignment and the vibrations in the system, associated with the high test frequency, amplified the misalignment effect. This could ultimately have led to the fracture surfaces of the specimens.

To avoid repetition, analysis of the areas is not further extended to the BM N_2 specimens. Such an evaluation is not required as the mentioned areas are present in all specimens and the information

provided is therefore representative for the H_2 and N_2 environments, independent of the material.

Fig. 4.23b shows that pores are present in the specimen. A macro pore was located at the edge of the notch and a micro pore was identified in Area I. Two macro pores could also be identified on the outer surface of Area III. The size of the weld pores and the effect they had on the fatigue behaviour will be discussed in the next section.

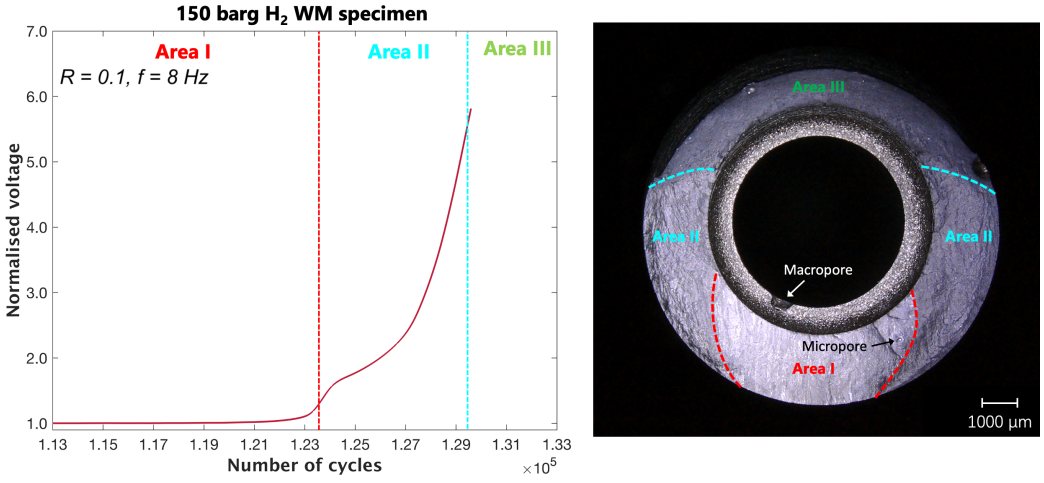

Figure 4.23: Normalised potential drop data of a 150 barg N_2 WM specimen with annotations indicating the areas spent in the characteristic fracture area. This figure should be read by combining the potential drop data a) with the information on the fracture surface b). A micro- and a macro pore have been identified in the figure which can be distinguished by their black and white coloured annotations, respectively.

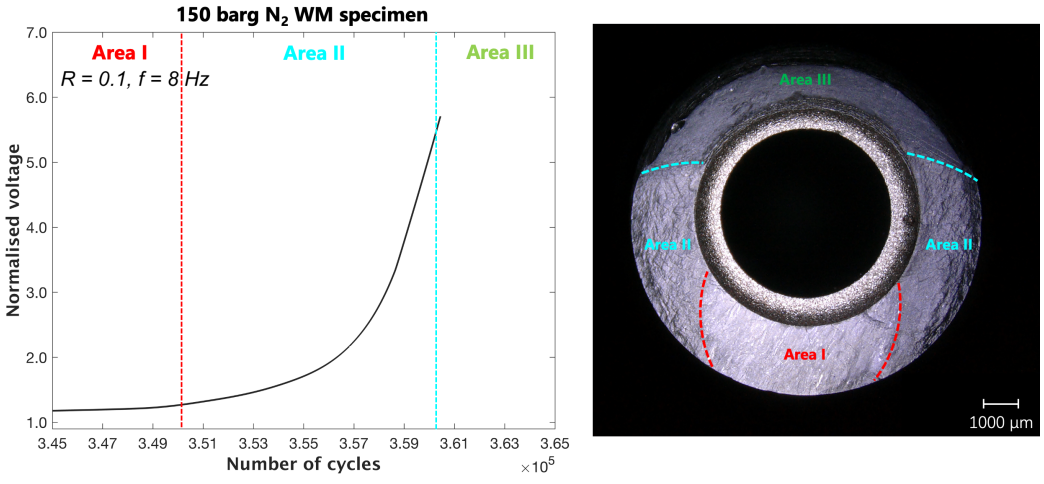

Figure 4.24: Normalised potential drop data of a 150 barg N_2 WM specimen with annotations indicating the areas spent in the characteristic fracture area. This figure should be read by combining the potential drop data a) with the information on the fracture surface b).

4.4.2. Weld Defects

From the fracture surface overview presented in the previous section, it became evident that the WM samples can contain defects. The damaging effects of such defects in 150 barg H_2 were directly visible from the fatigue results; on average the macro pores reduced the lifetime by a factor of 11.6 compared to 150 barg N_2. This section identifies the dimensions and locations of the defects, and discusses their effect on fatigue.

The (150 barg H_2) WM samples containing a macropore on the surface were considered defective as they were associated with a detrimental effect on fatigue life. However, the 'non-defective' samples also contained pores. The pores were smaller in size and are referred to as micro-pores. Based on literature, the pores in this work are classified to be macropores when their length and/or width exceed(s) 300 µm [100]. In Table 4.8, the effect of the size and location of the defect on (hydrogen) fatigue can be read. It can be deduced that two samples contained macropores, which are further identified in Fig. 4.25. In Fig. 4.25a, an overview is provided of a 150 barg H_2 fracture surface that contained a micro- and macropore. The macropore is shaped as a spheroid with a width and length of $\approx$ 500 µm. The micropore is significantly smaller with a diameter of $\approx$ 50 µm. The detrimental effect of the macropore

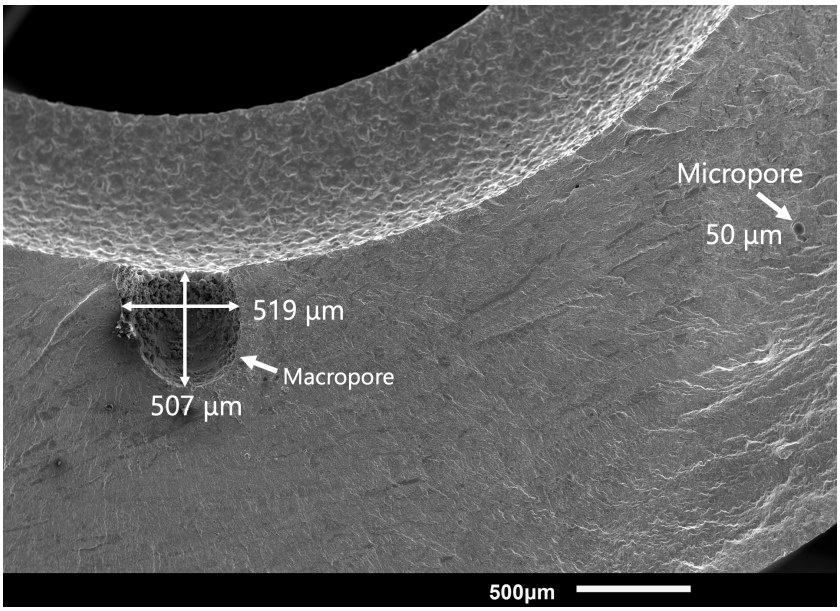

(a)

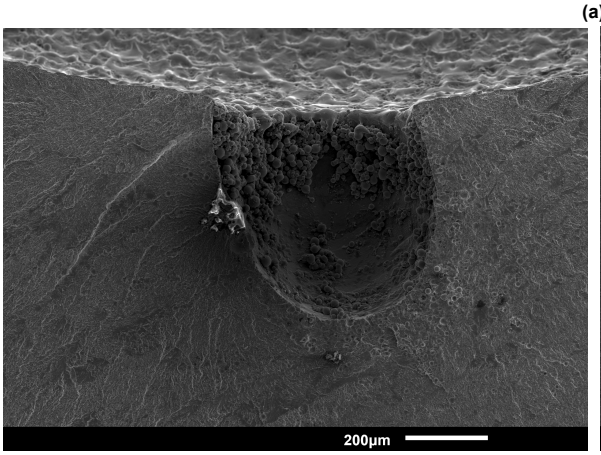

(b)

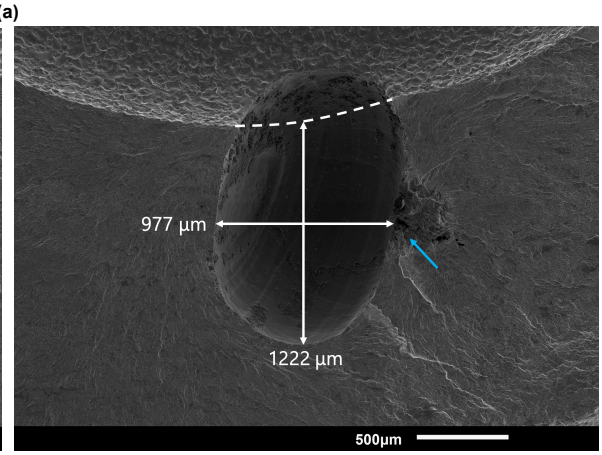

(c)

Figure 4.25: Macropore identification of 150 barg H_2 defected WM specimens. a) An overview of a macropore located at the notch. b) Zoomed-in projection of the macropore in a). c) Macropore of the second 150 barg H_2 defected WM specimen. In c) surface separation is indicated with a blue arrow. Dimensions of the pores are annotated. The corresponding fatigue life can be read from Table 4.8.

Table 4.8 Relation between weld defects and hydrogen fatigue. Fatigue initiation life and total life are provided in number of cycles.

Weld metal samples	Macropore length/width (µm)	Location	Micropore length/width (µm)	Location	Fatigue initiation life	Fatigue total life
150 barg H_2	1222/977	Area I, notch root	-	-	15,743	32,047
	507/519	Area I, notch root	50/50	Area II, subsurface	27,640	42,432
	-		236/200	Area II, subsurface	110,640	129,952
	-	-	62/62	Area I, subsurface	143,048	167,560
	-	-	-	-	100,775	119,135
150 barg N_2	-	-	102/102	Area I, near root	401,064	536,536

is evident from the ratchet marks visible in the zoomed-in projection of the pore in Fig 4.25b. From the other 150 barg H_2 WM specimen with a macropore, see Fig. 4.25c, the ratchet marks near the tip of the defect are clearly visible. In addition large cracking is involved, which can be seen from the surface separation indicated with the blue arrow. These features highlight the detrimental effects that are associated with a macro defect. This defect is also shaped as a spheroid, however larger in size. It measures a width of $\approx$ 1000 µm and a length of $\approx$ 1200 µm. Both defects are located at the notch of Area I. Hence, a direct comparison can be made regarding their size and their effect on the fatigue life. A larger defect size is more deleterious; when the size becomes twice as large (= 1000/500) the fatigue life reduces from 42,432 to 32,047 cycles. This is a 25% reduction of lifetime. To put this into perspective, when a non-defective 150 barg H_2 WM is considered (see table 4.8), the fatigue life is 119,135. For the largest macropore, the fatigue life is thus further reduced by 73%. This finding points to the importance of detecting welding defects in pipelines before they are repurposed for the transport of hydrogen gas. Whether such defects are detected in practice depends to a large extent on the calibration of the non-destructive measurement technique. For instance, considering automatic ultrasonic testing, the detection is dependent on the orientation of the defect (i.e. the length and width) with respect to the measuring direction. According to a report for Shaw Pipeline Services, a defect that is 4 mm wide and 0.3 mm long (or vice versa) can be detected at a depth of 2 mm from the surface [168]. In the worst case, i.e. the scanning direction with a detection limit of 4 mm, the defects mentioned here would not be detected. These findings indicate that such an (undetected) defect may lead to sudden failure of hydrogen transport pipelines during operation.

Micropores were also identified in this work. For instance, a micropore ($\approx$ 200 µm in length and width) was identified in Area II of a 150 barg H_2 WM specimen. As can be seen from Fig. 4.26a, this 'buried' micropore was located approximately in the middle of the ligament. However, the presence of this defect did not adversely affect fatigue. Most of the WM specimens contained micropores of small dimensions. In both environments (N_2 and H_2), these micropores did not accelerate the fatigue failure when compared to completely non-porous specimens. Therefore, it could be stated that minor weld defects like these can be neglected in fatigue life time analysis. To illustrate the appearance and distribution of such small micropores on a fracture surface, it is referred to Fig. 4.26b and Fig. 4.26c which represent a 150 barg H_2 WM and 150 barg N_2 WM specimen, respectively. Both specimens contained micropores (see white arrows) within the range of $\approx$ 10-100 µm.

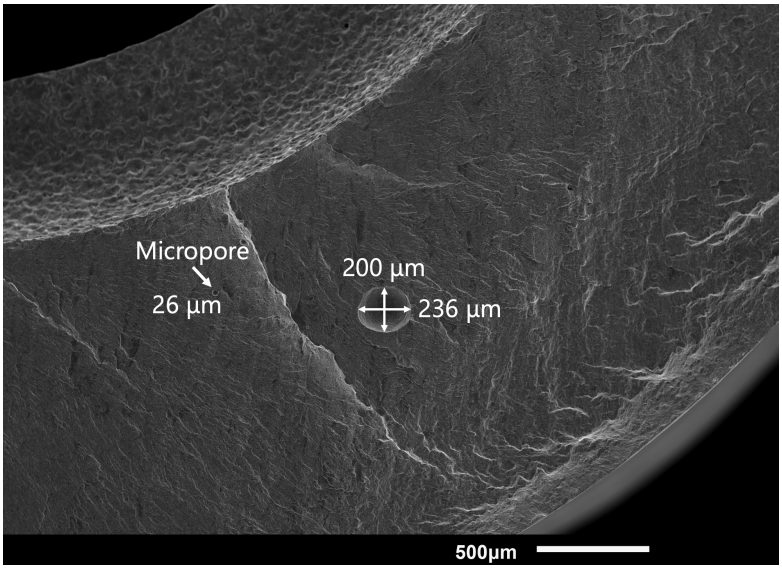

(a)

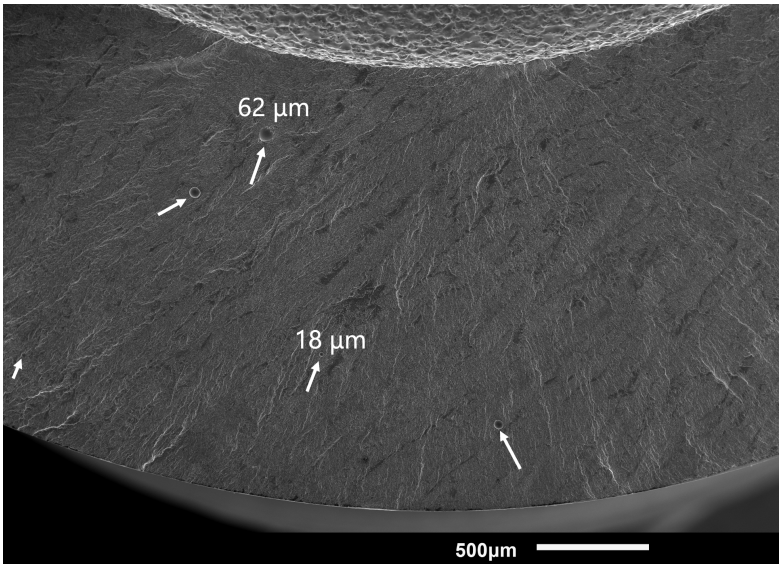

(b)

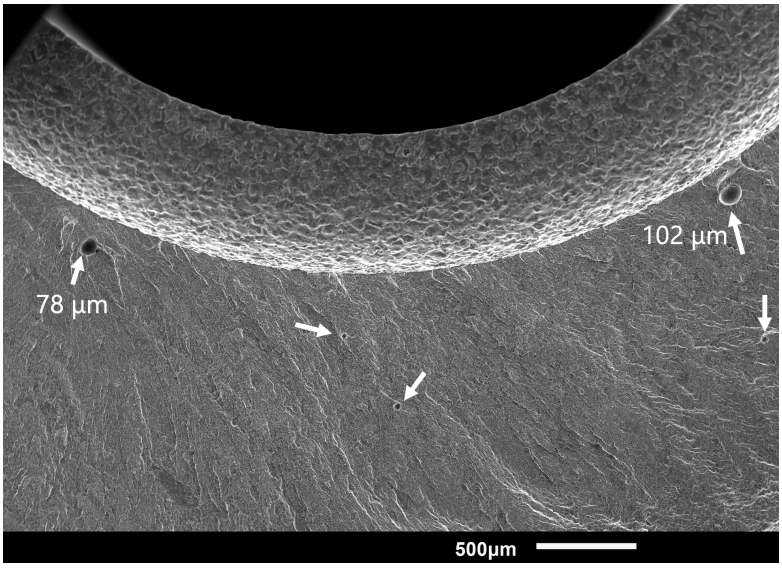

(c)

Figure 4.26: Micropore identification in 'non-defected' WM specimens. a) and b) Micropores in Area I of 150 barg H_2 WM specimens. c) Micropores in Area I of a 150 barg N_2 WM specimen. All the three specimens contain micropores with a diameter between $\approx$ 10-110 µm.

4.4.3. Base Metal

The fracture surfaces of base metal samples tested in the absence of gas and in the presence of N_2 were analysed as benchmarks to identify any differences that occur with the addition of H_2. This section is written with this structure in mind, and maintains it for the subsequent sections related to fracture surface analysis. This section focuses on 'Area I' and 'Area II'. Since Area III is virtually a tensile test, the results are provided in Appendix G.1. The main conclusion from Area III analysis is that the residual hydrogen concentration in the specimen did not influence the fatigue behaviour at this stage of fatigue. All images were produced with the same specimen orientation; Area I on the bottom and Area III on the top, as shown in Fig. 4.24.

Effect of Environment

An overview of Area I for the Air and 150 barg N_2 is provided in Fig. 4.27a and Fig. 4.27b, respectively. Focusing on the notch root (inner surface), it can be deduced that in the early phase of crack initiation, cracks initiate at multiple origins and propagate on different planes. These propagating fatigue cracks intersect through steps between neighbouring planes, thereby creating characteristic ratchet marks. The ratched marks are annotated with white arrows in the figures and are macroscopically visible as lines parallel to the overall crack growth direction, which is depicted with a black arrow. The formation of ratched marks is indicative for low stresses with high stress concentration [145].

Comparing both figures, it can be stated that the morphology of the samples tested in air and in 150 barg N_2 show similar macroscopic characteristics. In both cases, multiple cracks start from the notch that propagates to the outer end of the ligament.

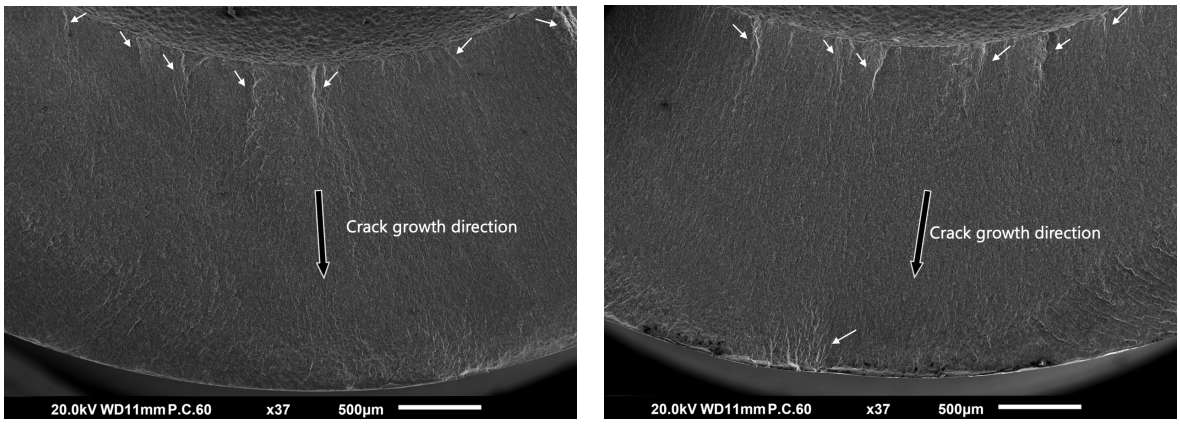

(a) (b)

Figure 4.27: SEM overview of Area I for air a) and 150 barg N_2 b) BM tested specimen. The white arrows indicate ratchet marks. The black arrows indicate the overall crack growth direction.

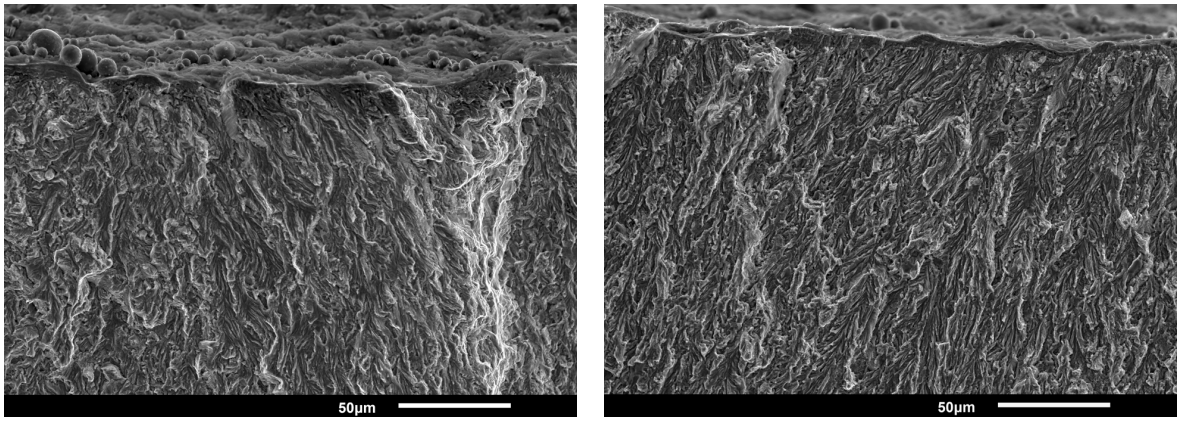

(a) (b)

Figure 4.28: SEM overview of the notch region in Area I for air a) and 150 barg N_2 b) BM tested specimen.

The fracture surfaces in Area I were completely ductile in nature. This can be more clearly deduced from the zoomed-in projection of the notch in air (Fig. 4.28a) and 150 barg N_2 (Fig. 4.28b). Furthermore, it can be concluded from these subfigures that the fracture was transgranular; no individual grains could be identified that would indicate an intergranular fracture. Over the whole ligament, the fracture behaviour in Area I can be considered macro- and microscopically similar for air and N_2. The air environment is therefore excluded for further discussion, as a description of 150 barg N_2 is sufficient. Note that the SEM images of the air environment are provided in the Appendix G.2.

Upon examination of the SEM image of 150 barg H_2 (Fig. 4.29a), a distinctive feature can be noted; the fatigue zone exhibits two different appearances. The boundary between the associated areas marks the transition between ductile transgranular fatigue and brittle quasi-cleavage. The existence of such a transition emphasises that the initial crack growth is not significantly affected by the presence of hydrogen. The resulting behaviour is therefore ductile, which is also demonstrated by the consistent ductile characteristics of the notch visible in Fig. 4.29b. These findings are in strong agreement with the fatigue results. Namely, that the crack initiation moment was not significantly affected by the presence of H_2. Thus, a critical ΔK is required for the onset of HA-FCG. This is in good agreement with findings in literature. The onset for HA-FCG in literature is associated with a $\Delta K \approx 8 - 15$ MPa$\sqrt{\text{m}}$ [53, 6]. It is therefore expected that the observed quasi-cleavage transition corresponds to the ΔK range reported in literature.

Fig. 4.30a is a higher magnification image of the section I enclosed by the red rectangle in Fig. 4.29a. The same respective section for the N_2 environment is imaged in Fig. 4.30b. From Fig. 4.30a, the quasi cleavage can be identified as smooth features on an irregularly faceted fracture surface. In literature, the fracture surface at the onset of HA-FCG is often characterised to be predominantly intergranular [174, 173, 53, 6]. In this work however, the onset of HA-FCG is primarily transgranular, but exists as a mixed-mode of intergranular features. The intergranular features are identified by the triple points (red arrows) on the fracture surface. In N_2 and in the ductile region of H_2, however, the triple points are less evident and thus transgranular fracture dominates. The other arrows (blue) indicate the locations of secondary cracking in the material. As can be seen in Fig. 4.30b, secondary cracking also exists in this stage of fatigue for the N_2 environment.

Fig. 4.31a is a higher magnification image of section II enclosed by the red rectangle in Fig. 4.29a. The same respective section for the N_2 environment is imaged in Fig. 4.31b. It can be seen from these figures that as the crack front progressed, the prevalence of secondary cracking increased. This is visible from the larger material separation (see blue arrows). The main difference is that for H_2 the secondary cracks became more extended in length. The N_2 environment is also accompanied by some extent of (ductile) striations (see yellow arrows), which are absent in H_2.

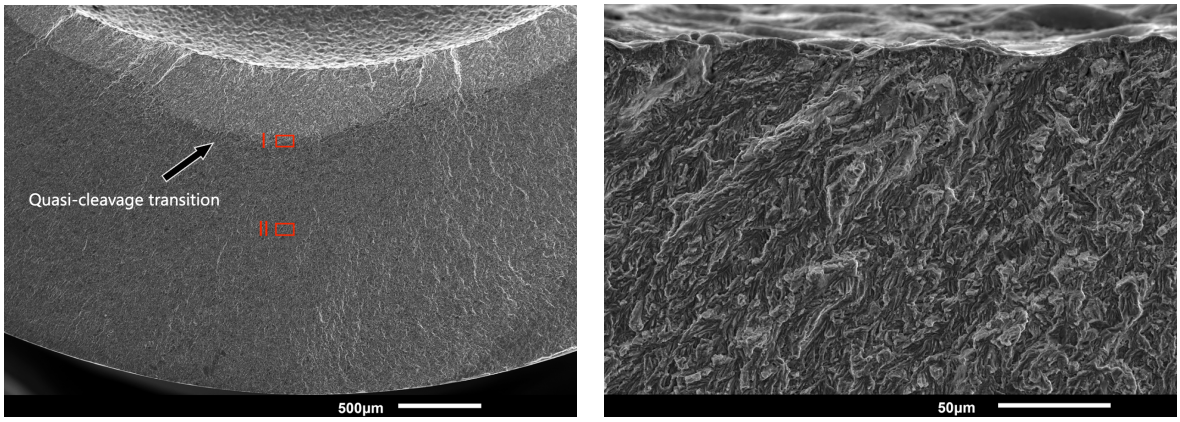

(a) (b)

Figure 4.29: a) SEM overview of Area I and b) the notch region for a H_2 BM tested specimen. The black arrow in a) indicates the quasi-cleavage transition. In a) the red annotated regions I and II are magnified in Fig. 4.30a and Fig. 4.31a, respectively.

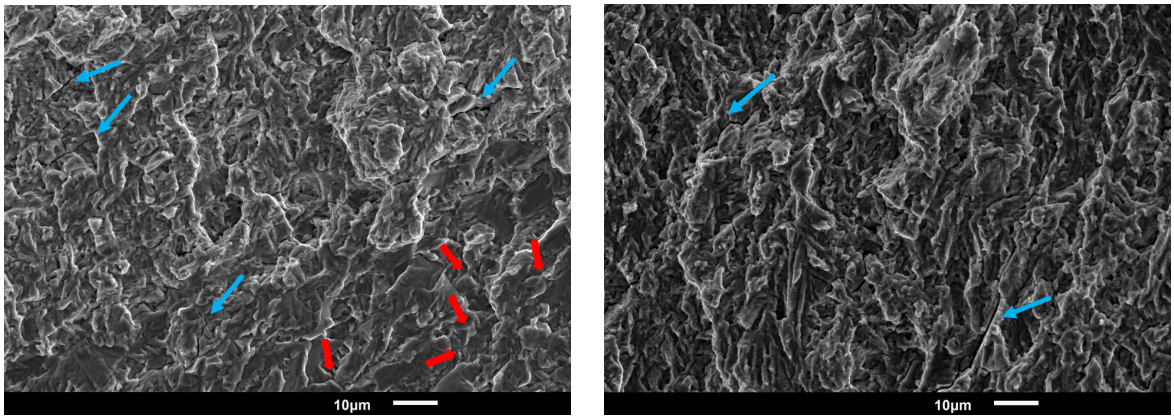

(a) (b)

Figure 4.30: Magnification of region I (see Fig. 4.29a) for a 150 barg H_2 a) and 150 barg N_2 b) BM tested specimen. The blue arrows indicate secondary cracking. The red arrows mark triple points.

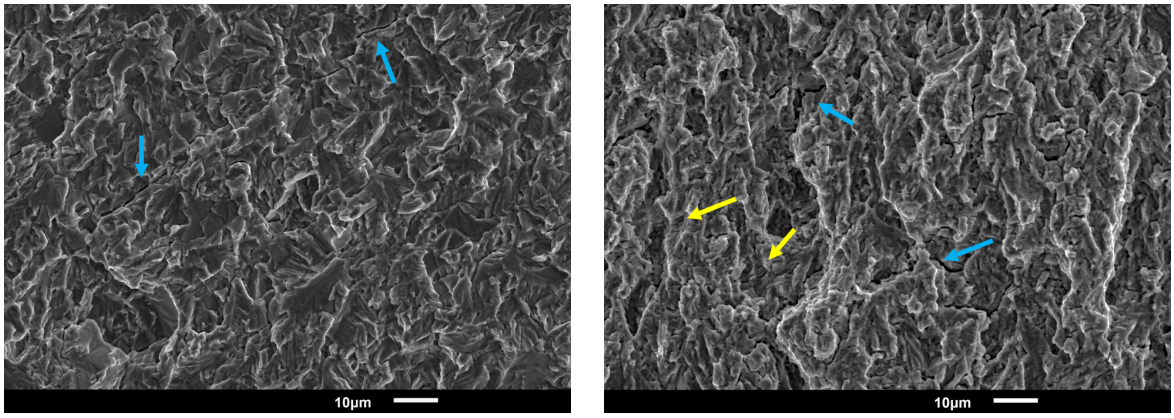

(a) (b)

Figure 4.31: Magnification of region II (see Fig. 4.29a) for a 150 barg H_2 a) and 150 barg N_2 b) BM tested specimen. The blue arrows indicate secondary cracking. The yellow arrows mark ductile striation formation.

In Area II, the specimens had in common that there was no internal gas involved. This enables a direct comparison between all environments; air (Fig. 4.32a), H_2 (Fig. 4.32b) and N_2 (Fig. 4.32c). Those figures were imaged at the middle of the ligament in Area II. This stage of fatigue corresponds to the phase after the HA-FCG inflection point (see section 4.2.2 Fig. 4.16). The significant increase in crack growth in Area II can be recognised on the fracture surface by the appearance of fatigue striations. The fact that striations appear on the surface for H_2, is inconsistent with the trend in literature [53, 5, 135]. In specific, there exists consensus that hydrogen exposed specimens exhibit cleavage-like facets on the fracture surface. The ductile characteristics in Area II of the H_2 sample indicate that it was the gaseous hydrogen supply that governed HA-FCG. Shortly after complete hydrogen escape the 150 barg H_2 voltage response converged to the ones of air and 150 barg N_2. The fact that the HA-FCG disappears at this stage of fatigue indicates that the hydrogen diffusion (of residual hydrogen) can not keep up with the newly formed crack surface area to maintain the embrittlement effect.

At the transition from Area II to Area III, the striations increase in spacing and height, to a macroscopic scale, which can be seen in Fig. 4.33a. Fig. 4.33b shows a close-up of the area marked in Fig 4.33a. The increase in striation size is evident, indicating that with each subsequent cycle, crack growth increases significantly. If we relate this to the potential drop data, the nearly vertical stress response is reached at this stage. Since the crack growth direction is perpendicular to the striations, and including the discussion from Area I, it can be confirmed that the crack front originates from Area I and expands through Area II to finally reach Area III.

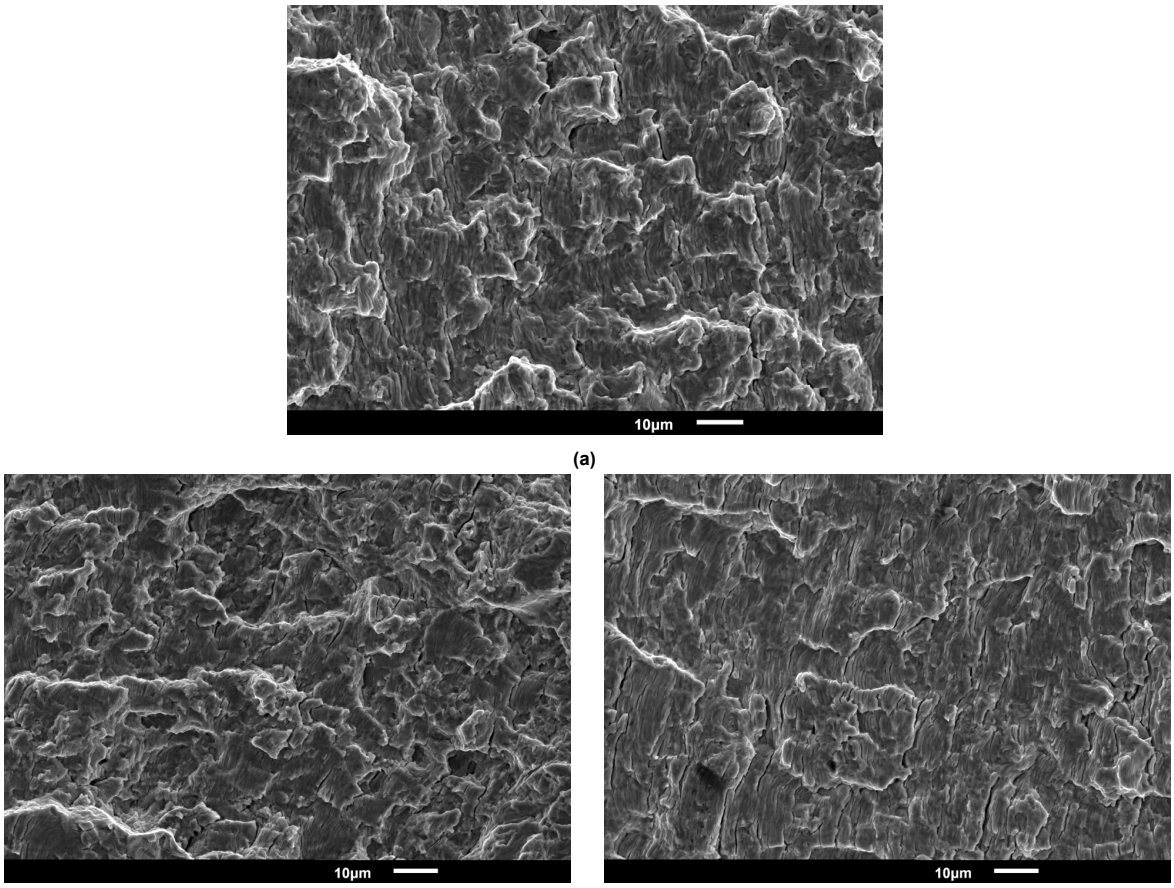

(a) (b) (c)

Figure 4.32: Striations in Area II in air a), 150 barg H_2 a) and 150 barg N_2 b) BM tested specimen.

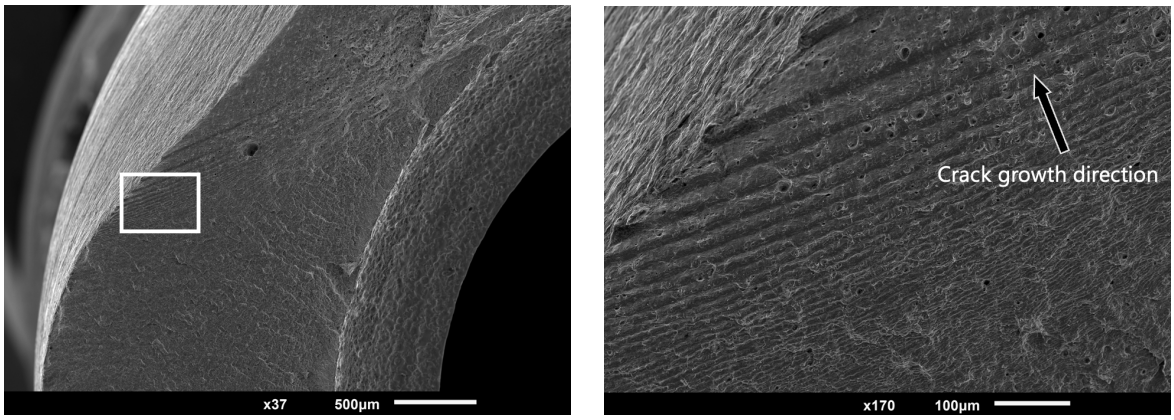

(a) (b)

Figure 4.33: Transition from Area II to Area III in 150 barg N_2 BM tested specimen. a) Indicates an overview of the transition and b) a close-up view where the increase in spacing of striations can be seen. The crack growth direction is perpendicular to striation formation and is indicated with an arrow.

4.4.4. Weld Metal

An overview of Area I in 150 barg H_2 and 150 barg N_2 WM tested specimens is provided in Fig. 4.34a and Fig. 4.34b, respectively. The 70 barg H_2 SEM fractographs are excluded from this section, since no differences were observed with respect to 150 barg H_2. This is as expected as no distinguishing features were identified in the potential drop data. Nevertheless, the 70 barg H_2 images are provided in Appendix G.3. Similarly to the BM samples, the cracks initiated at the inner surface of the notch. The associated ratchet marks are illustrated with white arrows in Fig. 4.34. As can be seen, the extent of ratchet marks has markedly reduced for the H_2 specimen. This indicates that in H_2 crack initiation occurs more frequent on the same fracture plane. In the N_2 sample, river patterns are visible (red arrows). River markings occur most frequently in the relatively fast growing parts of the fatigue zone. These markings occur because individual cleavage facets are connected by steps that create the river-like morphology. The morphology shows that multiple cracks converge into a single crack as they pass through the material. This confirms that the cracks in Area I started strictly from the inside and grew towards the external edge of the ligament.

There are two main distinctive features that distinguishes the H_2 environment from N_2: i) brittle cleavage facets are present in H_2 (yellow arrows) and ii) a fracture behaviour transition region exists near the notch root. Regarding the first characteristic, the cleavage facets are consistent in orientation and relatively uniform in shape and length. They correlate well with the prior austenite grain boundaries. Considering its brittle flat appearance, it could be hypothesised that this feature arose from transgranular cleavage along the prior austenite grain boundaries. The second characteristic can be investigated with Fig. 4.35, which compares the fracture surfaces at the notch region for 150 barg H_2 and 150 barg N_2. In Fig. 4.35a, the H_2 specimen, the fatigue transition of finer grains (acicular ferrite) is approximately estimated and indicated with a white dotted line. From this figure it can be inferred that the fatigue transition is less uniform than observed in the BM. In addition, the offset would relate to a smaller ΔK since this transition is closer to the crack initiation surface. This is consistent with the WM potential drop data which showed that hydrogen affects the crack initiation, and thus also the short crack growth stage. On the other hand, as can be seen from Fig. 4.35b, the initial crack growth is fully ductile in the N_2 environment. Fig. 4.35c provides a zoomed-in image of the area enclosed by the red rectangle in Fig. 4.35a. The white arrow indicates finer grains exhibiting quasi-cleavage, which is not observed from the region annotated with the black arrow. Therefore, the earlier introduced fatigue transition boundary could be related to the onset of quasi-cleavage and thus HA-FCG.

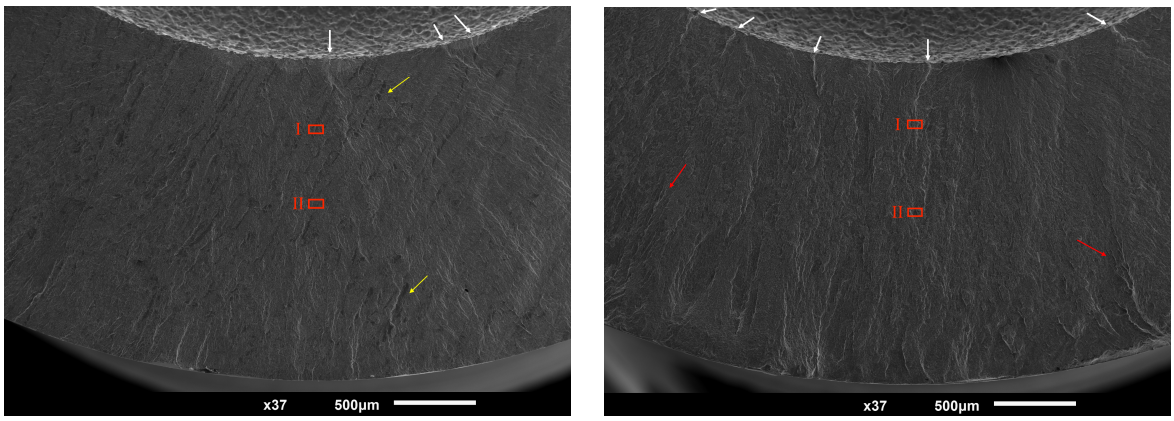

(a) (b)

Figure 4.34: Overview of Area I in a) 150 barg H_2 and 150 barg N_2 b) WM tested specimen. In a) yellow arrows indicate brittle transgranular cleavage facets, which are postulated to manifest in prior austenite grain boundaries. In b) river patterns are depicted with red arrows. The white arrows in both subfigures indicate ratchet marks. Regions I and II annotated in red, are further magnified in Fig. 4.36 and 4.37, respectively.

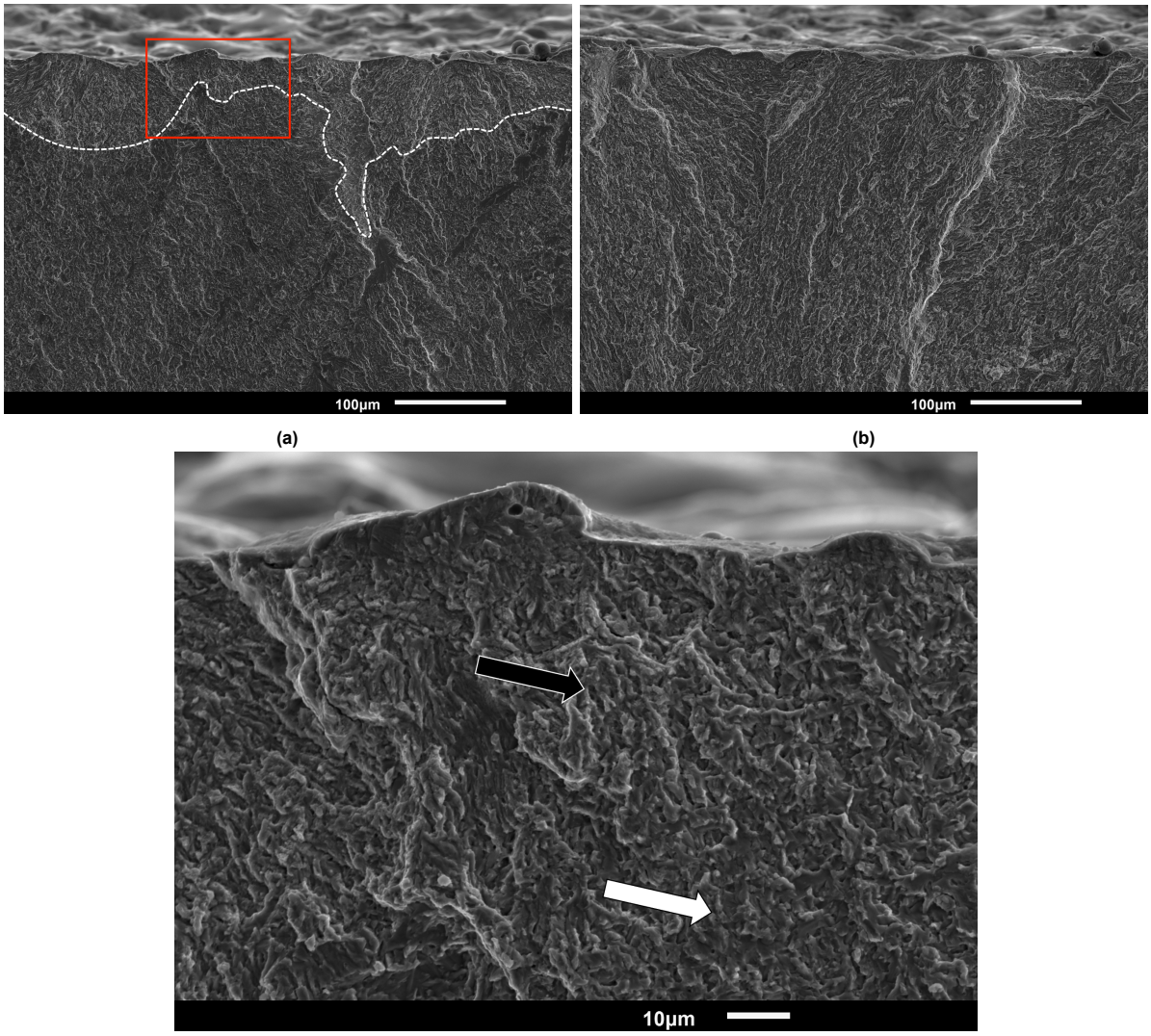

Figure 4.35: Magnification of the fracture surface close to the notch of 150 barg H_2 a) and 150 barg N_2 b) WM tested specimens. In a) the white dotted lines indicate the quasi-cleavage onset for the fine acicular ferrite grains. The area enclosed in the red rectangle is magnified in c). The arrows indicate the differences between the fatigue transitions; the black arrow indicates the area of ductile cracking, while the white arrow indicates the grains that are apparent for quasi-cleavage.

Fig. 4.36a (150 barg H_2) and Fig.4.36b (150 barg N_2) provide a higher magnification image of the annotated region I in Fig. 4.35a and Fig. 4.35b, respectively. The main difference between the H_2 and N_2 samples are that secondary cracking is absent for H_2. Examples of secondary cracking in N_2 are illustrated with blue arrows in Fig.4.36b. In addition, a metal crumb is identified that appears as a rough fragment protruding from the surface on the fracture. The characteristics of metal crumbles are further discussed in section 4.4.5. In the H_2 sample, intergranular granular features can be clearly identified from the triple points (see Fig. 4.36a). The combination of the fine grains and the ductile features in N_2 precludes a substantiated statement about the fracture path in N_2. However, this will be investigated with more detail in section 4.4.5.

Fig. 4.37b (150 barg H_2) and Fig. 4.37a (150 barg N_2) provide a higher magnification image of the annotated region II in Fig.4.35a and Fig. 4.35b, respectively. From these figures it becomes evident that even at a later stage (higher ΔK) of fatigue, secondary cracking is not observed for H_2. On the contrary, for N_2 the extent of secondary cracking and metal crumb formation increases with the progression of fatigue (and thus ΔK). This implies that hydrogen reduces the crack tortuosity.

From Fig. 4.38 it can be deduced that the H_2 specimen exhibits striations and secondary cracking in Area II. This could be related to the combination of two features: i) the loss of internal H_2 results in the loss of crack tip sharpening by HELP (and AIDE), and (ii) generally at this stage of fatigue, the reduction of the load-bearing area is so extensive that the material is no longer capable of dissipating the energy which would cause it to fail by a single crack. In essence, the fracture behaviour in Area II

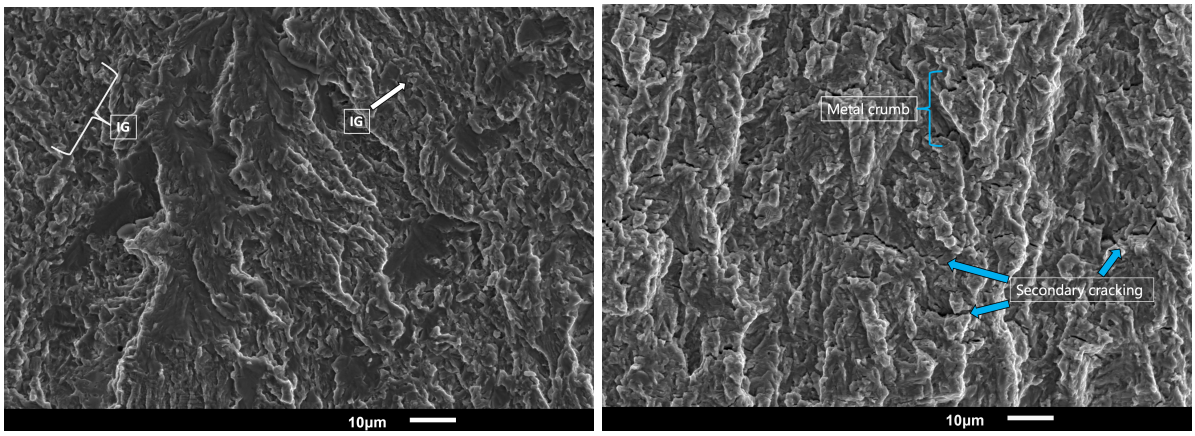

(a) (b)

Figure 4.36: Magnification of region I from 150 barg H_2 a) and 150 barg W_2 b) WM tested specimens. In a) intergranular fracture is annotated in white. In b) secondary cracking is indicated with blue arrows. In addition, a metal crumb is identified (blue bracket).

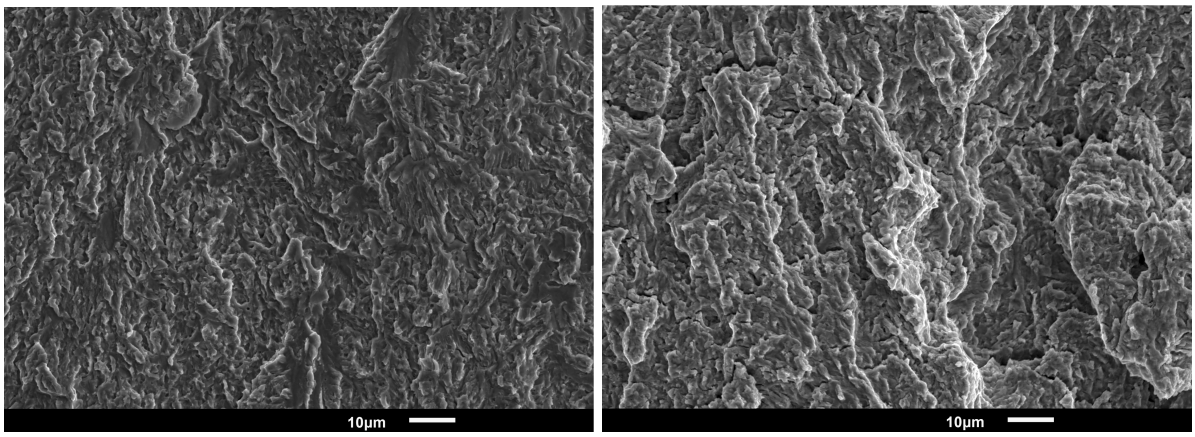

(a) (b)

Figure 4.37: Magnification of region II from 150 barg H_2 a) and 150 barg N_2 b) WM tested specimens.

is thus similar for N_2 and H_2. This statement holds for both the BM and WM material.

A noticeable difference however exists in the transition from Region II to Region III fatigue (see Fig. 4.39. While the BM showed an apparent transition from the increase of striation width to MVC, the WM directly shows MVC. Also, the WM exhibits large cavities that could result from both weld defects being elongated during the tensile overload and cavities created by pulling out of material. The exact underlying principles have not been derived in this thesis, as this part of fatigue is virtually a tensile test. No noticeable effects of hydrogen on Area III was observed, which once more indicates that the gaseous hydrogen supply governed the HA-FCG behaviour. An analysis of Area III can be found in Appendix G.4.

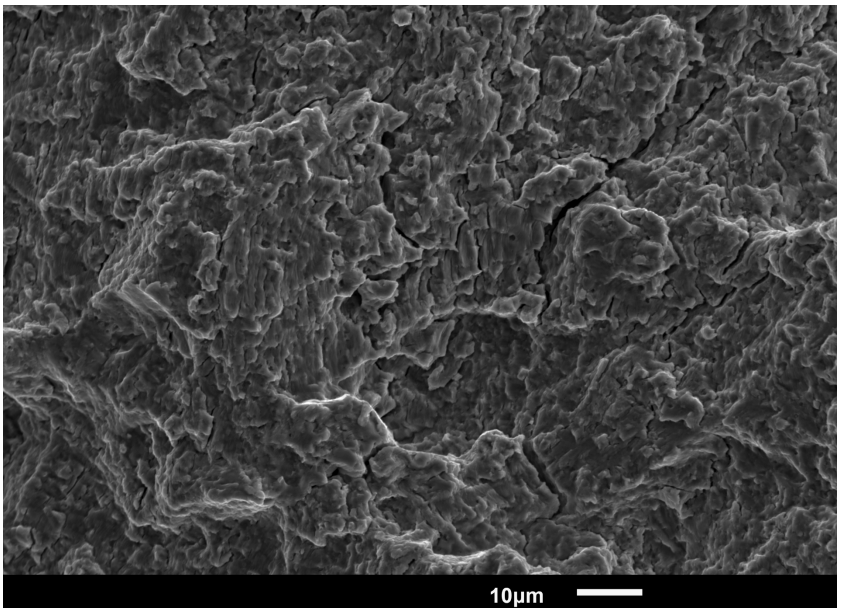

Figure 4.38: Striations in Area II in 150 barg H_2 WM tested specimen.

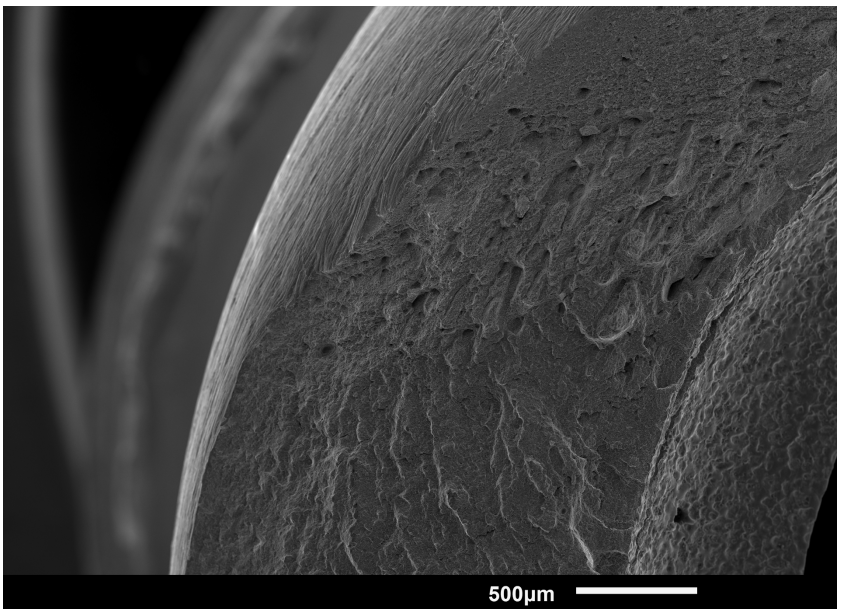

Figure 4.39: Transition from Area II to Area III in 150 barg N_2 WM tested specimen.

4.4.5. Crack Path Analysis

This section studies the crack path behaviour for BM and WM, in 150 barg N_2 and 150 barg H_2. First, characteristic features are mentioned for each environment. The main discussion of those results can be found in the last subsection; 'Weld Metal: 150 barg H_2'.

Base Metal: 150 barg N_2

Crack path analysis was performed on specimens prepared as described in section 3.1.3. A separate analysis showed that the EDM recast layer had a dimpled surface and that crack initiation predominantly occurred in the thinner parts of the layer. The overall fatigue behaviour, however, was not influenced. The recast layer is therefore not further addressed in the results presented in this section. Information regarding the characterisation of the EDM recast layer can be found in Appendix H.

The images related to the crack path analysis of 150 barg N_2 BM are provided in Fig. 4.40. A macroscopic view of the notch is given in Fig. 4.40a. In this figure, several crack initiation sites can be identified and the leading crack can be seen. A magnified view of the area indicated by the white arrow in Fig. 4.40a, is provided in Fig. 4.40b. It can be seen that five cracks have initiated in close proximity to each other and merged to form the leading crack controlling fatigue crack growth. A higher magnification of the left crack (black arrow in Fig. 4.40a) is shown in Fig. 4.40c. From Fig. 4.40c and Fig. 4.40b, it can be deduced that the fracture path of the initial crack growth is predominantly transgranular. Fig. 4.40d and 4.40e are 100X magnifications of region I and region II in Fig. 4.40a, respectively. From these figures it can be inferred that the entire fracture path was predominantly transgranular.

It can be noted that the crack is tortuous; exhibiting crack deflection and crack branching features. In Fig. 4.40d, it can be seen that the crack deflects almost of the order of 90°. Examples of such high angle deflections are annotated with blue arrows in Fig. 4.40d. In the following paragraphs, when the term 'high angle crack deflection' is used, it refers to a deflection of the order of 90°. Korda et al., with their study on ferrite-pearlite micro-structured steels, postulated that a nearly 90°deflection angle arises from encountering a hard pearlite phase below the surface of the steel [95]. However, this could not be demonstrated from the presented figures, instead it seems that the ferrite grain boundaries play an important role in the deflection. Korda et al. also emphasised that crack branching mainly occurs after passage of the crack tip through pearlite. This statement is in line with the results of the fracture path presented in Fig. 4.40e. In addition, in this figure, the phenomenon of crack arrest at pearlite is annotated with blue arrows. The leading crack terminated at the interface of ferrite-pearlite (bottom blue arrow). The discussed features regarding the cracking behaviour of the specimen are common for a ferrite-pearlite banded microstructure [83]. The extent of crack branching increased with crack length, thus ΔK, which explains the increased amount of secondary cracking at higher ΔK observed during SEM fracture surface analysis (see Fig. 4.31). It should be noted that it is primarily the pearlite phase that causes these tortuous characteristics.

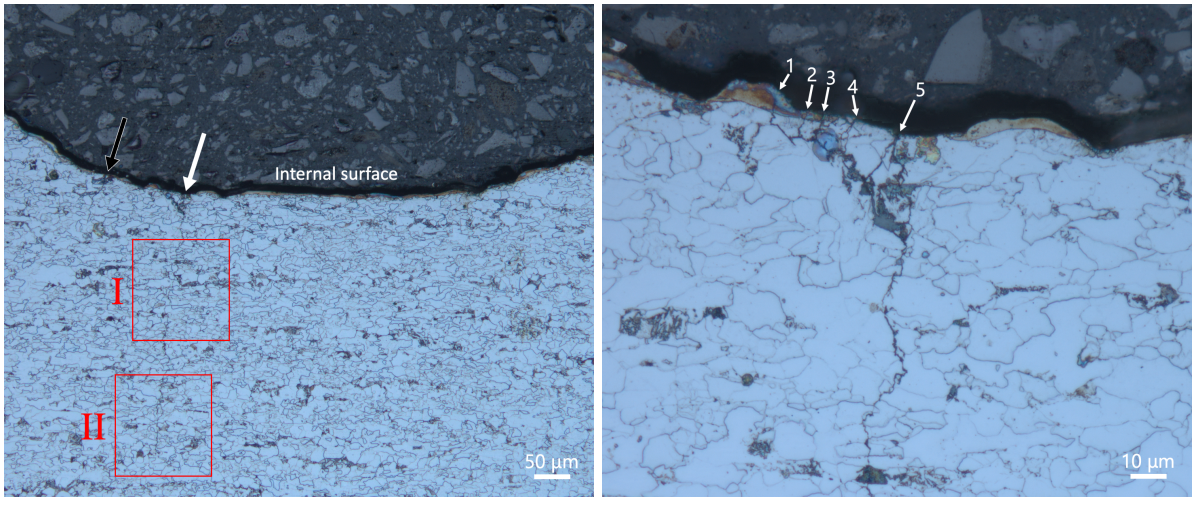

(a) (b)

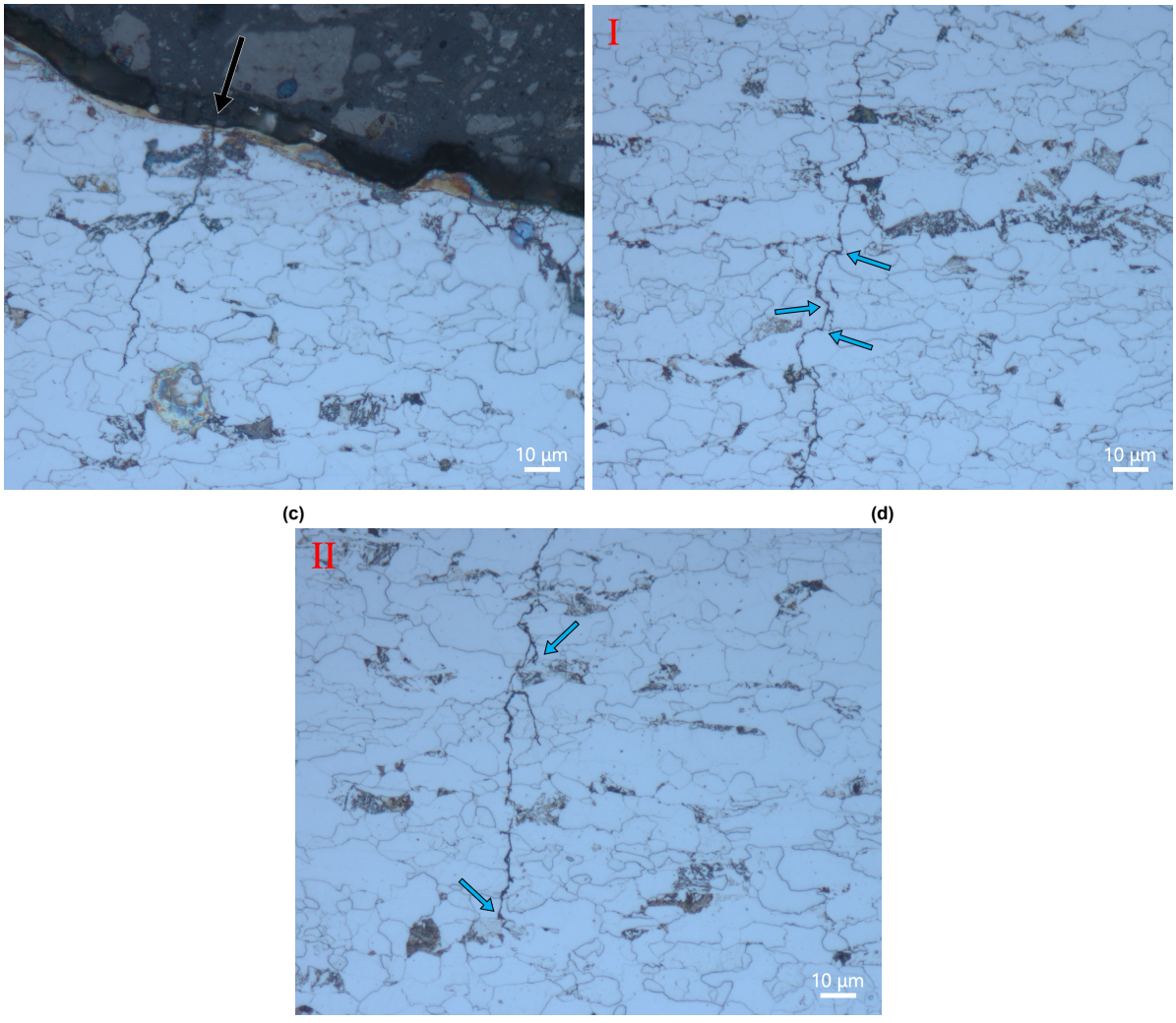

(c) (d)

(e)

Figure 4.40: Crack path analysis on 150 barg N_2 BM specimen. a) An overview of the notch from which the initiated cracks can be identified. The (internal) surface of the notch is annotated. The white arrow indicates the region of the leading crack. A magnified view of this region is provided in b). The five cracks that initiated on the surface are numbered. A crack that initiated but arrested is identified in a) with a black arrow. A zoomed in view of this crack is provided in c). A magnified view of region I in a) is provided in d). A magnified view of region II in a) is provided in e).

Base Metal: 150 barg H_2

A similar approach was used to analyse the 150 barg H_2 BM specimen. The results are presented in Fig. 4.41. From the overview of the crack in 4.41a, it appears that the crack is shorter, but it initiated at a relatively similar location in the notch. The difference in crack length can be attributed to the (slight) angular variation in the orientation of the specimen during embedding. This misorientation consequently influenced the layer removal with the lathe, which was used for the preparation of the specimens. Thus, the observed plane may vary with respect to the crack direction.

Fig. 4.41b shows an enlarged view of region I in Fig. 4.41a. The three cracks that initiated at the notch root surface are identified with numbers. In the presence of H_2, the crack is also tortuous; exhibiting high angle deflection points in the crack path. The upper blue arrow in Fig. 4.41b indicates a crack deflection at the ferrite-pearlite interface. The crack deflection enables crack nr. 1 to bypass the pearlite phase, resulting in it eventually merging with the leading crack, crack nr. 3. This finding once more highlights the tortuous effect of pearlite on the cracking behaviour. By examining the entire crack path in Fig. 4.41b and Fig. 4.41c, it can be concluded that the crack path is predominantly transgranular.

The projected crack length of the leading crack (nr. 3) is approximately 160 µm. This corresponds to the ductile transgranular region (see fracture surface analysis, Fig. 4.30a). Thus, the imaged crack

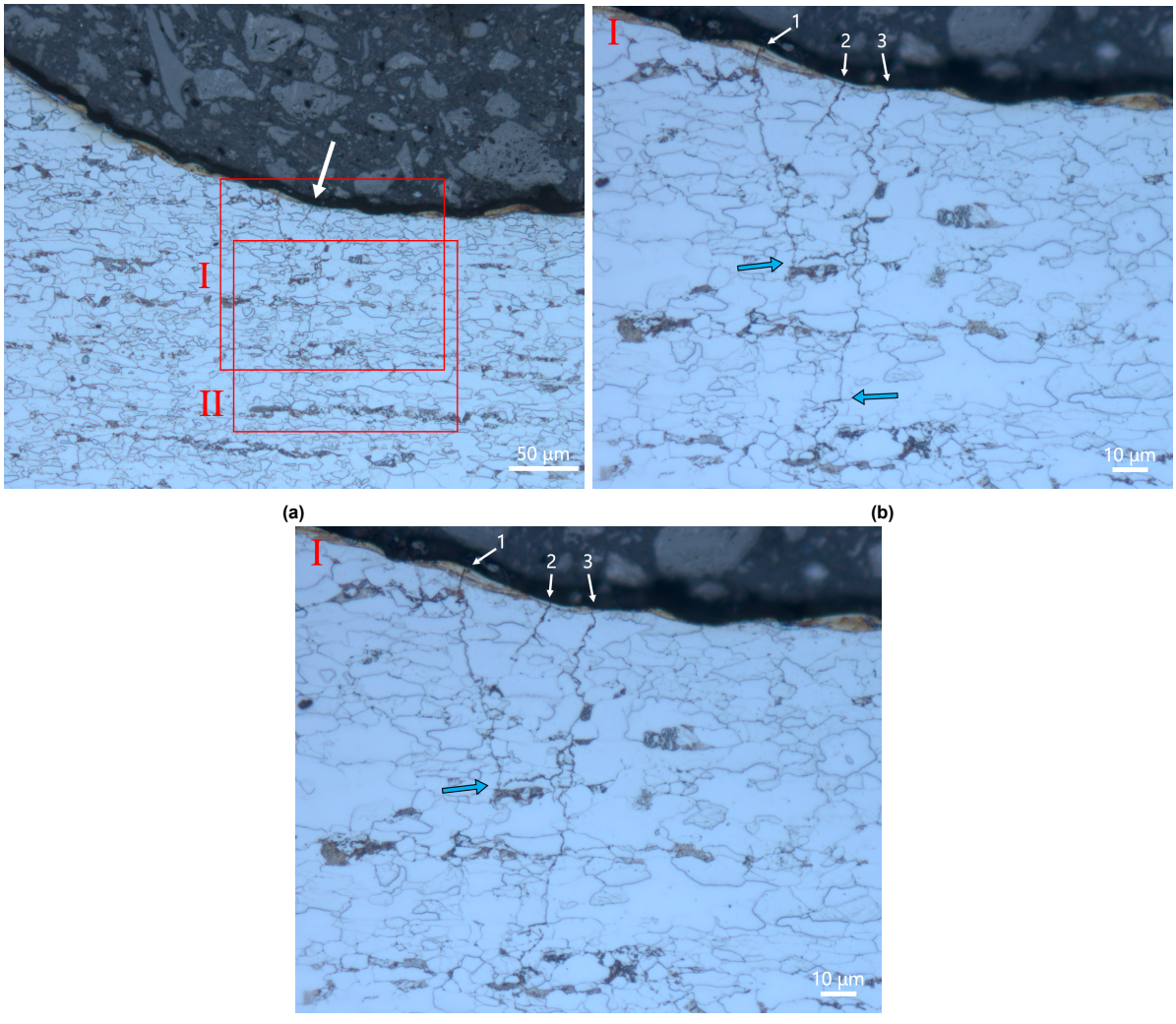

Figure 4.41: Crack path analysis on 150 barg H_2 BM specimen. a) an overview of the notch from which the initiated cracks can be identified. The white arrow indicates the dominant crack. b) Magnified view of region I (top square) in a). The three cracks that initiated at the surface are identified and numbered. c) Magnified view of region II (bottom square) in a). The blue arrow in b) indicates a high angle (nearly 90°) crack deflection point at the pearlite phase.

length of the 150 barg H_2 BM specimen is associated with a ΔK below the critical value related to the onset of HA-FCG. This explains the nearly identical crack path behaviour that is observed for the 150 barg N_2 and 150 barg H_2 BM specimens.

Weld Metal: 150 barg N_2

In order to shed light on the effect of 150 barg H_2, the results of 150 barg N_2 are explained first. The crack analysis results of WM N_2 are compiled in Fig. 4.42. An overview of the crack trajectory, and its initiation location with respect to the notch, is provided in Fig. 4.42a. The black spots on the root surface of the notch are caused by the run-off of etchant that remained between the steel surface and the resin surface. As can be seen, this specimen had one leading crack (white arrow). Its crack trajectory is separated into three regions, which are shown in distinct subfigures: I Fig.4.42b, II Fig. 4.42c and III Fig. 4.42d.

In Fig. 4.42b it can be observed that the crack exhibits tortuous events; it exhibits crack branches rejoining the main crack (red arrows). The rejoining of the branched crack is often referred to in literature as 'circular cracks' or 'metal crumble formation' [84, 82]. In Fig. 4.42c it can be seen that the crack strikes perpendicular to a prior austenite grain boundary (blue arrow), and is deflected therein. However, as can be seen from the area enclosed by the red lines, instead of bifurcation the crack can also take the metal crumb form. The high crack tortuosity was also evident from the extent of secondary cracking observed during the SEM fracture surface analysis (see section 4.4.4). It should be noted that a higher degree of crack tortuosity, e.g. due to crack branching or metal crumbling, is related to slower crack growth due to plasticity and roughness-induced crack closure.

Proceeding to observe Fig. 4.42d, it can be remarked that when the crack approaches parallel to the prior austenite grains, the preferred growth direction is to follow the interface of the prior austenite and acicular ferrite. This intergranular fracture, even in inert environments, is inherent to the microstructure (and composition) of the weld; cracking at prior austenite grain boundaries is often attributed to decohesion associated with impurity segregation [150]. Depending on the exact orientation of the prior austenite grains, the trajectory can be severely tortuous. This effect can be seen in the figure by the variation in growth direction, crack branching (blue arrow) and the presence of a metal crumb (red arrow). Note that the black spot in the figure is the result of etchant run-off from the crack.

Although intergranular features are observed at the interface of the prior austenite grain boundaries and acicular ferrite, the crack pathway is primarily transgranular. This statement is based on SEM analysis of the entire crack trajectory. To emphasise the transgranular crack path in acicular ferrite, the enclosed area in Fig. 4.42c was magnified using the SEM. The resulting SEM image is provided as Fig. 4.42e.

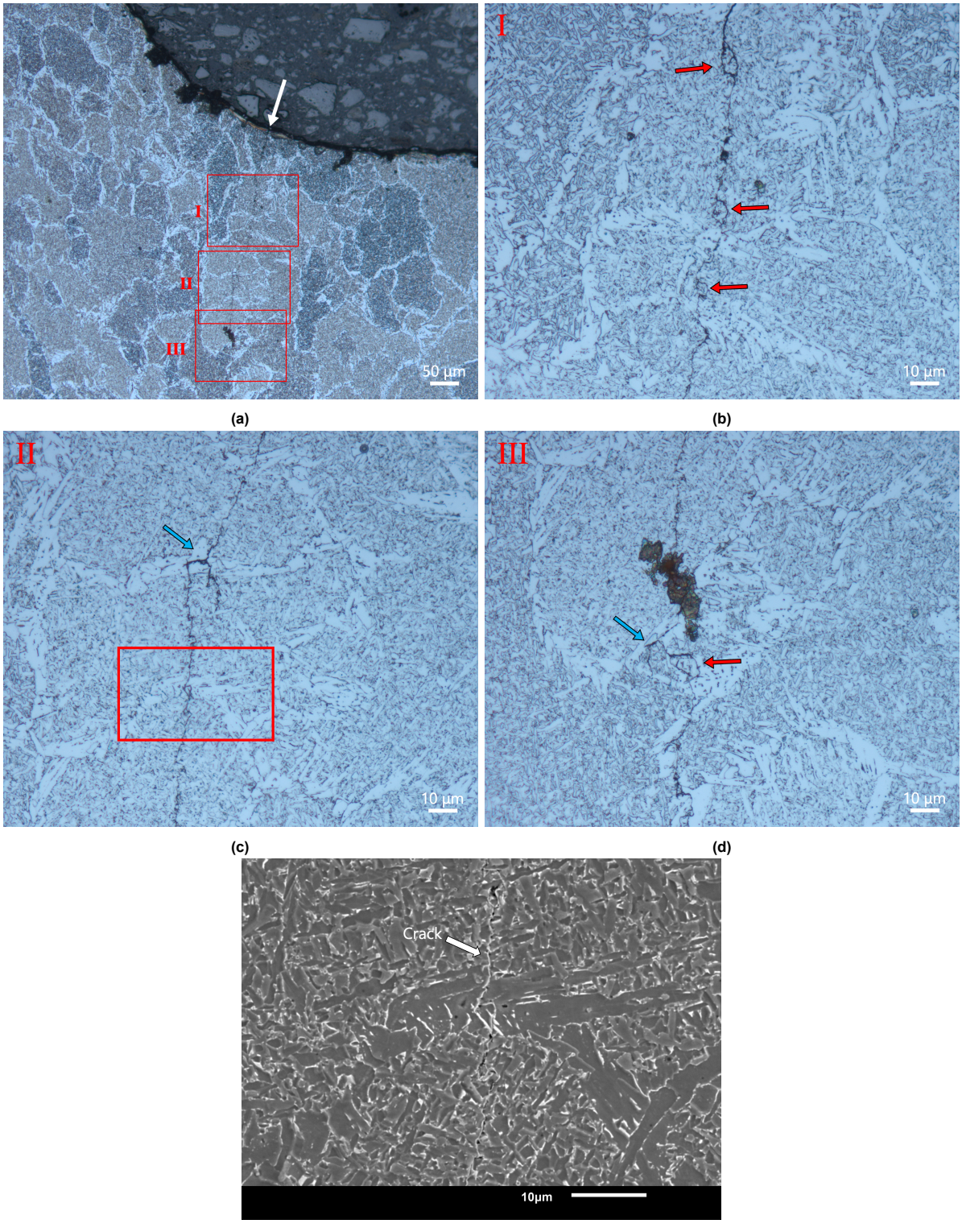

Figure 4.42: Crack path analysis on 150 barg N_2 WM specimen. a) an overview of the notch from which the leading crack can be identified (white arrow). Zoomed-in images are provided of the annotated regions in a): I b), II c), III d). The area enclosed by the red rectangle in c) is provided as a SEM image in e). In all subfigures the red and blue arrows indicate crack branching and metal crumbs, respectively.

Weld Metal: 150 barg H_2

The crack analysis results of WM H_2 are compiled in Fig. 4.43. An overview of the crack trajectory, and its initiation location (white arrow) with respect to the notch, is provided in Fig. 4.43a. In this macroscopic view, a distinguishing feature of the H_2 sample is directly apparent: the tortuosity of the crack has markedly reduced. Note that the reduced crack tortuosity was also evident from the absence of secondary cracking observed during the SEM fracture surface analysis (see section 4.4.4). It has even diminished to the extent that the projected crack shows an almost straight path.

Region I in Fig. 4.43a is visualised in Fig. 4.43b. From the examination of Fig. 4.43b, it can be concluded that the initial crack growth is transgranular and accompanied by metal crumb formation (red arrow). Throughout the entire crack trajectory, this was the only appearance of this feature. Fig. 4.43c provides a magnified view of region II in Fig. 4.43a. From comparing this figure to the 150 barg N_2 environment, it can be clearly seen that the degree of crack branching decreased, and secondly, if crack branching did occur, the branched crack ceased after a mere short crack growth. Examples of these features in the material are indicated with blue arrows.

The crack deflection significantly reduced compared to N_2. The angle of crack deflection in H_2 is more dependent on the microstructure. This is clearly shown in Fig. 4.43d, which is a higher magnification (SEM) image of the section indicated with a red arrow in Fig. 4.43a. From Fig. 4.43d, a distinguishing feature is evident: the fracture in acicular ferrite is a mixed-mode of transgranular (TG) and intergranular (IG) crack growth in H_2. Note that in the N_2 environment, the acicular ferrite microstructure predominantly fractured in a transgranular fashion. Intergranular fracture in N_2 solely manifested at the interface between prior austenite grain boundaries and acicular ferrite. One can see that the TG and IG behaviour in H_2 depends on the microstructural orientation. When the crack is perpendicular to the acicular ferrite grains, transgranular growth is preferred. This is particularly evident in the first notation of TG, when read from the top of the image plane. In other instances, the crack orientation can be accommodated by crack deflection, enabling an intergranular path to be followed. The fact that IG crack growth is observed for the H_2 tested specimen, emphasises that the deleterious role of hydrogen fatigue manifests in the grain boundaries. This finding follows the trend in literature [43, 80, 81]. The exact relationship between grain orientation and the onset of TG has not been established in this thesis.

From the fatigue results, it became evident that the 150 barg H_2 tested specimens experienced HA-FCG. The accelerated crack growth in the H_2 environment can be linked to its fracture behaviour. Lower crack deflection angles, shorter crack length of branched cracks, and a reduction in the number of metal crumbs have been found to increase the FCGR [84]. This finding from literature agrees well with the presented fracture behaviour of WM H_2 in this thesis. On the contrary, there exists a general tendency that high tortuosity of a crack path can provide enhanced fatigue performance [32]. Higher fatigue performance is related to crack tip stress-shielding induced by crack deflection and branching. In addition, the phenomena of plasticity- and roughness-induced crack closure play a profound role in the relation between crack tortuosity and fatigue performance. The uneven crack surfaces that during unloading do not match perfectly reduce the effective stress intensity at the crack tip.

The reduced tortuosity of the WM H_2 crack path evidences the HELP and HEDE mechanisms. The presence of hydrogen decreased the plastic zone wake at the crack tip, which in turn caused the continuous sharpening of the crack tip during each cycle. Crack tip sharpening in H_2 is directly related to a higher crack tip driving force when compared to the N_2 environment. The fact that H_2 causes the plastic zone at the crack tip to be decreased, also explains that the 'region' for crack tip branching (and its growth) significantly reduced. The increased sharpening of the crack tip could also be the result of AIDE. However, this study did not include the examination of the dislocation emission. Therefore, it could not be directly demonstrated whether AIDE occurred. The HEDE mechanism can be related to the fact that the hydrogen effect manifests in the grain boundaries. The HEDE mechanism proposes that the hydrogen atoms adsorbed at a crack tip or segregated at the grain boundaries weaken interatomic bonds and cause atomic decohesion. As shown with the crack path analysis, the decohesion manifested intergranularly. This finding suggests that the fine grains of the weld are susceptible to HA-FCG due to the hydrogen trapping in the grain boundaries. This is in line with the research of Masoumi et al. [118].

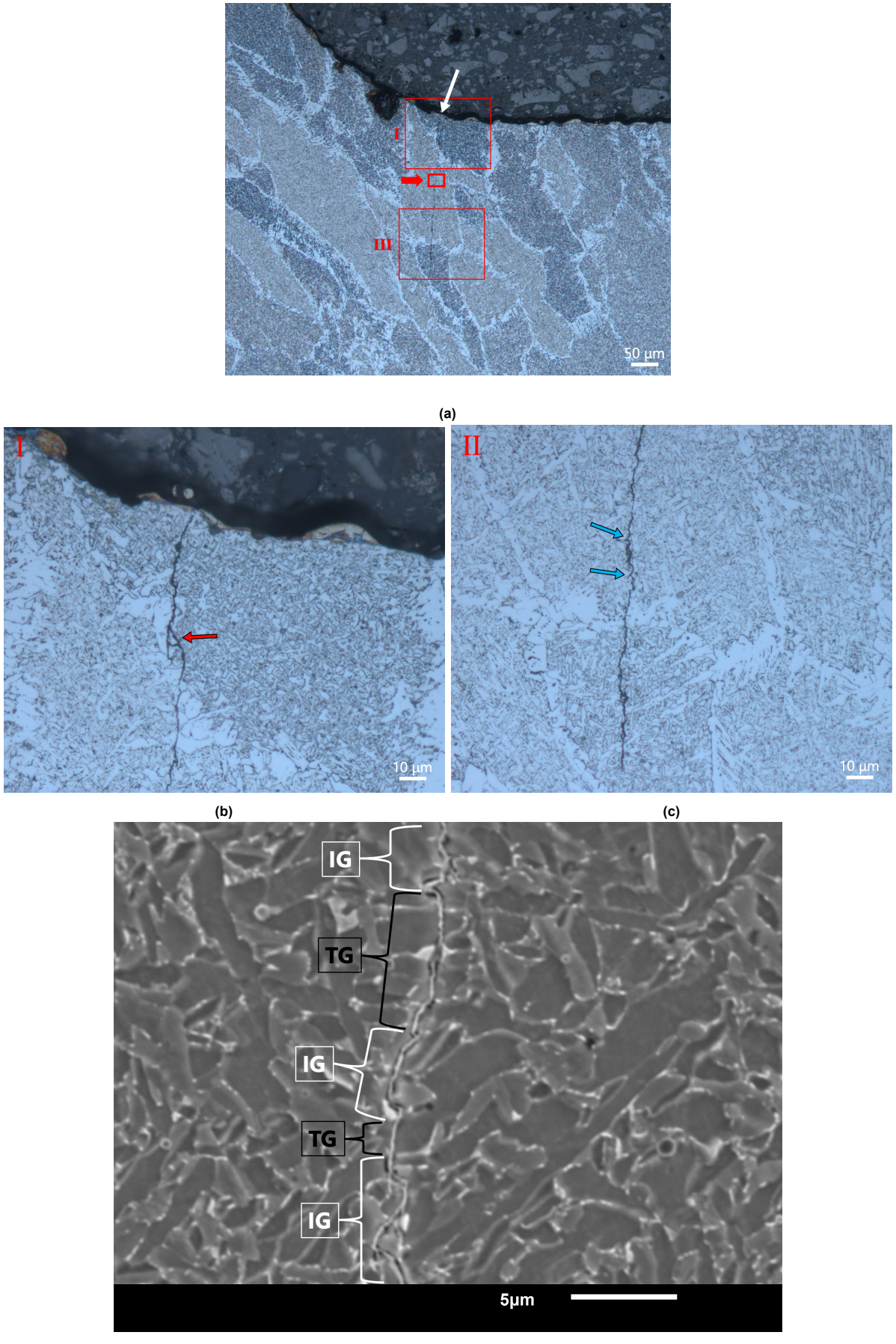

Figure 4.43: Crack path analysis on 150 barg H_2 WM specimen. a) an overview of the notch from which the initiated crack can be identified (white arrow). b) Magnified view of region I in a). c) Magnified view of region II in a). d) Zoom of the area indicated with a red arrow in a). This subfigure emphasises the intergranular and transgranular parts of the crack path. The red arrow, apart from the one in a), indicates a metal crumb. The blue arrows indicate crack branching.

4.4.6. Base Metal versus Non-Defected Weld Metal

The crack path analysis allowed for relating the microstructure to the potential drop data. From the presented analysis, it can be stated that fine grains are advantageous in inert environments and disadvantageous in hydrogen environments. Fine grains may inhibit crack growth in inert environments due to the large number of grain boundaries present. This is the reason why the WM showed superior fatigue resistance in the N_2 environment. The normalised results of the potential drop data indicated that the hydrogen effect was more deleterious on WM than on BM. The finer grains in the WM increases the grain boundary area per unit volume. This increased density of grain boundaries efficiently traps a high volume fraction of hydrogen, thereby promoting crack growth. The fact that 150 barg affected the N_{CI} of WM, and not that of BM, could be related to the microstructure. A study conducted by Marsh and Gerberich concluded that hydrogen fatigue cracks initiate at grain boundaries located at the specimen surface [116]. WM contains finer ferrite grain sizes, which means that the grain boundary area in the material is larger. Therefore, in terms of grain boundary density at the surface of the notch, there is a higher probability of cracking at the grain boundaries. This aspect found in the literature, together with the finding in this thesis that hydrogen fatigue manifests intergranularly, emphasises that it could be the locally trapped hydrogen in grain boundaries near the surface that governs the susceptibility to crack initiation.

In addition, it could be hypothesised that the ratio of the plastic zone size ahead of the crack tip versus the grain size itself, is higher for the WM. A higher ratio is related to a relatively shorter length to allow the effect of microstructural features (i.e. grain boundaries) to act as barriers that cannot accommodate the initial crack growth direction. In other words, compared to the BM, a shorter crack length is required for the plastic zone in front of the crack tip to exceed the grain size. This might explain that, unlike in BM, no clear dependency on crack size with respect to the onset of HA-FCG was found.

5

Conclusions and Recommendations

The final chapter of this thesis presents the conclusions that can be drawn from the research. Moreover, several recommendations for future research are formulated.

5.1. Conclusions

Based on the objectives formulated in Chapter 2, the following conclusions can be drawn:

1. To develop an *in-situ* gaseous hydrogen charging fatigue set-up, suitable for internally pressurised specimens with an internal circumferential notch (in the weld) and capable to monitor fatigue crack initiation and growth.

   An *in-situ* gaseous hydrogen charging fatigue set-up was developed. A sample geometry was designed with an internal circumferential notch that induces a stress concentration factor (K_t = 3.0) which mimics the worst case scenario for actual pipelines. Because of the interior notch in the hollow design, a test environment was created that represents pipeline defects under service conditions. Fatigue crack initiation and growth were successfully measured using a newly designed DCPD setup which probes the outer surface of the specimen. The crack initiation was successfully determined by investigating the number of cycles at which the voltage response deflected from the baseline voltage. The method to accurately determine crack initiation and growth was validated through a linear relationship between the (normalised) voltage response and crack surface area.

2. To quantify the effect of high-pressure hydrogen gas on the crack initiation in, and total fatigue lifetime of, X60 pipeline steel and its girth weld.

   The study showed no significant influence of hydrogen on the fatigue crack initiation in the base metal, which was explained by the elastic stress conditions of the fatigue cycles. Nevertheless, the presence of hydrogen reduced the total lifetime by 37% which was due to hydrogen assisted fatigue crack growth (HA-FCG); hydrogen accelerated the crack growth by a factor of 4. It should be noted that it is the stress intensity range (ΔK) that marks the onset of HA-FCG.

   In contrast, for the weld metal the presence of hydrogen reduced the resistance to crack initiation by 57%, as well as induced HA-FCG (accelerated growth by a factor of $\approx$ 8). The total reduction in fatigue life due to hydrogen was 68% for the weld. The effect of hydrogen on the reduction in lifetime was twice ($\approx$ 68/37) as high for the weld compared to the base metal. Thus, the deleterious effect of hydrogen on fatigue is more pronounced in the weld metal.

   No difference on the fatigue behaviour was observed between the gas pressures of 70 barg and 150 barg hydrogen. It is postulated that the maximum hydrogen saturation in the crack process zone was already reached at 70 barg.

3. To identify how the hydrogen gas (pressure) affects the fracture behaviour of the X60 base and weld metal, and what embrittlement mechanisms induced fatigue failure.

   The presence of hydrogen influenced the fracture behaviour in both materials:
   - The fracture path of the base metal in nitrogen was transgranular and ductile in nature. In hydrogen, similar fracture behaviour was observed prior to HA-FCG. However, after the onset of HA-FCG, the fracture surface transitioned to a mixed-mode transgranular and intergranular quasi-cleavage fracture.

   - The fracture path of the weld metal in N_2 was predominantly transgranular and ductile in nature. The exact crack path in this environment was found to be dependent on the grain orientation. Intergranular fracture manifested at the interface between acicular ferrite and prior austenite grain boundaries when the crack met parallel to the prior austenite grain boundaries. The weld metal in hydrogen exhibited mixed-mode transgranular and intergranular quasi-cleavage fracture. Transgranular fracture in the acicular ferrite microstructure was observed when the crack was oriented perpendicular to the grain. In other cases, intergranular fracture was observed. The intergranular fracture features can be attributed to the HEDE mechanism. The increased crack tip sharpening and reduced crack tortuosity shows that HELP was also a dominant mechanism. HELP reduced the roughness- and plasticity-induced closure of the crack surfaces, thereby giving rise to the characteristic accelerated crack growth in the hydrogen environment.

4. To evaluate the safety of hydrogen transport in X60 (welded) pipes, by assessing their resistance against HA-FCG.

   The weld metal showed superior fatigue resistance in nitrogen. It is however more susceptible to hydrogen fatigue compared to the base metal, as the normalised lifetime was reduced by a factor of 2. The fatigue life reduced by a factor of 3.1 for the weld metal in the hydrogen environments. The worst case scenario of hydrogen fatigue is for weld defects; at 150 barg hydrogen the crack growth rate increased to 11.6 for the specimens including macropores. The macropores were identified as spheroids and located on the notch root surface. The largest macropore, with a length and width of $\approx$ 1.0 mm, reduced the lifetime by 25% with respect to the smallest identified macropore, which had a length and width of $\approx$ 0.5 mm. On average, these macropores reduced the resistance to crack initiation by 92% compared to the non-porous specimen in nitrogen. The detrimental effect of weld defects should therefore not be overlooked in design and repurposing of gas pipelines.

From the research carried out in this thesis, it can be concluded that the suitability of assessment methods for the acceptance of defects needs to be reviewed. The work in this thesis unveiled that defects in commercial X60 pipeline steel can severely affect the hydrogen fatigue life. Considering the fact that this pipe was accepted for service life, emphasises the need for reliable identification of defects before pipes can be safely used for hydrogen transport. Moreover, the existing old pipeline network may have suffered geometrical anomalies (i.e. dents) or bending stresses (i.e. colliding marine structures against the pipe). As a result, the structure might comprise flaws that may not be acceptable for safe hydrogen transport. Identification of such flaws, along with the re-purpose of the associated pipe segments, could create (unexpected) economic obstacles during the transition to a hydrogen economy.

Additional conclusions can be drawn other than those of the research questions:

1. The fatigue behaviour was modelled to validate the fatigue test conditions. It was shown that, apart from the single plastic overload, the test conditions were performed in the elastic range. The fatigue in this research can therefore be considered as high cycle fatigue. High cycle fatigue

modelling is relevant for offshore pipelines; existing offshore pipelines mainly fail due to fatigue on 'free spans' experiencing elastic vibrations.

2. The crack growth rate in 150 barg nitrogen was higher than that observed in air. This is attributed to the internal gas that increases the stress triaxiality at the crack tip.

3. Upon release of the hydrogen gas, the HA-FCG effect is significantly decreased. After the gas has completely escaped, the HA-FCG effect remains present, albeit to a lesser extent, due to residual hydrogen diffusion to the crack tip. Shortly thereafter, the HA-FCG effect disappears as the hydrogen assisted crack growth is now dominated by the hydrogen diffusion rate to the crack tip.

4. The fatigue in the pressurised environments underwent three 'phases': i) pressurised phase, ii) non-pressurised phase due to gas escape, iii) fast fracture phase. The hydrogen effect was solely observed in phase i), which was observed from the DCPD results and confirmed with SEM fractography as the disappearance of striations on the fracture surface after phase i).

5.2. Recommendations

The recommendations for further investigations that would assist in this research field, and in its applications, are as follows:

- The effect of fatigue frequency should be evaluated. In this work, fatigue testing was performed at 8 Hz. However, on- and offshore operating pipelines experience pressure fluctuations of ≤ 1 Hz during service life. Our results remain valid because there exists a general trend in literature that varying the frequency from 0.1 - 10 Hz does not affect the HA-FCG. However, according to Yamabe et al., the onset of HA-FCG occurs when $(P_{H2} \times f)^{1/2} \geq 0.1$. In this formula, P_{H2} and f denote the hydrogen (partial) pressure and frequency, respectively. A value greater than 0.1, is associated with a sufficiently steep hydrogen concentration at the crack tip to induce HA-FCG. Applying the fatigue test conditions of this thesis to this formula gives: $(15 \times 8)^{1/2} = 10.95$, which is clearly above the threshold. From this formula, it can be deduced that at a pressure of 150 barg, the effect of hydrogen would be maintained for frequencies higher than 6.67×10^{-4} Hz. It would be interesting to validate this parameter by performing experiments at different frequencies and to determine what (embrittlement) mechanisms are at play. The industry would benefit from such an approach, as the limits for safe operating parameters in the transport of hydrogen could be defined more precisely.

- Tests should be carried out with different gas mixtures (of hydrogen and air). There is a general tendency in literature that oxygen impurities can inhibit hydrogen-induced fatigue. However, studies with gas mixtures do not consider weld defects. Performing fatigue tests at different gas mixtures could establish whether crack initiation and growth of weld defects are affected. This could reveal whether the gas mixture can counteract the normally adverse effects of weld defects on hydrogen fatigue, thereby enhancing the safety of hydrogen transport.

- It is recommended to investigate the effect of different microstructures (orientations with respect to microstructure banding) and/or grain morphology. Regarding the weld metal, it is suggested to study material welded at different weld parameters. Such an approach allows the effect of hydrogen on the microstructure of the weld to be further elaborated. For example, it can be determined whether grain size and orientation can be improved in terms of resistance to hydrogen fatigue. Regarding the base metal, it could be useful to perform experiments with respect to different rolling directions of the pipe (i.e. position the notch in different directions). This could determine the worst case scenario of hydrogen fatigue for the base metal.

- Different hydrogen pressures should be tested, accompanied by hydrogen concentrations measurements. This thesis did not directly validate the hydrogen concentration in the material. However, as became evident, at the pressures tested there was no difference in hydrogen fatigue.

This research could be further improved by determining the critical hydrogen concentration at the crack process zone, and by relating how it is affected by the applied gas pressure.

- The effects of defects should be further studied. The macropores in this work were located on the notch root surface. Additional data is needed regarding the effect of their size and location on hydrogen fatigue. An assessment of whether those defects would be identified by non-destructive testing techniques (i.e. ultrasonic testing) should be included. The feasibility of repurposing hydrogen pipelines would be more reliably assessed through such an approach.

Two additional recommendations can be formulated regarding the fatigue set-up:

- The underlying reason for the asymmetry must be looked at more critically. In this study, it was observed that the fracture surfaces exhibited asymmetric crack growth. Several approaches were taken to improve the alignment of the system; however, no noticeable differences were observed under fatigue tests. However, using the same alignment for tensile testing led to symmetrical failure. It is well known that crack initiation occurs at the weakest link in the material, so the influence of local variations in the thickness of the processed electrical discharge machining layer could have changed the cracking behaviour with respect to symmetry. From an application point of view; however, the presented results are more valuable than in the case of being symmetric. For instance, fatigue failure of operating pipelines also occurs asymmetrically. Nevertheless, by finding the underlying reason for the asymmetric fracture, the results of the newly introduced specimen design can be more readily compared with literature studies dealing with symmetric crack growth.

- The crack front could be precisely located by using DCPD system equipped with multiple output channels. The possibility to read off the voltages on individual probes ultimately makes it possible to localise the crack front. In this way, the crack growth behaviour can be assessed more precisely.

References

[1] Elektriska Svetsning-Aktiebolaget (ESAB). *Weld 70S-6*. Specification Sheet. 2018.

[2] Daniel P Abraham and Carl J Altstetter. “Hydrogen-enhanced localization of plasticity in an austenitic stainless steel”. In: *Metallurgical and Materials transactions A* 26.11 (1995), pp. 2859–2871.

[3] BR Alamri and AR Alamri. “Technical review of energy storage technologies when integrated with intermittent renewable energy”. In: *2009 International Conference on Sustainable Power Generation and Supply*. IEEE. 2009, pp. 1–5.

[4] Antonio Alvaro et al. “Hydrogen enhanced fatigue crack growth rates in a ferritic Fe-3 wt% Si alloy and a X70 pipeline steel”. In: *Engineering Fracture Mechanics* 219 (2019), p. 106641.

[5] Robert L Amaro, Elizabeth S Drexler, and Andrew J Slifka. “Fatigue crack growth modeling of pipeline steels in high pressure gaseous hydrogen”. In: *International journal of fatigue* 62 (2014), pp. 249–257.

[6] Robert L Amaro et al. “Development of a Model for Hydrogen-Assisted Fatigue Crack Growth of Pipeline Steel”. In: *Journal of Pressure Vessel Technology* 140.2 (2018).

[7] Robert L Amaro et al. “Modeling the fatigue crack growth of X100 pipeline steel in gaseous hydrogen”. In: *International Journal of Fatigue* 59 (2014), pp. 262–271.

[8] Teng An et al. “Influence of hydrogen pressure on fatigue properties of X80 pipeline steel”. In: *International Journal of Hydrogen Energy* 42.23 (2017), pp. 15669–15678.

[9] Teng An et al. “Synergistic action of hydrogen and stress concentration on the fatigue properties of X80 pipeline steel”. In: *Materials Science and Engineering: A* 700 (2017), pp. 321–330.

[10] Teng An et al. “Synergistic action of hydrogen gas and weld defects on fracture toughness of X80 pipeline steel”. In: *International Journal of Fatigue* 120 (2019), pp. 23–32.

[11] Ted L Anderson. *Fracture mechanics: fundamentals and applications*. CRC press, 2017, pp. 478–487.

[12] American Petroleum Institute. *API 5L: Specification for Line Pipe*. 43th edition. 2004.

[13] Nikolai Arnaudov. *Micromechanical simulation of fatigue crack initiation under hydrogen influence*. Stuttgart: Materialprüfungsanstalt (MPA), Universität Stuttgart, 2021.

[14] Michael F Ashby and D Cebon. *Materials selection in mechanical design*. 4th ed. Butterworth-Heinemann, 2010, pp. 548–549.

[15] ASTM. “E8/E8M-21, Standard Test Methods for Tension Testing of Metallic Materials”. In: *ASTM International* (2021).

[16] ASTM. “G142-98, Standard Test Method for Determination of Susceptibility of Metals to Embrittlement in Hydrogen Containing Environments at High Pressure, High Temperature, or Both”. In: *ASTM International* (2016).

[17] Ming Au. “High temperature electrochemical charging of hydrogen and its application in hydrogen embrittlement research”. In: *Materials Science and Engineering: A* 454 (2007), pp. 564–569.

[18] Pierre-Louis Auvret et al. “Statistical Approach of Stress Concentration Factor (SCF) Within Pipeline Girth Welds”. In: *ASME 2014 Pressure Vessels and Piping Conference*. American Society of Mechanical Engineers Digital Collection. 2014.

[19] Michael Ball and Martin Wietschel. “The future of hydrogen–opportunities and challenges”. In: *International journal of hydrogen energy* 34.2 (2009), pp. 615–627.

[20] Jürgen Bär. “Crack Detection and Crack Length Measurement with the DC Potential Drop Method–Possibilities, Challenges and New Developments”. In: *Applied Sciences* 10.23 (2020), p. 8559.

[21] Afrooz Barnoush and Horst Vehoff. “Electrochemical nanoindentation: A new approach to probe hydrogen/deformation interaction”. In: *Scripta Materialia* 55.2 (2006), pp. 195–198.

[22] O Barrera et al. “Understanding and mitigating hydrogen embrittlement of steels: a review of experimental, modelling and design progress from atomistic to continuum”. In: *Journal of materials science* 53.9 (2018), pp. 6251–6290.

[23] Claude Bathias. “There is no infinite fatigue life in metallic materials”. In: *Fatigue & fracture of engineering materials & structures (Print)* 22.7 (1999), pp. 559–565.

[24] Cedric D Beachem. “A new model for hydrogen-assisted cracking (hydrogen “embrittlement”)”. In: *Metallurgical and Materials Transactions B* 3.2 (1972), pp. 441–455.

[25] T Bellahcene et al. “Effect of hydrogen on mechanical properties of pipeline API 5L X70 steel”. In: *Applied Mechanics and Materials*. Vol. 146. Trans Tech Publ. 2012, pp. 213–225.

[26] I Melvin Bernstein and Gerald M Pressouyre. *The Role of Traps in the Microstructural Control of Hydrogen Embrittlement of Steels.* Tech. rep. Carnegie Melon Univ Pittsburgh PA Dept. of Metallurgical Engineering and Materials Science, 1984.

[27] Harshad Kumar Dharamshi Hansraj Bhadeshia. “Prevention of hydrogen embrittlement in steels”. In: *ISIJ international* 56.1 (2016), pp. 24–36.

[28] ASME Boiler and Pressure Vessel Code. *section VIII, Division 3, KD-10*. 2007.

[29] Tim Boot. “Assessing the susceptibility of existing pipelines to Hydrogen Embrittlement”. MA thesis. Technical University Delft, 2020.

[30] Tim Boot et al. “In-Situ Hollow Sample Setup Design for Mechanical Characterisation of Gaseous Hydrogen Embrittlement of Pipeline Steels and Welds”. In: *Metals* 11.8 (2021), p. 1242.

[31] Laurent Briottet et al. “Fatigue crack initiation and growth in a CrMo steel under hydrogen pressure”. In: *International Journal of Hydrogen Energy* 40.47 (2015), pp. 17021–17030.

[32] Thao Phuong Bui et al. “Contributions of grain size and crystal orientation to fatigue crack deflection and branching behavior in low carbon steel plates”. In: *ISIJ International* 61.1 (2021), pp. 424–433.

[33] Flake C Campbell. *Elements of metallurgy and engineering alloys*. ASM International, 2008, p. 252.

[34] Bo Cao et al. “Development of impact small punch test for investigating energy absorption”. In: *International Journal of Mechanical Sciences* 208 (2021), p. 106675.

[35] J Capelle, J Gilgert, and G Pluvinage. “Hydrogen effect on fatigue and fracture of pipe steels”. In: *Ecole Nationale d’Ingénieurs de Metz, Metz, France* (2009).

[36] Julien Capelle et al. “Sensitivity of pipelines with steel API X52 to hydrogen embrittlement”. In: *International journal of hydrogen energy* 33.24 (2008), pp. 7630–7641.

[37] J Carlsson. “Fracture mechanics for cracks in weldments”. In: *Fracture 84*. Elsevier, 1984, pp. 751–762.

[38] I Černỳ. “The use of DCPD method for measurement of growth of cracks in large components at normal and elevated temperatures”. In: *Engineering Fracture Mechanics* 71.4-6 (2004), pp. 837–848.

[39] J.P. Chateau, D. Delafosse, and T. Magnin. “Numerical simulations of hydrogen–dislocation interactions in fcc stainless steels. Part I: hydrogen–dislocation interactions in bulk crystals”. In: *Acta Materialia* 50.6 (2002), pp. 1507–1522. ISSN: 1359-6454.

[40] CS Chiou, JR Yang, and CY Huang. “The effect of prior compressive deformation of austenite on toughness property in an ultra-low carbon bainitic steel”. In: *Materials chemistry and physics* 69.1-3 (2001), pp. 113–124.

[41] Klaus Christmann. “Some general aspects of hydrogen chemisorption on metal surfaces”. In: *Progress in surface science* 48.1-4 (1995), pp. 15–26.

[42] Henry Cialone and John Holbrook. “Sensitivity of steels to degradation in gaseous hydrogen”. In: *Hydrogen embrittlement: prevention and control*. ASTM International, 1988.

[43] HJ Cialone and JH Holbrook. “Microstructural and fractographic features of hydrogen-accelerated fatigue-crack growth in steels”. In: *Welding, Failure Analysis, and Metallography* (1985), pp. 407–422.

[44] James A Clum. “The role of hydrogen in dislocation generation in iron alloys”. In: *Scripta Metallurgica* 9.1 (1975), pp. 51–58.

[45] Mohsen Dadfarnia et al. “Recent advances on hydrogen embrittlement of structural materials”. In: *International Journal of Fracture* 196.1-2 (2015), pp. 223–243.

[46] Geogre E Dieter. “Mechanical Metallurgy, Mc Graw Hill Book”. In: *New York (1988)* (1986).

[47] A Díaz, JM Alegre, and II Cuesta. “Numerical simulation of hydrogen embrittlement and local triaxiality effects in notched specimens”. In: *Theoretical and Applied Fracture Mechanics* 90 (2017), pp. 294–302.

[48] MB Djukic et al. “Hydrogen embrittlement of low carbon structural steel”. In: *Procedia Materials Science* 3 (2014), pp. 1167–1172.

[49] Milos B Djukic et al. “Hydrogen damage of steels: A case study and hydrogen embrittlement model”. In: *Engineering Failure Analysis* 58 (2015), pp. 485–498.

[50] Milos B Djukic et al. “The synergistic action and interplay of hydrogen embrittlement mechanisms in steels and iron: Localized plasticity and decohesion”. In: *Engineering Fracture Mechanics* 216 (2019), p. 106528.

[51] Ihor Dmytrakh, Andriy Syrotyuk, and Rostyslav Leshchak. “Specific effects of hydrogen concentration on resistance to fracture of ferrite-pearlitic pipeline steels”. In: *Procedia Structural Integrity* 16 (2019), pp. 113–120.

[52] GL DNV. “RP-C203 Fatigue design of offshore steel structures”. In: *Recomm Pract DNVRPC203* 126 (2005).

[53] Elizabeth S Drexler et al. “Fatigue crack growth rates of API X70 pipeline steel in a pressurized hydrogen gas environment”. In: *Fatigue & Fracture of Engineering Materials & Structures* 37.5 (2014), pp. 517–525.

[54] Yaojun A Du et al. “First-principles study on the interaction of H interstitials with grain boundaries in α-and γ-Fe”. In: *Physical Review B* 84.14 (2011), p. 144121.

[55] EN. “ISO 11782-1, Corrosion of metals and alloys - Corrosion fatigue testing - Part 1: Cycles to failure testing.” In: *International Organization for Standardization* (2008).

[56] European Union Agency for the Cooperation of Energy Regulators (ACER). *Transporting Pure Hydrogen by Repurposing Existing Gas Infrastructure: Overview of existing studies and reflections on the conditions for repurposing*. 2021. URL: https://acer.europa.eu/Official_documents/Acts_of_the_Agency/Publication/Transporting%5C%20Pure%5C%20Hydrogen%5C%20by%5C%20Repurposing%5C%20Existing%5C%20Gas%5C%20Infrastructure_Overview%5C%20of%5C%20studies.pdf.

[57] S Felber. “Welding of the high grade pipeline-steel X80 and description of different pipeline-projects”. In: *Welding in the World* 52.5 (2008), pp. 19–41.

[58] Rui Feng et al. “The Influence of Abnormal Segregation Band on Mechanical Properties of Hot Rolled Ferrite/Pearlite Steel Plate”. In: *Materials Sciences and Applications* 9.01 (2018), p. 81.

[59] Rebeca Fernández-Sousa, Covadonga Betegón, and Emilio Martínez-Pañeda. “Analysis of the influence of microstructural traps on hydrogen assisted fatigue”. In: *Acta Materialia* 199 (2020), pp. 253–263.

[60] KO Findley, MK O’Brien, and H Nako. “Critical Assessment 17: Mechanisms of hydrogen induced cracking in pipeline steels”. In: *Materials Science and Technology* 31.14 (2015), pp. 1673–1680.

[61] PJE Forsyth. “A two stage process of fatigue crack growth. vol. 1, 76–94”. In: *The college of aeronautics, Cranfield* (1961).

[62] Olav Fyrileiv et al. “Deepwater pipelines–status, challenges and future trends”. In: *Proceedings of the institution of mechanical engineers, Part M: Journal of engineering for the maritime environment* 227.4 (2013), pp. 381–395.

[63] Richard P Gangloff and Brian P Somerday. *Gaseous hydrogen embrittlement of materials in energy technologies: mechanisms, modelling and future developments*. Elsevier, 2012.

[64] Supriyo Ganguly, Jibrin Sule, and Mustapha Y Yakubu. “Stress engineering of multi-pass welds of structural steel to enhance structural integrity”. In: *Journal of Materials Engineering and Performance* 25.8 (2016), pp. 3238–3244.

[65] WM Garrison. “Steels: classifications”. In: *Encyclopedia of materials: science and technology* (2011), pp. 8840–8843.

[66] Gasunie. *Hydrogen network Netherlands*. 2022. URL: https://www.gasunie.nl/en/projects/hydrogen-network-netherlands (visited on 06/29/2022).

[67] Anastasios G Gavras, Brendan F Chenelle, and Diana A Lados. “Effects of microstructure on the fatigue crack growth behavior of light metals and design considerations”. In: *Matéria (Rio de Janeiro)* 15 (2010), pp. 319–329.

[68] Leonardo Barbosa Godefroid, Betânia Mendes Sena, and Vicente Braz da Trindade Filho. “Evaluation of microstructure and mechanical properties of seamless steel pipes API 5L type obtained by different processes of heat treatments”. In: *Materials Research* 20.2 (2017), pp. 514–522.

[69] Antonio Gorni and José Dolabela da Silveira. “Accelerated cooling of steel plates: the time has come”. In: *Quenching and Cooling, Residual Stress and Distortion Control*. ASTM International, 2010.

[70] Hans Jürgen Grabke, Frank Gehrmann, and Ernst Riecke. “Hydrogen in microalloyed steels”. In: *steel research* 72.5-6 (2001), pp. 225–235.

[71] J Malcolm Gray and Fulvio Siciliano. “High strength microalloyed linepipe: half a century of evolution”. In: *Microalloyed Steel Institute* (2009), pp. 20–45.

[72] Guidehouse. *European Hydrogen Backbone: a european hydrogen infrastructure vision covering 28 countries.* 2022. URL: https://gasforclimate2050.eu/wp-content/uploads/2022/04/EHB-A-European-hydrogen-infrastructure-vision-covering-28-countries.pdf (visited on 07/15/2022).

[73] Hung M Ha, Jia He Ai, and John R Scully. “Effects of prior cold work on hydrogen trapping and diffusion in API X70 line pipe steel during electrochemical charging”. In: *Corrosion* 70.2 (2014), pp. 166–184.

[74] D Hardie, EA Charles, and AH Lopez. “Hydrogen embrittlement of high strength pipeline steels”. In: *Corrosion Science* 48.12 (2006), pp. 4378–4385.

[75] Yang He et al. “Diffusion coefficient of hydrogen interstitial atom in -Fe, -Fe and ε-Fe crystals by first-principle calculations”. In: *International Journal of Hydrogen Energy* 42.44 (2017), pp. 27438–27445.

[76] G Henry and D Horstmann. *De Ferri Metallographia 5: Fractography and Microfractography*. 1979.

[77] MD Herynk et al. “Effects of the UOE/UOC pipe manufacturing processes on pipe collapse pressure”. In: *International Journal of Mechanical Sciences* 49.5 (2007), pp. 533–553.

[78] John P Hirth. “Effects of hydrogen on the properties of iron and steel”. In: *Metallurgical Transactions A* 11.6 (1980), pp. 861–890.

[79] Jui-Ting Ho and Ge-Ping Yu. “Effect of hydrogen on the fatigue behavior of alloy 600 at cathodic potential”. In: *Scripta metallurgica et materialia* 32.11 (1995).

[80] JH Holbrook et al. *Effect of hydrogen on low-cycle-fatigue life and subcritical crack growth in pipeline steels*. Tech. rep. Battelle Columbus Labs., OH (USA), 1982.

[81] JH Holbrook et al. “Hydrogen degradation of pipeline steels (Final Report)”. In: (1986).

[82] Yunfeng Hu et al. “Investigation on the Fatigue Crack Propagation Behavior of L360MS Pipeline Steel Welded Joints with Inconel 625 Weld Metal”. In: *Transactions of the Indian Institute of Metals* 73.9 (2020), pp. 2387–2402.

[83] K Hussain and RR De Los Rios. “Microstructural effect on tensile and fatigue behaviour of C–Mn steel”. In: *Journal of materials science* 32.13 (1997), pp. 3565–3569.

[84] Victor Igwemezie, Ali Mehmanparast, and Feargal Brennan. “The influence of microstructure on the fatigue crack growth rate in marine steels in the Paris Region”. In: *Fatigue & Fracture of Engineering Materials & Structures* 43.10 (2020), pp. 2416–2440.

[85] ASTM International. *ASTM EE92-17: Standard Test Methods for Vickers Hardness and Knoop Hardness of Metallic Materials*. Tech. rep. 2017.

[86] JJ Irani et al. “Strong tough structural steels”. In: *ISI Special Rep* 104 (1967), p. 135.

[87] Tonye Alaso Jack et al. “Investigation of the hydrogen induced cracking behaviour of API 5L X65 pipeline steel”. In: *International Journal of Hydrogen Energy* 45.35 (2020), pp. 17671–17684.

[88] Urszula Janus-Galkiewicz and Jaroslaw Galkiewicz. “Analysis of the Failure Process of Elements Subjected to Monotonic and Cyclic Loading Using the Wierzbicki–Bai Model”. In: *Materials* 14.21 (2021), p. 6265.

[89] DE Jiang and Emily A Carter. “Diffusion of interstitial hydrogen into and through bcc Fe from first principles”. In: *Physical Review B* 70.6 (2004), p. 064102.

[90] B Kagay et al. “Hydrogen Effects on Fatigue Life of Welded Austenitic Stainless Steels Evaluated With Hole-Drilled Tubular Specimens”. In: *Pressure Vessels and Piping Conference*. Vol. 83860. American Society of Mechanical Engineers. 2020, V006T06A090.

[91] Ivaylo H Katzarov and Anthony T Paxton. “Hydrogen embrittlement II. Analysis of hydrogen-enhanced decohesion across (111) planes in α-Fe”. In: *Physical Review Materials* 1.3 (2017), p. 033603.

[92] K Kiuchi and RB McLellan. “The solubility and diffusivity of hydrogen in well-annealed and deformed iron”. In: *Perspectives in Hydrogen in Metals*. Elsevier, 1986, pp. 29–52.

[93] Ryosuke Komoda et al. “Inhibitory effect of oxygen on hydrogen-induced fracture of A333 pipe steel”. In: *Fatigue & Fracture of Engineering Materials & Structures* 42.6 (2019), pp. 1387–1401.

[94] Akhmad A Korda, Y Miyashita, and Y Mutoh. “The role of cyclic plastic zone size on fatigue crack growth behavior in high strength steels”. In: *AIP Conference Proceedings*. Vol. 1677. 1. AIP Publishing LLC. 2015, p. 070013.

[95] Akhmad A Korda et al. “In situ observation of fatigue crack retardation in banded ferrite–pearlite microstructure due to crack branching”. In: *Scripta Materialia* 54.11 (2006), pp. 1835–1840.

[96] George Krauss. “Steels: Processing”. In: *Structure, and Performance* 2 (2005), pp. 30–31.

[97] George Krauss. “Steels: processing, structure, and performance”. In: ASM International, 2015, p. 184.

[98] Campbell Laird. “The influence of metallurgical structure on the mechanisms of fatigue crack propagation”. In: *Fatigue crack propagation*. ASTM International, 1967.

[99] Woei-Shyan Lee, Chi-Feng Lin, and Tsung-Ju Liu. “Strain rate dependence of impact properties of sintered 316L stainless steel”. In: *Journal of Nuclear Materials* 359.3 (2006), pp. 247–257.

[100] Pierre-Alexandre Legait. “Formation and distribution of porosity in Al-Si welds”. PhD thesis. Worcester polytechnic institute, 2006.

[101] W Leighty et al. “Compressorless hydrogen transmission pipelines deliver large-scale stranded renewable energy at competitive cost”. In: *Proceedings of the 16th World Hydrogen Energy Conference, Lyon, FR, June*. Vol. 6. Citeseer. 2006.

[102] SHI Leishi, Takeshi IWAMOTO, and Shinya HASHIMOTO. “An experimental study on rate sensitivity of J-integral and its evaluation by small punch test for TRIP steel”. In: *Engineering Transactions* 61.2 (2013), pp. 119–136.

[103] Daoming Li, Richard P Gangloff, and John R Scully. “Hydrogen trap states in ultrahigh-strength AERMET 100 steel”. In: *Metallurgical and materials transactions A* 35.3 (2004), pp. 849–864.

[104] JCM Li, RA Oriani, and LS Darken. “The thermodynamics of stressed solids”. In: *Zeitschrift für Physikalische Chemie* 49.3_5 (1966), pp. 271–290.

[105] Pengfei Li et al. “Effect of post-heat treatment on residual stress and tensile strength of hybrid additive and subtractive manufacturing”. In: *The International Journal of Advanced Manufacturing Technology* 103.5 (2019), pp. 2579–2592.

[106] SHOU YING LI, WEI MIN ZHAO, and YONG WANG. “Hydrogen Permeation Property and Hydrogen Embrittlement Susceptibility of Pipeline Steel with Oxide Film”. In: *DEStech Transactions on Environment, Energy and Earth Sciences* peems (2019).

[107] Xinfeng Li et al. “Review of hydrogen embrittlement in metals: Hydrogen diffusion, hydrogen characterization, hydrogen embrittlement mechanism and prevention”. In: *Acta Metallurgica Sinica (English Letters)* 33.6 (2020), pp. 759–773.

[108] Qian Liu and Andrej Atrens. “A critical review of the influence of hydrogen on the mechanical properties of medium-strength steels”. In: *Corrosion Reviews* 31.3-6 (2013), pp. 85–103.

[109] E Lunarska, Y Ososkov, and Y Jagodzinsky. “Correlation between critical hydrogen concentration and hydrogen damage of pipeline steel”. In: *International journal of hydrogen energy* 22.2-3 (1997), pp. 279–284.

[110] Sander P. Lynch. “Mechanisms of Environment Sensitive Fracture of Materials, F.P. Ford, and A.R.C. Westwood”. In: (1977), pp. 201–212.

[111] SP Lynch. “Environmentally assisted cracking: overview of evidence for an adsorption-induced localised-slip process”. In: *Acta Metallurgica* 36.10 (1988), pp. 2639–2661.

[112] SP Lynch. “Mechanisms of hydrogen assisted cracking–a review”. In: *Hydrogen effects on material behaviour and corrosion deformation interactions* (2003), pp. 449–466.

[113] Stan P Lynch. “Hydrogen embrittlement (HE) phenomena and mechanisms”. In: *Stress corrosion cracking: theory and practice*. Elsevier, 2011, pp. 90–130.

[114] Philippe Marcus. *Corrosion mechanisms in theory and practice*. CRC press, 2011, p. 145.

[115] I Maroef et al. “Hydrogen trapping in ferritic steel weld metal”. In: *International Materials Reviews* 47.4 (2002), pp. 191–223.

[116] PG Marsh and WW Gerberich. “Influence of microstructure and texture on fatigue crack initiation in HSLA steel in hydrogen and nitrogen atmospheres”. In: *First International Conference on Microstructures and Mechanical Properties of Aging Materials*. Publ by Minerals, Metals & Materials Soc (TMS). 1993, pp. 287–292.

[117] ML Martin, IM Robertson, and P Sofronis. “Interpreting hydrogen-induced fracture surfaces in terms of deformation processes: A new approach”. In: *Acta Materialia* 59.9 (2011), pp. 3680–3687.

[118] Mohammad Masoumi et al. “Texture and grain boundary study in high strength Fe-18Ni-Co steel related to hydrogen embrittlement”. In: *Materials & Design* 91 (2016), pp. 90–97.

[119] Saburo Matsuoka, Junichiro Yamabe, and Hisao Matsunaga. “Criteria for determining hydrogen compatibility and the mechanisms for hydrogen-assisted, surface crack growth in austenitic stainless steels”. In: *Engineering Fracture Mechanics* 153 (2016), pp. 103–127.

[120] Giovanni Meneghetti et al. “Notched Ti-6Al-4V titanium bars under multiaxial fatigue: Synthesis of crack initiation life based on the averaged strain energy density”. In: *Theoretical and Applied Fracture Mechanics* 96 (2018), pp. 509–533.

[121] E Merson et al. “Quantitative characterization of cleavage and hydrogen-assisted quasi-cleavage fracture surfaces with the use of confocal laser scanning microscopy”. In: *Materials Science and Engineering: A* 665 (2016), pp. 35–46.

[122] MA Mohtadi-Bonab, M Eskandari, and JA Szpunar. “Texture, local misorientation, grain boundary and recrystallization fraction in pipeline steels related to hydrogen induced cracking”. In: *Materials Science and Engineering: A* 620 (2015), pp. 97–106.

[123] MA Mohtadi-Bonab, JA Szpunar, and SS Razavi-Tousi. “A comparative study of hydrogen induced cracking behavior in API 5L X60 and X70 pipeline steels”. In: *Engineering Failure Analysis* 33 (2013), pp. 163–175.

[124] WL Morris. “A comparison of microcrack closure load development for stage I and II cracking events for Al 7075-T651”. In: *Metallurgical Transactions A* 8.7 (1977), pp. 1087–1093.

[125] H Mughrabi. “On the life-controlling microstructural fatigue mechanisms in ductile metals and alloys in the gigacycle regime”. In: *Fatigue and fracture of engineering materials and structures* 22.7 (1999), p. 633.

[126] Y Murakami. “The effect of hydrogen on fatigue properties of metals used for fuel cell system”. In: (2006), pp. 167–195.

[127] Yukitaka Murakami and Saburo Matsuoka. “Effect of hydrogen on fatigue crack growth of metals”. In: *Engineering Fracture Mechanics* 77.11 (2010), pp. 1926–1940.

[128] Yukitaka Murakami and Robert O Ritchie. “Effects of hydrogen on fatigue-crack propagation in steels”. In: *Gaseous Hydrogen Embrittlement of Materials in Energy Technologies*. Elsevier, 2012, pp. 379–417.

[129] Y Mutoh et al. “Stress shielding and fatigue crack growth resistance in ferritic–pearlitic steel”. In: *Materials Science and Engineering: A* 468 (2007), pp. 114–119.

[130] Naoaki Nagaishi et al. “Fatigue Life Properties of Circumferentially-Notched, Type 304 Austenitic Stainless Steel in Hydrogen Gas”. In: *Pressure Vessels and Piping Conference*. Vol. 58004. American Society of Mechanical Engineers. 2017.

[131] Mater Nagumo. “Hydrogen related failure of steels–a new aspect”. In: *Materials Science and Technology* 20.8 (2004), pp. 940–950.

[132] NE Nanninga et al. “Comparison of hydrogen embrittlement in three pipeline steels in high pressure gaseous hydrogen environments”. In: *Corrosion Science* 59 (2012), pp. 1–9.

[133] Nicholas Nanninga et al. “A review of fatigue crack growth for pipeline steels exposed to hydrogen”. In: *Journal of research of the national institute of standards and technology* 115.6 (2010), p. 437.

[134] AW Nelson HG. InThompson and IM Bernstein. *Effect of hydrogen on behavior of materials*. Tech. rep. Metallurgical Society of AIME, New York, 1976, p. 602.

[135] Thanh Tuan Nguyen et al. “Fracture properties and fatigue life assessment of API X70 pipeline steel under the effect of an environment containing hydrogen”. In: *Journal of Mechanical Science and Technology* (2021), pp. 1–11.

[136] Kevin A Nibur et al. “Notched Fatigue of Austentic Alloys in Gaseous Hydrogen”. In: *Pressure Vessels and Piping Conference*. Vol. 58004. American Society of Mechanical Engineers. 2017, V06BT06A044.

[137] Yuhei Ogawa et al. “The role of intergranular fracture on hydrogen-assisted fatigue crack propagation in pure iron at a low stress intensity range”. In: *Materials Science and Engineering: A* 733 (2018), pp. 316–328.

[138] Enyinnaya Ohaeri, Ubong Eduok, and Jerzy Szpunar. “Hydrogen related degradation in pipeline steel: A review”. In: *International Journal of Hydrogen Energy* 43.31 (2018), pp. 14584–14617.

[139] RA Oriani and PH Josephic. “Equilibrium aspects of hydrogen-induced cracking of steels”. In: *Acta metallurgica* 22.9 (1974), pp. 1065–1074.

[140] Richard A Oriani. “The diffusion and trapping of hydrogen in steel”. In: *Acta metallurgica* 18.1 (1970), pp. 147–157.

[141] Chinedu I Ossai. “Advances in asset management techniques: An overview of corrosion mechanisms and mitigation strategies for oil and gas pipelines”. In: *International Scholarly Research Notices* 2012 (2012).

[142] Michele Panico et al. “Effect of testing variables on fracture toughness in sour environment”. In: *The Twenty-fifth International Ocean and Polar Engineering Conference*. OnePetro. 2015.

[143] Paul Paris and Fazil Erdogan. “A critical analysis of crack propagation laws”. In: *ASME J. Basic Eng.* (1963), pp. 528–533.

[144] Gyu Tae Park et al. “Effect of microstructure on the hydrogen trapping efficiency and hydrogen induced cracking of linepipe steel”. In: *Corrosion science* 50.7 (2008), pp. 1865–1871.

[145] Ronald J Parrington. “Fractography of metals and plastics”. In: *Practical failure analysis* 2.5 (2002), pp. 16–19.

[146] RW Pasco and PJ Ficalora. “Entry of Hydrogen From the Gas Phase (Retroactive Coverage).” In: *Noyes Publications, Hydrogen Degradation of Ferrous Alloys,* (1985), pp. 199–214.

[147] SR Pemberton et al. “The effect of surface condition on primary water stress corrosion cracking initiation of Alloy 600”. In: *Proceedings of the 18th International Conference on Environmental Degradation of Materials in Nuclear Power Systems–Water Reactors*. Springer. 2019, pp. 203–216.

[148] Robert S Piascik. *Fatigue and fracture mechanics: 27th volume*. Vol. 1296. ASTM International, 1997, pp. 87–89.

[149] A Pramanik and AK Basak. “Effect of wire electric discharge machining (EDM) parameters on fatigue life of Ti-6Al-4V alloy”. In: *International journal of fatigue* 128 (2019), p. 105186.

[150] Dierk Raabe et al. “Grain boundary segregation engineering in metallic alloys: A pathway to the design of interfaces”. In: *Current Opinion in Solid State and Materials Science* 18.4 (2014), pp. 253–261.

[151] Klaus Rademann. “PW Atkins: Physical Chemistry”. In: Oxford: Oxford University Press, 1990, p. 995.

[152] VP Ramunni, T De Paiva Coelho, and PE Valadaes de Miranda. “Interaction of hydrogen with the microstructure of low-carbon steel”. In: *Materials Science and Engineering: A* 435 (2006), pp. 504–514.

[153] RO Ritchie and JF Knott. “Mechanisms of fatigue crack growth in low alloy steel”. In: *Acta Metallurgica* 21.5 (1973), pp. 639–648.

[154] Robert O Ritchie. “Mechanisms of fatigue-crack propagation in ductile and brittle solids”. In: *International journal of Fracture* 100.1 (1999), pp. 55–83.

[155] IM Robertson. “The effect of hydrogen on dislocation dynamics”. In: *Engineering fracture mechanics* 68.6 (2001), pp. 671–692.

[156] IM Robertson and HK Birnbaum. “An HVEM study of hydrogen effects on the deformation and fracture of nickel”. In: *Acta Metallurgica* 34.3 (1986), pp. 353–366.

[157] Joseph Ronevich, Chris San Marchi, and Dorian K Balch. “Evaluating the Resistance of Austenitic Stainless Steel Welds to Hydrogen Embrittlement”. In: *Pressure Vessels and Piping Conference*. Vol. 58981. American Society of Mechanical Engineers. 2019, V06BT06A035.

[158] Joseph A Ronevich, Brian P Somerday, and Chris W San Marchi. “Effects of microstructure banding on hydrogen assisted fatigue crack growth in X65 pipeline steels”. In: *International Journal of Fatigue* 82 (2016), pp. 497–504.

[159] Joseph A Ronevich et al. “Fatigue crack growth rates in high pressure hydrogen gas for multiple X100 pipeline welds accounting for crack location and residual stress”. In: *Engineering Fracture Mechanics* 228 (2020), p. 106846.

[160] Joseph Allen Ronevich and Brian P Somerday. *Assessing Steel Pipeline and Weld Susceptibility to Hydrogen Embrittlement.* Tech. rep. Sandia National Lab (SNL-CA), Livermore, CA (United States), 2016.

[161] Joseph Allen Ronevich, Brian P Somerday, and Zhili Feng. “Hydrogen accelerated fatigue crack growth of friction stir welded X52 steel pipe”. In: *International Journal of Hydrogen Energy* 42.7 (2017), pp. 4259–4268.

[162] Diego Belato Rosado et al. “Latest developments in mechanical properties and metallurgical features of high strength line pipe steels”. In: *International Journal Sustainable Construction & Design* 4.1 (2013).

[163] P Rozenak, IM Robertson, and HK Birnbaum. “HVEM studies of the effects of hydrogen on the deformation and fracture of AISI type 316 austenitic stainless steel”. In: *Acta metallurgica et materialia* 38.11 (1990), pp. 2031–2040.

[164] K Sakaki et al. “The effect of hydrogen on vacancy generation in iron by plastic deformation”. In: *Scripta Materialia* 55.11 (2006), pp. 1031–1034.

[165] Christopher W San Marchi, Brian P Somerday, and Kevin A Nibur. *Fatigue Crack Initiation in Hydrogen-Precharged Austenitic Stainless Steel.* Tech. rep. Sandia National Lab.(SNL-CA), Livermore, CA (United States), 2012.

[166] J Sanchez et al. “Ab initio molecular dynamics simulation of hydrogen diffusion in α-iron”. In: *Physical Review B* 81.13 (2010), p. 132102.

[167] Karl-Heinz Schwalbe, J Heerens, and JD Landes. *Classical fracture mechanics methods*. Tech. rep. GKSS-Forschungszentrum Geesthacht GmbH (Germany), 2007.

[168] Shaw Pipeline Services. *Energy Report Shaw Pipeline Services Phased Array AUT Qualification*. 2009. URL: https://docs2.cer-rec.gc.ca/ll-eng/llisapi.dll/fetch/2000/90464/90550/189912/441384/481632/561480/A1K3R4_%5C%2D_DNV_Report_No._123R8IY%5C%2D6_Rev_01.pdf?nodeid=561418&vernum=-2 (visited on 07/29/2022).

[169] Tomoki Shinko et al. “Controlling factors and mechanisms of fatigue crack growth influenced by high pressure of gaseous hydrogen in a commercially pure iron”. In: *Theoretical and Applied Fracture Mechanics* 112 (2021), p. 102885.

[170] Roch J Shipley, Brett A Miller, and Ronald J Parrington. “Introduction to Failure Analysis and Prevention”. In: *Journal of Failure Analysis and Prevention* 22.1 (2022), pp. 9–41.

[171] A Sieverts. “Die aufnahme von gasen durch metalle”. In: *Zeitschrift für Metallkunde* 21 (1929), pp. 37–46.

[172] Adolf Sieverts. “Absorption of gases by metals”. In: *Zeitschrift für Metallkunde* 21 (1929), pp. 37–46.

[173] Andrew J Slifka et al. “Fatigue crack growth of two pipeline steels in a pressurized hydrogen environment”. In: *Corrosion Science* 78 (2014), pp. 313–321.

[174] Andrew J Slifka et al. “The effect of microstructure on the hydrogen-assisted fatigue of pipeline steels”. In: *ASME 2013 Pressure Vessels and Piping Conference*. American Society of Mechanical Engineers Digital Collection. 2013.

[175] Petros Sofronis and Ian M Robertson. *Hydrogen embrittlement of pipeline steels: causes and remediation*. Tech. rep. University of Illinois at Urbana-Champaign, 2013.

[176] BP Somerday et al. “Elucidating the variables affecting accelerated fatigue crack growth of steels in hydrogen gas with low oxygen concentrations”. In: *Acta Materialia* 61.16 (2013), pp. 6153–6170.

[177] SM El-Soudani and RM Pelloux. “Anisotropy of fatigue crack propagation in aluminum alloy butt welded joints”. In: *Weld. J* 54.5 (1975).

[178] Aleksandar Staykov, Junichiro Yamabe, and Brian P Somerday. “Effect of hydrogen gas impurities on the hydrogen dissociation on iron surface”. In: *International Journal of Quantum Chemistry* 114.10 (2014), pp. 626–635.

[179] EA Steigerwald, FW Schaller, and AR Troiano. “The role of stress in hydrogen induced delayed failure”. In: *Trans. Met. Soc. AIME* 218 (1960).

[180] S Suresh and RO Ritchie. “Mechanistic dissimilarities between environmentally influenced fatigue-crack propagation at near-threshold and higher growth rates in lower strength steels”. In: *Metal Science* 16.11 (1982), pp. 529–538.

[181] Yoshimasa Takahashi et al. “Hydrogen-induced slip localization around a quasi-brittle fatigue crack observed by high-voltage electron microscopy”. In: *Scripta Materialia* 61.2 (2009), pp. 145–148.

[182] K Takai et al. “Lattice defects dominating hydrogen-related failure of metals”. In: *Acta Materialia* 56.18 (2008), pp. 5158–5167.

[183] Osamu Takakuwa et al. “A mechanism behind hydrogen-assisted fatigue crack growth in ferrite-pearlite steel focusing on its behavior in gaseous environment at elevated temperature”. In: *Corrosion Science* 168 (2020), p. 108558.

[184] Hiroshi Tamehiro et al. *Ultra-high strength, weldable steels with excellent ultra-low temperature toughness*. US Patent 6,264,760. July 2001.

[185] Anatolii I Titov et al. “Hydrogen accumulation and distribution in pipeline steel in intensified corrosion conditions”. In: *Materials* 12.9 (2019), p. 1409.

[186] Andrej Turk et al. “Grain boundary carbides as hydrogen diffusion barrier in a Fe-Ni alloy: a thermal desorption and modelling study”. In: *Materials & Design* 160 (2018), pp. 985–998.

[187] A Turnbull. “Hydrogen diffusion and trapping in metals”. In: *Gaseous hydrogen embrittlement of materials in energy technologies*. Elsevier, 2012, pp. 89–128.

[188] Det Norske Veritas. “Offshore Standard DNV-OS-F101 Submarine Pipeline Systems”. In: *Høvik, Norway: Det Norske Veritas, DNV* (2007).

[189] Stephanie Vervynckt. “Control of the Non-Recrystallization Temperature in High Strength Low Alloy (HSLA) Steels.” PhD thesis. Ghent University, 2010.

[190] O Vosikovsky. “Fatigue crack closure in an X70 steel”. In: *International Journal of Fracture* 17.3 (1981), pp. 301–309.

[191] Harry F Wachob and Howard G Nelson. “Influence of microstructure on the fatigue crack growth of A516 in hydrogen”. In: (1980).

[192] JQ Wang et al. “Microstructure of X52 and X65 pipeline steels”. In: *Journal of Materials Science* 34.8 (1999), pp. 1721–1728.

[193] Maoqiu Wang, Eiji Akiyama, and Kaneaki Tsuzaki. “Effect of hydrogen and stress concentration on the notch tensile strength of AISI 4135 steel”. In: *Materials Science and Engineering: A* 398.1-2 (2005), pp. 37–46.

[194] RP Wei and GW Simmons. *Environment enhanced fatigue crack growth in high-strength steels*. Tech. rep. 1973.

[195] Malwina Witczak. “Fatigue performance of over-stressed beadweld due to pulling on the bead”. MA thesis. Technical University Delft, 2019.

[196] HB Xue and YF Cheng. “Hydrogen permeation and electrochemical corrosion behavior of the X80 pipeline steel weld”. In: *Journal of materials engineering and performance* 22.1 (2013), pp. 170–175.

[197] Junichiro Yamabe et al. “Effects of hydrogen pressure, test frequency and test temperature on fatigue crack growth properties of low-carbon steel in gaseous hydrogen”. In: *Procedia Structural Integrity* 2 (2016), pp. 525–532.

[198] CA Zapffe and CE Sims. “Hydrogen embrittlement, internal stress and defects in steel”. In: *Trans. AIME* 145.1941 (1941), pp. 225–271.

[199] Shuai Zhang et al. “The effects of double notches on the mechanical properties of a high-strength pipeline steel under hydrogen atmosphere”. In: *International Journal of Hydrogen Energy* 45.43 (2020), pp. 23134–23141.

[200] Timing Zhang et al. “Effects of surface oxide films on hydrogen permeation and susceptibility to embrittlement of X80 steel under hydrogen atmosphere”. In: *International Journal of Hydrogen Energy* 43.6 (2018), pp. 3353–3365.

[201] Weimin Zhao et al. “Hydrogen permeation and embrittlement susceptibility of X80 welded joint under high-pressure coal gas environment”. In: *Corrosion Science* 111 (2016), pp. 84–97.

[202] Yakai Zhao et al. “The role of hydrogen in hardening/softening steel: Influence of the charging process”. In: *Scripta Materialia* 107 (2015), pp. 46–49.

[203] Chengshuang Zhou et al. “Effects of internal hydrogen and surface-absorbed hydrogen on the hydrogen embrittlement of X80 pipeline steel”. In: *International Journal of Hydrogen Energy* 44.40 (2019), pp. 22547–22558.

[204] Cynthia G Zoski. “Handbook of electrochemistry”. In: *Elsevier* (2006), p. 935.

Appendices

A. Test Details

A.1. Engineering Drawing of Specimen with Full Specifications

The engineering drawing with full specifications is on the next page. Each sample was inspected after delivery by the manufacturer. All tested samples had dimensions within the tolerances.

A.2. Test Procedure DCPD

After the hydrogen pre-charging, the DCPD set-up was attached to the specimen. At this stage, the specimen was mounted only in the upper adapter. First, the location of the notch was estimated by measuring from the end of the specimen. It is desirable to position the probe holders symmetrically over the notch. There was a small discrepancy between the depth of the adapter and the threaded portion of the specimen. A glass fibre ring (1 mm) was placed between the top adapter and the top of the probe holder. This allowed for symmetrical placement of the probes. When both probe holders were attached and centrally located around the specimen, an M14x2 nut was screwed onto the lower thread of the specimen. This nut was tightened until it touched the surface of the lower probe holder. This construction allows the probe holders to be firmly placed, which is essential for positioning the probes. The orientation of the bolts, and the bolts themselves, were consistent throughout all tests. Marking the bolts or eye clamps, can serve as a visual confirmation.

The sharpened bolts were inserted into the inserts until they touched the surface of the sample. Then the bolts were tightened firmly, leaving an indentation in the steel surface. This groove prevents the bolts from slipping during fatigue.

Once the bolts were in place, the measuring wires were inserted. First, an eye clamp for each bolt was compressed with two M2 nuts. At each of the heights of the bolts, three probes were arranged equidistantly around the circumference of the meter. For ease of interpretation, it is now assumed that there are three sides. The connections of one side were completed first, then the other side, and finally the last side. The reference wires above the notch were connected to the blue wire of cable ’Y’. The reference wires below the notch were connected to the red wire of cable ’Y’. The notch wires above the notch were connected with the blue wire of cable ’X’. The notch wires below the notch were connected to the red wire of cable ’X’. All connections were made with welding clamps. After a connection was made on one side, a multimeter was used to confirm the correct placement of the probes. This method makes it possible to determine which bolt needs to be tightened (more).

After placing the probes, the bottom adapter was attached. After this, the current cable was connected to the bottom adapter. Next, the long pipe of the relief valve was removed. This would otherwise cause vibrations during the fatigue which would affect the test. The DCPD was then turned on to read the signal. The WM has a slightly higher starting voltage (15-20%) than the BM, due to the conductivity differences of the materials. The bolts were re-sharpened after approximately 7-10 measurements to exclude voltage differences due to flattening of the bolts (difference in contact area). Once everything was in place and the DCPD was switched on, the polycarbonate safety box was closed and the test started.

Notes:

- The drilled hole is cleared.
- The internal (M6x1) and external (M14x2) threads are deburred.
- For the dimensions that do not directly show a tolerance, there holds a general tolerance of $\pm$ 0.1

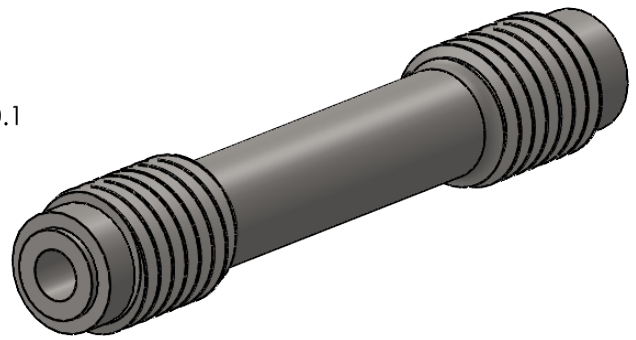

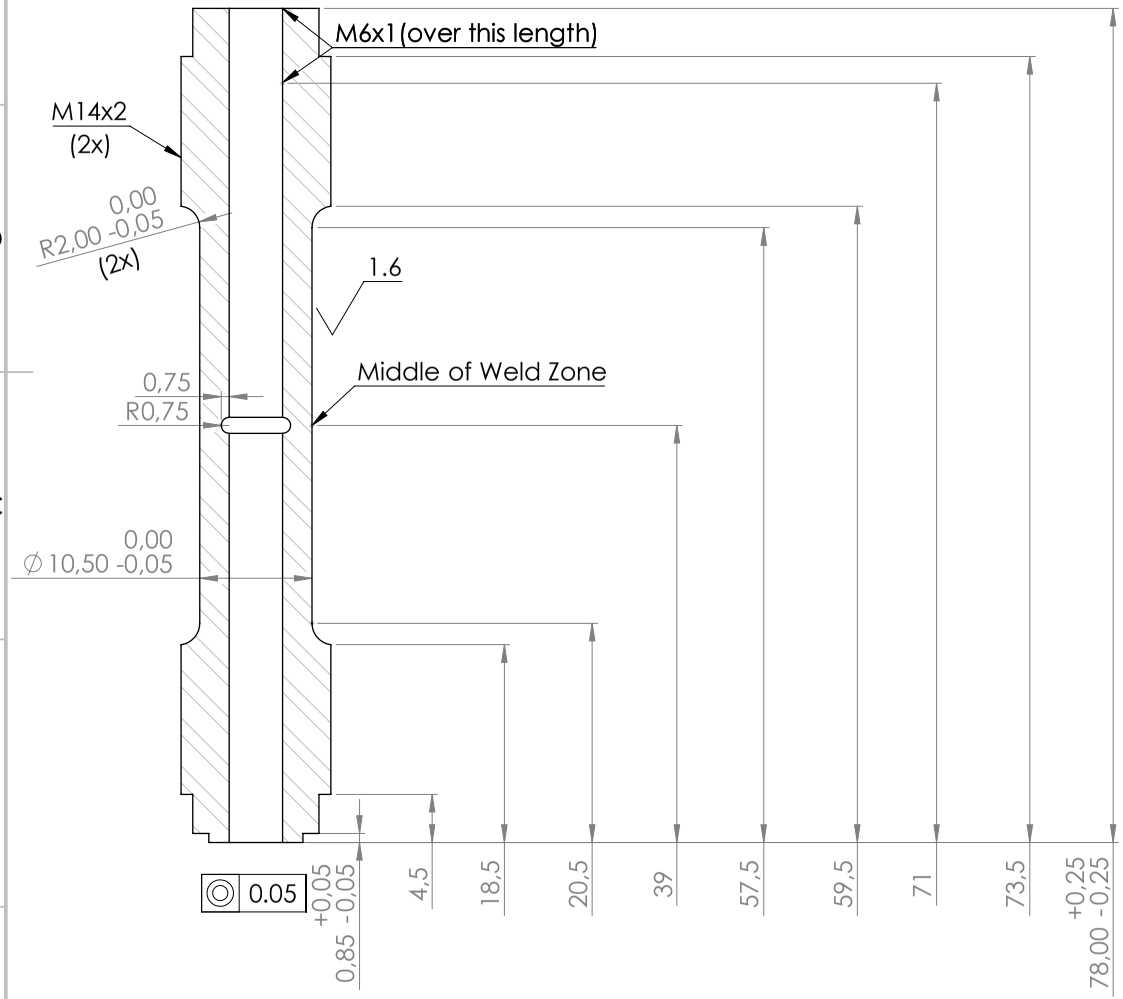

Cross section view

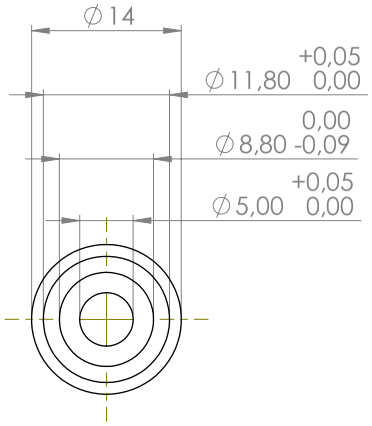

Bottom View

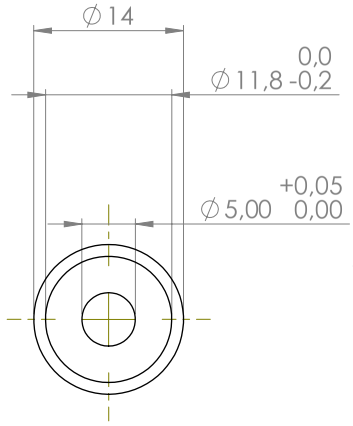

Top view

UNLESS OTHERWISE SPECIFIED: DIMENSIONS ARE IN MILLIMETERS SURFACE FINISH: see above TOLERANCES: see above LINEAR: ANGULAR:		FINISH:		DEBURR AND BREAK SHARP EDGES	DO NOT SCALE DRAWING	REVISION
	NAME	SIGNATURE	DATE		TITLE: TU Delft hollow cylindrical specimen design	
DRAWN	L. Faucon					
CH'K'D						
APPV'D						
MFG						
Q.A				MATERIAL: API 5L X60 pipeline steel	DWG NO. Cylindrical Specimen	A3
				WEIGHT:	SCALE: 2:1	SHEET 1 OF 1

SOLIDWORKS Educational Product. For Instructional Use Only.

B. Insulation

B.1. Electrical Insulation for Electromechanical Testing Machine

This chapter describes the precautions taken and the components designed to achieve an electrically insulated system for the electromechanical tensile testing machine (*Zwick Z100*). This set-up is proved to be working, however was ultimately not used for the experiments. Therefore, this chapter serves as a guidance for researchers that are in need of insulating the electromechanical testing machine for DCPD measurements. A properly insulated system excludes electrical contact of the power and voltage leads with the load cell. Improper insulation could lead to apparent effects of the machine on the measured (output) potential. In addition, such a situation could significantly damage the tensile test machine card in- and output cards by interfering or overloading the load cell current control [167].

Figure B.1 illustrates the insulation of the (base of the) adapter from the fixed traverse. The proposed insulation is based on insulating contact points that act as conductive paths:

1. The contacting surfaces of the circular disc to which the bottom adapter is connected, and the fixed traverse.
2. The surface of the M16 bolt, including the bottom of the bolt head, that penetrates from the bottom adapter into the fixed traverse.

The first issue is solved by separating the contacting surfaces by an 8 mm thick piece of polymethylmethacrylate, also commercially known as ”plexiglass”. This thermoplastic is renowned as an excellent electrical insulator; it has a volume resistivity of 2 - 14 x 10^{15} Ω/cm.

The solution for the second concern consists of two modifications. First, the contact between the bolt (including the head) with the adapter and fixed traverse was eliminated with vinyl plastic electrical tape (*3M Teflex^{TM} 1500*). Second, a 1.5 mm glass fibre plate was laser cut to fit underneath the bolt. This piece was specifically engineered in order to avoid contact between the bottom of the bolt head with the surface of the bottom adapter. The components/modifications made were tested for stability and (structural) integrity at the test conditions; in other words, to conform whether the components would not fracture under the cyclic loading.

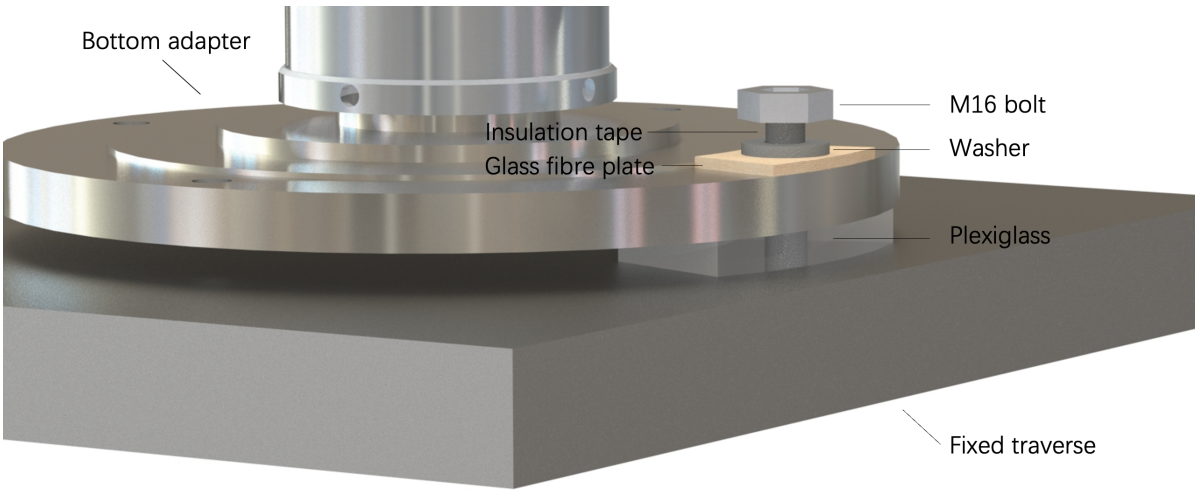

Figure B.1: Illustration of the insulation designed for the DCPD experiments.

C. Additional information for design and computational models

C.1. Specimen Design

For the study of the number of cycles to failure, circumstantially notched cylindrical specimen are commonly used [127, 173, 8]. In the case when the fatigue life of weld metal is of interest, the notch should be located at the center of the width of the weld, as specified in ASME Section VIII, Division 3, KD-10 [28]. In fatigue studies it is often aimed to adhere to standards designed for a corrosive or hydrogen environment:

- EN ISO 11782-1: "Corrosion of metals and alloys - Corrosion fatigue testing - Part 1: Cycles to failure testing [55]." This standard excludes details about the specimen design.
- ASTM G142: "Standard Test Method for Determination of Susceptibility of Metals to Embrittlement in Hydrogen Containing Environments at High Pressure, High Temperature, or Both [16]."

Even though ASTM G142 is designed for a hydrogen environment, the specimens shall conform to the dimensions and guidelines provided in Test Methods E8 (ASTM E8/E8M-21: "Standard Test Methods for Tension Testing of Metallic Materials [15]"), which is a standard for inert environments. In addition, this standard is not specifically written for fatigue studies, but rather for tension testing. Nevertheless the circumferentially-notched cylindrical specimen described in this standard has been often used for fatigue studies in the past [130, 165, 173]. The tendency to follow the guidelines of test method E8 could be attributed to the fact that research on hydrogen fatigue is still in the process of being standardised.

C.2. Effect of Stress Concentration Factors on HE and HA-FCG

Sharp notches, surface irregularities, scratches, small cracks or pits can be created in the pipeline steel during production. These factors can influence the fatigue life of the structure. In addition, welds drastically influence the fatigue life; the fatigue performance of welded joints is considered poor compared to that of the base metal. This is attributed to the residual stresses and stress concentration arising from weld defects or (small) geometry defects. According to Auvret et al., a stress concentration factor (SCF) of 1.5 is common practice within pipeline girth welds [18]. Malwina Witczak, in her MSc thesis 'Fatigue performance of over-stressed beadweld due to pulling on the beads', reported that in the beadwelds a SCF of 2.24 was present due to local misalignment [195]. The influence of these defects on the mechanical performance can be studied by machining notches in the specimen that are representative to the change in local stress intensity. Notches are often used in fatigue studies, as they allow the location of crack initiation, and thus failure, to be controlled. The induced stress intensity (factor) of the notch must be chosen carefully in studies on hydrogen fatigue, as it affects the extent of the deleterious effects of hydrogen.

An et al. machined X80 circumferentially-notched cylindrical specimen with stress concentration factors ranging from 1.2-4.09 [9]. When loaded under identical fatigue test conditions, an increasing K_t results in a shorter fatigue life. This trend is present for both hydrogen and inert environments. However, it applied only for K_t's up to 2.1 as no significant change was observed for K_t's from 2.1 to 4.09. However the effect of hydrogen became more evident with an increasing K_t. Evidenced by the observation that the reduction in fatigue lifetime in an hydrogen environment became more pronounced with the increase of K_t.

A recent (2020) study of Zhang et al. used two (circumferential exterior) notches on one specimen, to determine the effect of stress concentrators (induced by different radii) on hydrogen tensile (displacement rate of 0.01 mm/min) and fatigue tests (R = 0.1 and f = 1 Hz) [199]. The double-notched specimens ruptured at notches with a lower K_t value during the tensile tests while at notches with a higher K_t value during the fatigue life tests. The failure occurred at the lower K_t notch during the tensile tests because the strain hardening caused by plastic deformation occurred at the first notch which had a higher K_t. During the fatigue life tests, the imposed stress is below the yield strength and therefore plastic deformation is limited at the notches and the notch with the higher K_t is the site of failure.

C.3. Stress Concentration Factor of Designed Notch

The SCF, K_t was determined by calculating the fraction of $\sigma_{22,notch}/\sigma_{22,gauge}$. The longitudinal stress was used since the applied loads in the fatigue tests were applied in the longitudinal direction. There-

fore, the specimens underwent the highest stress in this direction as well. Moreover, this stress virtually governed the value for the Von Mesis equivalent stress, and thus 'controlled' the susceptibility to damage of the fatigue samples.

This model focused only on the effect of the notch and therefore the internal gas pressure was not included. A nominal stress of 100 MPa was modelled by applying a pressure load of -100 MPa to the gauge in the longitudinal direction. From Fig. C.1, it can be seen that the maximum longitudinal stress (σ_{22} = 303 MPa) is experienced at the notch root (node 127429). The value for the gauge (node 92572), is 100 MPa. The calculation for K_t would result in:

$$\frac{\sigma_{22,notch}}{\sigma_{22,gauge}} = \frac{303}{100} = 3.03$$

The local stress rising effect induced by the notch thus resulted in a K_t of 3.0 at the notch root.

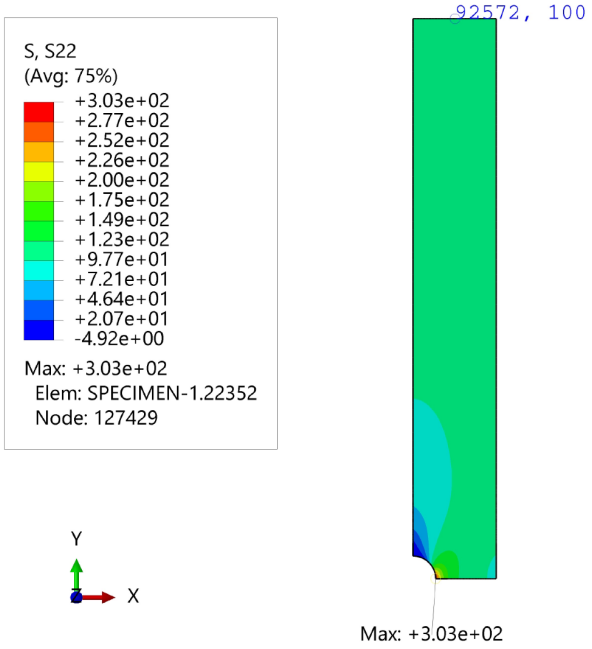

Figure C.1: Display of the longitudinal stress in the specimen when subjected to a nominal stress of 100 MPa. The maximum longitudinal stress (303 MPa) is experienced at node 127429, which denotes the notch root. The longitudinal stress (100 MPa) of the gauge is extracted from node 92572.

C.4. Calculation Sievert's Law

This section is written to provide the reader the calculations of the hydrogen concentration at the inner surface of the specimen.

The atomic mass of iron states that 1 mol Fe is equivalent to 55.845 g. The density of iron is 7.874 g/cm^3. Relating 1 gram Fe to mm^3 gives: 1 gram Fe = $\frac{1}{7.874}$ cm^3 = 127.00 mm^3. Then the atomic mass was used to convert from gram to moles: $\frac{1}{55.845}$ mol Fe = 0.0179 mol Fe = 127.00 mm^3. Lets consider:

$$\beta = 1.4098 \times \frac{mol}{mm^3} \text{ Fe} \tag{1}$$

Then Sievert's law was used to determine the atomic fraction (c_0) of hydrogen in equilibrium with hydrogen gas at pressure *P*:

$$c_0 = 0.00185\sqrt{P}e^{-3440/T} \tag{2}$$

The pressure, *P*, was set to 150 bar and temperature (*T*) to 293.15 K (room temperature):

$$c_0 = 0.00185\sqrt{150}e^{-3440/239.15} = 1.815 \times 10^{-7}$$

Thus, the hydrogen concentration (c_h) is:

$$c_{\mathrm{h}} = c_0 \times \beta \tag{3}$$

$$c_{\mathrm{h}} = 1.815 \times 10^{-7} \times 1.410 \times 10^{-4} = 2.559 \times 10^{-11} \frac{mol}{mm^3}$$

D. Direct Current Potential Drop Calibration Results

Calibration was performed to validate the development of the potential drop design. A correlation between the potential drop signal and the crack area was obtained by terminating fatigue tests after crack initiation, and by forcing brittle fracture (in pure tension) using liquid N_2. The crack surface was then measured subsequent to the induced brittle fracture. An example of a normalised potential drop data and the related fracture surface is provided in Fig. D.1. It should be noted that the experiments were not repeated. However, the result of the crack area of each experiment is given as an average of two measurements. The calibration of the potential drop should therefore be considered as an approximation. It serves mainly to validate the onset of crack initiation and to facilitate the interpretation of data

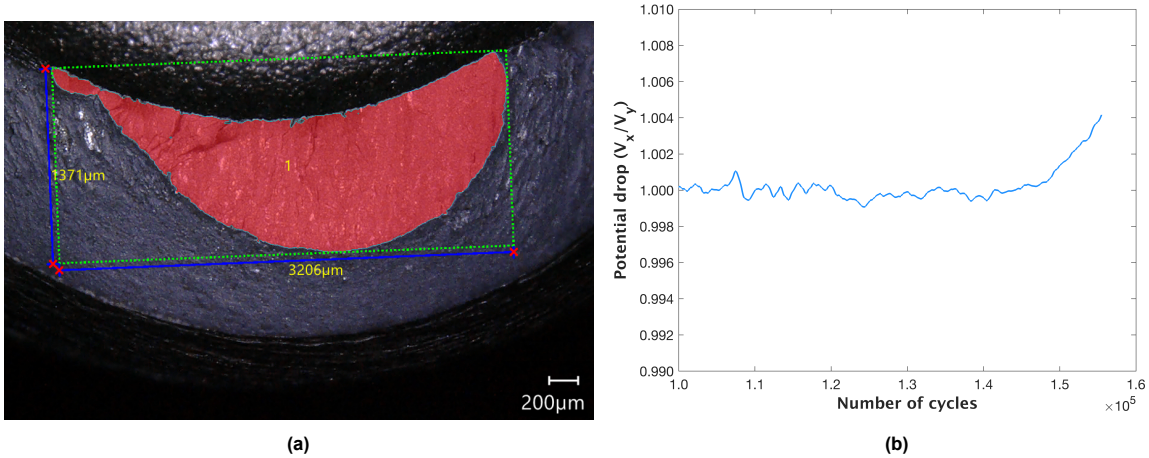

(a) (b)

Figure D.1: Identification of the crack surface area a) that corresponds to the potential drop data b).

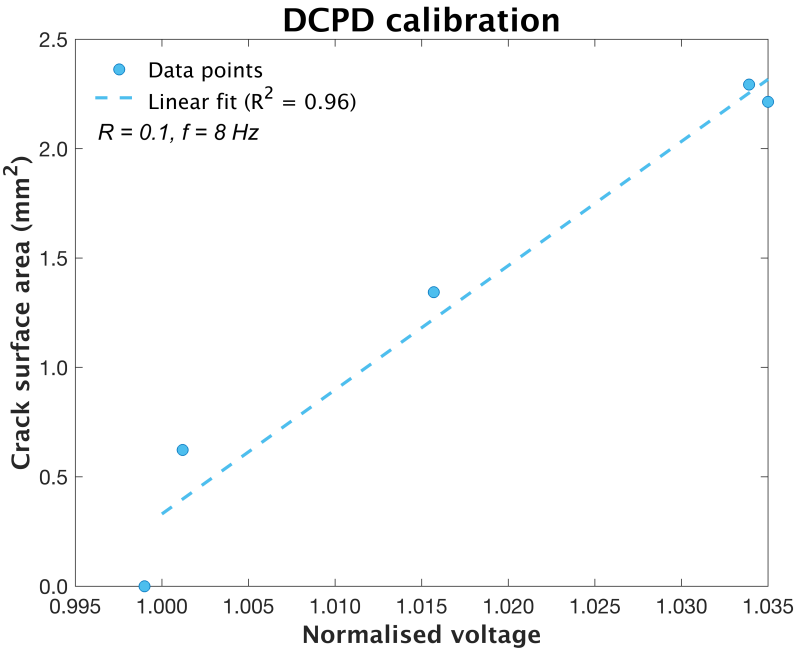

Figure D.2: Relation of potential drop signal to crack surface area (mm^2). The linear trend of the data has a R^2 of 0.96.

from other sections.

The results of the DCPD calibration are provided in Fig. D.2. This figure presents the relation of the crack surface area to different normalised voltages. The coefficient of determination, R^2, has a value of 0.96 when a linear model is applied. Therefore, it can be assumed that the crack area is linearly related to the normalised voltage. It can thus be concluded that the novel design is well calibrated and that the presented crack initiation data truly reflects the occurrence of crack initiation.

In this thesis, the data is presented as cracked area (instead of crack length) because it provides a more accurate estimate for asymmetric crack growth in a (hollow) cylinder. The data representation in this thesis is therefore comparable to the approach of Bär, which was introduced in the state of the art (see section 2.6.2) [20].

E. Additional Information For Fatigue Model

E.1. Plastic strain in air specimen

The plastic strain distribution in the air specimen is displayed in Fig. E.1.

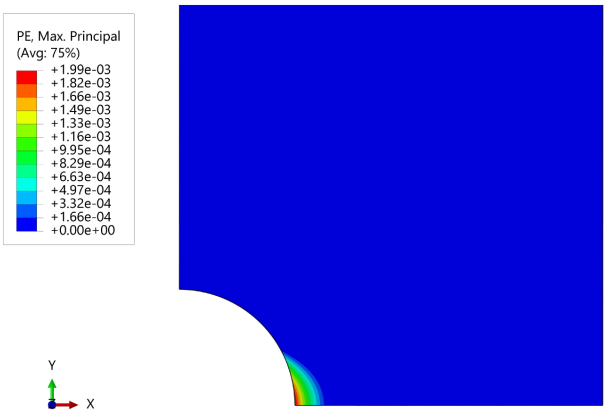

Figure E.1: Display of the maximum principal plastic strain present in the internally pressurised (150 barg) specimen after loading to F_{max}. Values represented in the legend can be interpreted as % plastic strain when multiplied by a factor 100.

E.2. End-cap Effect

In reality, pipelines experience an end-cap effect; when a pressure acts on the internal surface of a closed vessel, the pressure induces stresses in the longitudinal, circumferential and radial directions. The last direction is only of relevance for thick-walled pipes (wall thickness $> \frac{1}{4} *$outer radius) [14]. In the fatigue model, the closed ends of the test pieces have not been modelled and therefore it does not fully correspond to the real conditions of pipelines. Nevertheless, the end-cap effect is experienced to some extent in the notch, as evidenced by the pressure-induced stress in the longitudinal direction (Fig. 4.9, red crosses). The pressure acts perpendicular to the surface of the specimen and has its direction parallel to the radial axis for the entirety of the gauge. Since the applied pressure also acts perpendicular to the surface of the notch, the 'orientation' of the pressure applied to the notch varies locally due to the geometry. For instance, as can be seen in Fig. 3.13 where the boundary conditions of the model were discussed, the pressure acting on the notch root has its orientation parallel to the radial direction, while it translates to being perpendicular to the radial direction when moving towards the notch edges. On a local scale, the notch can therefore be considered as a partially enclosed space where the end-cap effect acts on the edges of the notch. The finding that the pressure did not affect the global longitudinal stress range, results from the end-cap effect not being incorporated in the model.

E.3. Stress Triaxiality

The Von Mesis equivalent stress can be used to determine the stress triaxiality:

$$\text{Stress triaxiality} = \frac{\sigma_h}{\sigma_v} \tag{4}$$

In this equation, σ_h is the hydrostatic stress, which is defined as $\sigma_h = \frac{1}{3}(\sigma_1 + \sigma_2 + \sigma_3)$. Abaqus does not have the option to represent the hydrostatic stress in a meshed structure. An alternative would be to calculate the inverse of the pressure, as they relate as: $\sigma_h = -\sigma_p$. In this work, however, the stress triaxiality for a 150 barg pressurised BM specimen is directly plotted in Fig. E.2. Higher values of the stress triaxiality controls the location of crack initiation [88] and drives crack propagation in the material [148]. Moreover, it increases the effect of hydrogen embrittlement. Since failure is expected at the notch, utmost triaxiality must be reached in the notch (root) ligament. This is coherent with the representation of the triaxial stress state in Fig. E.2.

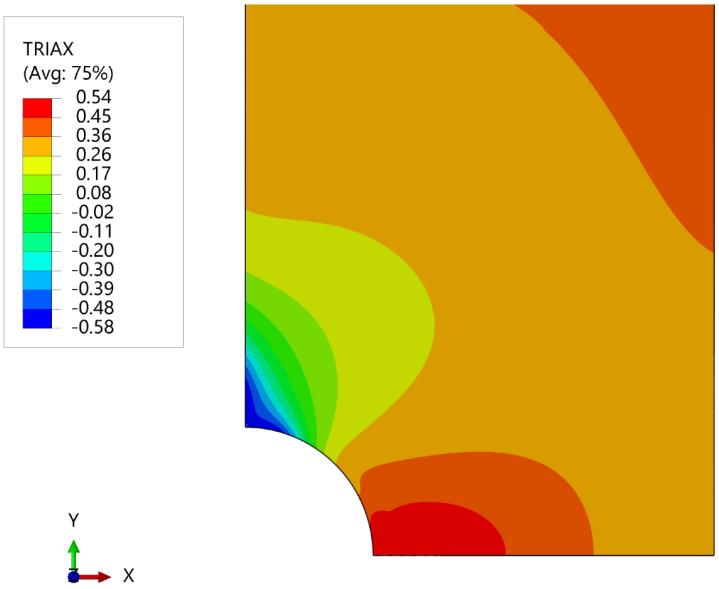

Figure E.2: Display of the triaxial stress-state at F_{max} in a 150 barg pressurised BM specimen.

F. Supplementary Figures Weld Metal Outgassing Effect

All WM H_2 normalised potential drop curves with zoomed in data on the outgassing phase are provided in Fig. F.1. This figure also includes the normalised potential drop data of WM N_2 (subfigure a), specimen B1.2, in order to emphasise the difference in outgassing effect in both environments. Note that the anomaly (visible as a reduction in voltage response) in sub-figure F.1.c is due to a momentary error in the DCPD machine.

Examination of the subfigures in Fig. F.1 reveals that the moment of degassing occurs at slightly different normalised potential drop voltages. This indicates that the area of the leading fatigue fractured surface varies (in asymmetry) for each specimen, resulting in variation in the commencement of outgassing. Relating the findings of Fig. F.1 with the previously discussed results of N_{CI}, N_G, N_F and LT_{CI}, it becomes evident that the asymmetry of leading crack front (thus moment of outgassing) has no significant influence on the overall fatigue behaviour. Moreover, the variation in onset can be considered minor since the inflection is consistently between the normalised voltage range of 1.6-2.0. Since this period of fatigue is close to failure, the differences in the onset of outgassing can be neglected when assessing the total fatigue life.

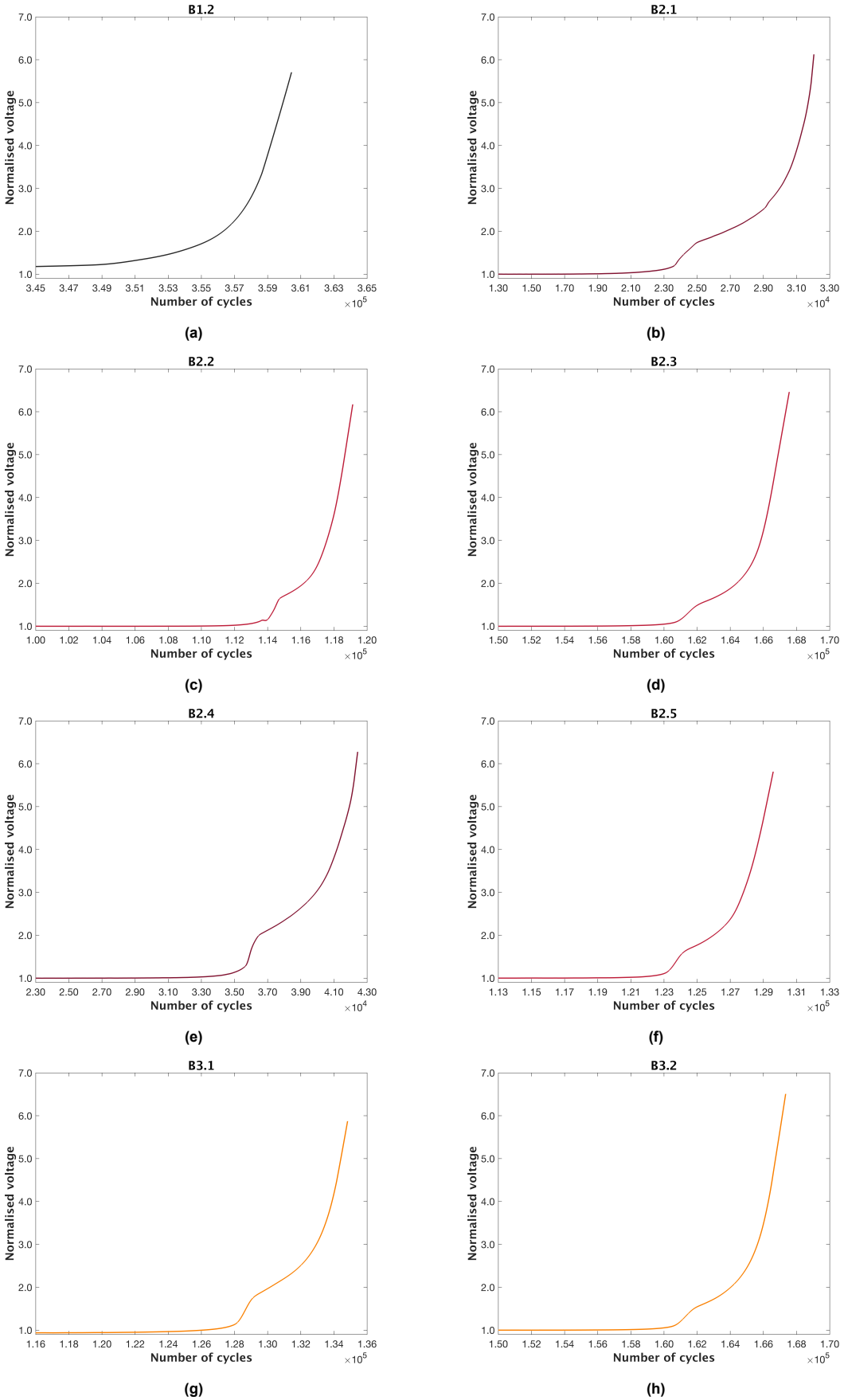

Figure F.1: Zoomed-in projection on the potential drop curves visualising the effect of outgassing on fatigue behaviour. The figures include data representative of: a) N_2, c) d) and f) 150 barg H_2 non-porous, b) and e) 150 barg H_2 macropores and, g) and h) 70 barg H_2. The abnormality in c) results from an error in the DCPD machine.

G. Supplementary Figures Fracture Surface Analysis

G.1. SEM Fractography Area III BM

For the reason that air and N_2 can be considered to behave equally in Area II and Area III, the images of air are excluded in this section.

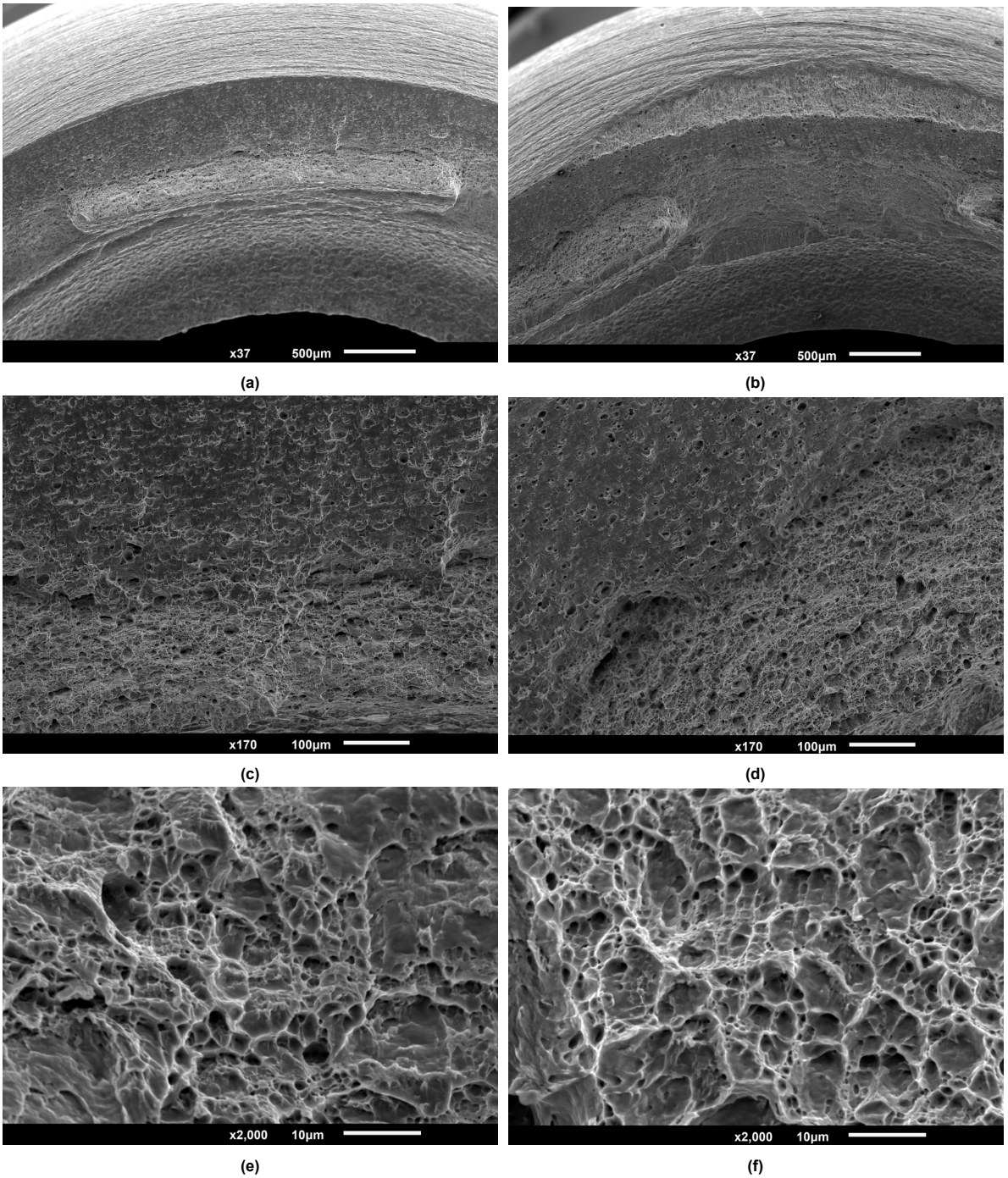

Figure G.1: SEM Analysis of Area III for 150 barg N_2 and 150 barg H_2 BM tested specimens. This figure comprises several subfigures: H_2 a) and N_2 b) overview of Area III, H_2 c) and N_2 d) magnified view where the transition in dimple density is imaged and, H_2 e) and N_2 zoomed-in projection on the voids in the high density dimple region.

In Area III, the entire fracture surface can be described by microvoid coalescence. Fatigue failure occurred due to the continuous reduction of the load-bearing cross-section of the specimen. Moreover, the plastic flow was no longer limited to the crack tip, but extended to the cross-section which gave

rise to yielding. This Area can therefore be referred to as Region III fatigue. Depending on the environmental conditions, Region III can be characterised by microvoid coalescence or cleavage. Fig. G.1a (H_2) and Fig. G.1b (N_2) provide an overview of Area III. From these figures it can be observed that the fracture surface can be characterised by microvoid coalescence. Note that in G.1b, on the inner edge, characteristics of Area I behaviour are visible.

The dimple density varies in the specimens. The H_2 specimen shows highest density near the inner edge, whereas N_2 also has a region of high dimple density at the outer edge. An increased density of dimples could be the result of the higher hydrostatic stress state, which in turn promotes void nucleation and growth. Considering the local stress condition induced by the notch, this could explain the high density observed at the inner edge. Lee et al. stated that the density and depth of voids on a fracture surface decreases with increasing strain rate [99]. The force controlled test conditions causes the remaining load-bearing cross-section to increase in plastic strain rate when the area reduces. Thus, applying this to Fig. G.1a, for H_2 the plastic strain increased when traversing from the inner to outer edge. For the N_2 specimen, this would indicate that the necking was relatively more symmetric.
Fig. G.1c and Fig. G.1d provide a higher magnification of dimple density transition for H_2 and N_2, respectively. The dimples are relatively similar in size. It can be deduced from the larger dimple area that the dimples are elongated in the vertical direction in the image plane. This is indicative of ductile tearing. The elongated dimples point downwards in the image plane, which indicates that the fracture originated from the internal surface. Usually in a hydrogen environment, the dimples are smaller in size due to the enhanced formation of voids that allow coalescence under less growth [117]. However, when inspecting Fig. G.1e (H_2) and Fig. G.1f (N_2), which are a zoomed-in projections on the voids, it can be stated that the voids are similar in size. Therefore, the residual hydrogen concentration in the specimen did not influence the fatigue behaviour in Area III.

G.2. SEM Fractography BM Air

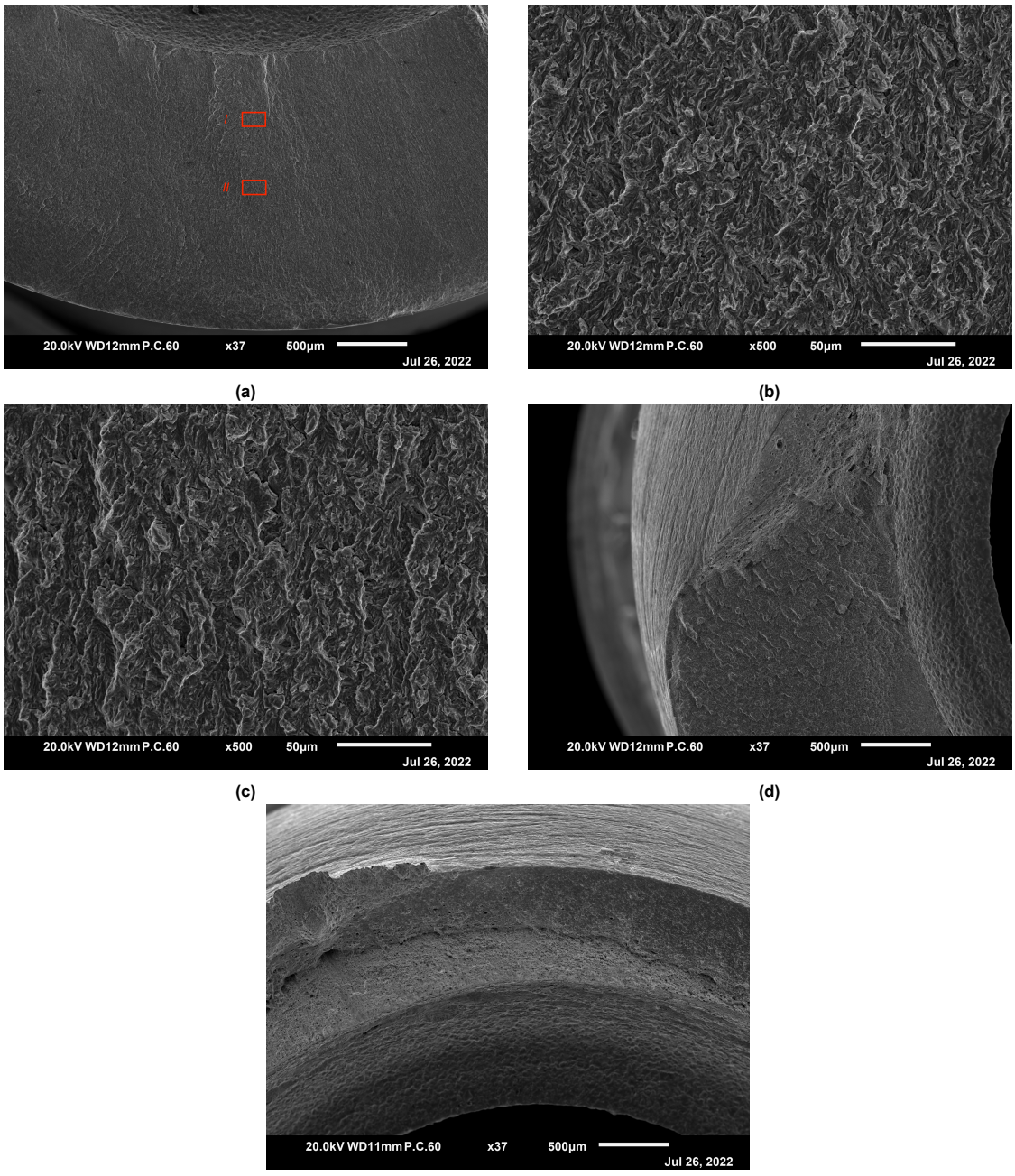

Figure G.2: SEM fracture surface pictures of BM air specimen (A1.2). a) Overview of the notch region, b) zoom of annotated region I, c) zoom of annotated region II, c) transition to fast fracture zone and e) fast fracture zone (also referred to as Area III in main text).

G.3. SEM Fractography 70 barg Hydrogen WM

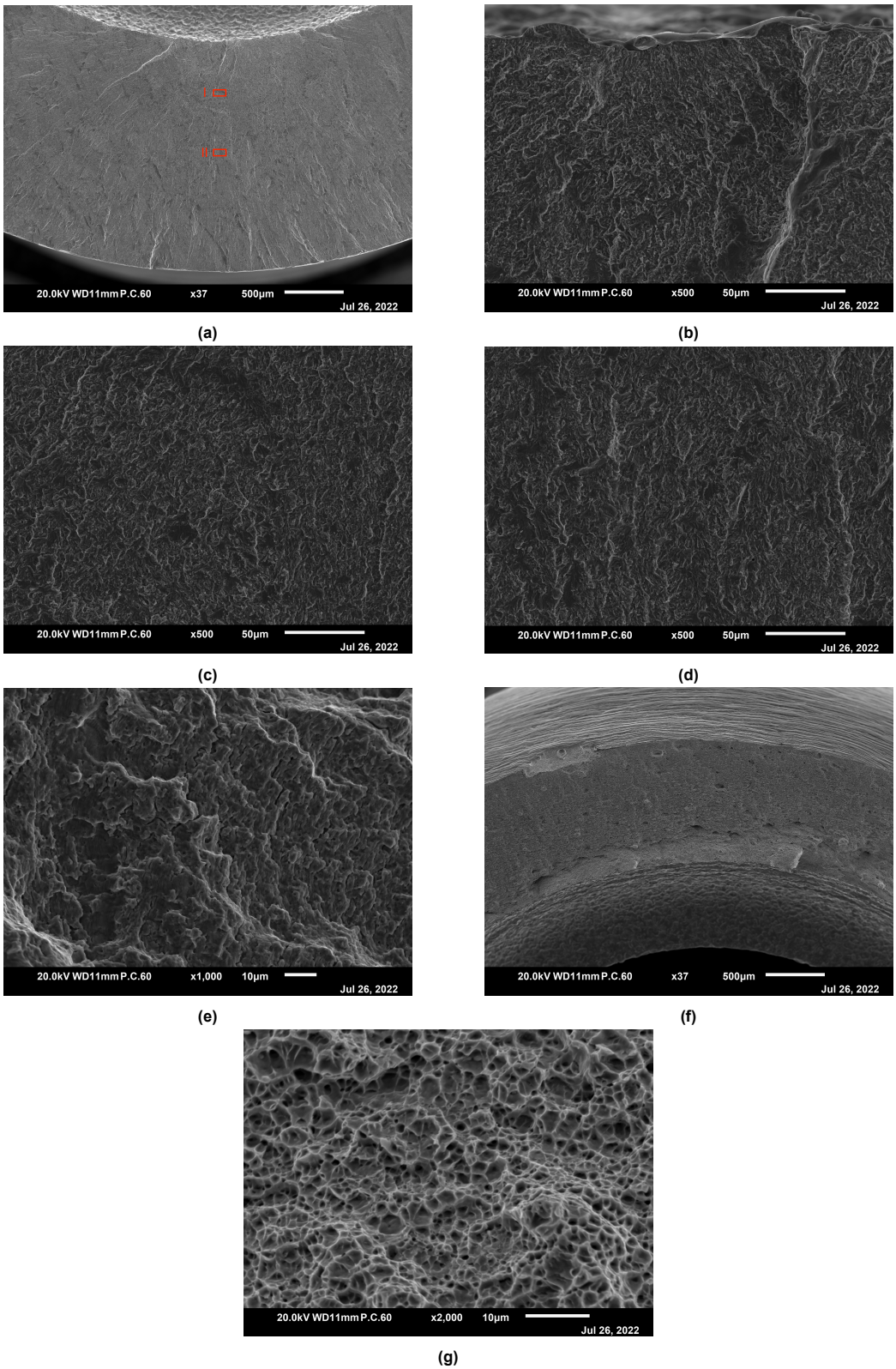

Figure G.3: SEM fracture surface images of 70 barg H_2 WM specimen. a) Overview of the notch region, b) zoom of notch c) zoom of annotated region I, d) zoom of annotated region II, e) striations in area II fatigue, e) fast fracture zone (also referred to as Area III in main text) and f) microvoids in fast fracture zone.

G.4. SEM Fractography Area III WM

Fig. G.4 provides an overview of Area III for a 150 barg N_2 WM tested specimen. This figure shows that the fracture surface contains areas where material is protruding (black arrow). This will result in cavities of equal size in the other half of the specimen. Examples of such cavities are indicated (blue arrow) in the figure. This also proves that the large cavities observed in Fig. 4.39 are primarily due to the protrusion of the material, rather than the contribution of welding defects. The WM shows a transition from a fine-dimple region at the inner surface to a larger sized dimple region when traversing through the ligament. The mechanics behind this are similar to the BM. The main difference however is, that the dimples in the WM are of a much smaller size than those in the BM. This is directly visible from Fig. G.5a and Fig. G.5b, which show a high magnification image of the fine-dimple region of a 150 H_2 and 150 barg N_2 specimen, respectively. The WM dimples are of smaller size, namely approximately 1-3µm. The BM dimples on the other hand have a size between 1-6 µm. The smaller WM dimples are related to the finer microstructure of the material. From the second-phase particles (blue arrows), it can be inferred that the microvoids originated by decohesion of the particle-interface matrix G.5. From a comparison of the two sub-figures, it can be concluded that the test environment did not cause any differences in terms of void morphology. Thus, for WM, and also for BM, the residual hydrogen concentration in the specimen did not influence the fatigue behaviour in Area III.

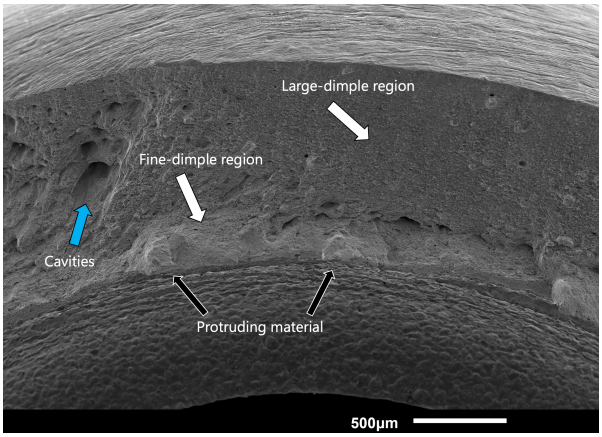

Figure G.4: Transition from Area II to Area III in 150 barg N_2 WM tested specimen. Black arrows indicate protruding material. Blue arrows define the cavities. White arrows indicate different dimple regions. The associated text determines whether it denotes the fine or large dimple region.

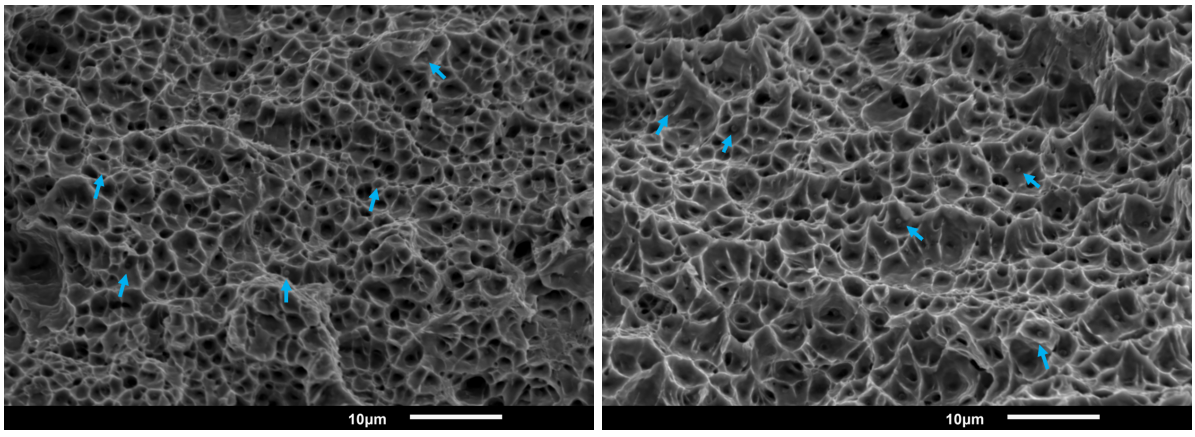

(a) (b)

Figure G.5: Magnification of the fine-dimple void region from 150 barg H_2 a) and 150 barg N_2 b) WM tested specimens. Second phase particles are indicated with blue arrows in both subfigures.

H. Electrical Discharge Machined Surface

The circumferential notch on the inside of the test piece was produced using electrical discharge machining. Inevitable in this process is the surface that is formed on the workpiece as a result of the solidification of the removed material. This layer is often referred to as the recast layer. From a post-mortem specimen whose (polished and etched) surface was analysed with SEM, the recast layer is visible in Fig. H.1 as a grey layer on the surface of the base metal. Note that this specimen was embedded in resin, and hence the area above the recast layer should be omitted in analysis. The recast layer is a thin layer that varies in thickness from 0.83 µm to 6.41 µm. The nonuniform thickness, or high roughness, results from the large number of current discharges involved for removing material. These so-called 'sparks' create small craters of different sizes in the recast layer. In Fig. H.1, such a crater could be linked with the deepest point in the material and thus the thinnest recast layer section (0.83 µm - 2.05 µm). The size of the craters in the formed layer is a function of the technological parameters set. Since the machining process was conducted by an external party, the parameters are unknown. Nevertheless, it can be stated that the recast layer has an average thickness of $\approx$ 2.78 µm.

The recast layer may have properties different from the bulk material and can negatively affect the structural performance. For instance, it has been evidenced that a higher surface roughness of a recast layer increases the likelihood of crack nucleation, thereby ultimately reducing the lifetime of the structure [149]. Since all samples were processed with identical test parameters, differences in lifetime cannot be attributed to the recast layer. Unless, of course, a defect has formed during the machining process.

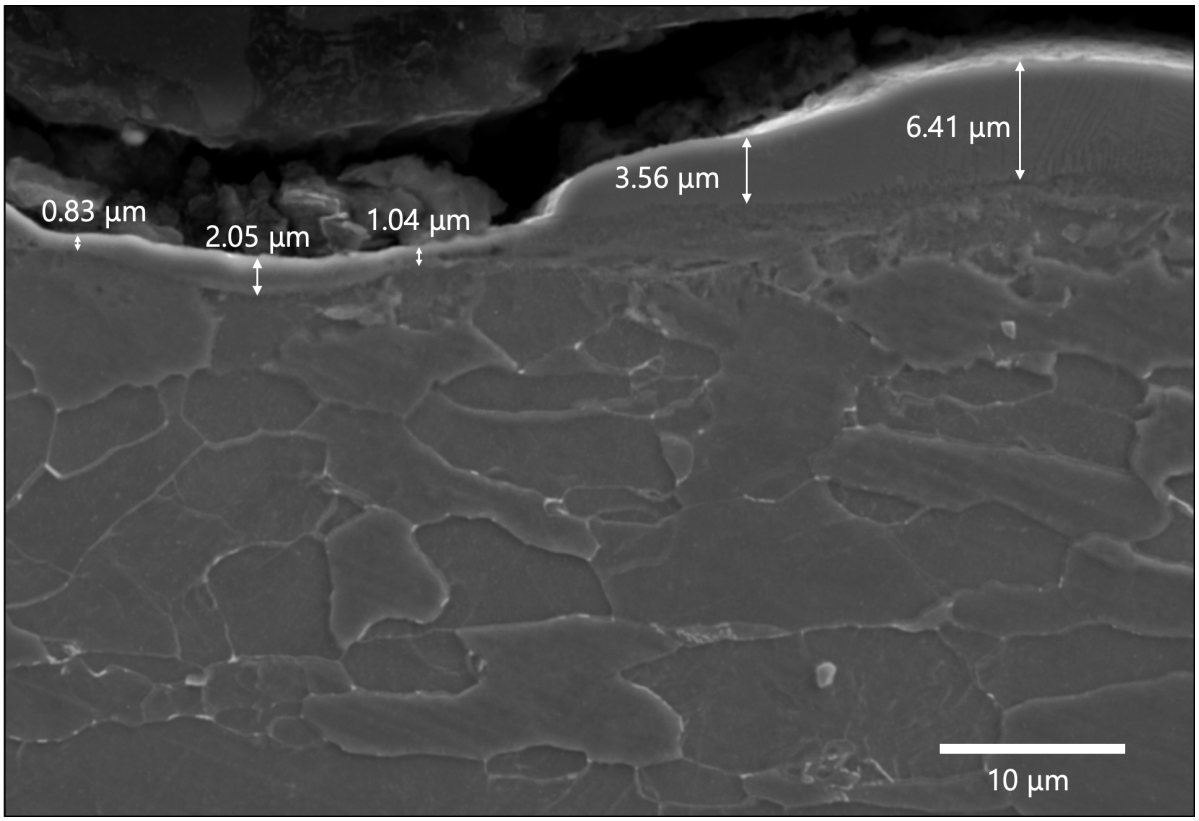

Figure H.1: The recast layer on the surface of the specimen, resulting from the electrical discharge machining to produce the notch. The recast layer can be identified as the layer on top of the surface of the base metal, which can be readily distinguished by the grains. The dark (black) area above the recast layer is the conductive resin used to embed the base material.